

The Eurasia Proceedings of Science, Technology, Engineering & Mathematics

EPSTEM

ISSN: 2602-3199

ICRES 2019: International Conference on Research in Education and Science

April 28 – May 01, 2019

Cesme, Turkey

Edited by: Mehmet Ozaslan (Co-chair), Gaziantep University, Turkey

ICRES 2019 DECEMBER

Volume 6, Pages 1-194 (December 2019)
The Eurasia Proceedings of Science, Technology, Engineering & Mathematics
EPSTEM

e-ISSN: 2602-3199

©2019 Published by the ISRES Publishing

Address: Istanbul C. Cengaver S. No 2 Karatay/Konya/TURKEY

Website: www.isres.org

Contact: isresoffice@gmail.com

Edited by: Mehmet Ozaslan

Articles: 1-30

Conference: ICRES 2019: International Conference on Research in Education and Science

Dates: April 28 – May 01

Location: Cesme, Turkey

Conference Chair(s): Prof.Dr. Mack Shelley, Iowa State University, USA & Prof.Dr. Mehmet Ozaslan, Gaziantep University, Turkey

CONTENTS

Obtaining of Ceramic Pigments Suitable for Silicate Industry / Pages: 1-10

Irena MARKOVSKA, Tsvetalina IBREVA, Tsvetan DIMITROV, Sevdzan CHITALJOVA

Buried Objects Segmentation and Detection in GPR B Scan Images / Pages: 11-17

Gozde ALTIN, Arif DOLMA

Broadband CPW-Fed U-Shaped Dielectric Resonator Antenna for Wireless and WiMAX/WLAN Applications / Pages: 18-24

Emad AHMED

Simulation Analyses of Flow in the Wake Region of Non-uniform Bridge Pier by using Computational Fluid Dynamic / Pages: 25-31

Sulaiman Dawood JASIM, Adnan A. ISMAEL, Manahil A.t. AL DABBAGH

Preparation and Characterization of Na-Alginate Hydrogel Beads / Pages: 32-38

Mehlika PULAT, Duygu OZUKAYA

The Synergism and Antagonism behavior of Aqueous Extraction for Black Tea, Green Tea and Coffee against the Effectiveness of Certain Antibiotics / Pages: 39-42

Tahreer Hadi Saleh AL-NADDAWI, Shaymaa Fadhel Abbas ALBAAYIT, Zainab Zamel KHALAF

Synthesis and Characterization of some New Dinuclear Complexes of Ni(II), Pd(II) and Pt(II) with Bulky Substituted Thioether Ligands / Pages: 43-51

A.m. AMEEN, N. H. BUTTRUS, Omar K. HASSAN

Determination of the Effect of Age of Broiler Breeders on General Performance, Egg Interior-Exterior Quality and Some Incubation Features / Pages: 52-62

Hakan YILDIRIM, Zekeriye AKCIMEN

The Interaction of a Charged Particle in the Generalized Woods-Saxon Potential / Pages: 63-67

Orhan BAYRAK

Investigation of Electronic Properties of Substituted Pyrimidine Derivatives with Density Functional Theory / Pages: 68-73

Erdem ERGAN, Esvet AKBAS

Domestic Battery Charge Unit Design and Production for Military Vehicle / Pages: 74-80

Ahmet AKTAS

ParEncrypt: A Two-phased Encryption for Improved Security / Pages: 81-87

Haneya KHAN, Asim SIDDIQUI, Fariha ISLAM, Elham HAMID, Ebru CELIKEL CANKAYA

Impact of the Chemical Mutagenesis on Biomass and Productivity of some Micro Green Algae / Pages: 88-95

Rasha Kareem Mohammed AL-SAEDI, Ali Muaed NAJEM, Ibrahim Jabber ABED

Synthesis and Characterization of Novel 1-(Morpholin-4-yl-methyl)-3-alkyl(aryl)-4-[3-ethoxy-4-(2-furylcarbonyloxy)-benzylidenamino]-4,5-dihydro-1H-1,2,4-triazol-5-ones / Pages: 96-100

Onur AKYILDIRIM, Haydar YUKSEK, Sevda MANAP

Theoretical Studies of the Molecular Structure, Conformational and Nonlinear Optical Properties of (2-Benzyloxy-Pyrimidin-5-Yl) Boronic Acid / Pages: 101-105

Guventurk UGURLU

Vitamin D Status And Parathyroid Hormone In Albanians / Pages: 106-110

Merita RUMANO, Anila MITRE, Elvisa RUMANO

Preparation of Gelatin and Chitosan Hydrogels Beads / Pages: 111-117

Mehlika PULAT

A New Potential Model for Cluster Decay of the Heavy Nuclei / Pages: 118-121

Orhan BAYRAK

Upconversion Emission Properties of Nb₂O₅ Modified Tellurite-Based Glasses Activated with Rare Earth Ions / Pages: 122-125

Huseyin ERTAP, Gokhan BILIR, Lidong MA, Baldassare DI BARTOLO

Theoretical Investigation of Nmr, Conformational, Vibrational and Electronic Structure of 3-Bromo-4-(2-Pyridyl) Thiophene / Pages: 126-130

Guventurk UGURLU

Nonlinear Optical Properties of Tellurite-based Glasses / Pages: 131-134

Gokhan BILIR, Mustafa YUKSEK, Ahmet KARATAY, Ayhan ELMALI

Isolation, Identification and Role of Glyphosate-Degrading Bacteria from Soils of Baghdad /

Pages: 135-137

Hala M. RADIF, Shaymaa Fadhel Abbas ALBAAÿIT

Optical Properties and Natural Radioactivity Levels of Turkish Natural Glass Obsidian / Pages: 138-141

Gulcin Bilgici CENGIZ, İlyas CAGLAR, Gokhan BILIR

Quantum Chemical Calculations for Corrosion Inhibition of Pyrimidine Derivatives / Pages: 142-147

Esvet AKBAS, Erdem ERGAN, Hakan DONMEZ

A Perturbative Approach in the Minimal Length of Quantum Mechanics / Pages: 148-150

Bekir Can LUTFUOGLU

Synthesis, Investigation and X-Ray Powder Diffraction (XRD) of Some Oxadiazole Complexes /

Pages: 151-161

Amerah Jihad AHMED SHAHEEN

Spectroscopic, Electronic and Non-Linear Properties of 2-[3-Phenyl-4,5-dihydro-1H-1,2,4-triazol-5-one-4-yl]-phenoxyacetic Acide / Pages: 162-170

Murat BEYTUR, Haydar YUKSEK

Comparison of Bridge Piers Shapes According to Local Scour Countermeasures / Pages: 171-180

Abdulnaser KASHMOOLA, Adnan ISMAEL, Saleh SULEIMAN

Comparison of Conventional and Encapsulated Urea on Growth and Yield of Wheat (*triticum aestivum* L.) / Pages: 181-187

Saima Kalsoom BABAR, Nazeer Ahmed HASSANI, İnayattullah RAJPAR, Shakeel Ahmed BABAR, Zia-ul-hassan SHAH, İmran KHAN

Enhancement Conventional Concrete using locally available Waste Material / Pages: 188-194

Ali Hussein ALI, Saleh Jaafer SULEIMAN, Mahmoud Majid HAMEED

Obtaining of Ceramic Pigments Suitable for Silicate Industry

Irena MARKOVSKA
Assen Zlatarov University

Tsvetalina IBREVA
Assen Zlatarov University

Tsvetan DIMITROV
Ruse University

Sevdzan CHITALJOVA
Assen Zlatarov University

Abstract: This study shows the possibility to synthesis ceramic pigments via solid-state high temperature sintering. The preparation of high temperature ceramic pigments using colourless stable crystal carcasses turns out to be quite suitable method in the case of $ZrSiO_4$ and their colouring by introducing different chromophores. The paper reports for experiments carried out on the synthesis of zircon pigments with the participation of following chromophore ions: Fe^{3+} , Co^{2+} , Ni^{2+} using the technology of solid phase sintering. Many analyses were used to determine the phase composition and check the chromophore ions valency state at temperature higher than the optimal temperature of synthesis. The colour of the pigments was determined using a Lovibond Tintometer RT 100 Color. The willemite ceramic pigments and rice husk ash were studied by X-ray analysis, scanning electron microscopy (SEM). It has been found that the synthesized pigments are suitable and can be successfully applied in glaze tiles and sanitary ceramics. The results obtained indicated that it depends on the sintering temperature isothermal soaking and the type of chromophore ion. In most pigments, the basic phase was obtained as low as 900 - 1000°C. The best pigments obtained were added to white faience glaze.

Keywords: Ceramic pigments, CIELab color measurement, Oxide additives, Chromophore ions

Introduction

The object of the present study is investigation of possibility of obtaining ceramic pigments by utilizing a widespread bio-waste - rice husks. The use of industrial waste (by-products) as raw materials in the ceramic industry has been under study for decades due to the economical, energy and environmental advantages [1-7]. The combustion of rice husk in air medium results in the production of white rice husk ash (RHA). Rice husk ash contains a high amount of SiO_2 - more than 90% [1]. In our work, as a source of SiO_2 , we have used white rice husk ash. Rice husk is waste product containing about 20 % SiO_2 . Rice husk is a by-product of rice milling process. Annually, about 500 mln tons of rice are processed to obtain 100 mln tons of rice husk. The latter contain 70-75% organic components and the rest is inorganic components, mainly SiO_2 . The use of bio-waste as raw materials in the ceramic industry has been studied for many years due to the economic, energy and environmental advantages.

Ceramic pigments are inorganic colored finely dispersed powders which, when added to some medium, impart certain color and change some of its properties. Beside their coloring ability, the ceramic pigments are resistant to atmospheric and chemical influences, high temperatures, decomposing activity of silicate melts and the effects of light [8-12]. These colored inorganic substances have high coefficient of light refraction, they are insoluble in water, organic solvents and binding materials but possess the ability to disperse in them and impart specific color.

- This is an Open Access article distributed under the terms of the Creative Commons Attribution-NonCommercial 4.0 Unported License, permitting all non-commercial use, distribution, and reproduction in any medium, provided the original work is properly cited.

- Selection and peer-review under responsibility of the Organizing Committee of the Conference

The coloring of the pigment occurs due to the selective absorption of certain wavelengths of light by its crystal lattice. As a result, the pigments are colored in a color complementary to the absorbed one. Most often, the color carriers in the pigments are the chromophores. These are atoms and atomic agglomerates which have the ability to impart one or another color to the substances where they are present.

The ceramic pigments must have the following properties: resistance to high temperatures, resistance to the eroding effects of silicate melts at the temperatures of sintering, high color intensity, cover ability, light stability. Most of the compounds obeying these requirements are colorless. To make them play the role of pigment, they are artificially colored by introducing substances imparting the desired color. Such properties have the compounds of transition d- and f- elements, e.g. vanadium, iron, cobalt, manganese, nickel, chromium, copper, praseodymium, etc. One of the most suitable materials complying with the requirements for pigments mentioned above is willemite. For this reason, it is more and more used for these purposes. Willemite is a mineral – zinc silicate. It has been discovered in the form of small brown crystals and in 1830 was named after the King of Holland Willem I (Willem Frederik). Willemite can be green, yellow, brown, red-brown, orange and blue. It can be found in nature as small prismatic or stubby crystals. It is one of not many silicates with trigonal singony which is more characteristic for the carbonates.

In our earlier studies, we have proved the effect of CoO as an oxide imparting saturated blue color to the willemite pigments [13, 14]. In the present work, the efforts were focused on the effects of other oxides, e.g. NiO and Fe₂O₃, besides CoO, on the synthesis and properties of willemite pigments suitable for the ceramic industry.

Materials and Methods

Materials

The synthesis of pigments is carried out by a solid state reaction using the following chemically pure initial materials: ZnO, CoO, Fe₂O₃, NiO. In these synthesized pigments ZnO was substituted particularly by CoO, Fe₂O₃, NiO. As a source of SiO₂, white rice husks were used.

Methods

The willemite ceramic pigments and rice husk ash were studied by X-ray analysis, infrared spectroscopy (FT-IR), differential thermal analysis (DTA) and scanning electron microscopy (SEM) as well as by the system of color measurement – CIELab.

The X-ray analyses were carried out by the method of powder diffraction using X-ray apparatus equipped D2 PHASER AXS- Bruker, with Cu anode and K_α emission, (CuK_α, λ=1.5406Å). The following operating regime was used during the experiments: current 10 mA and voltage 30 kV.

The FT-IR - studies were performed on a Tensor 27 Fourier infrared spectrophotometer FTIR (Bruker, Germany) in the interval 400 – 4000 cm⁻¹ at resolution of 1 cm⁻¹. Measurements were carried out at room temperature. The sample (0,3 mg) was tableted with KBr (100 mg) at a pressure of 2-4 atm.

The DTA experiments were performed on an apparatus for complex thermal analysis (STA 449 F3 Jupiter), NETZSCH, Germany by heating to 1100°C at a rate of 10°C min⁻¹.

The morphology and microstructure of the rice husk were examined by scanning electron microscopy (SEM). The electron microscope photographs of rice husk were taken using scanning electron microscope “Philips SEM525M/EDAX9900” with attached X- ray microanalyst. The microphotographs were made in a regime of secondary electrons at acceleration of 20 kV.

Color is one of the most important indicators of pigment quality. Colored substances absorb and convert light rays of a certain wavelength into the visible portion of the spectrum, due to their atomic structure. The CIELab system defines colors not only of ceramic pigments but also of other materials, which indicates that this system is universal and widely used. In the present paper the color determination of the pigments is determined spectrally by a tintometer of Lovibond Tintometer RT 100 Color. The colour measurements were performed using the CIELab method. This method, which is the standard analysis in the ceramic industry, especially for the

ceramic pigments allows to determine the whiteness and colour degree of tiles by measuring the three parameters: L^* , a^* and b^* , where:

- L^* (brightness), from absolute white $L^* = 100$ to absolute black $L^* = 0$
- a^* - green color (-) / red color (+)
- b^* - blue color (-) / yellow color (+)

The color space of the CIELab system is shown in Figure 1.

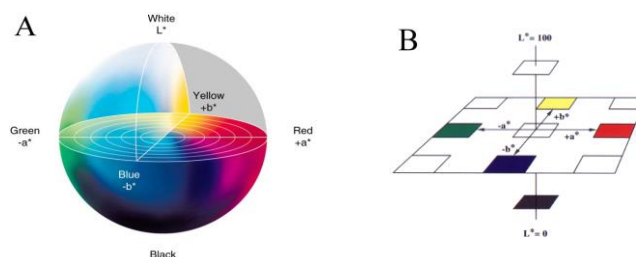


Figure 1. (A,B) The color space of CIELab system

Experiment

Quantities of the starting oxides (ZnO, CoO, Fe₂O₃, NiO) in the 100 g batch recipe are weighed to the nearest 0,1 g, then mixed and homogenized in a PULVERIZETE6 planetary mill of FRITCH. The blends' recipes are calculated as to partially replace ZnO with CoO, Fe₂O₃, NiO in the formation of the willemite. As a source of SiO₂ to the feedstocks, we have added rice husk oxidized at 650°C in air - rice husk ash (RHA). The present study was carried out with rice husk obtained during processing of rice variety Krasnodarski 424 grown in Bulgaria. They are arc-shaped and size approximately: 8 mm length, 2-3 mm width and 0,10±0,15 mm thickness. The husk contain 74,5% organic matter (cellulose, hemicellulose and lignine) and water, and the rest is inorganic matter containing 20% SiO₂ and 5,5% mixture of the following oxides: CaO, Fe₂O₃, MgO, Al₂O₃, Na₂O, K₂O, MnO₂, as well as traces of Cu and Pb [15-17]. These oxides, accompanying SiO₂ play the role of a mineralizer in the synthesis of pigments.

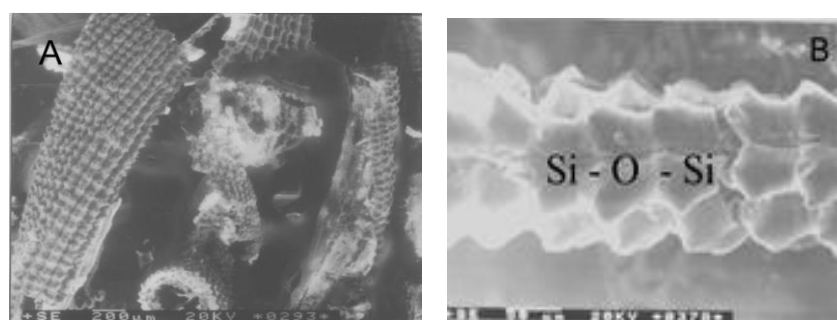


Figure 2. Microphotographs of oxidized rice husk

Figure 2. (A, B) shows images of rice husks burnt in air at greater (Figure 2A) and smaller (Figure 2B) magnification. It can be seen from the two images that mainly inorganic mass forming the silicon-oxygen carcass remains after the removal of the organics. The silicon-oxygen carcass (Si-O-Si) which builds the oxidized husk is clearly seen in Figure 2B.

The synthesis of pigments was carried out by the method of solid state sintering. The sintering of the initial blends, the compositions of which are presented in Table 1., was performed in a laboratory muffle furnace at heating rate 6 °C/min and 2 h isothermal period at the final temperature. The pigments were sintered at 900°C, 1000°C, 1100°C and 1150°C. After the sintering, additional homogenization was carried out in a planetary mill PULVERIZETE6, product of "FRITCH" Co.

Results and Discussion

Characterization of the blends by DTA

The raw materials mixtures were subjected to differential-thermal analysis to study the processes occurring with them at heating to 1100 °C. Three mixtures prepared for synthesis of pigments were analyzed: C1 and C2, N1 and N2, F1 and F2. The results obtained are presented in Figures 3-5.

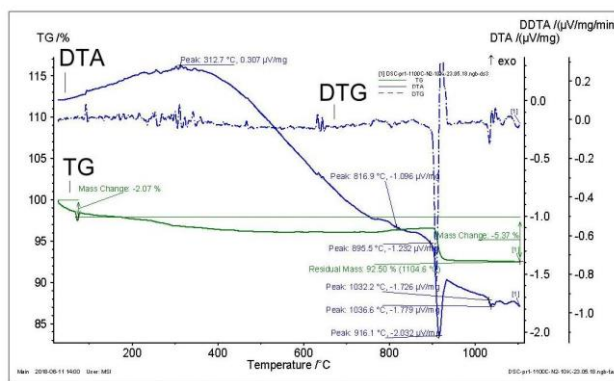


Figure 3. DTA of mixtures for samples C1 и C2 (synthesized at 1000 °C and 1150 °C)

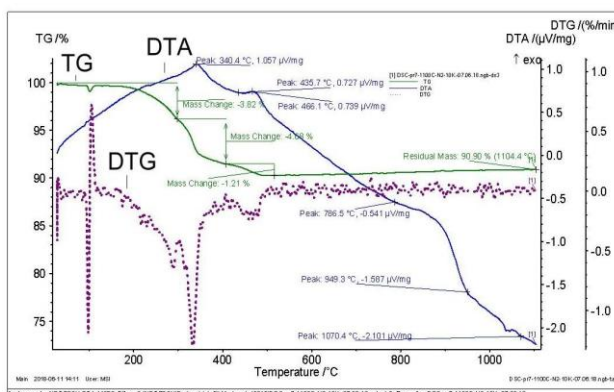


Figure 4. DTA of mixtures for samples N1 and N2 (synthesized at 1000 °C and 1150 °C)

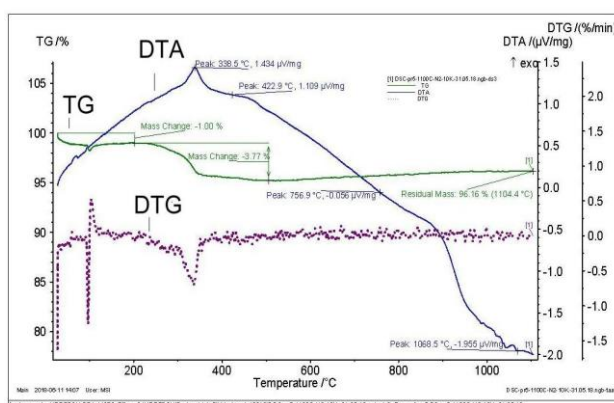


Figure 5. DTA of mixtures for samples F1 and F2 (synthesized at 1000 °C and 1150 °C)

The analysis of the TG curves showed that the biggest mass loss was observed for the mixtures containing NiO (N1 and N2) – 9,1% and the smallest – for mixtures F1 and F2 – 3,84%. The mass loss for the mixtures C1 and










C2 was 7,5 %. The peak observed at 100 °C was attributed to humidity elimination [18]. Further mass loss can be related to the finished oxidation of the residual carbon of the rice husk and release of volatile components of the rice husks and the mixtures.

Clearly distinguishable exothermic peak was observed in all the DTA curves: at 312 °C (fig.3), 340 °C (Figure 4.) and 338°C (fig.5) which was attributed to the finished oxidation of rice husks residual carbon. Figure 3. shows also a strong endothermic peak at around 920 °C which was can be connected with the transformation of willemite into cobaltine.

Color Measurement

One of the most characteristic properties of the pigments is their color. In this respect, one of the most important studies of pigments is connected with the determination of their color coordinates. The results obtained for color coordinates of the pigments synthesized from mixtures C1 – C5, F1 – F2 and N1 – N2 were determined in the system CIELab and they are shown in Table 1.

Table 1. Results of color coordinates measurements using CIELab system

| № sample | Composition | Color | T, °C | L* | a * | b * |
|----------|--|---|-------|-------|--------|--------|
| C1 | CoO.ZnO.SiO ₂ |  | 1000 | 31,50 | -3,35 | -9,50 |
| C2 | CoO.ZnO.SiO ₂ |  | 1150 | 28,25 | 3,03 | -17,74 |
| C3 | 0,375 CoO.1,625.ZnO.SiO ₂ |  | 900 | 35,82 | -6,93 | -14,26 |
| C4 | 0,375 CoO.1,625.ZnO.SiO ₂ |  | 1000 | 35,68 | 2,08 | -41,24 |
| C5 | 0,375 CoO.1,625.ZnO.SiO ₂ |  | 1100 | 34,70 | 10,72 | -39,08 |
| F1 | Fe ₂ O ₃ .ZnO.SiO ₂ |  | 1000 | 53,14 | 23,23 | 44,16 |
| F2 | Fe ₂ O ₃ .ZnO.SiO ₂ |  | 1150 | 35,91 | 14,12 | 17,17 |
| N1 | NiO.ZnO.SiO ₂ |  | 1000 | 69,86 | -3,94 | 21,62 |
| N2 | NiO.ZnO.SiO ₂ |  | 1150 | 63,29 | -13,75 | 15,97 |

It can be seen from the data presented that the best results were obtained by the synthesis of the Co-willemite pigments. The most saturated color had the pigment with composition C4 (0,375CoO.1,625ZnO. SiO₂) sintered at 1000 °C where the amount of blue color measured in the CIELab system was b* = -41.24. The results shown in Table 1. indicated that the optimal temperature for synthesis of cobalt-willemite pigments is 1000 °C.

The pigments synthesized which contained iron – mixtures F1 and F2 had brown color with the values of the coordinates a* and b* decreasing with the increase of the sintering temperature – they were a* - 23,23 and b* - 44,16 at 1000 °C and a* - 14,12 and b* -17,17 at 1100 °C.

The color observed for the nickel-willemite pigments was green and the amount of green color increased with the increase of the sintering temperature (-a*) while parameter (+b*) decreased.

A tendency of decrease of luminance L* was observed for all the pigments (they became darker) with the increase of the sintering temperature.

X - ray Analysis

The X-ray analysis carried out showed that cobalt-willemite ceramic pigments were synthesized in the system x.CoO.(2-x).ZnO.SiO₂, where x=0,375 and 1,00, as well as nickel-willemite ceramic pigments in the system NiO.(2-x).ZnO.SiO₂, where x=1,00 (Figures 6-9). The addition of iron resulted in synthesis of spinel pigments containing smaller amounts of willemite. (Figure 8.). The results shown in Figures6-9 correlate excellently with these for color and luminance presented in Table 1.

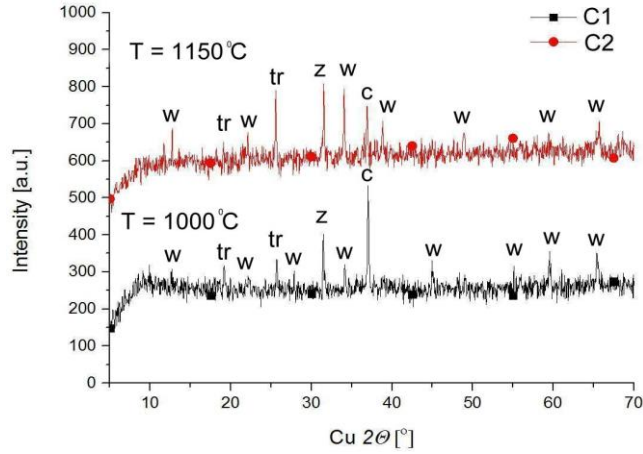


Figure 6. XRD parents of Co - doped zinc silicate annealed at 1000 and 1150 °C. Legend: w- willemite, tr- trydimite (SiO_2), z- ZnO, c- CoO

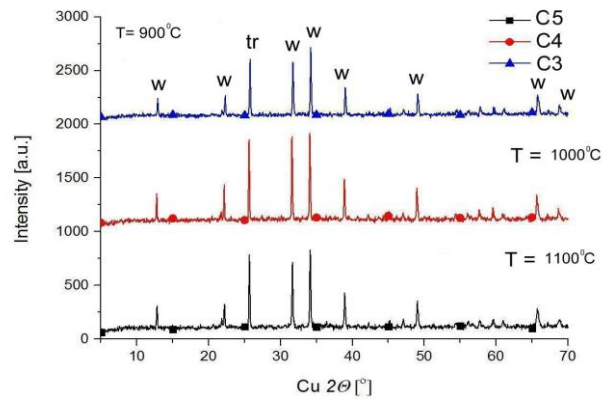


Figure 7. XRD parents of Co - doped (0,375CoO) zinc silicate annealed at 900, 1000 and 1100 °C. Legend: w- willemite, tr- trydimite (SiO_2)

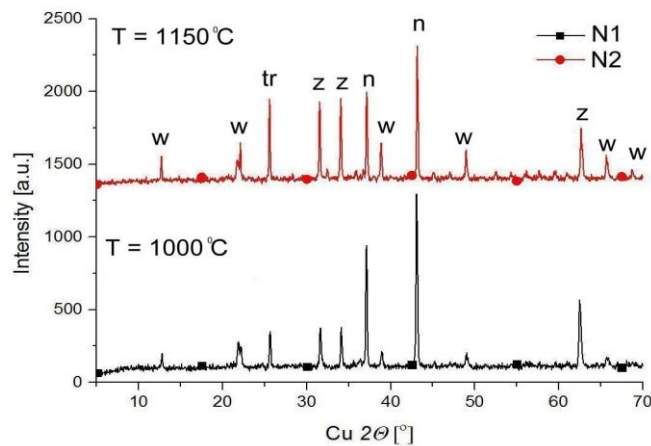


Figure 8. XRD parents of Ni - doped zinc silicate annealed at 1000 and 1150 °C. Legend: w- willemite, tr- trydimite (SiO_2), z- ZnO, n - NiO

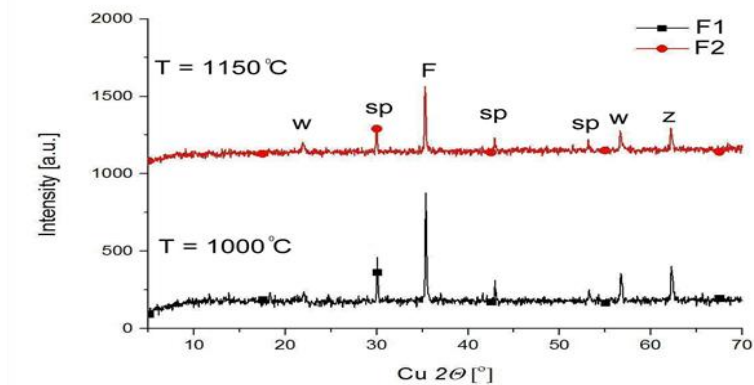


Figure 9. XRD parents of Fe - doped zinc silicate annealed at 1000 °C and 1150 °C. Legend: w- willemite, sp- spinel ($ZnO \cdot Fe_2O_3$), z- ZnO, f- Fe_2O_3

The diffraction patterns shown above (Figures 6-9) indicated that it is possible to obtain willemite pigments by substitution of ZnO with CoO and NiO. It can be concluded from the four figures that the best results were obtained for the mixtures with 0,375 CoO – C3÷C5. The powder heated at 900 °C, 1000 °C and 1100 °C consisted mainly of crystalline Zn_2SiO_4 (willemite). X- ray data shows that the quality of Zn_2SiO_4 is achieved at 1000°C – composition C4 (Figure 7.). This fact is confirmed by the work of T. Pangilinan-Ferolin and R. Vequizo [19] who studied the synthesis of zinc silicate by solid-state reaction using silica from rice husks ash (RHA). In mixture C4 sintered at 1000 °C, obviously, complete substitution of zinc by cobalt in the crystal lattice of zinc silicate was achieved to form willemite-cobaltine and this is the reason for the better values determined by the measurement of color coordinates of the pigments ($b^* = -41,24$ and $L^* = 39,08$). Significant amount of cobaltine was obtained with the mixtures containing 1 mole CoO but the color coordinates measured were worse than these for the compositions with 0,375 CoO.

By the addition of BiO in the initial mixture, a weaker interaction was observed between ZnO and SiO_2 from the rice husks and, respectively, less zinc was substituted by nickel in willemite lattice (Figure 8.).

The smallest amount of willemite was obtained by the addition of Fe_2O_3 to the initial mixtures. In this case, Fe_2O_3 bonds predominantly with ZnO to form a new compound – chemically bonded spinel $ZnO \cdot Fe_2O_3$ (Figure 9.). Most probably, the reason for this was preservation of the electroneutrality of the lattice.

In the system $Fe_2O_3 - ZnO - SiO_2$, practically brown spinel pigments with very good characteristics were obtained. Better color characteristics had the pigments synthesized at 1000°C – mixture F1 ($b^* = 44,16$, $L^* = 53,14$). With this composition, the amount of the spinel phase predominates the willemite phase (Figure 8.). The works of Masslennikova et al. confirm our results for Ni and Fe doped pigments [20-21]. By the high temperature sintering of the four initial mixtures, beside the newly formed chemical compounds – willemite or spinel, remain unreacted initial oxides the peaks of which can be observed in the diffraction patterns. The results obtained from the XRD analysis showed that almost all of the SiO_2 from the rice husks reacted with ZnO in mixtures C1 – C5, N1 and N2 to give willemite, while in mixtures F1 and F2 (Figure 9.) SiO_2 binds to ZnO mainly before the formation of spinel - $ZnO \cdot Fe_2O_3$ so the willemite synthesized was less. It can be seen in all the four Figures 6 -9 that due to the presence of alkali impurities in the rice husks (Na_2O , K_2O), the high temperature modification of SiO_2 was α - tridymite but not α - cristobalite, as it usually occurs in practices.

FT-IR Analysis

Three kinds of pigments synthesized at 1150°C and containing: CoO (composition C2), NiO (composition N2) and Fe_2O_3 (composition F2) were subjected to FT-IR analysis. The FT-IR spectra of $Zn_{2-x}Co_x SiO_4$, $Ni_{2-x}Co_x SiO_4$, and Fe- Zn spinel pigments sintered at 1150 °C are shown in Figures 10-12.

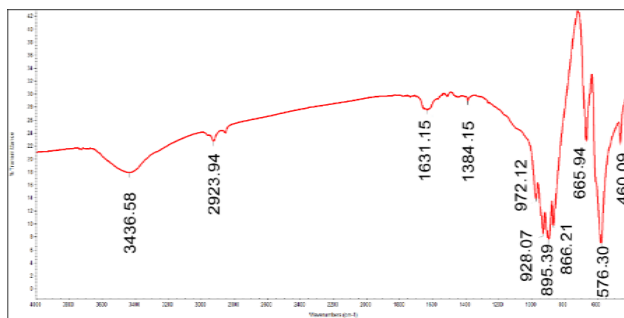


Figure 10. FTIR spectrum of composition C2 (CoO.ZnO.SiO₂)

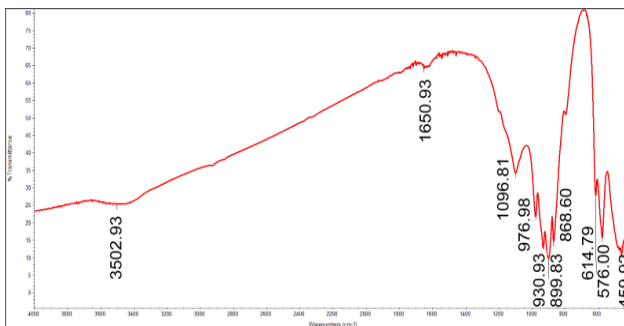


Figure 11. FTIR spectrum of composition N2 (NiO.ZnO.SiO₂)

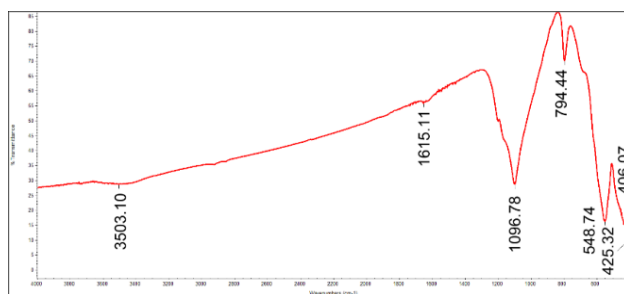


Figure 12. FTIR spectrum of composition F2 (Fe₂O₃.ZnO.SiO₂)

The weak absorption bands present in all the three spectra with maximum at about 3436 - 3500 cm⁻¹ can be attributed to the valent vibrations of the OH bond in the water molecules with hydrogen bonds. The weak absorption band at 1631,15, 1650,93 and 1615,11 cm⁻¹, resp., results from the deformation vibrations of the water molecules (δ -H₂O) [16]. The intense band at 1096.81 cm⁻¹, resp. 1096,78 cm⁻¹, was due to the valent vibrations of the silicon-oxygen tetrahedrons - ν_{as} (SiO₄). The characteristic bands at 976,98 cm⁻¹, respectively 972,12 cm⁻¹; 928,07 cm⁻¹, respectively 930,93 cm⁻¹ and 895,39 cm⁻¹, respectively 899,83 cm⁻¹ corresponds to asymmetric stretching vibration modes as (SiO₄) [22]. The characteristic bands at 866,21 cm⁻¹, respectively 868,60 cm⁻¹, and the presence of an absorption band at 794 cm⁻¹ can be explained by symmetric stretching vibration (s) of Si-O bonds from silicon-oxygen tetrahedra (SiO₄). The two vibrations at 576,30 cm⁻¹, respectively 576,00 cm⁻¹ and 614,79 cm⁻¹, characterize the willemite structure and probably correspond to the asymmetric modes of vibrations (ν_{as} ZnO₄) and symmetric (ν_{s} ZnO₄) [22].

The existence of absorption bands in the low-frequency part of the spectra at about 460/459,92 cm⁻¹ can be attributed to the deformation vibrations (δ_{as}) of the bonds Si - O in the SiO₄, tetrahedrons, as well as to the symmetric stretching vibration of ZnO₄ (ν ZnO₄) [16,22].

Conclusion

The possibility to synthesize willemite pigments by substitution of ZnO with CoO and NiO: Zn_{2-x}Co_x SiO₄ and Ni_{2-x}Co_x SiO₄ was proved. It was found that the best results were obtained with the cobalt doped pigment with composition C4 (0,375CoO.1,625ZnO.SiO₂) synthesized at temperature of 1000 °C.

In those case, zinc was totally substituted by cobalt in the crystal lattice of the zinc silicate to form willemite-cobaltine and this stipulates the better result obtained by the measurement of the color coordinates of the pigments where the amount of blue color measured in the system CIELab was $b^* = -41.24$. The same composition showed also the highest luminance ($L^* = 39,08$) and saturation of the color.

The XRD analyses indicated that the addition of NiO to the initial mixture leads to worse substitution of zinc by nickel in the willemite lattice so the amount of willemite formed was less. The pigments synthesized had green color.

By the addition of Fe_2O_3 resulted in simultaneous synthesis of willemite and iron-zinc spinel where the Fe-Zn spinel ($ZnO.Fe_2O_3$) predominated. At temperature of synthesis $1000^\circ C$, the spinel phase was the biggest one and pigments were colored in light-brown. The optimal parameters for the process of synthesis of all the initial mixtures were established. The synthesized pigments are suitable and can be successfully applied in glaze tiles and sanitary ceramics.

Acknowledgements

The financial support of this work by the Bulgarian Ministry of Education and Science, National Research Fund under the contract number KP-06-H27/14 - 2018 is gratefully acknowledged.

References

- Serra, M. F., Conconi, M. S., Gauna, M. R., Suárez, G., Aglietti, E. F., Rendtorff, N. M. (2016, March). Mullite ($3Al_2O_3 \cdot 2SiO_2$) ceramics obtained by reaction sintering of rice husk ash and alumina, phase evolution, sintering and microstructure. *Journal of Asian Ceramic Societies*, 4, 1, pp 61-67.
- Sutcu, M., Akkurt, S. (2009, September). The use recycled paper processing residues in making porous brick with reduce thermal conductivity. *Ceramics International*, 35, 7, pp 2625-2631.
- Quaranta, N., Unsen, M., López, H., Giansiracusa, C., Roether, J. A., Boccac-cini, A. R. (2011, January). Ash from sunflower husk as raw material for ceramic products. *Ceramics International*, 37, 1, pp. 377-385.
- Vieira, L. A., Folgueras, M. V., Tomiyama, M., Prim, S. R. (2018, January). Rice husk ash as a raw material to produce willemite pigments. *Materials Science. Forum*, 912, pp.44-49.
- Raupp-Pereira, F., Hotza, D., Segadães, A. M., Labrincha, J. A. (2006). Ceramic formulations prepared with industrial wastes and natural sub-products. *Ceramics International*, 32, 2, pp. 173-179.
- Kumar, P., Srivastava, A., Kumar, V., Majhi, M., Singh, V. (2014). Implementation of industrial waste ferrochrome slag in conventional and low cement castables: Effect of microsilica addition. *Journal of Asian Ceramic Societies*, 2, 2, pp. 169-175.
- Sultana, M., Ahmed A., Zaman, M., Rah man M., Biswas, P., Nandy, P. (2015) Utilization of hard rock dust with red clay to produce roof tiles. *Journal of Asian Ceramic Societies*, 3, 1, pp. 22-26.
- Ozel, E., Yurdakul, H., Turan, S., Ardit, M., Cruciani, G., Dondi, M. (2010, December). Co-doped willemite ceramic pigments: Technological behaviour, crystal structure and optical properties. *Journal of the European Ceramic Society*, 30, 16, pp. 3319-3329.
- Galindo R., Llusar, M., Tena, M. A., Monros, G., Badenes, J. A. (2007). New pink ceramic pigment based on chromium (IV)-doped lutetium gallium garnet. *Journal of the European Ceramic Society*, 27, 1, pp. 199-205.
- Alarcon, J., Escribano P., Gargallo, J. (1984). Cr-CaO-SiO₂ Based Ceramic Pigments, *British Ceramics Transactions*, 83, 3, 81-83.
- Carda, J., Monros, G., Escribano, P., Alarcon, J. (1989, January). Synthesis of uvarovite Garnet. *Journal of the American Ceramic Society*, 72, 1, pp. 160-162.
- Klemme, S., van Miltenburg, J., Javorsky, P., Wastin, F. (2005). Thermodynamic properties of uvarovite garnet ($Ca_3Cr_2Si_3O_{12}$). *American Mineralogist*, 90, 4, pp. 663-666.
- Dimtrov, Ts., Markovska I., Ibrevva Ts. (2018). Synthesis and investigation of cobalt-willemite pigments, *Eurasian Union of Scientists (EUS)*, 5 (50), pp. 55-58.
- Dimitrov Ts., (2016). Synthesis and study of Co-doped willemite ceramic pigments. *Proceedings of University of Ruse Angel Kanchev*, 55, book 10.1, pp. 102-107.
- Vlaev, L. T., Markovska, I. G., Lyubchev, L. A. (2003). Non-isothermal kinetics of pyrolysis of rice husk. *Thermochimica Acta*, 406, 1-2, pp. 1-7.
- Markovska, I. G., Lyubchev, L. A. (2007). A study on the thermal destruction of rice husk in air and nitrogen atmosphere. *Journal of Thermal Analysis and Calorimetry*, 89, 3, pp. 809-814.

- Vlaev, L. T., Markovska, I. G., Lyubchev, L. A. (2004). Kinetics compensation effect at thermal degradation of rice husk. *Oxidation communication*, 27, 2, pp. 444-452.
- Cannio, M., Bondioli, F. (2012, March). Mechanical activation of raw materials in the synthesis of Fe₂O₃-ZrSiO₄ inclusion pigment. *Journal of the European Ceramic Society*, 32, 3, pp. 643-647.
- Tender Pangilinan-Ferolin., Reynaldo M. (2013). Vequizo. Synthesis of Zinc Silicate Using Silica from Rice Hull Ash (RHA). *Through Solid-State Reaction. International Engineering and Technology Education Conference '13. Conference Proceedings*. Ho Chi Minh City, Vietnam.
- Masslennikova, G. N., Glebicheva, A. I., Fomina, N. P. (1974). Willemite pigments with NiO addition. *Glass and Ceramics*, 8, pp. 23-25.
- Masslennikova, G. N., Fomina N. P., G. N., Glebicheva A. I. (1975). Synthesis of iron-containing Willemite pigments. *Glass and Ceramics*, 4, pp. 26-27.
- Chandra Babup B., Vengla Ra, B., Ravi, M., Babu, S. (2017, January). Structural, microstructural, optical, and dielectric properties of Mn²⁺: Willemite Zn₂SiO₄ nanocomposites obtained by a sol-gel method. *Journal of Molecular Structure*, 1127, 5, pp. 6-14.

Author Information

Irena Markovska

Assen Zlatarov University - Burgas
Prof. Yakimov Str. 1,
8010, Bulgaria
Contact E-mail: imarkovska@btu.bg

Tsvetalina Ibrev

Assen Zlatarov University - Burgas
Prof. Yakimov Str. 1,
8010, Bulgaria

Tsvetan Dimitrov

Ruse University Angel Kanchev,
Branch Razgrad, bul. Aprilsko Vastanie, 47
Razgrad, Bulgaria

Sevdzan Chitaljova

Assen Zlatarov University - Burgas
Prof. Yakimov Str. 1,
8010, Bulgaria

Buried Objects Segmentation and Detection in GPR B Scan Images

Gozde ALTIN
Kocaeli University

Arif DOLMA
Kocaeli University

Abstract: Identification of buried objects through Ground Penetrating Radar B scan (GPR-B) images needs high computational techniques and long processing time due to curve fitting or pattern recognition methods. In this study, an efficient and fast recognition system is proposed for detection of buried objects region. Previously, GPR-B scan images of objects with different shapes in various depths were obtained by using gprMax simulation program. The detection process is categorized into four steps. The GPR-B images are transformed at first step. Then, they are thresholded to obtain potential buried object regions. Third step of the system is hough transform in order to eliminate ground surface. Finally, an estimated region analysis is performed. The results show high performance with fully automatic segmentation. The processing time for detection of buried object is in the range of 1.234 - 2.232 seconds. It can be observed that this technique is faster than other studies in the literature. Consequently, it may be used in real time applications for GPR devices.

Keywords: Ground penetrating radar, GprMax, image processing, Otsu thresholding, Hough transform

Introduction

The non-destructive techniques to explore underground materials have recently had great interest by public. Especially, private entities have applied it on widespread areas such as gas exploration, pipe localization, geology and archaeology etc. It is necessary to use an appropriate sensor for underground imaging in accordance with types of applications. Ground Penetrating Radar (GPR) has been widespread for subsurface mapping via using electromagnetic waves with high frequency [1]. GPR can scan in the range from various centimeters to a few meters because it operates on the principle of transmitting and receiving electromagnetic waves. There are several studies for automatic detection of buried objects from GPR images. Capineri et al. suggested hough transform to describe the ground plane in GPR image [2]. Brunzell could separate the reflected signal from soil surface and underground objects by means of appropriate algorithms and classical detection methods [3]. Delbo et al. used wavelet transform to reduce noise on GPR images and on top that hyperbolic identification is provided via fuzzy clustering algorithms [4]. With some preprocessing algorithms, hyperbolic structures in the GPR image are foregrounded and automatically classified with artificial neural networks by Gamba et al. [5]. Noise reduction on GPR image is provided by preprocessing algorithms and then artificial neural network segmented them. Hyperbolic lines are identified using hough transform [6]. Youn et al. examined the effects of different levels of clutter and noises on performance of artificial neural networks in GPR images [7]. Rossini detected underground objects by using wavelet transform and mathematical interpolation model [8]. Shihab et al. computed higher order statistical features for neural network classification in order to distinguish between soil ground and underground objects [9]. Gamba et al. obtained high performance for detection of buried objects by combination of artificial neural network and template matching algorithms [10]. Falorni et al. used monodimensional gradient filter to identify hyperbolic patterns [11]. Dell'Acqua et al. presented an approach based on 3-D Radon transform to eliminate interference and masking in GPR images [12]. Ting-Jun extracted hyperbola apexes by using peak tracing and hyperbola symmetry [13].

The aim of this paper is to offer an efficient and fast fully automatic image processing method for detection of buried objects in GPR images. The attractive feature of this method is able to analyze GPR images without the

- This is an Open Access article distributed under the terms of the Creative Commons Attribution-Noncommercial 4.0 Unported License, permitting all non-commercial use, distribution, and reproduction in any medium, provided the original work is properly cited.

- Selection and peer-review under responsibility of the Organizing Committee of the Conference

need of any specialist support. The proposed system includes preprocessing, segmentation, object detection stages. The preprocessing process for GPR images require to separate different RGB color space. Red channel of GPR images is the most appropriate platform for the image segmentation. Then, the images are segmented by Otsu thresholding method. The hyperbolas is identified by hough transform. Finally, the region analysis is implemented. The rest part of the paper is organized as follows. It is introduced that how to obtain GPR signals and images in Section II. The proposed image processing algorithm is described in Section III. The experimental results drawn in Sections IV. Section V inserts the conclusion part.

Materials

Python is used for design of gprMax program which has not any user interface. It is open source program based on simulation of electromagnetic wave propagation. It tries the Finite Difference Time Domain (FDTD) method in order to solve Maxwell equations in three dimension. GPR data can be obtained by gprMax program. GPR data can be obtained in three ways: A-scan, B-scan and C-scan.

The data is taken by an unique transceiver antenna at a fixed position (x, y) as shown in Figure 1 for GPR A scan signal. The propagation duration of the electromagnetic wave varies depending on its speed. A scan signals can be used to detect locations of buried objects via propagation duration.

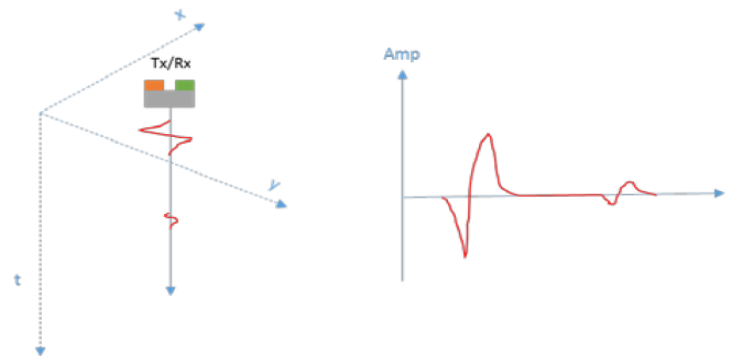


Figure 1. Example of GPR A Scan Signal

GPR B scan images consist of A scan signals along the x axis measured at regular intervals as shown in Figure 2. A GPR image is generated in accordance with the characteristic of the received signal. The vertical axis (y) represents the depth of the ground in relation to the signal time (t), while the horizontal axis (x) symbolizes the surface distance. Buried objects in B scan image are displayed as hyperbola.

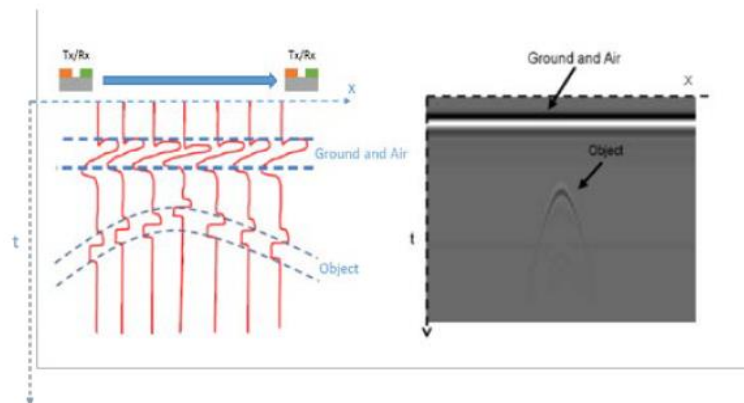


Figure 2. Example of GPR B Scan Image

GPR C scan is three-dimensional image which is generated by combining simultaneous B scan images on the xy plane. Signal time (t) represents depth of the ground. Particularly, y axis is important role for construction GPR C scan which is not preferred over other scan types because it is too expensive and taking much more time.

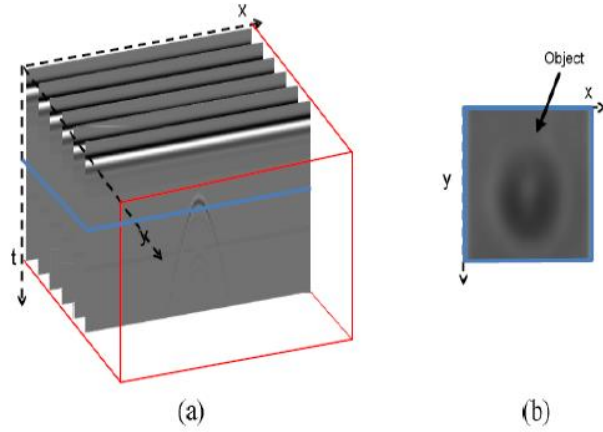


Figure 3. a) C-scan Measurement b) C scan image

Methods

RGB Color Space

The basic three colors are Red (R), Green (G) and Blue (B) which are mixed to get any color in digital color image. The RGB color space can be transformed into a 3D color space with coordinate axes red, green, and blue. In grayscale digital images, the pixels contain all the intensity information starting from the weakest to the strongest. A colored image is converted to a grayscale, which makes it easier to perceive desired regions for image segmentation. The R, G, B pixel values in the color images are converted to gray values as shown in Eq. 1. Also, Y represents gray level of color image.

$$Y = 0.2989R + 0.587G + 0.114B \quad (1)$$

Otsu Thresholding

Otsu thresholding method is applied on the Red channel of GPR B scan images. Gray scale distribution histogram and average gray pixel value are used in the most of threshold segmentation method. The pixels are divided into two classes as C_0 and C_1 at gray level t . C_0 is in the range from 0 to $t-1$ and C_1 is between t and $L-1$. Gray level probability distributions are calculated for C_0 and C_1 as in Eq.2 and Eq.3.

$$\omega_0 = P(C_0) = \sum_{i=0}^{t-1} P_i \quad (2)$$

$$\omega_1 = P(C_1) = \sum_{i=t}^{L-1} P_i \quad (3)$$

The means of C_0 and C_1 classes are computed as in Eq.4 and Eq.5.

$$\mu_0 = \sum_{i=0}^{t-1} i.P_i / \omega_0 \quad (4)$$

$$\mu_1 = \sum_{i=t}^{L-1} i.P_i / \omega_1 \quad (5)$$

The total mean of C_0 and C_1 classes is denoted by Eq.6.

$$\mu_T = \omega_0\mu_0 + \omega_1\mu_1 \quad (6)$$

The variances of C_0 and C_1 classes are

$$\sigma_0^2 = \sum_{i=0}^{l-1} (i - \mu_0)^2 p_i / \omega_0 \quad (7)$$

$$\sigma_1^2 = \sum_{i=l}^{k-1} (i - \mu_1)^2 p_i / \omega_1 \quad (8)$$

The within-class variance is computed as in Eq. 9.

$$\sigma_w^2 = \sum_{k=0}^M \omega_k \sigma_k^2 \quad (9)$$

The between-class variance is formulated as Eq. 10.

$$\sigma_b^2 = (\omega_0)(\mu_0 - \mu_T)^2 + (\omega_1)(\mu_1 - \mu_T)^2 \quad (10)$$

The total gray variance is

$$\sigma_T^2 = \sigma_w^2 + \sigma_b^2 \quad (11)$$

In Otsu method, the within-class variance is maximized and the between-class variance is minimized by threshold value t .

Hough Transform and Region Analysis

The Hough transform can be defined as a transformation of a point to a parameter space of x, y plane. The parameter space is occurred in accordance with the shape of interest objects. A straight line passing through the x_1, x_2 point on the x, y plane is expressed as shown in Eq. 12.

$$y_1 = ax_1 + b \quad (12)$$

In this notation, which expresses an equation of a straight line in the Cartesian coordinate system, it represents the parameters a and b . This equation is not used in the Hough transformation for straight line description. Because the lines perpendicular to the x axis have infinite value. This requires that the parameter space of a and b be in infinite size. Therefore, θ and p are used for representation of a straight line. Line equation in parameter space is given in Eq. 13.

$$p = x \cos(\theta) - y \sin(\theta) \quad (13)$$

Circles can be expressed more simply in parameter space than line representation. Because the parameters of the domain can be transferred directly to the parameter space as in Eq. 14.

$$r^2 = (x-a)^2 + (y-b)^2 \quad (14)$$

There are three parameters of the circle as a, b and r which denote direction and radius of circle, respectively. The parametric representation of the circle is as in Eq. 15 and Eq. 16.

$$x = a + r \cos(\theta) \quad (15)$$

$$y = b + r \sin(\theta) \quad (16)$$

The parametric space of the circle belongs to R_3 ; on the other hand, the parametric space of line belongs to R_2 . As the parameters representing the shape increase, the parameter space R will also increase and the Hough transformation will become more complex. a, b , and r are the parameters to be used for the circular Hough transformation. The circles that can be drawn are centered at any point on the ab plane. When r is radius of the

circle, this circle can be plotted on the parameter space. Region analysis bases on regionalization and hyperbolic identification. One or more connected pixel region can be combined in a single region. Regionalization starts by evaluating each pixel. If a pixel is found, the other pixels in the same region are checked in the algorithm loop. It is ensured that the hyperbolas regions are drawn by taking the eccentricities and their areas into consideration after all regions are obtained.

Proposed Method

In GPR B scan images, many different methods have been proposed for extracting the ground plane and plotting the estimated location of the buried objects. Within the scope of this study, working in RGB color space is suitable platform for segmenting of the ground plane and the location of the buried objects. For this reason, red channel is selected in RGB space and soil and objects are segmented by using the Otsu threshold method. Soil planes are extracted by Hough transformation. Estimated buried object region is drawn by region analysis method.

Results and Discussion

Implementation results and performance results of proposed algorithms are described in this section. The algorithm is applied on 8 pieces GPR B scan images which are produced by gprMax program based on python software. All images are resized as 2629x1441 pixel. It is performed in a computer with Aspire 5930 Intel Core 2 Duo P8600 2.0 GHz Montevina processors. 2GB of RAM with 256 MB of GDDR3 GeForce supported system memory with nVIDIA 9600M GT graphics card is used. The image processing results of the algorithm are described in Figure 4.

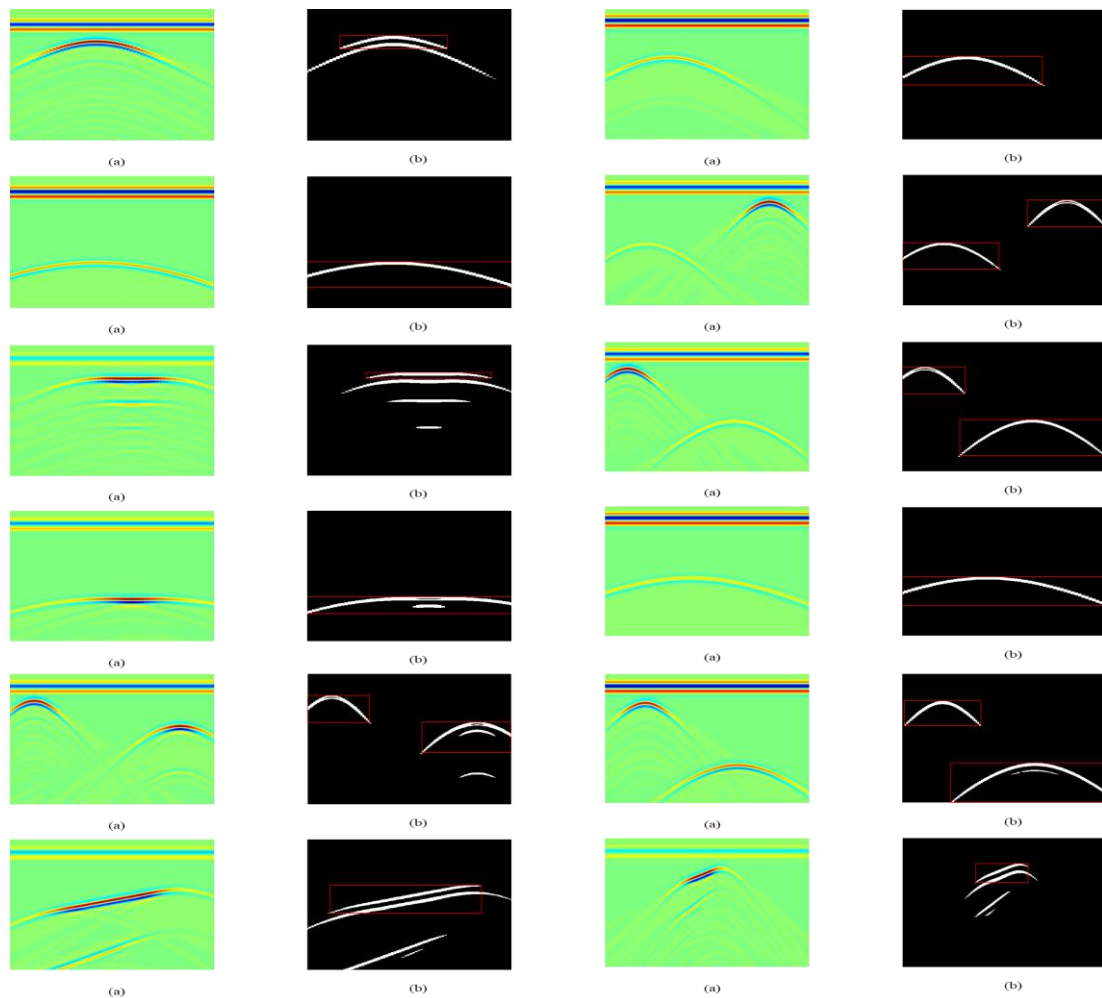


Figure 5. a) Original images, b) Segmented images using proposed algorithm

The proposed algorithm performance changes between 0.3794s and 2.232s. The average processing time is 1.4066s. Table 1 shows that processing time of proposed algorithm for each GPR B scan images.

Table 1. Proposed algorithm performance

| Image ID | Performance |
|----------|-------------|
| 1 | 1.5009 |
| 2 | 0.7490 |
| 3 | 1.0557 |
| 4 | 0.7583 |
| 5 | 0.9374 |
| 6 | 0.9883 |
| 7 | 1.2123 |
| 8 | 2.2320 |
| 9 | 0.8567 |
| 10 | 0.9547 |
| 11 | 0.3794 |
| 12 | 1.5009 |

The obtained results are compared with results of other studies in the literature. Comparison results can be seen in Table 2.

Table 2. Comparison of performance

| Study | Performance |
|----------------------------|-----------------|
| | 8s |
| Singh and Nene, 2013 [14] | 43.8s – 255.6s |
| Chomdee et. al., 2014 [15] | |
| Proposed Method | 0.3794s-2.2320s |

Conclusion

In this paper, fast and effective fully automated GPR B scan image segmentation method is presented. The proposed method is basically based on thresholding and hough transform. The general purpose is to segment the hyperbolas by eliminating background noise and ground plane. Thus, it is easy to detect buried objects location. It is performed in 8 different GPR B scan images. Hyperbolas of segmented images is quite successful. Finally, estimated buried object regions is drawn. Also, the process time is between 1.2342s-2.2320s. Compared to other proposed algorithms it works pretty fast. So, it can be under consideration in real time GPR applications. In the future, segmented GPR images which are obtained from proposed method can be used to detect buried object such as mines and pipe lines.

References

- Levent Seyfi, Ercan Yıldız, A simulator based on energy efficient GPR algorithm modified for the scanning of all types of regions, Turk J Elec Eng & Comp Sci, Vol. 20 (3), 381-389, **2012**. DOI: 10.3906/elk-1011-955
- L. Capineri, P. Grande, and J. A. G. Temple, Advanced image-processing technique for real-time interpretation of ground-penetrating radar images, Int. J. Imaging Syst. Technol., vol. 9, no. 1, pp. 51–59, 1998.
- H. Brunzell, “Detection of shallowly buried objects using impulse radar,” IEEE Trans. Geosci. Remote Sens., vol. 37, no. 2, pp. 875–886, Mar. 1999.

- S. Delbò, P. Gamba, and D. Roccatò, "A fuzzy Shell clustering approach to recognize hyperbolic signatures in subsurface radar images," *IEEE Trans. Geosci. Remote Sens.*, vol. 38, no. 3, pp. 1447–1451, May 2000.
- P. Gamba and S. Lossani, "Neural detection of pipe signatures in ground penetrating radar images," *IEEE Trans. Geosci. Remote Sens.*, vol. 38, no. 2, pp. 790–797, Mar. 2000.
- W. Al-Nuaimy, Y. Huang, M. Nakhkash, M. T. C. Fang, V. T. Nguyen, and A. Eriksen, "Automatic detection of buried utilities and solid objects with GPR using neural networks and pattern recognition," *J. Appl. Geophys.*, vol. 43, no. 2–4, pp. 157–165, Mar. 2000.
- H. S. Youn and C. C. Chen, "Automatic GPR target detection and clutter reduction using neural network," in *Proc. 9th Int. Conf. Ground Penetrating Radar*, Santa Barbara, CA, 2002, vol. 4758, pp. 579–582.
- M. Rossini, "Detecting objects hidden in the subsoil by a mathematical method," *Comput. Math. Appl.*, vol. 45, no. 1, pp. 299–307, Jan. 2003.
- S. Shihab, W. Al-Nuaimy, and Y. Huang, "A comparison of segmentation techniques for target extraction in ground penetrating radar data," in *Proc. 2nd Int. Workshop Advanced GPR*, Delft, The Netherlands, 2003, pp. 95–100.
- P. Gamba and V. Belotti, "Two fast buried pipe detection schemes in ground penetrating radar images," *Int. J. Remote Sens.*, vol. 24, no. 12, pp. 2467–2484, Jan. 2003.
- P. Falorni, L. Capineri, L. Masotti, and G. Pinelli, "3-D radar imaging of buried utilities by features estimation of hyperbolic diffraction patterns in radar scans," in *Proc. 10th Int. Conf. Ground Penetrating Radar*, Delft, The Netherlands, 2004, vol. 1, pp. 403–406.
- A. Dell'Acqua, A. Sarti, S. Tubaro, and L. Zanzi, "Detection of linear objects in GPR data," *Signal Process.*, vol. 84, no. 4, pp. 785–799, Apr. 2004.
- L. Ting-Jun and Z. Zheng-Ou, "Fast extraction of hyperbolic signatures in GPR," in *Proc. ICMMT*, 2007, pp. 1–3.
- N. P. Singh and M. J. Nene, "Buried object detection and analysis of GPR images: Using neural network and curve fitting," *2013 Annual International Conference on Emerging Research Areas and 2013 International Conference on Microelectronics, Communications and Renewable Energy*, 2013.
- P. Chomdee, A. Boonpoonga and A. Prayote "Fast and Efficient Detection of Buried Object for GPR Image" *The 20th Asia-Pacific Conference on Communication*, pp. 350- 355, 2014.

Author Information

Gozde Altin

Electronical and Telecommunication Engineering
Kocaeli University (Kocaeli, Turkey)
HAVELSAN (Istanbul, Turkey)
Contact E-mail: gozde.altin06@gmail.com

Arif Dolma

Electronical and Telecommunication Engineering
Kocaeli University (Kocaeli, Turkey)

Broadband CPW-Fed U-Shaped Dielectric Resonator Antenna for Wireless and WiMAX/WLAN Applications

Emad AHMED
University of Technology

Abstract: In this article, a new U-shaped dielectric resonator antenna (DRA) for broadband applications is proposed. The antenna consists of a modified stepped CPW trimmed to excite the U-shaped dielectric resonator with a relative dielectric constant of 10.2. A parasitic strip along the other side of the DRA is joined to the coplanar waveguide structure acts as tuning element for the antenna frequency band. The proposed antenna is designed using the FR4 substrate of 4.6 relative dielectric constant and 1.6 mm thickness. The antenna is designed, analyzed, and optimized using a full-wave electromagnetic simulator. The results reveal that the proposed DRA has an impedance bandwidth for $V_{SWR} < 2$ from (3.22-5.92) GHz with 59 % bandwidth efficiency. The antenna operating band covers the IEEE 802.11 and many bands of wireless systems like C-band, 5.2, 5.5 & 5.8 GHz-WLAN and WiMAX. The antenna provides a stable quasi-omnidirectional radiation pattern in the H plane and bidirectional radiation pattern in the E plane with a gain ranging from (2.5- 4.6) dB across the operating bandwidth. The proposed antenna could be also used for lower European UWB frequency band (3.4-5.0) GHz applications and for medical microwave imaging purposes. The overall dimension of the antenna is 26mm×32mm×1.6mm and the thickness of the dielectric resonator is only 8.12 mm; so, the antenna can be categorized as a compact size and low profile antenna.

Keywords: Broadband applications, Dielectric resonator antenna, Low profile antenna, CPW feed

Introduction

The large bandwidths and high capacity are the important parameters in modern communication requirements. The researchers have been focusing on using a resonators with minimum radiation loss in the design and implementation of modern antennas. Microstrip is one of the most famous types of antennas used in the modern communications. The properties of microstrip antennas in terms of ease of design and manufacturing as well as cost have made it the most widely used and preferred by designers and researchers in the field of wireless communications. In general, dielectric resonators (DRs) works at microwave and millimeter wave bands. As metal surfaces become more lossy reflectors at millimeter wavelengths, so the dielectric resonators are used at these frequencies. When a DR is not totally surrounded by a conductive boundary, it can behaves as radiators, and so it becomes an antenna.

In the last two decades, many research topics related to the design and implementation of dielectric resonator antennas (DRAs) have been published. Many designs and implementations of the DRAs can be found in literature. Some of those will be reviewed to highlight the important features of the DRAs design.

(Sheng-M. D., Tsung-W. C., Hsiao-H. K., 2001) presents an open-ended coplanar waveguide (CPW) fed rectangular DRA with a high dielectric constant. The input impedance of the CPW-fed DRA can be tuned by changing the distance from the open-ended slot center to the center of the dielectric resonator.

(Rao Q., Denidni T. A., 2005) demonstrate experimental technique for enhancing impedance matching of an aperture coupled CPW fed DRA array. He was employ a CPW feed line into a coupled slot. Good impedance matching simply achieved by tuning the location of the LPDRAs on the coupled slot.

(Rezaei P., Hakkak M., Forooraghi K., 2006) use a configuration consist of two rectangular dielectric sections separated by a metal plate to stimulate two contiguous resonant frequencies. Exploiting the two-segment thin DRA and changing its aspect ratio, more than 76.8% bandwidth efficiency at (3.32–7.46) GHz frequency band has been achieved.

(Tze-H. C., Jean-F. K., 2007) propose a broadband DRA comprises of a DR coated with metal on three sides and placed on a ground plane. A terminating slots with coplanar waveguide (CPW) is used as a feeder to the designed antenna. The obtained results show a wide bandwidth over which the pattern on the horizontal plane is quasi omnidirectional and it can be used for WLAN 802.11a applications.

(Jungsuek O., Taejong B., Donghoon S., Jinkoo R., Sangwook N., 2007) presents a coplanar waveguide fed DRA above patch antenna operate at 60 GHz using μ -machining technology. A dielectric post was used to support the patch in the air and the DRA is fixed above the patch. The realized antenna demonstrates wideband features of 17.5 GHz with a fractional bandwidth of 29.2%. The measured antenna gain found at 60 GHz was about 3.6 dBi.

(Aldo P., Apisak I., 2010) offerings a historical evaluation of the accomplished studies on DRAs over the last three decades. The studies accomplishments are emphasized and the state of the art of DRA technology is revised. The miniaturization, wideband, low profiles, and high gain were considered as an important features of DRAs.

(Joshua M. P., Satish K. S., 2012) propose an aperture-coupled right hand circular polarization DRA working in Ku-band that was excite through a bow-tie cross-slots driven by single feeding system. The realized DRA displayed operation centered at 12GHz, with adequate radiation patterns. This DRA can be used in Ku-band satellite communication applications.

(Mohsen K., Mohamad K. A., Ahmed A. K, Shadi D., 2013) presents a P-shaped dielectric DRA for wideband wireless application. Wideband impedance bandwidth was achieved and the antenna covers the C-band, 5.2, 5.5 & 5.8 GHz WLAN and WiMAX wireless communication applications. The dielectric resonator thickness is 5.12 mm that has been considered as a low profile antenna.

(Roslan S. F., Kamarudin M. R., Khalily M., Jamaluddin M. H., 2015) introduce a CPW rectangular DRA with metallic strip operating at 2.6 GHz for long term evolution (LTE) mobile device. The proposed antenna operate with two bands of 67 % bandwidth efficiency (1.74 - 3.47 GHz) and 66 % bandwidth efficiency (1.83–3.54 GHz) respectively. The antenna has a cause-omnidirectional radiation pattern and it provides gain of 3.12dBi.

(Aftab A. K., Rizwan K., Sajid A., Jamal N., Owais, 2016) present a two port multiple input multiple output (MIMO) antenna system using DRA. The antenna is operating at 3.6 GHz and covers WiMAX band from 3.4 to 3.7 GHz. Two symmetric feed lines excite two different TE modes at 3.6 GHz with high isolation was achieved and compared with other DRAs in literature. A gain of 5.84 dBi for port one and 5.87 dBi for port two has been achieved, respectively.

(Massinissa B., Salih A., Idris M., Boualem H., Farouk C., Youcef B. C., 2016) introduce a reconfigurable cylindrical DRA fed by switching network and proposed to use for wireless applications. The antenna operating bands are (3.77-3.81) GHz and (5.38-5.6) GHz that covers the WiMAX band and the WLAN. The radiation pattern of the designed antennas is omnidirectional at E-plane and unidirectional at H-plane for the designed frequency band.

(Messsaoudene I, Denidni T. A., Benghalia A., 2016) designed, and fabricate a DRA that has a U-shaped and fed by microstrip feeding system. The antenna operates at (5.45-10.8) GHz. A modified ground plane was used to improve the impedance bandwidth. A second modification have been achieved by introducing a microstrp patch through the DRA. The designed antenna shows an improved bandwidth that attained an operative band from (2.65-10.9) GHz. The obtained results indicate that the suggested antenna can deliver an UWB and a symmetric radiation patterns.

(Bhayana E., Agarwal A., 2017) presents an analysis of investigation on DRA's over the last three decades. It is mentioned that the evaluation has been done depending on vital parameters that include bandwidth, efficiency, realized gain, dielectric constant, dimensions, and DRA material used. A comparison of various configurations of DRA's for various applications have been reviewed. From the comparison, it is clear that rectangular DRA gives the best results.

This paper introduces a wideband antenna using U-shaped dielectric resonator with 10.8 relative dielectric constant. Stepped CPW structure was used to feed the proposed antenna. A frequency tuning element was attached to the feeding system in order to tune the impedance bandwidth. The antenna is designed to cover the C-band and the IEEE 802.11 band used for WLAN and WiMAX as well as the lower European UWB frequency applications. The antenna dimensions and results are optimized using full wave electromagnetic simulator. The resonator and the feeding structure is placed on substrate with relative dielectric constant of 4.6 and thickness of 1.6 mm.

The paper is organized as follows: section one gives a literature review on the design aspects of DRAs. Antenna configuration and design analysis are presented in section two. In section three, parametric study of the frequency tuning element is demonstrated. The simulation and results are given in section four. The last section concludes and highlights the main consideration points in this work.

Antenna Configuration and Design

The proposed DR antenna configuration is shown in Figure 1. The proposed antenna is designed to operate within the frequency (3-6) GHz. The antenna consists of dielectric resonator with dielectric constant 10.8 and thickness of 8.2 mm in the form of U-letter in English. A 50 ohm CPW feeder is designed in a stepped manner to ensure the matching between the feeder and the resonator.

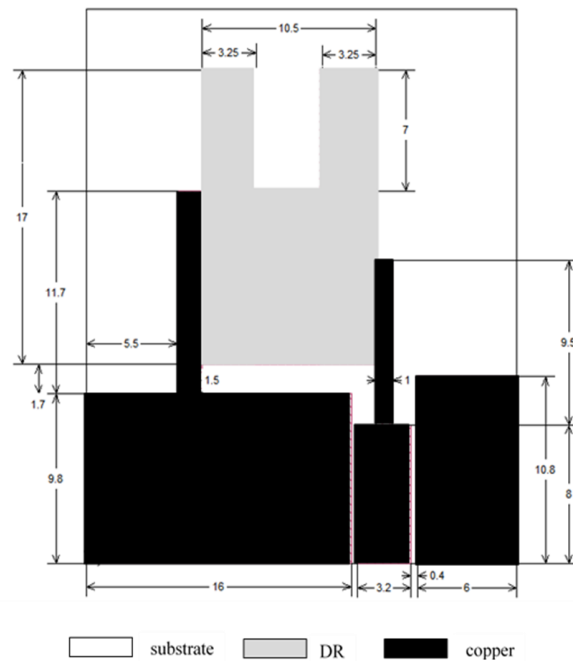


Figure 1. Proposed antenna configuration

This feeder is edge type feeding commonly used to feed the DRs. This type of feeding is used to expand the antenna frequency band. The heights of the ground planes for CPW feeding structure are asymmetric; this gives another expansion to the impedance frequency response. A piece of metal stripe is connected from the lower side to the upper edge of the left CPW ground and extends along the left edge of the resonator. The upper end of the metal strip is used to tune the frequency range of the resonator. The resonator and feeding system are all placed on the substrate with 4.6 relative dielectric constant and 1.6 mm thickness. All dimensions are given in millimeters (mm) and they have been optimized to meet the proposed antenna requirements.

Parametric Study of the Frequency Tuning Element

In this section, the effect of changing the length of the metallic strip on the antenna impedance bandwidth will be discussed. For this purpose, the full wave electromagnetic simulator is used to find the optimum frequency

characteristics of the suggested DRA for different lengths of the metallic strip (L_s). The return loss (S11) of the proposed antenna against frequency for different lengths of a metallic strip is drawn in Figure 2.

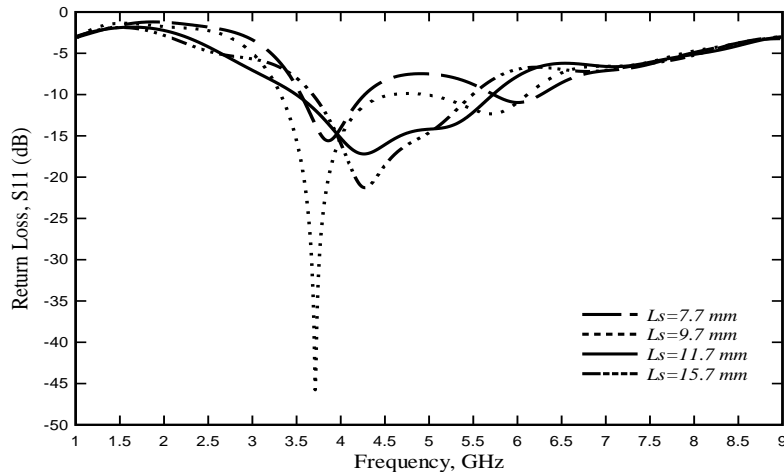


Figure 2. The effect of metallic strip length on DRA impedance bandwidth

It is clearly noted that the variation of L_s from 7.7 mm to 15.7 mm has a substantial influence on the frequency impedance variation. When the length $L_s=7.7$ mm and 9.7 mm, it was observed that for these lengths the frequency impedance did not meet the requirements for the proposed antenna. When $L_s=11.7$ mm, the results demonstrate that the planned DRA has an impedance bandwidth from 3.22-5.92 GHz with $S_{11}=-16$ dB and 59 % bandwidth efficiency. For $L_s=15.7$ mm the impedance bandwidth is from 3.68-5.48 GHz with $S_{11}=-21.26$ dB and 39.3 % bandwidth efficiency. Accordingly, the length L_s is fixed to 11.7 mm to meet the proposed DRA requirements.

Simulation and Results

In this section, the final design of the proposed antenna with optimized dimensions will be simulated using full wave simulator. These dimensions give the optimal impedance response that's meets the specifications of the proposed DR antenna. The length of the metal segments has been fixed at 11.7 mm and the response is redrawn in Figure 3. It is observed that the operating frequency band of the proposed antenna (the gray region in Figure 3) covers the suggested frequency specification of the designed antenna.

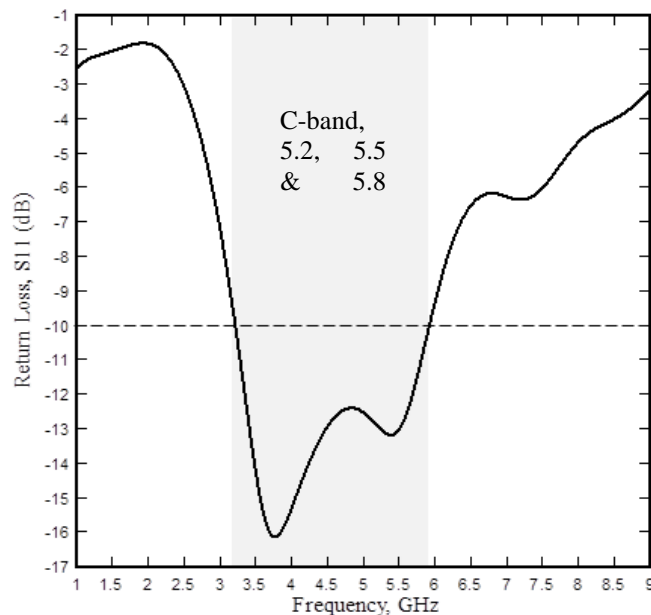


Figure 3. Return loss of the proposed DRA

The far field radiation pattern simulated results of the suggested DRA is illustrated in Figure 4. From the figure it can be realized that the E-plane radiation patterns are almost symmetrical and stable through the operating frequency range, while the radiation patterns in the H-plane are not as symmetrical as in the E-plane. The proposed antenna exhibits good broadside radiation patterns in both planes.

Figure 5 plots the simulated peak gain of the proposed DR antenna. The gain is plotted against frequency range from 3.5 GHz to 6 GHz which covers all the designed antenna bands. It can be noted that the peak gain is about 0.9 dBi for frequency equal to 3.5 GHz and 4.7 dBi for frequency equal to 6 GHz and it is almost linearly and stable in the entire operating frequency range.

These results reveal that the proposed antenna can demonstrate very stable radiation patterns within the designed frequency range. With orientation to Figures 4 and 5, the proposed DRA shows good features that highly recommended in the modern wireless communication applications.

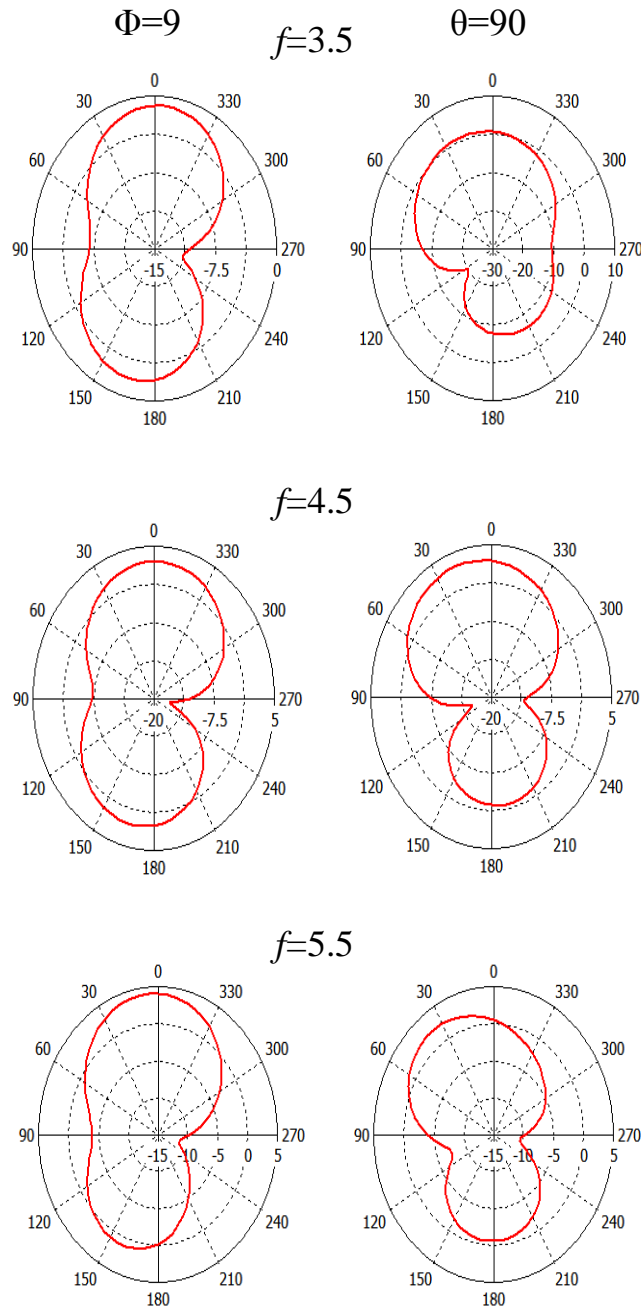


Figure 4. Radiation pattern of the proposed

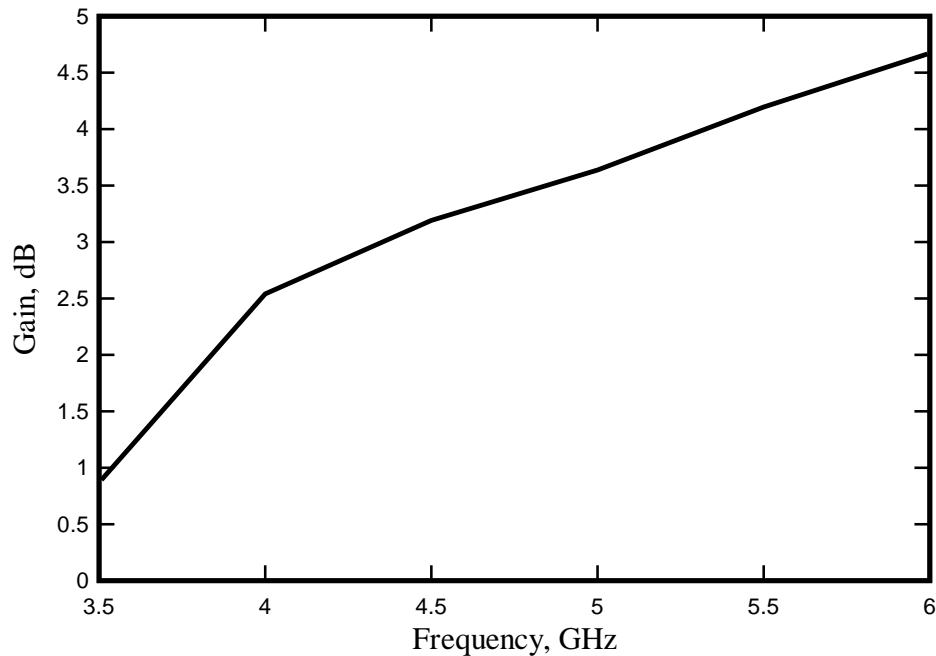


Figure 5. The proposed DRA gain against frequency

Conclusion

In this study, a CPW-fed broadband DRA is recommended for wireless applications. The operating band of the dielectric resonator is coupled to extract a wideband operation with bandwidth efficiency of 59%. The impedance bandwidth can be adjusted by tuning the frequency modes of the dielectric resonator. Further tuning can be achieved by adding a metal strip to the CPW structure and close to the edge of the dielectric resonator. The proposed antenna covers a useful bands that used in wireless communication. The designed DR antenna demonstrate good broadside radiation field patterns in both the principal planes as well as high, stable and linear gain over the whole antenna band. The size of the proposed DRA is 26mm×32mm×1.6mm with DR thickness of only 8.12 mm. The antenna can be categorized as a compact size and low profile antenna.

References

- Aftab A. K., Rizwan K., Sajid A., Jamal N., Owais (2016). Dual-Port MIMO DRA with High Isolation for WiMAX Application, *Proceedings of the 3rd International Conference on Engineering & Emerging Technologies (ICEET), Superior University, 7-8 April, Lahore, Pakistan.*
- Aldo P., Apisak I. (2010). Dielectric Resonator Antennas: A Historical Review and the Current State of the Art, *IEEE Antennas and Propagation Magazine*, Vol. 52, No. 5, pp. 91-116.
- Bhayana E., Agarwal A. (2017). A Review on Dielectric Resonator Antenna & Its Industrial Applications, *International Journal of Scientific & Engineering Research*, vol. 8, no. 4, pp. 107-110.
- Joshua M. P., Satish K. S. (2012). Single Feed Aperture-Coupled Wideband Dielectric Resonator Antenna with Circular Polarization for Ku-Band Applications, *International Journal of Antennas and Propagation, Hindawi Publishing Corporation*, vol. 2012, Article ID 378798. Doi:10.1155/2012/378798.
- Jungsuek O., Taejong B., Donghoon S., Jinkoo R., Sangwook N. (2007). 60-Ghz Cpw-Fed Dielectricresonator-Above-Patch (Drap) Antenna for Broadband WLAN Applications Using Micromachining Technology, *Microwave and Optical Technology Letters*, vol. 49, no. 8, pp. 1859-1861.
- Massinissa B., Salih A., Idris M., Boualem H., Farouk C., Youcef B. C. (2016). A Reconfigurable Cylindrical Dielectric Resonator Antenna for WiMAX/WLAN Applications, *The 12th International Conference on Innovations in Information Technology (IIT), College of Information Technology, 28-30 Nov. , United Arab Emirates.*
- Messaoudene I, Denidni T. A., Benghalia A. (2016). Low-Profile U-Shaped DRA for Ultra-Wideband Applications, *International Journal of Microwave and Wireless Technologies*, Cambridge University Press, pp. 1-7. Doi: 10.1017/S1759078716000155.

- Mohsen K., Mohamad K. A., Ahmed A. K., Shadi D. (2013). Wideband P-Shaped Dielectric Resonator Antenna, *Radioengineering*, vol. 22, no. 1, pp. 281-285.
- Rao Q., Denidni T. A. (2005). On Improving Impedance Matching Of A CPW Fed Low Permittivity Dielectric Resonator Antenna, *Progress In Electromagnetics Research, PIER*, vol. 53, pp. 21–29.
- Rezaei P., Hakkak M., Forooraghi K. (2006). Design of Wide-Band Dielectric Resonator Antenna with a Two-Segment Structure, *Progress In Electromagnetics Research, PIER*, vol. 66, pp. 111–124.
- Roslan S. F., Kamarudin M. R., Khalily M., Jamaluddin M. H. (2015). A Coplanar Waveguide Rectangular Dielectric Resonator Antenna (RDRA) for 4G Applications, *Jurnal Teknologi (Sciences & Engineering)*, vol. 73, no. 1, pp. 97–100.
- Sheng-M. D., Tsung-W. C., Hsiao-H. K. (2001). A CPW-Fed Rectangular Dielectric Resonator Antenna. *Proceedings of Asia-Pasific Microwave Conference (APMC), Dec. 3-6, Taipei, Taiwan, R.O.C.*
- Tze-H. C., Jean-F. K. (2007). Broadband Dielectric Resonator Antenna With Metal Coating, *IEEE Transactions on Antennas and Propagation*, vol. 55, no. 5.

Author Information

Emad S. Ahmed

University of Technology

Baghdad-IRAQ

Contact E-mail: 30029@uotechnology.edu.iq

Simulation Analyses of Flow in the Wake Region of Non-uniform Bridge Pier by using Computational Fluid Dynamic

Sulaiman Dawood JASIM
Northern Technical University

Adnan A. ISMAEL
Northern Technical University

Manahil A.T. AL DABBAGH
Northern Technical University

Abstract: The study presents a three-dimensional numerical simulation of turbulent flow field around non uniform bridge piers which they are downstream-facing round-nosed (DS-FRNP) and upstream-facing round-nosed (US-FRNP), were compared with a circular pier in fixed-bed using the computational fluid dynamics (CFD). In this paper, the flow field passing around the bridge piers is predicted using $k-\omega$ standard turbulence model. The predicted flow velocity in x-direction and turbulent kinetic energy (TKE) compares with tested data. Simulated flow velocity and turbulent kinetic energy are in good agreement with experimental data. Numerical model predicts the flow features such as flow reversal upstream the pier, down flow upstream the pier and flow in wake region, the shape of vortices (horse shoe vortex and wake vortex) also captured by simulation. The discussion of the relation between bridge pier shape and turbulent kinetic energy in this study will help to control the scour around bridge piers.

Keywords: CFD, $k-\omega$ model, 3D turbulence flow and uncoventional bridge pier

Introduction

Local scour around bridge pier is the leading cause of bridge failure, effecting significantly on the total construction and maintenance costs. Therefore, scouring around uniform pier with cylindrical shape is commonly used in the field. The shape of bridge piers has important effect on the local scour. Previous studies showed that there is still a deficiency of experimental studies on the effects of non-uniform pier. The flow around a pier is three-dimensional and turbulent. CFD models have become suitable tool to predict and analysis flow for different river engineering problems. However, their applicability has to be proven using experimental data or field measurements.

For flow around bridge pier in a fixed-bed, the existence of vortices from the bridge pier initiates a scour hole. This local scour may lead to failure of bridge pier.

Several experimental and numerical have been conducted to investigation the 3D flow and turbulence around piers in a fixed-bed Graf and Istiarto (2002) detected velocities, turbulence intensities, Reynolds stresses, and bed-shear stresses in different azimuthal planes within the equilibrium scour hole at a circular pier by using Acoustic Doppler Velocity Profiler (ADVP).

Nagata et al. (2005) performed a model based on the Reynolds Averaged Navier Stokes equations, together with the k-epsilon turbulence model for bed deformation around bridge pier.

Afzal M, S. (2013) performed two turbulence models ($k-\omega$ and $k-\epsilon$) to simulate a complex sediment transport using CFD around abutment and pier. The numerical results have been validated with physical experiment.

- This is an Open Access article distributed under the terms of the Creative Commons Attribution-Noncommercial 4.0 Unported License, permitting all non-commercial use, distribution, and reproduction in any medium, provided the original work is properly cited.

- Selection and peer-review under responsibility of the Organizing Committee of the Conference

Comparison in performance of (k- ω and k- ϵ) turbulence models is done for abutment and pier scour under constant discharge. The result reveals that the performance of the k- ω model is similar to the k- ϵ in the pier scour case.

Guemou et al. (2013) performed DES to simulate the flow around two bridge piers (circular and round-nosed pier) fixed in flat-bed. The authors chose the DES turbulence model for his ability to capture the dynamics of the horseshoe vortex, at the upstream of pier. Mammam and Soudani (2012) numerically tested the flow field around a cylinder on a fixed-bed open channel using CFD code to analysis the flow field and kinetic energy field around the pier with the standard k- ϵ turbulence model. The predicted velocity and turbulent kinetic energy were compared with those of measured data. Roulund et al. (2005) calculated the flow and scouring around a cylindrical pile, using a model that uses the rigid- bed.

The objective of the present study is predicting the flow field and turbulent kinetic energy around bridge piers using CFD, k- ω standard turbulent model. The prediction will use the same hydraulic condition as in laboratory experiments; this permits a direct comparison between the simulation and experimental data.

Geometric Setup

Figures (1, 2) shows location of the pier and the mesh around the pier

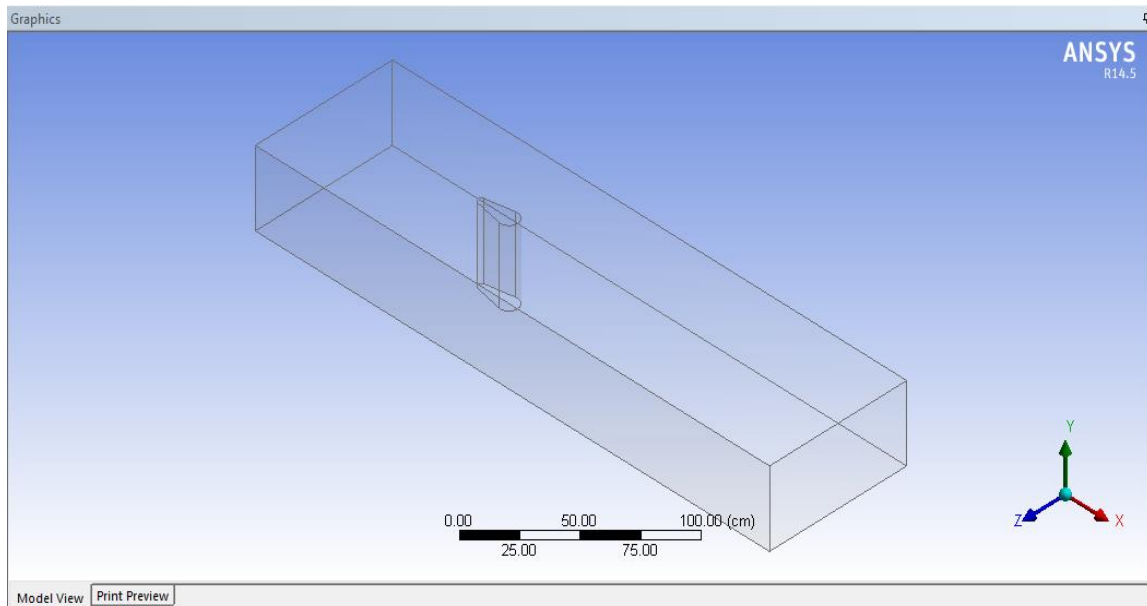


Figure 1. The geometric setup for the numerical simulation

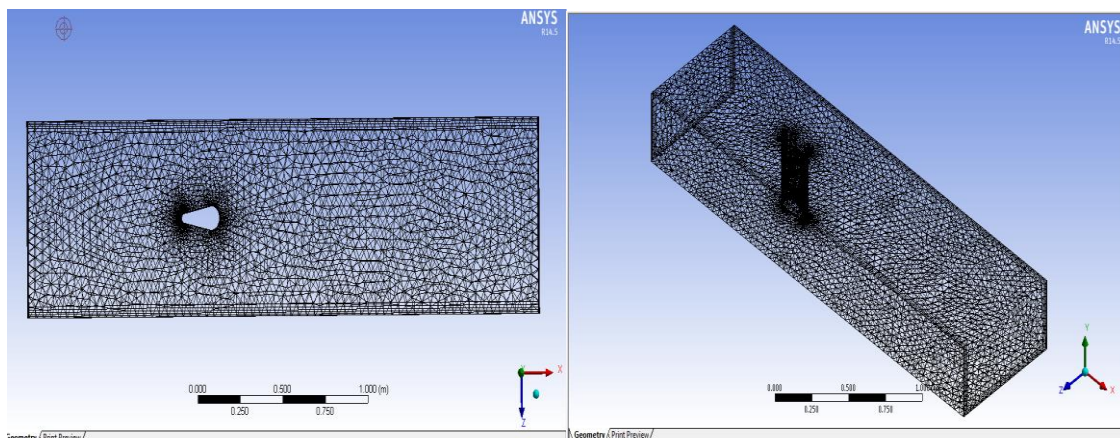


Figure 2 Mesh refinements around bridge pier

Numerical Simulation

k- ω consist of two transported variable 1. is turbulent kinetic energy k. 2. is the specific turbulent dissipation using ω . The turbulent eddy viscosity v_t is calculated using k and ω . Using average and a fluctuating components in the Navier-Stokes equation (equation1), yields after averaging of the equations, the Reynolds equation as in equation 2 below.

$$\frac{\partial U_i}{\partial t} + U_j \frac{\partial U_i}{\partial x_j} = -\frac{1}{\rho} \frac{\partial P}{\partial x_i} + \frac{\partial}{\partial x_j} \left[v \left(\frac{\partial U_i}{\partial x_j} + \frac{\partial U_j}{\partial x_i} \right) \right] + g_i \quad (1)$$

$$\frac{\partial U_i}{\partial t} + U_j \frac{\partial U_i}{\partial x_j} = -\frac{1}{\rho} \frac{\partial P}{\partial x_i} + \frac{\partial}{\partial x_j} \left[(v + v_t) \left(\frac{\partial U_i}{\partial x_j} + \frac{\partial U_j}{\partial x_i} \right) \right] + g_i \quad (2)$$

The equations for turbulent kinetic energy k and the specific turbulent dissipation is as follows:

$$\frac{\partial k}{\partial t} + U_j \frac{\partial k}{\partial x_j} = \frac{\partial}{\partial x_j} \left[\left(v + \frac{v_t}{\sigma_k} \right) \frac{\partial k}{\partial x_j} \right] + P_k - \beta_k k \omega \quad (3)$$

$$\frac{\partial \omega}{\partial t} + U_j \frac{\partial \omega}{\partial x_j} = \frac{\partial}{\partial x_j} \left[\left(v + \frac{v_t}{\sigma_\omega} \right) \frac{\partial \omega}{\partial x_j} \right] + \frac{\omega}{k} \alpha P_k - \beta_\omega \omega^2 \quad (4)$$

P_k is the turbulent production rate given by equation (5), the coefficients in equation 3 and 4 have the values $\alpha = \frac{5}{9}, \beta_k = \frac{9}{100}$ and $\beta = \frac{3}{40}$.

$$P_k = v_t \frac{\partial U_i}{\partial x_j} \left(\frac{\partial U_i}{\partial x_j} + \frac{\partial U_j}{\partial x_i} \right) \quad (5)$$

The eddy viscosity v_t in the RANS-equations is obtained using the two-equation k- ω model Wilcox (1994).

$$v_t = \min \left(\frac{k}{\omega}, \sqrt{\frac{2}{3} \frac{k}{|S|}} \right) \quad (6)$$

Experiments

The experiments for validation purpose were conducted in the Hydraulics Laboratory with a rectangular channel 1100 cm long, 80 cm wide and 89 cm deep. Non-uniform and circular piers were used as shown in Figure 3.

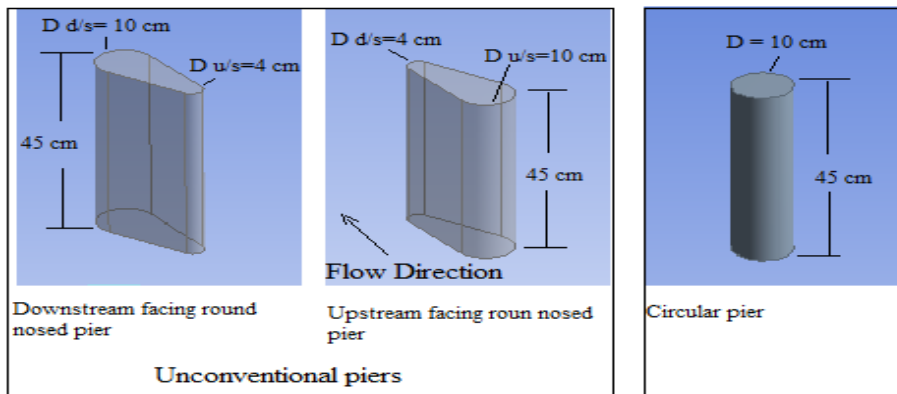


Figure 3. Dimension of non-uniform and circular bridge piers

Result and Discussion

In Figure 4, velocity vectors in the vertical cross section along the channel centerline are plotted. Upstream face of (US-FRNP), the flow has more or less uniform velocity profiles, with no sign to the vertical velocities. Close to bridge pier, the vertical velocity is downward and the longitudinal velocity decreases with decreasing distance to the pier and exhibit negative values meaning that the flow reversal direction happens. At the end of the pier, the vertical velocities are downward while the longitudinal velocities exhibit negative values in the vicinity of the pier.

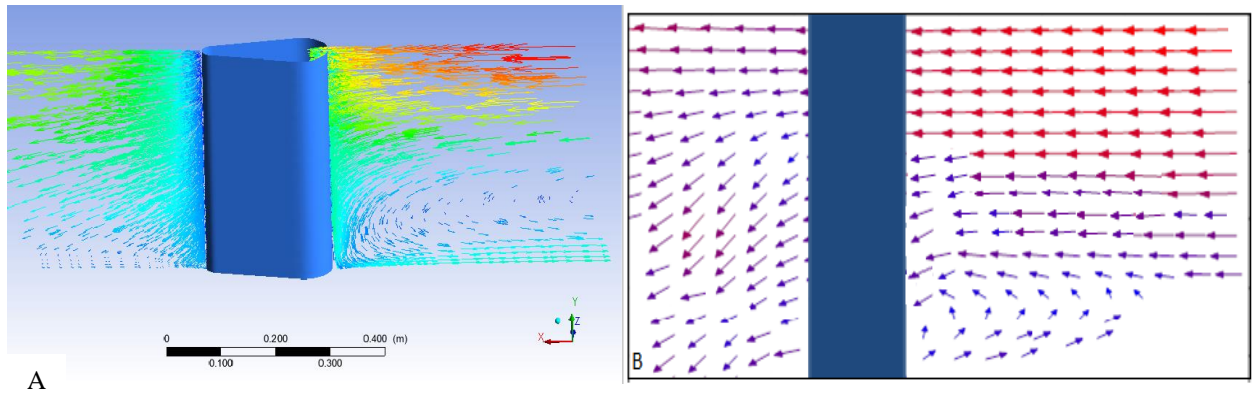


Figure 4 A) Predicted velocity vectors and B) Measured velocity vectors at a vertical cross section along the centerline of the model channel

Vortices feature are well capture in the front and behind of normal bridge pier. In spite of the model applied in this simulation is not expected to capture details of the features, Figure 5 show some interesting patterns upstream and downstream of the pier. The three-dimension feature of the horseshoe vortex clockwise and extent toward downstream.

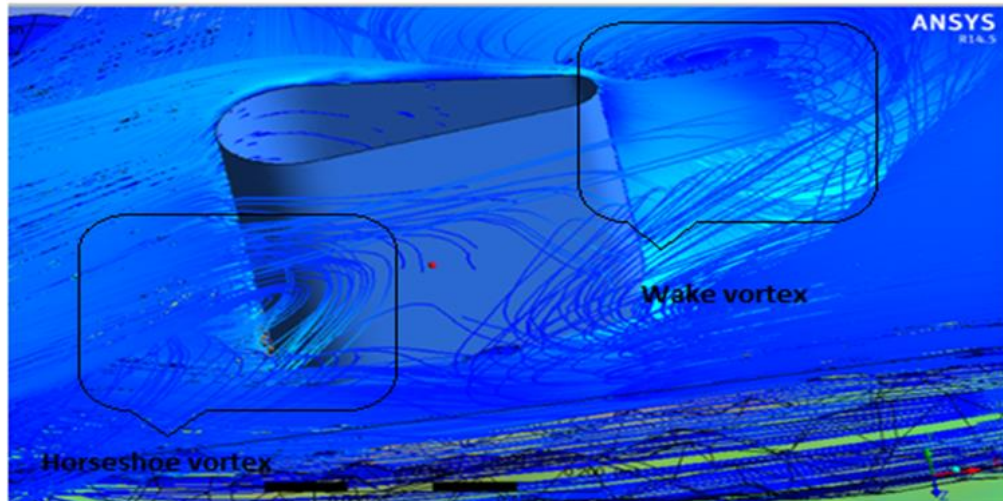


Figure 5. Vortices upstream and downstream bridge pier.

In Figure 6, volume rendering of (TKE) in the plane $z = 0.25H$ above the bed are plotted for three bridge piers. The maximum value of TKE for (DS-FRNP) is (0.002425 J/kg) reduced as compared to (US-FRNP) (0.0679 J/kg) and circular (0.06944 J/kg) piers. That is mean the magnitude of vortices is more reduced in case of (DS-FRNP), which results in reduced local scour.

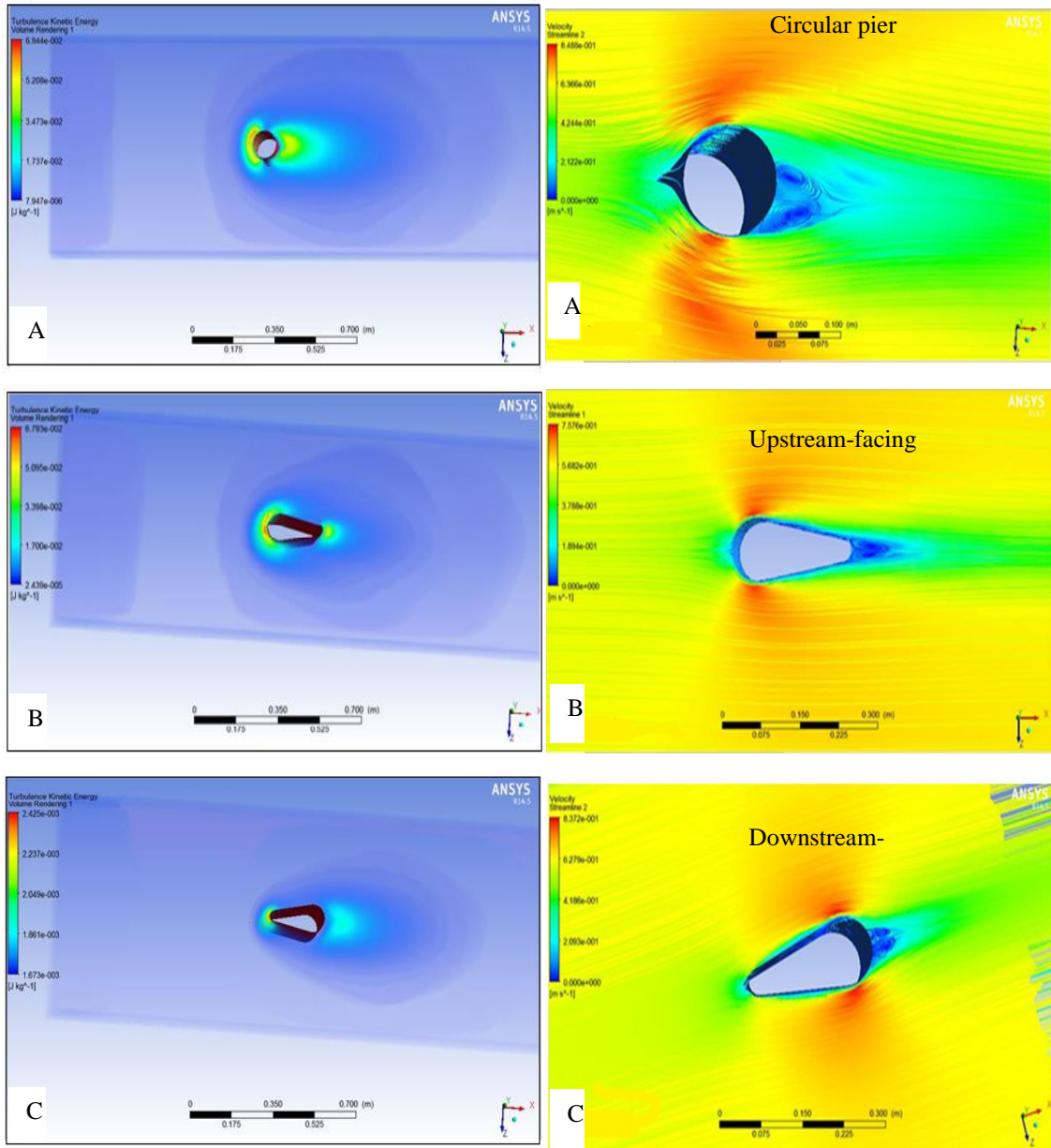


Figure 6. Volume rendering of TKE ($J kg^{-1}$) for A) Circular, B) (US-FRNP) and C) (DS-FRNP)

Figure 7. Streamlines shows flow separations around A) Circular, B) (US-FRNP) and C) (DS-FRNP)

Figure 7 shows flow separation as the flow passes around the three bridge piers, flow separation produces wake vortex behind the bridge piers. Maximum velocities for circular and (US-FRNP) are observed about 75° Oliveto and Hager (2002).

Figures (8-9) show a comparison between predicted and measured velocities and turbulent kinetic energy respectively upstream face of the bridge piers. For standard $k-\omega$ model the correlation coefficient show a good agreement for longitudinal velocity (v_u) and (TKE) with R^2 (0.898) and R^2 (0.96) respectively.

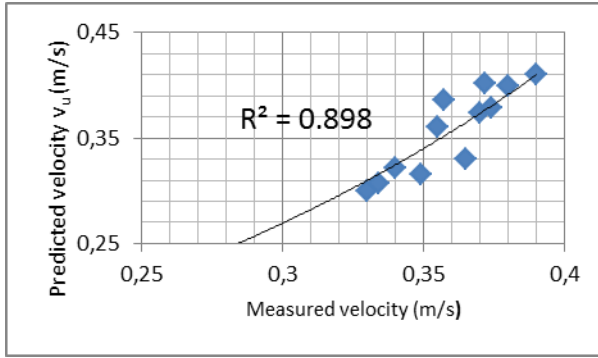


Figure 8 A comparison between predicted and measured velocities at upstream face of piers located along the centerline of the models channel.

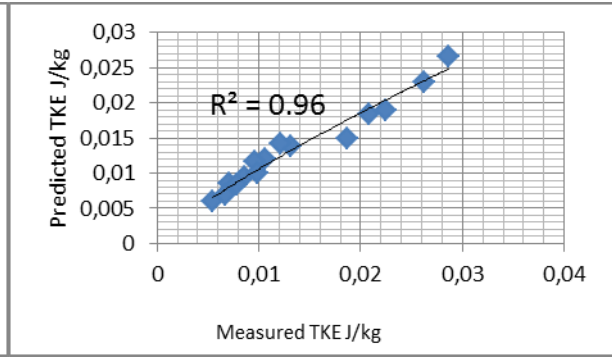


Figure 9 A comparison between predicted and measured TKE at upstream face of piers located along the centerline of the models channel

Validation of Results

The standard (k- ω) model has been then applied to simulate the case of flow around (DS-FRNP), (US-FRNP) and circular piers in a channel with a fixed bed. The experimental data compared with the results of CFD.

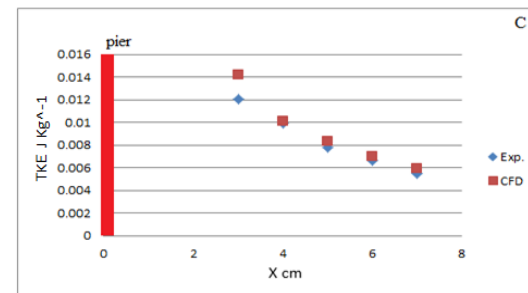
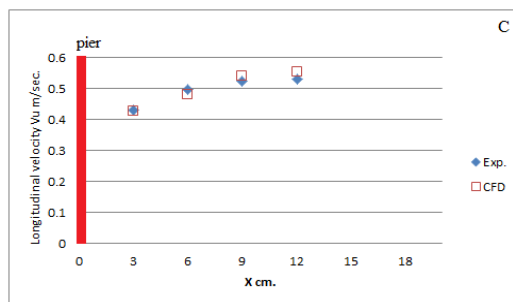
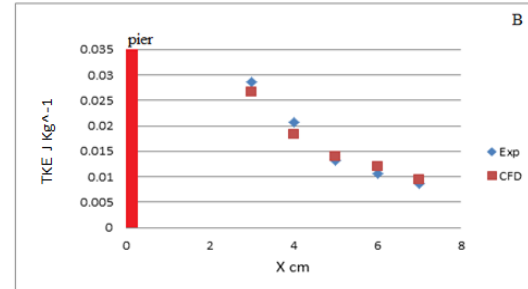
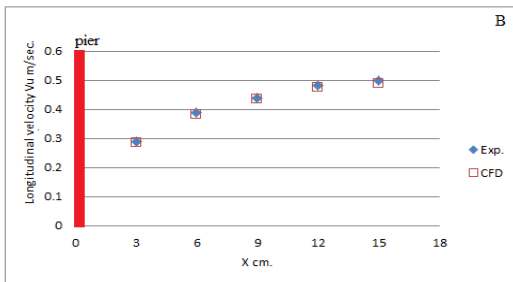
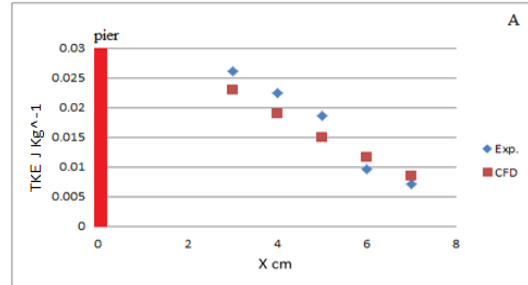
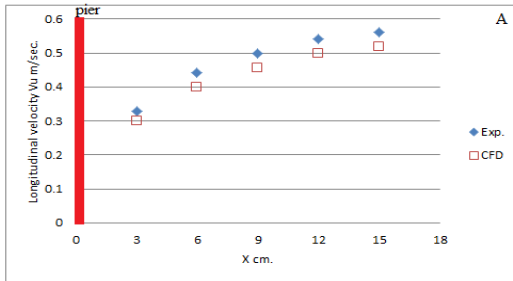


Figure 10 Longitudinal velocity upstream A) Circular pier, B) (US-FRNP) and C) (DS-FRNP)

Figure 11 TKE values with distance near A) Circular pier, B) (US-FRNP) and C) (DS-FRNP)

Figure 10 (A,B and C) shows the longitudinal velocity upstream three piers, we notice that longitudinal velocity increases as far as from piers, but decreases when approaching the piers. For the turbulent kinetic energy as shown in Figure 11 (A,B and C), there is a good agreement between the simulated and experimental results. Maximum TKE observed close to pier then decreased a way from the pier.

Conclusion

CFD simulation shows the ability of k-omega turbulent model to capture the features of the complicate 3D flow field (flow velocity, turbulent kinetic energy and vortices in wake region of the pier) around the bridge pier. Predictions of the flow field and the TKE are well correlated with experimental data, with a correlation coefficient of 0.898 and 0.96 respectively. Other features predicted include the horseshoe vortex and wake vortex.

For model validation, the experimental data was chosen for the bridge piers. The following conclusions could be drawn: -

- 1- Flow reversal upstream of the pier and downstream of the pier, flow wake occurs,
- 2- (DS-FRNP) minimizes the turbulent kinetic energy at the upstream face of the pier as compared with circular and (US-FRNP) respectively. This reduction of TKE indicates that the vorticity magnitude is more reduced for downstream-facing round- nosed pier, which results in reduced local scour.

References

- Graf, W. and Istitato, I. (2002) "Flow pattern in the scour hole around a cylinder", Journal of Hydraulic Research, Vol. 40, No. 1, pp. 13-20.
- Nagata, N., Hosoda, T., Nakato, T., and Muramoto, Y. (2005) "Three-dimensional numerical model for flow and bed deformation around river hydraulic structures", Journal of Hydraulic Engineering, ASCE, Vol. 131, No. 12, pp. 1074-1087.
- Afzal M, S. (2013). 3D Numerical Modeling of Sediment Transport under Current and Waves, Thesis presented to the Norwegian University of Science and Technology, in partial fulfillment of the requirements for the degree of Master of Engineering.
- Guemou, (2013). Numerical investigations of the bridge pier shape influence on the bed shear. Academic Center of Ain Temouchent, Algeria, vol. 18, Bund. Y. 5686.
- M. Mammam and A. Soudani (2012) Numerical study of external turbulent flow. Revue des Energies Renouvelables Vol. 15 N°1 (2012) 155 – 164
- Roulund, A., Sumer, B. M, Fredsoe, J. and Michelsen, J. (2005) "Numerical and experimental investigation of flow and scour around a circular pile", Journal of Fluid Mechanics, Vol. 534, pp. 351–401.
- Wilcox D. C (1994). Turbulence Modeling for CFD. DCW Industries Inc., La Canada, California
- Oliveto, G. and Hager, W.H. (2002). Temporal evolution of clear-water pier and abutment scour. Journal of Hydraulic Engineering, ASCE. 128(9): 811-820.

Author Information

Sulaiman Dawood Jasim

Technical Institute
Northern Technical University, Mosul, Iraq.
Contact E-mail: sulaimanrnd@yahoo.com

Adnan A. Ismael

Technical Institute
Northern Technical University, Mosul, Iraq.

Manahil A.T. Al Dabbagh

Technical Institute
Northern Technical University, Mosul, Iraq.

Preparation and Characterization of Na-Alginate Hydrogel Beads

Mehlika PULAT
Gazi University

Duygu OZUKAYA
Gazi University

Abstract: A series of Na Alginate (Na-Alg) hydrogel beads were prepared by using ionic cross linking method. The beads were obtained by dropping of Na-Alg solution in chilled oil bath at $-18\text{ }^{\circ}\text{C}$ first and then leaving the hardened beads into the cross linker solution. CaCl_2 solution was used for ionic cross linking of Na-Alg molecules. While the concentration of Na-Alg solution was kept constant, crosslinking time was changed from 5 to 30 minutes. In general, longer crosslinking times negatively affect hydrogel formation. Swelling behaviors of the hydrogels were studied by changing time, temperature and pH. The higher crosslinker / polymer rates caused lower swelling values. It was determined that the swelling percentages regularly decreased with increasing the crosslinking time. While the time increased from 5 to 30 minute, swelling percentages decreased from 158 % to 33 %. Temperature changing negligibly affects the swelling percentages. The prepared Na-Alg hydrogels could not be commended as temperature sensitive.

Keywords: Hydrogel, Na-Alginate, CaCl_2 , Swelling

Introduction

Hydrogels are three-dimensionally cross-linked hydrophilic polymers that can absorb and retain large amounts of water up to thousands of times of their own weight. The hydrophilic property is due to presence of chemical residues such as $-\text{OH}$, $-\text{COOH}$, $-\text{NH}_2$, $-\text{CONH}_2$, $-\text{SO}_3\text{H}$ and others with in molecular structure. Hydrogels have been extensively studied and preferred for a large number of industrial fields [Pulat and Asil, 2009, Akalin and Pulat, 2018]. Because of their excellent characteristics, they can also be used for a large number of applications in the medical field such as controlled drug release matrices, enzyme and yeast cell immobilization, blood-contacting applications, and others. Hydrogels are also very useful in production of agricultural and horticultural materials [Pulat and Yoltay, 2016].

Most of the synthetic polymers used to prepare hydrogels causes some problems because of their long degradation times and degradation products. Natural polymers are a good choice to overcome this issue [Pulat M. & Uğurlu N., 2016].

Sodium alginate (Na-Alg) is sodium salt of alginic acid, a naturally occurring polysaccharide obtained from marine brown algae [Sapana A et al., 2014]. Alginic acid is a linear copolymer composed of D-mannuronic acid (M) and L-guluronic acid (G). Alginates are linear unbranched copolymers of -d-mannuronic acid (M) and -l-guluronic acid (G) units. The M and G monomers are 1 \rightarrow 4 linked by glycosidic bonds, forming homopolymeric M- or G-blocks and heteropolymeric MG blocks. In the presence of polyvalent cations such as Ca^{2+} or Al^{3+} , cross-linking occurs to form gels. The cations act as bridges between the anionic polymer chains, constituting junction zones, forming a hydrogel network. Ca^{2+} , a commonly used cross-linker, preferentially interacts with G blocks due to structurally favorable chelation sites formed by the corrugated chains.

Alginate is commonly employed as cross-linked matrices or coats in drug delivery systems. It is also extensively used to encapsulate living cells, such as yeasts for fermentation and pancreatic islets for clinical applications. Na-Alg is a biopolymer that is widely used as an encapsulation matrix due to its ability to form hydrogels upon

- This is an Open Access article distributed under the terms of the Creative Commons Attribution-Noncommercial 4.0 Unported License, permitting all non-commercial use, distribution, and reproduction in any medium, provided the original work is properly cited.

- Selection and peer-review under responsibility of the Organizing Committee of the Conference

cross-linking. Its ability to gel under mild conditions makes alginate the polymer-of-choice in food, pharmaceutical and biotechnological applications. Its unique property of forming water insoluble calcium alginate gel through ionotropic gelation with calcium ions is a simple, mild and eco-friendly condition has made possible to encapsulate macromolecular bio-active agents like cell, enzyme, protein and vaccine.

The aim of this study is to develop a series of hydrogel beads via ionic gelation method using Na-Alg and CaCl₂ as crosslinker. By changing the polymer/crosslinker ratio and crosslinking time, it is planned to obtain 21 types of hydrogel beads having different swelling values.

Methods

Preparing of Hydrogel Beads

A series of Na-Alg hydrogel beads were prepared by using ionic cross linking method (Reddy S. Giridhar et al, 2011). Aqueous Na-Alg solutions at different concentrations were dropped into chilled oil bath at -18 °C and waited for 15 minutes. Then the hardened beads were collected and left into 100 mL of crosslinker solution. CaCl₂ (Sigma-Aldrich) solution was used for ionic cross linking of Na-Alg molecules. The mixture was gently stirred with a speed of 60 rpm. This procedure was carried out by changing the concentrations of Na-Alg and CaCl₂ solutions and crosslinking time. Two of the hydrogels, A-6 and A-7 were obtained by intermittently crosslinking. At this step, the beads were exposed with crosslinker solution for 5+5 and 5+5+5 minutes. After first 5 minute, the beads were taken out from crosslinker medium, waited for 5 minutes and then left again into crosslinker solution. Preparation conditions were summarized into Table 1.

Table 1. The preparation conditions of Na-Alg hydrogel beads

| Hydrogel | Na-Alg (%) | CaCl ₂ (%) | Crosslinking Time (min) |
|----------|------------|-----------------------|-------------------------|
| A-1 | 10 | 10 | 30 |
| A-2 | 10 | 10 | 20 |
| A-3 | 10 | 10 | 15 |
| A-4 | 10 | 10 | 10 |
| A-5 | 10 | 10 | 5 |
| A-6 | 10 | 10 | 5+5 |
| A-7 | 10 | 10 | 5+5+5 |
| A-8 | 10 | 5 | 5 |
| A-5 | 10 | 10 | 5 |
| A-9 | 10 | 15 | 5 |
| A-10 | 10 | 20 | 5 |
| A-13 | 10 | 35 | 5 |
| A-16 | 8 | 5 | 5 |
| A-19 | 6 | 5 | 5 |

The formed beads were collected by filtration and immersed in distilled water in order to remove unreacted ingredients. After purification, the beads were dried in oven at 30 °C.

The schematic representation was given in Figure 1.

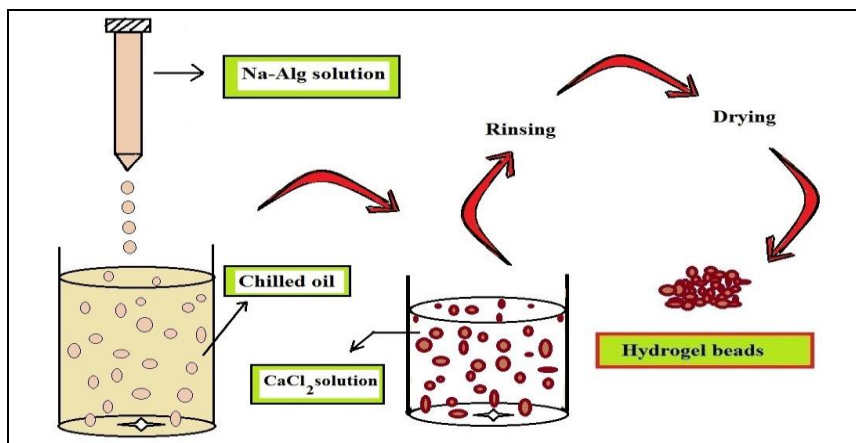


Figure 1 Preparation of hydrogel beads by dropping gelation method

Swelling Tests

Swelling tests of hydrogel beads were gravimetrically carried out in three steps. In the first step, the weighed dried hydrogels were immersed in 100 mL of distilled water at 30°C. Swollen beads removed from the swelling medium at regular intervals. Then, they were dried superficially with a filter paper, weighed, and placed into the same bath. The tests were performed until constant weight was reached. The swelling percentages (%) of hydrogels were calculated from [Pulat and Asil 2009, Hsiue et al. 2001]:

$$S (\%) = \frac{M_w - M_d}{M_d} \times 100 \quad (1)$$

where M_w is the wet weight of the sample and M_d is the dry weight of the sample before swelling.

In the second step, it is decided to work with only 5 types of hydrogel beads for determining the temperature effect on swelling behaviors. According to the swelling values A-5, A-8, A-9, A-10 and A-13 hydrogels were chosen. The dried hydrogels were swollen in distilled water (pH = 7.0) at different temperatures ranging from 10 to 60°C to determine the effect of temperature on swelling behaviors. Equilibrium swelling time was kept as 12 hours. The swollen hydrogels were taken out from swelling medium, dried, and weighed. Swelling values were calculated from Equation 1.

In the third step, the tests were repeated for 2 hydrogels used in the second step. The dried hydrogels were immersed in different Britton–Robinson buffer (BRB) solutions at various pH values (from 2.0 to 12.0) to investigate the effect of pH on the swelling behaviors. At the end of 12 h incubation, the swollen hydrogels were taken out from swelling medium, dried, and weighed [Pulat M., Akalın G.O.,2013]. Swelling values were calculated using Equation 1.

The reproducible results for all swelling studies were obtained with triplicate measurements.

Results and Discussion

13 of Na-Alg beads were prepared by ionic gelation method based on the interaction of oppositely charged macromolecules. Ionic gelation involves simply the interaction of an ionic polymer with oppositely charged ion to initiate cross linking [Sapana A et al., 2014]. CaCl_2 has often been used to prepare Na-Alg particles because of its nontoxic and ionic interactions properties. Na-Alg polymers and CaCl_2 are a favorable pairs for crosslinking mechanism. Na-Alg molecules are ionized in water by losing of their Na^+ ions and meanwhile Ca^{2+} ions cross-linked two different polymer rings. The positive charged Ca^{2+} ions can react with negative charged alginates molecules via electrostatic attraction to form ionic crosslinked networks. A schematic mechanism about ionic crosslinking of Na-Alg was presented in Figure 2 [Kühbeck D et al., 2015].

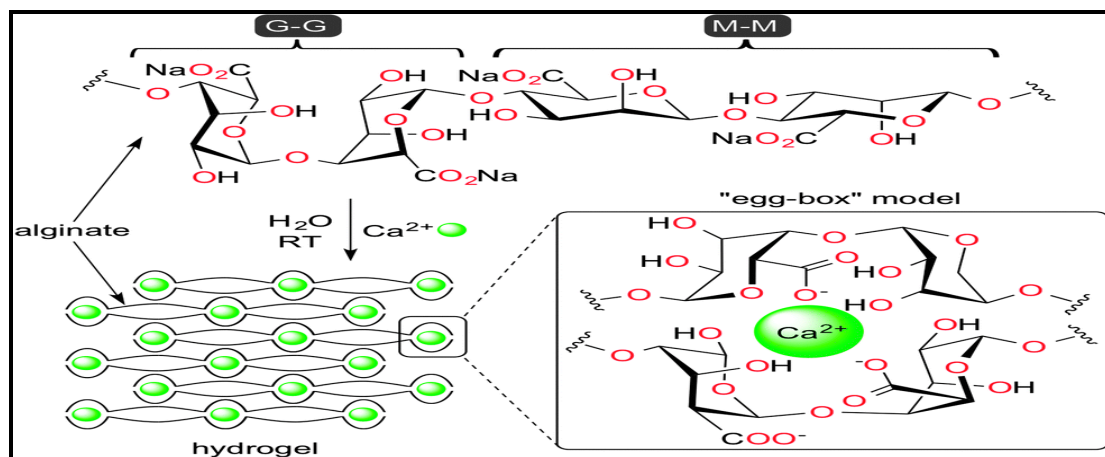


Figure 2. A schematic presentation for crosslinking mechanism of Na-Alg polymers with Ca^{2+}

Swelling Results

All of the swelling percentages belong to hydrogel beads were calculated from Equation 1. As explained in Experimental Part, the beads could be divided into four groups.

In the first group, the effect of crosslinking time to S% was investigated. A-1, A-2, A-3, A-4, A-5, A-6 and A-7 beads were prepared by changing crosslinking time while polymer and crosslinker concentration were kept constant. As indicated in Table 2, crosslinker/polymer (C/P) rate was 1.0 for these samples. Swelling variations with time were given in Figure 3. The swelling increased with time initially and then remained constant at close to 8 h. As crosslinking time increased from 5 to 30 minutes, swelling values dramatically decreased. S% values were determined to be 158% for the most swollen hydrogel A-5, and 33% for the least swollen hydrogel A-1. In this step, A-6 and A-7 hydrogels were prepared by intermittent exposing of the beads with crosslinker. The results show that not any considerable amounts of variation on swelling values were obtained.

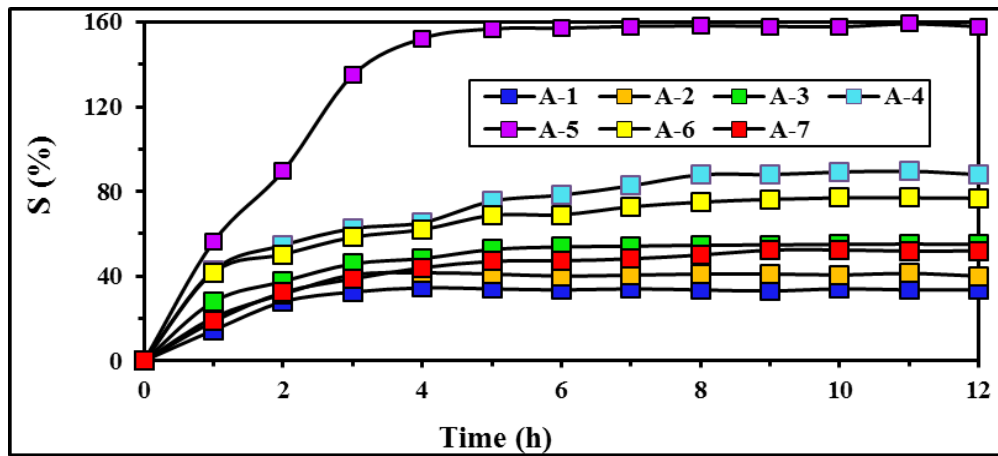


Figure 3. The variations of S% values of A-1 – A-7 beads with time (30°C; pH=7.0)

According to these results, it is decided to keep the crosslinking time as 5 minutes for other three steps.

Table 2. C/P and swelling values of Na-Alg hydrogel beads

| Hydrogel | Na-Alg (%) | C/P | Swelling (%) |
|----------|------------|------|--------------|
| A-1 | 10 | 1.00 | 33.5 |
| A-2 | 10 | 1.00 | 40.6 |
| A-3 | 10 | 1.00 | 54.6 |
| A-4 | 10 | 1.00 | 87.9 |
| A-5 | 10 | 1.00 | 157.8 |
| A-6 | 10 | 1.00 | 76.3 |
| A-7 | 10 | 1.00 | 52.3 |
| A-8 | 10 | 0.50 | Dispersed |
| A-5 | 10 | 1.00 | 157.8 |
| A-9 | 10 | 1.50 | 75.6 |
| A-10 | 10 | 2.00 | 55.4 |
| A-13 | 10 | 3.50 | 1.9 |
| A-16 | 8 | 0.62 | 88.5 |
| A-19 | 6 | 0.83 | 45.2 |

In the second group, the effect of crosslinking concentration to S% was investigated. A-5, A-8, A-9, A-10 and A-13 beads were prepared by changing crosslinker percentages while polymer concentration and crosslinking time were kept constant. C/P rates were changed from 0.5 to 3.5.

As seen from Figure 4, the swelling increased with time initially and then remained constant at close to 8 h. While crosslinker concentration increased from 5% to 35%, swelling values decreased. S% values were determined to be 158% for the most swollen hydrogel A-5, and 2% for the least swollen hydrogel A-13. Swelling values were directly connected with composition, monomer ratio, ionic charge content, polymerization route, type and density of cross-linker, and so forth [El-Sherbiny *et al.*, 2005]. As C/P ratio increased from A-

8 to A-13, S% values decreased. This behavior is attributed to the fact that the network chains became inflexible at higher crosslinker density and thus, fewer amounts of water molecules penetrated the hydrogel structure. A-8 hydrogel which prepared at the minimum C/P rate dispersed in a short time.

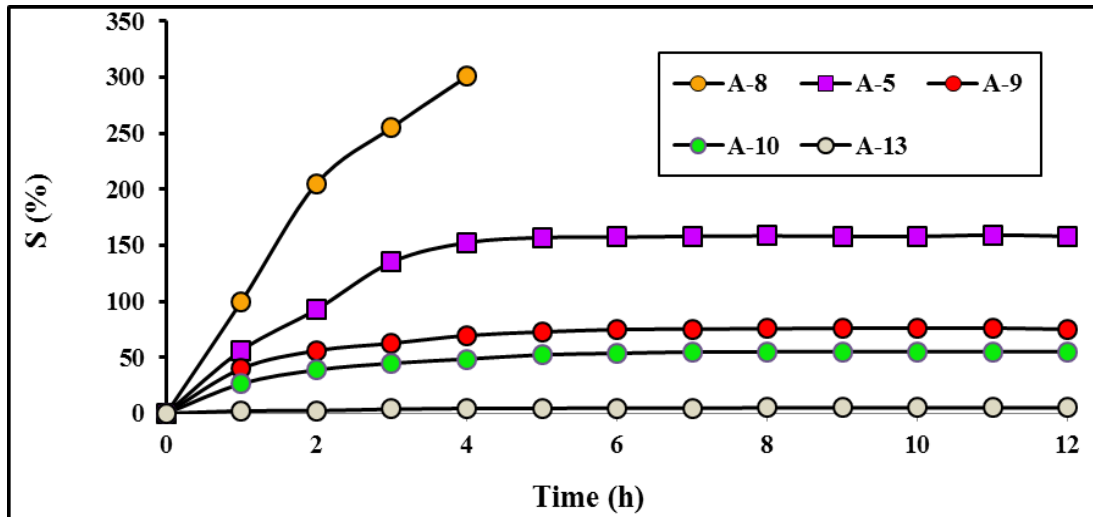


Figure 4. The variations of S% values of A-8 – A-15 beads with time (30°C; pH=7.0)

In the last group, 2 types of hydrogel beads were prepared by minimizing of the polymer amount to obtain various C/P rates. In general, higher crosslinker amounts per Na-Alg causes less S% values. It is observed that, as C/P ratio increased from A-16 to A-19, S% values sharply decreased. The results were presented in Figure 5.

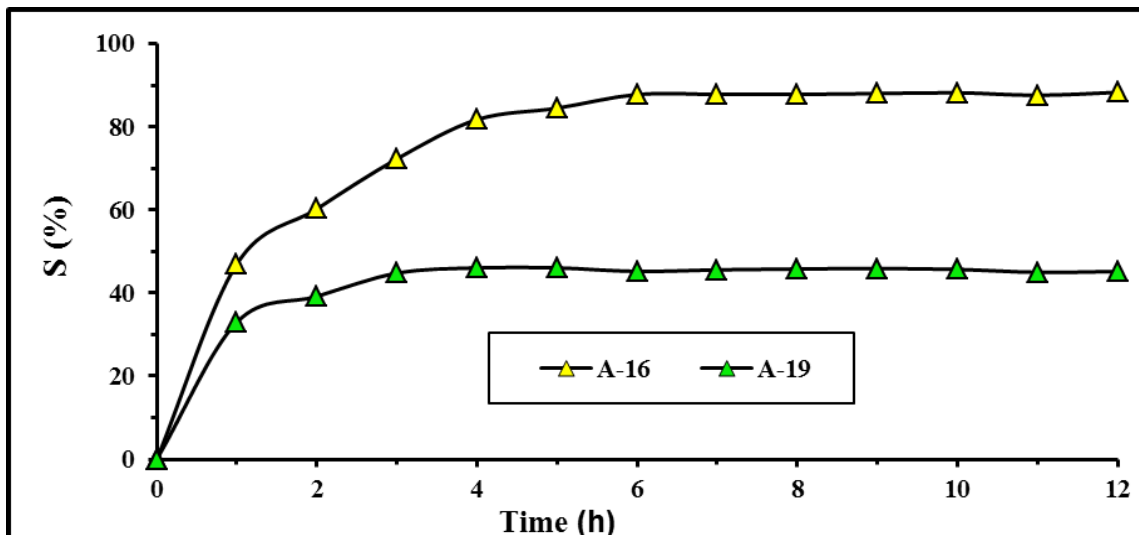


Figure 5. The variations of S% values of A-16 – A-19 beads with time (30°C; pH=7.0)

The variations of swelling values with temperature at pH 7.0 and 12 h are presented in Figure 6. Swelling percentages slightly increased with temperature and then remained constant. The most swollen bead is A-5. As the temperature increases, thermal mobility of the polymer chains increases and H-bonds were broken, and hydrogels can easily swell [Esposito, E et al, 1996]. A-8 rapidly degraded over 20°C. It is commended that, Na-Alg hydrogels are suitable for using in wide temperature ranges.

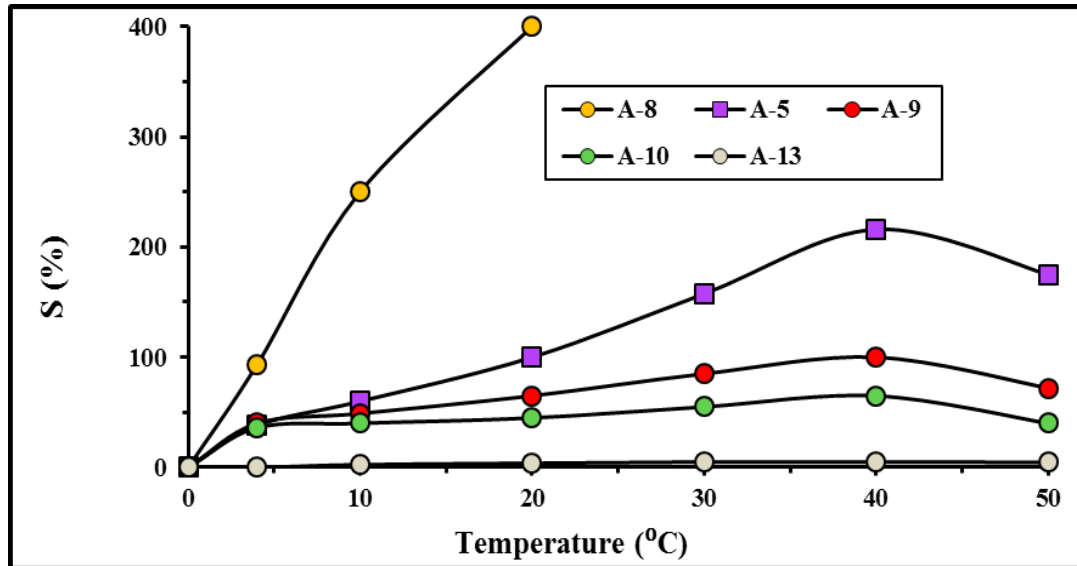


Figure 6. The variation of S% values with temperature at pH = 7.0 and 12 h.

Figure 7 presents the variation of S% values of hydrogels with pH at 30°C and 12 h. As the pH is increased from 2 to 7, a sharp increment was observed. At low pH's, ionization of Na⁺ is not easy and it is thought that the polymer molecules are in neutral position. While pH values rise, ionization could be active and swelling values increases. The ionized negatively charged pendant groups on the polymer chains caused repulsion leading to swelling. As swelling pressure increased, hydrogel expanded and thereby maximizes the repulsion between the ionized groups. After a summit was observed near pH= 7, the swelling sharply decreased. A-5 hydrogel degraded near pH=8.

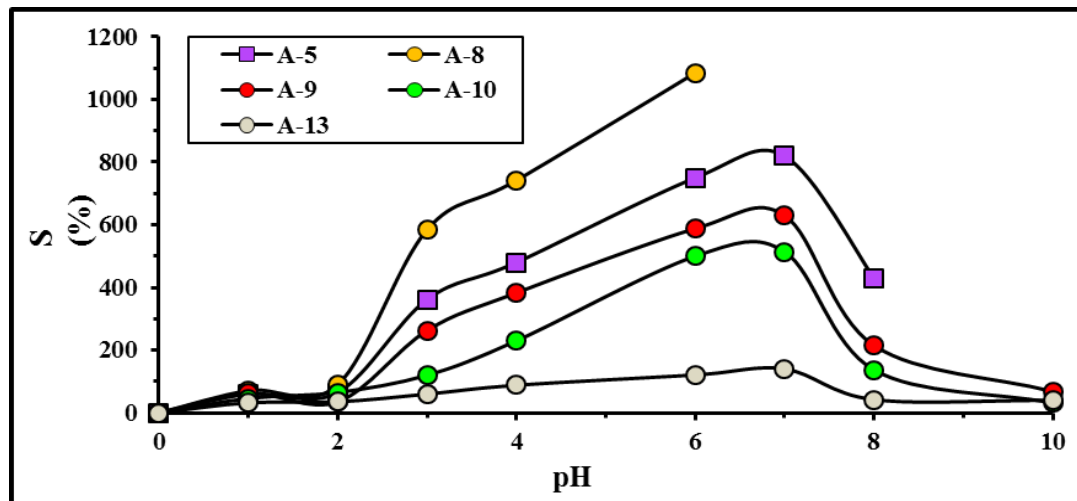


Figure 7. The variation of S% values with pH at 30°C, 12 h

Conclusion

The results of the present work indicate that the Na-Alg hydrogels in a wide range of swelling behaviors could be prepared by dropping method. It can be concluded that the hydrogel beads obtained in this study is much promising in utilizing a natural resource like Na-Alg in the production of matrix material which could significantly reduce the production costs and offering a quite environmental friendly alternative technique.

References

- El-Sherbiny I.M., Lins R.J., Abdel-Bary E.M., Harding D.R.K.(2005). Preparation, characterization, swelling and in vitro drug release behaviour of poly(*N*-AG-chitosan) interpolymeric pH and therm.-responsive hydrogels. *Europ. Polym. J.* 41, 2584-2591.
- Esposito, E., Cortesi, R., Nastruzzi, C., (1996). Gelatin microspheres: Influence of preparation parameters and thermal treatment on chemico-physical and biopharmaceutical properties”, *Biomaterials*, 17: 2009–2020.
- Akalin G.O and Pulat M. (2018). Preparation and Characterization of nanoporous Sodium Carboxymethyl Cellulose Hydrogel Beads, *Journal of Nanomaterials*, Volume 2018, 1-12.
- Hsiue, G.H., Guu, J.A., and Cheng, C.C. (2001) Poly (2-hydroxyethyl methacrylate) film as a drug delivery system for pilocarpine. *Biomaterials*, 22:1763–1769.
- Kühbeck, D., Mayr, J., Häring, M., Hofmann, M., Quignard, F., Díaz, D. D. (2015). Evaluation of the nitroaldol reaction in the presence of metal ion-crosslinked alginates” *New Journal of Chemistry*, 39(3), 2306-2315.
- Pulat M., Akalin G.O. (2013). Preparation and characterization of gelatin hydrogel support for immobilization of *C. Rugosa* lipase. *Artif. Cells Nanomed. Biotechnol.* 41, 145-151.
- Pulat M., Asil D. (2009). Fluconazole release through semi-ipn hydrogels based on chitosan, AA, and citraconic acid. *J. Appl. Polym. Sci.* 113, 2613-2619.
- Pulat M. & Uğurlu N. (2016). Preparation and characterization of biodegradable gelatin-PAAM-based IPN hydrogels for controlled release of maleic acid to improve the solubility of phosphate fertilizers, *Soft Materials*, , 14:4, 217–227.
- Pulat M., Yoltay N. (2016). Smart fertilizers: preparation and characterization of gelatin-based hydrogels for controlled release of MAP and AN fertilizers, *Agrochimica*, 60:4, 249-261.
- Reddy S. Giridhar and Saxena Pandit Akanksha (2011). Swelling Behavior of Calcium–Ions Crosslinked Bipolymeric Sodium Alginate–Lignosulphonic Acid Blends, *International Journal of Polymeric Materials*, 60:1123–1129.
- Sapana P. A., Paraag S.G., Shrivastav B and Sharma P. (2014). Ionotropic gelation: a promising cross linking technique for Hydrogels, *Research and reviews: journal of pharmaceutics and nanotechnology*, Volume 2, Issue 1, 1-6.

Author Information

Mehlika Pulat

Gazi Üniversitesi, Fen Fakültesi,
Kimya Bölümü–Teknikokullar, Ankara/Türkiye
Contact E-mail: mpulat@gazi.edu.tr

Duygu Ozukaya

Gazi Üniversitesi, Fen Fakültesi,
Kimya Bölümü–Teknikokullar, Ankara/Türkiye

The Synergism and Antagonism behavior of Aqueous Extraction for Black Tea, Green Tea and Coffee against the Effectiveness of Certain Antibiotics

Tahreer Hadi Saleh Al-NADDAWI
Al- Mustansyria University

Shaymaa Fadhel Abbas ALBAAYIT
University of Baghdad

Zainab Zamel KHALAF
University of Baghdad

Abstract: Increasing antibiotic resistance is the most common concern in the world. *Escherichia coli* are a well-known causative agent of various infectious diseases. The bacterial resistance on the *E.Coli* was noted against various antibacterial agents. Thus, the objective of this study is to evaluate the assessment of the green, black tea and coffee in improving antibiotic susceptibility towards *E.Coli*. Antimicrobial susceptibility test was performed to determine the sensitivity of *E.Coli* to Augmentin, Amikacin, Imipenem, Ciprofloxacin, Nitrofurantoin, Pincillin, Cefixime, Tetracyclin, Chloramphenicol and Ceftriaxone. The results show that the *E.Coli* was resistant to all antibacterial agents, while Pincillin, amikacin and Nitrofurantoin was appeared sensitive to moderate respectively. The aqueous extract of green and black tea have synergistic effect for Chloramphenicol and Nitrofurantoin susceptibility, on the other hand, the antagonistic effect was on Tetracyclin, Ciprofloxacin and Amikacin activities. The aqueous extract of coffee was strongly inhibitory to bacteria at concentrations 5 and 7.5%. These results may suggest using this natural product for increasing some of antibacterial agents' effect.

Keywords: *Escherichia coli*, Antibiotic resistance, Black tea and coffee

Introduction

Black tea, green tea and coffee can be widely consumed in the Middle East; these products contain biological active compounds, which help to reduce microbial infection. The pharmacological validation have been reported the anti-microbial activity of these natural product (Mbuthia et al., 2014); however, there is limited knowledge about the combination effect with some antibiotics against resistant microbes.

Phenomenon of resistance among microorganisms against currently antimicrobial is the most common concern in the world. Although developments in antimicrobial drugs therapy, these therapies associated with resistance and often infectious diseases are hard to treat. For over years, the step of development of novel antimicrobial drugs has slowed down when the prevalence of resistance has grown at a formidable rate, there have been interesting to use combination therapy (Usha et al., 2010; Aiyegoro et al., 2009). Since the Combination therapy can be used to expand the antimicrobial spectrum due to its role in preventing the germination of resistant mutants and minimizing the toxicity, thereby exhibiting antimicrobial activity greater than that would be expected from each antimicrobial drug individually (Si et al., 2008). Thus, the present study was undertaken to evaluate the Synergistic or antagonistic effects of black tea, green tea and coffee extracts with common antibiotics, which might provide natural solution for increasing some of antibacterial agents' effect.

Method

Bacterial Strain

The *Escherichia coli* was obtained from postgraduate student in biology department- College of science- Mustansiriyah University and diagnostic by morphological characteristic and biochemical tests beside to re-conform by API 20 E system. It was isolated from patient suffering Urinary tract infection; it has been cultured on nutrient agar plate and activated in Brain heart infusion broth then incubated for 24 h at 37°C. Bacterial strain was maintained on nutrient agar slant for 4-5 weeks and in LB broth supplemented with 20-25% glycerol at -20°C for long time preservation. Test bacterial isolate was sub-cultured onto fresh plates of nutrient agar at 37°C for 24 h. Colonies from these plates were suspended in Mueller-Hinton broth to a turbidity matching 0.5 mc McFarland standard (108 cfu/ml) for bacteria (McFarland, 1970).

Antimicrobial susceptibility test

Disc diffusion method was performed to determine the sensitivity of *E. coli* to Augmentin, Amikacin, Imipenem, Ciprofloxacin, Nitrofurantoin, Pincillin, Cefixime, Tetracyclin, Chloramphenicol and Ceftriaxone. The diameters of inhibition zone for individual antibiotics were measured to the nearest millimeters and values were interpreted as resistant and sensitive categories referring to interpretation table of national board for clinical laboratory standard recommended by National Committee for Clinical Laboratory Standards (Ferraro, 2001).

Preparation of aqueous extraction

The black tea, green tea, and coffee used in this study were brought from local markets in Baghdad. Aqueous extraction for above plants were prepared at 2.5, 5 and 7.5 % by mixing the required quantity of dry Leaves and coffee powder with distilled water, then heated with slowly at boiling degree 100 °C for 15 min. The solution was allowed to cool at room temperature for 1- 2 hours and then filtrated by Whatman filter paper no1; the supernatant was collected and used as crud extract and kept in refrigerator at 4 °C until used. 100 ml from all above extraction was mixed together with Mueller-Hinton agar powder and dissolved well and then sterilized by autoclave. The antibiotics discs were fixed on cultured plates and incubated for 24h at 37°C. The diameters of inhibition zone for single antibiotics were measured by millimeters and values were interpreted as resistant and sensitive categories referring to interpretation chart that recommended by National Committee for Clinical Laboratory Standards (Ferraro, 2001). The extract that decreased sensitivity activity it was categorized as antagonism effect, while the extract that gave enhanced of sensitivity greater than the control was considered Synergism.

Results and Discussion

The results are illustrated in Table 1. Showed that *E. coli* isolate was sensitive to Imipenem, Ciprofloxacin, ceftriaxone, Tetracyclin, Cefixime, Chloramphenicol and Augmentin respectively, while to amikacin and Nitrofurantoin was moderate, but against to Pincillin it was appeared resistance. This pattern was changed when the *E. coli* was cultured on different aqueous extraction plate agar for green tea, black tea and coffee which regulated with gradient concentration. The results were exhibit all concentration of green tea and Back tea appeared synergistic for Chloramphenicol and Nitrofurantoin susceptibility; but antagonistic effect was shown on Tetracyclin, Ciprofloxacin and amikacin activity. The inhibition effect of coffee was appeared strongly when the bacteria was cultured on 5 and 7.5% of coffee and no growth was appeared.

The increased level of inhibition zone diameter on combination of the aqueous extract with Chloramphenicol and Nitrofurantoin might be related to the presence of two binding sites on the bacterial surface for antibiotic and extract. Furthermore, the enhanced level might be explained by capacity of extracts to induced damage of the bacterial cell wall and the possible interference, resulting in the inhibition its biosynthesis (Esimone et al., 2006; Hosseini et al., 2006). The result in this study is in agreement with outcomes reported by Souto de Oliveira et al who reported the effect of combination of extraction plant with antimicrobial drugs on pathogenic bacterial growth, the synergistic activity of tetracycline, norfloxacin, and erythromycin combined with ethanol extract of *Mangifera indica* L. peel was investigated against different *S. aureus* strains. Single extract did not show considerable antibacterial activity at (MIC \geq 2048 μ g/ml), but it adjust the activity of antibiotics at (MIC = 512 μ g/ml) when combined with antibiotics, a four-fold drooping in the MIC values for erythromycin and

tetracycline was detected. The study demonstrates that mango peel may act as a source of potential enhancement of antibiotics, which adds significant value to mango by-product. Toroglu who proved that the effective of various spices and herbs include *Coriandrum sativum*, *Rosmarinus officinalis*, *Cuminum cyminum*, *Micromeria fruticosa* L., and *Mentha piperita* were combined with different antibiotics such as cephalothin, gentamicin, ceftriaxone, nystatin; these combination were investigated against thirty bacterial species. The results were pointed that the combination of antibiotics with plant extract further decreased drug resistance. The synergistic effects acquired may progression to new choices for the treatment of diseases that caused by pathogens (Toroglu et al., 2000; Falcão-Silva et al., 2000).

Table 1. Combination effect of salts with antibiotics

| Antibiotic | control mm on Mueller Hinton Agar | Green tea% | | | Black tea % | | | Coffee % | | |
|--------------------------|-----------------------------------|------------|----|-----|-------------|----|-----|----------|-----------|-----------|
| | | 2.5 | 5 | 7.5 | 2.5 | 5 | 7.5 | 2.5 | 5 | 7.5 |
| Imipenem(10ug/ml) | 30 | 33 | 36 | 34 | 27 | 24 | 26 | 28 | No growth | No growth |
| Chloramphenicol(30ug/ml) | 22 | 26 | 25 | 27 | 25 | 24 | 33 | 26 | No growth | No growth |
| ceftriaxone(5ug/ml) | 30 | 27 | 40 | 30 | 30 | 27 | 35 | 39 | No growth | No growth |
| Cefixime(30ug/ml) | 24 | 25 | 35 | 35 | 24 | 25 | 32 | 35 | No growth | No growth |
| Augmantin(30ug/ml) | 21 | 22 | 25 | 30 | 20 | 25 | 30 | 30 | No growth | No growth |
| Nitrofurantoin(300ug/ml) | 17 | 27 | 35 | 25 | 25 | 26 | 33 | 30 | No growth | No growth |
| Penicillin(10ug/ml) | 9 | 12 | 11 | 19 | 12 | 17 | 20 | 8 | No growth | No growth |
| Tetracyclin(30ug/ml) | 29 | 13 | 9 | 10 | 19 | 19 | 14 | 20 | No growth | No growth |
| Ciprofloxacin(5ug/ml) | 30 | 8 | 7 | 9 | 11 | 8 | 0 | 14 | No growth | No growth |
| amikacin(30ug/ml) | 16 | 10 | 10 | 16 | 10 | 8 | 0 | 8 | No growth | No growth |

 Synergism
 Antagonism

Conclusion

In conclusion, the combination of aqueous extract of green tea, black tea and coffee with different antibiotics may increase their synergistic effectiveness resistance against pathogenic *E. coli* but other antibiotic was reduced their effectiveness. This study has suggested use these extraction during infection with antibiotics.

References

- Mbuthia, S. K., Wachira, F. N., & Koech, R. K. (2014). In-vitro antimicrobial and synergistic properties of water soluble green and black tea extracts. *African Journal of Microbiology Research*, 8(14), 1527-1534.
- Usha, P. T. A., Jose, S., & Nisha, A. R. (2010). Antimicrobial Drug Resistance-A global concern. *Veterinary World*, 3(3).
- Aiyegoro, O. A., Afolayan, A. J., & Okoh, A. I. (2009). Synergistic interaction of *Helichrysum pedunculatum* leaf extracts with antibiotics against wound infection associated bacteria. *Biological research*, 42(3), 327-338.
- Si, H., Hu, J., Liu, Z., & Zeng, Z. L. (2008). Antibacterial effect of oregano essential oil alone and in combination with antibiotics against extended-spectrum β -lactamase-producing *Escherichia coli*. *FEMS Immunology & Medical Microbiology*, 53(2), 190-194.
- McFarland, J. (1907). The nephelometer: an instrument for estimating the number of bacteria in suspensions used for calculating the opsonic index and for vaccines. *Journal of the American Medical Association*, 49(14), 1176-1178.
- Esimone, C. O., Iroha, I. R., Ibezim, E. C., Okeh, C. O., & Okpana, E. M. (2006). In vitro evaluation of the interaction between tea extracts and penicillin G against *Staphylococcus aureus*. *African Journal of Biotechnology*, 5(11).

- Hosseini Jazani, N., Ariga, T., Seki, T., Bauer, A. W., Kirby, W. M., Sherris, J. C., ... & Joly-Guillou, M. L. (2006). Synergistic antimicrobial activity of tea and antibiotics. *Journal of Biological Sciences*, 7(5), 93-103.
- Ferraro, M. J. (2001). Performance standards for antimicrobial susceptibility testing. NCCLS.
- Falcão-Silva, V. S., Silva, D. A., Souza, M. D. F. V., & Siqueira-Junior, J. P. (2009). Modulation of drug resistance in *Staphylococcus aureus* by a kaempferol glycoside from *Herissantia tiubae* (Malvaceae). *Phytotherapy Research: An International Journal Devoted to Pharmacological and Toxicological Evaluation of Natural Product Derivatives*, 23(10), 1367-1370.
- Toroglu, S. (2011). In-vitro antimicrobial activity and synergistic/antagonistic effect of interactions between antibiotics and some spice essential oils. *Journal of Environmental Biology*, 32(1), 23-29.

Author Information

Tahreer Hadi Saleh Al-Naddawi

Department of Biology, College of Science
Al- Mustansyria University
Palestine street, Iraq
Contact E-mail: tahreerhadi@yahoo.com

Shaymaa Fadhel Abbas Albaayit

Department of Biology, College of Science,
University of Baghdad
Al-Jadriya, Baghdad 10070, Iraq

Zainab Zamel khalaf

Department of Biology, College of Science,
University of Baghdad
Al-Jadriya, Baghdad 10070, Iraq

Synthesis and Characterization of some New Dinuclear Complexes of Ni(II), Pd(II) and Pt(II) with Bulky Substituted Thioether Ligands

A.M. AMEEN

University of Mosul

N. H. BUTTRUS

University of Mosul

Omar K. HASSAN

University of Mosul

Abstract: A series of new multidentate ligands (L1-L4), 1,1,2,2-tetrakis [2-(benzylthio)ethylthio]ethylene(L1), 1,1,2,2-tetrakis [2-(*o*-tolylthio) ethylthio] ethylene (L2) , 1,1,2,2-tetrakis [3-(*p*-chlorophenylthio) ethylthio] ethylene (L3) and 1,1,2,2-tetrakis [2-(*o*-aminophenylthio) ethylthio] ethylene (L4) were prepared from the reaction of equimolar amount of (4-mercapto-2-thia-1-butyl benzene or *o*-methyl-4-mercapto-1-thia-1-butyl benzene or *p*-chloro-4-mercapto-1-thia-1-butyl benzene or *o*-amino-4-mercapto -1-thia-1-butyl benzene and KOH) with tetrachloroethylene in (4:4:1) molar ratio . Reaction of the above ligands with nickel (II) , palladium (II) and platinum (II) chloride salts gave the complexes of the general formulas : $[M_2(L)Cl_4]$ and $[Ni_2(L)Cl_2]Cl_2$ $M=Ni(II)$, $Pd(II)$ and $Pt(II)$, $L=L1-L4$. The synthesized ligands have been characterized on the basis of their elemental analysis , FTIR, 1H , ^{13}C NMR , and their complexes were characterized by elemental analysis metal content, UV-Vis. spectroscopic technique , conductivity measurements and magnetic measurements. On the basis of these studies, a four coordinate tetrahedral or square planar geometry around the metal ions in the complexes has been proposed.

Keywords: Bulky substituted thioether, Ni(II), Pd(II), Pt(II) complexes, Square planar complexes

Introduction

A large number of dinucleating ligands containing thiophenolate subunits have been reported in the past several years¹⁻³. These ligands represents soft analogues of the more familiar phenolate systems , and offer the potential of forming dinuclear complexes of catalytically active soft late transition metal ions such as Rh , Ir , Pd and Pt⁴⁻⁵ . In order to enhance the affinity for these metal ions further soft donor may be introduced into the ligand backbone. Among these, Phosphane functions , R_2P or RS^- , are immediately evident , because these bind very strongly to the late 4d and 5d elements⁶⁻⁷.

4,5-disulfanyl-1,3-dithiole-2-thionate (dmit²⁻) has been used extensively for preparation of mononuclear bis-dmit and tris-dmit complexes of transition and main group metals . These sulfur rich molecules have the potential for novel electronic properties owing to the extensive π -overlap of the sulfur and metal based d-orbitals⁸⁻⁹

The two new bis-alkylpyridyl substituted dmit ligands , 4,5-bis(2-pyridylmethylsulfanyl)-1,3-dithiole-2-thione (bpmdmit), and 4,5-bis(2-pyridylmethylsulfanyl)1,3-dithiole-2-thione (bpedmit) and some of their transition metal complexes have been prepared. Two basic structural types for the complexes $[MX_2L]$, ($M=Ni, Co, Cu, Pd, L=bpmdmit$ or $bpedmit$, $X=Cl$ or Br) were determined by x-ray crystallography¹⁰ .

The coordination mode of thioether-pyrazole ligands , 1,5-bis(3,5-dimethyl-1-pyrazolyl)-3-thiapentane (bdtpp) and 1,8-bis(3,5-dimethyl-1-pyrazolyl)-3,6-dithiaoctane (bdodo) ligands in Pd(II) complexes containing a

- This is an Open Access article distributed under the terms of the Creative Commons Attribution-Noncommercial 4.0 Unported License, permitting all non-commercial use, distribution, and reproduction in any medium, provided the original work is properly cited.

- Selection and peer-review under responsibility of the Organizing Committee of the Conference

diphosphine ligand is determined by subtle changes in the size of the bridge between the two phosphorus atoms . The ^1H NMR and $^{31}\text{P}(^1\text{H})\text{NMR}$ at variable temperature prove that the hemilabile character of the bdtf ligand depend on the diphosphine ligand ¹¹.

Three new nickel complexes have been synthesized with the ligand Hbss (4-mercapto-2-thia-1-butylbenzene) and Hbsms (2-benzylsulfonyl-2-methyl-5-propanethiol) . The complex $[\text{Ni}(\text{bss})_2]$ is mononuclear with an S_4 coordination environment . The complexes $[\text{Ni}_3(\text{bss})_4](\text{BF}_4)_2$ and $[\text{Ni}_3(\text{bsms})_4](\text{BF}_4)_2$ are linear trinuclear complexes that can synthesized either directly from the ligands Hbss and Hbsms in a reaction with $[\text{Ni}(\text{BF}_4)_2]$. Crystals suitable for x-ray diffraction were obtained for $[\text{Ni}_3(\text{bss})_4](\text{BF}_4)_2$ and the structure was determined by single crystal X-ray, which indicate that the nickel centers are a square planar environment ¹² .

As a part of a chelating system thioether group are known to coordinate to metal ions ^{13,14} , and in view of these interesting results and as continuation to our studies on transition metal complexes with sulfur containing ligands ¹⁵⁻¹⁷ , we have prepared here a new ligands (L^1 - L^4) and their dinuclear complexes with Ni(II) , Pd(II) and Pt(II) ions .

Experimental

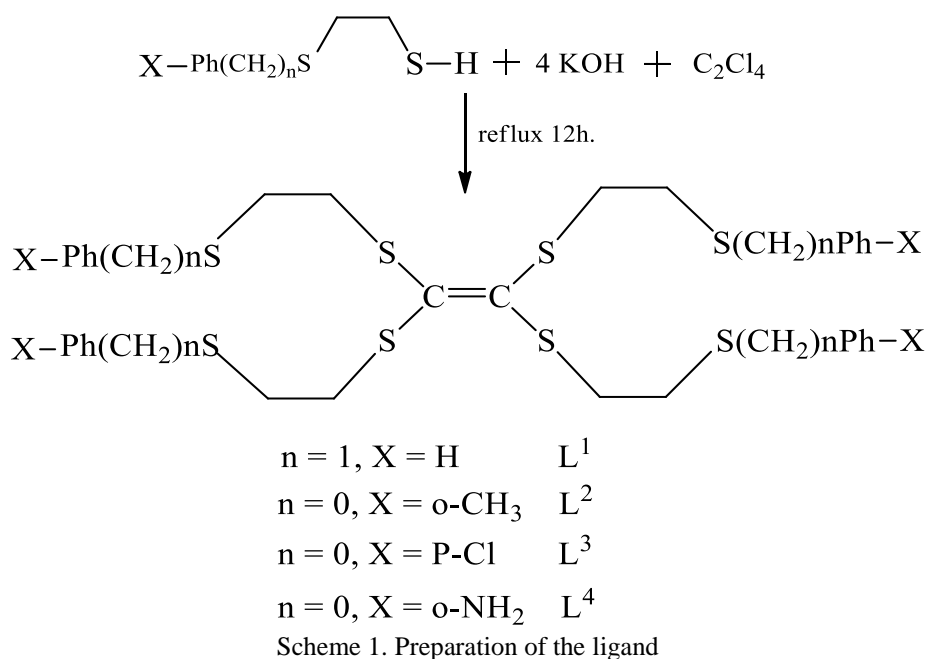
All preparation were carried out in reagent grade solvents. All chemicals used in the synthesis were obtained from Aldrich, Fluka or B.D.H and were used without further purification.

Preparation of the Ligands

The starting materials were prepared according to the literature method⁽¹³⁾.

Preparation of 1,1,2,2-tetrakis[2-(benzylthio)ethylthio]ethylene (L^1):

To a solution of 4-mercapto-2-thia-1-butyl benzene (0.73g , 0.004 mol) in 20 ml toluene was added to a solution of (0.23g , 0.004 mol) of KOH in ethanol 10 ml, then the mixture was added to a solution of tetrachloroethylene (0.17 g , 0.001 mol) in 10 ml ethanol . The mixture was stirred under reflux for 12h. on cooling the precipitate was obtained which was filtered off , washed several times with ethanol to remove the formed KCl , then it was washed with diethylether and then dried under vacuum for 4h . The preparation of the other ligands L^2 - L^4 using similar procedure as shown in Scheme (1).



Preparation of [Ni₂(L)Cl₄] or [Ni₂(L)Cl₂]Cl₂ complexes :

A solution of NiCl₂.6H₂O (0.47g, 0.002 mol) in (10 ml) ethanol was added to a stirred solution of the ligand (0.001 mol) in (10 ml) tetrahydro furan (THF). The mixture was refluxed for 2h. The mixture was left 12h. at room temperature to give the precipitate , which was filtered off several times with ethanol and diethylethe then dried under vacuum for several hours .

Preparation of [Pd₂LCl₄] : (L=L¹-L⁴) :

The salt Na₂PdCl₄ was prepared by heating (0.35 g , 0.002 mol) of PdCl₂ and (0.23 g , 0.004 mol) of NaCl in 5 ml distilled water and added gradually with continuous stirring to (0.76 g , 0.001 mol) of ligand (L¹) in 20 ml of tetrahydrofuran . The mixture was refluxed for 2h , the solvent was evaporated in vacuum . Red brown powder was obtained , it was washed several times with distilled water and diethylether , the precipitate was dried under vacuum . The other complexes were prepared similarly .

Preparation of [Pt₂LCl₄] : (L=L¹-L⁴) :

To a solution of L¹ (1,1,2,2-tetrakis[2-(benzylthio)ethylthio]ethylene) (0.76 g , 0.001 mol) in 20 ml tetrahydrofuran was added a solution of K₂PtCl₄ (0.83 g , 0.002 mol) in a 5 ml distilled water . The mixture was refluxed for 2h , the solvent was evaporated in vacuum to half volume , golden precipitate was obtained which washed several times with distilled water and diethylether , the precipitate was dried under vacuum for several hours .The other complexes were prepared similarly.

Physical Measurements

Elemental analysis of the isolated complexes were accomplished by using (elementar vario micro cube) at Department of Chemistry, Liverpool University (U.K.). Metal content estimation were done on Sens AA GBC SCIENTIFIC EQUIPMENT 3000 Atomic absorption spectrophotometer at Mosul University, College of Basic Education. Conductivity measurements for 10⁻³ M solution of the complexes in (DMF) were carried out on Jenway 4510 conductivity meter at Mosul University , College of Science .The infrared spectra for ligands and complexes were recorded on a FT-IR (Brucker Alpha Sample Compartment RT-D1aTGS at the range (200-4000 cm⁻¹) without using KBr or CsI .This measurements were carried out at Department of Chemistry , Liverpool University . The UV/Vis spectra were recorded on a Shimadzu UV-160 spectrophotometer for 10⁻³ M solution of the complexes in DMF using 1 cm quartz cell. Magnetic susceptibilities values were corrected for diamagnetic contribution using Pascal's constants and measured at 25°C on the solid state using Bruker B.M.6 instruments.

Results and Discussion

The multidentate ligands (L¹-L⁴) , not previously reported in the literature were prepared according to the following scheme (1) , by treatment of 4-mercapto-2-thia-1-butyl benzene or 2-methyl-4-mercapto-1-thia-1-butylbenzene or 4-chloro-4-mercapto-1-thia-1-butylbenzene or 2-amino-4-mercapto-1-thia-1-butylbenzene ,with potassium hydroxide and tetrachloroethylene , yielded the desired products . The ligands were characterized by elemental analysis, IR, ¹H, ¹³C NMR spectroscopy and electronic spectra. The IR and NMR data are in accordance with the proposed structures. Disappearance of the SH stretching vibration , related to the thiol functional group along with the growing of strong bond in the region 829-857 cm⁻¹ due to the C-S bands , indicates the formation of the ligands , as well as the removal of the chloride ions confirmed by sodium fusion test and elemental analysis.

The ligands (L¹-L⁴) are white to brown in color, are isolated in good yield and are pure by NMR and elemental analysis (Table 1) . the ¹H, ¹³C – NMR spectra of these ligands are first order at the field strength employed and peak assignment were straight forward . The ¹H NMR spectrum of (L¹) exhibit the aromatic protons were observed in the region 7.249 - 7.343 (m, 20 H) , 3.945 (t, H) , 3.946 – 3.879 (m, 8H , CH₂) , 3.819 (t, 1H) , 3.725 (s, 1H) , 3.146 (m, 3H) , 2.88 – 2.827 (m, 3H) , 2.693 – 2.646 (m, 5H) , 2.572 (d, 2H) for L¹ , and 6.840 – 7.411 (m, 16H , Ar) , 4.452 (S, 8H , NH₂) , 3.134 (m, 8H , CH₂) ; 2.898 (m, 8H , CH₂) for L⁴ , the ¹³C – NMR spectrum shows peaks at 30.4-35.33 ppm for (a – c) CH₂ , 127.5 for c = c and 128.9 – 139.0 ppm for

aromatic carbon for L^1 , and 22.0 – 38.2 for (a – c) CH_2 and 125.5 for (C = C) and 128.47 – 148.0 ppm for aromatic carbon for L^4 as in fig (1).

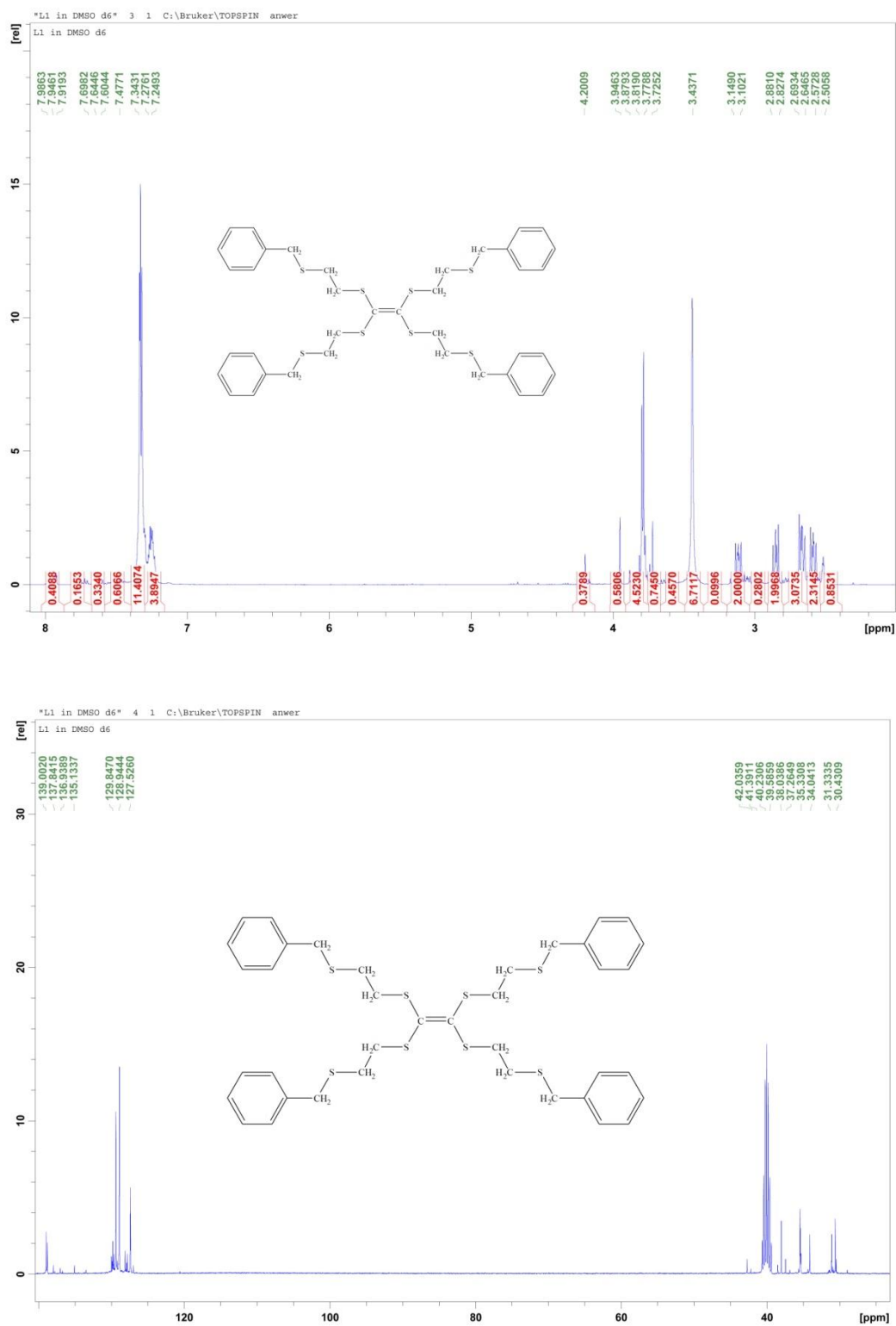


Fig 1a. ¹H, ¹³C, for ligand (L1)

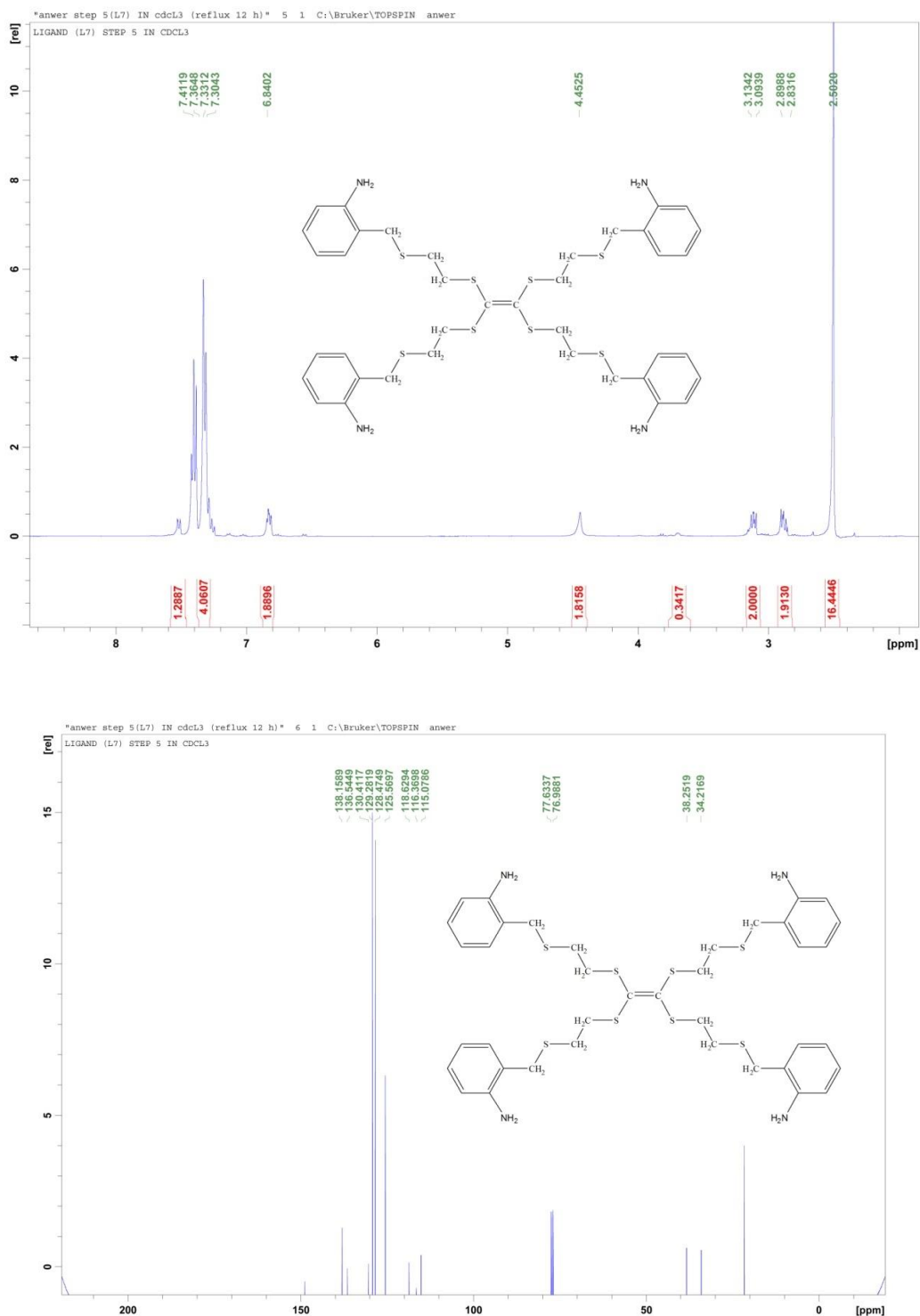


Fig. 1b. ¹H, ¹³C for ligand(L4)

The reaction of these ligands (L^1 - L^4) with nickel(II), palladium(II) and platinum(II) chloride in a (1:2) ligand to metal molar ratio gives the complexes of the formulas $[M_2(L)Cl_4]$ and $[Ni_2(L)Cl_2]Cl_2$, $M = Ni, Pd, Pt$, $L = L^1$ - L^4 . The elemental analysis are consistent with the proposal molecular formula that show the ratio of ligand to metal is (1:2).

The physical properties of the solid complexes are listed in Table (2). The complexes are quite stable in air, fairly stable to heat and melt or decompose at abouts 135 – 309 °C. They are insoluble in common organic solvents, however, soluble in dimethyl formamide (DMF) or dimethyl-sulfoxide (DMSO).The electrical molar

conductance of the complexes in 10^{-3} M (DMF) solution within the range $16 - 55 \text{ ohm}^{-1} \cdot \text{cm}^2 \text{ mol}^{-1}$, indicating the neutral nature of the complexes excepts for the complexes of the formula $[\text{Ni}_2(\text{L})\text{Cl}_2]\text{Cl}_2$ which are (1:2) electrolyte in nature¹⁸. This is consistent with stoichiometry assumed for the complexes on the basis of analytical data.

The most important IR assignments of the ligands as well as their bonding sites Table (3) have been determined by a careful comparison of the spectra of the ligands with those of their complexes. The IR spectra of the ligands showed a medium band at $(1618 - 1660) \text{ cm}^{-1}$ assigned to $\nu(\text{C} = \text{C})$ vibration and this band remained unchanged in the spectra of all complexes. The $\nu(\text{C} - \text{S})$ absorption band appeared at $(829-857) \text{ cm}^{-1}$ in the free ligands was found to appear at lower frequency in the spectra of all the complexes except in complexes (4,8,12) the shift of $\nu(\text{C} - \text{S})$ is upward by $(841-848 \text{ cm}^{-1})$ indicating the involvement of sulphur atoms of the ligands in the coordination with the metal ion¹⁹. The IR spectra of the ligand L^4 exhibited a band at the 3343 cm^{-1} region attributed to $\nu(\text{NH}_2)$ and this band remained almost constant upon coordination of this ligand with the metal ions. This indicates that the NH_2 group had not participated in the coordination.

Moreover, the IR spectra of the complexes showed new bands at $350-375 \text{ cm}^{-1}$ which tentatively assigned to $\nu(\text{M} - \text{S})$ respectively ($\text{M} = \text{Ni}, \text{Pd}, \text{Pt}$)²⁰. Further, the IR spectra of the complexes showed another new band in the region of $295 - 325 \text{ cm}^{-1}$ which may well be due to $\nu(\text{M} - \text{Cl})$ frequency²¹. This band split into two bands and this can be taken as evidence for square planar cis configuration of these complexes ($\text{M} = \text{Pd}$ or Pt). The effective magnetic moment values of the complexes and presented in Table (2). The Ni(II) complexes has a μ_{eff} value of $3.15 - 3.65 \text{ B.M}$ which suggest a tetrahedral geometry, while all Pd(II) and Pt(II) are diamagnetic as expected for d^8 -metal ion in a square plane field²².

In order to obtain some more information about the coordination behaviors of the metal ions, the electronic spectra of the complexes have been recorded. The tentative assignments of the absorption bands from the electronic spectra of the ligands and their complexes and listed in Table (3). Then π^* transition associated with the ligands were found in the region cm^{-1} . The Ni(II) complexes exhibits bands at $(12919 - 14492 \text{ cm}^{-1})$ indicating the transition ${}^3\text{T}_1(\text{F}) \longrightarrow {}^3\text{T}_1(\text{P})(\nu_3)$ in a tetrahedral geometry²³. The (d - d) bands for the spectrum of the complexes of Pd(II) and (II) having low intensities appeared at $(22727-25641 \text{ cm}^{-1})$ were assigned to the ${}^1\text{A}_1\text{g} \longrightarrow {}^1\text{A}_2\text{g}$ transition, in square planer environment around Pd(II) and Pt(II) with D_{4h} symmetry²⁴.

On the basis of the foregoing results, the ligand used in this study, coordinate to the metal ions in tetrahedral and square planer fashion from the S sites of the ligand forming the dinuclear complexes as shown in fig. (2).

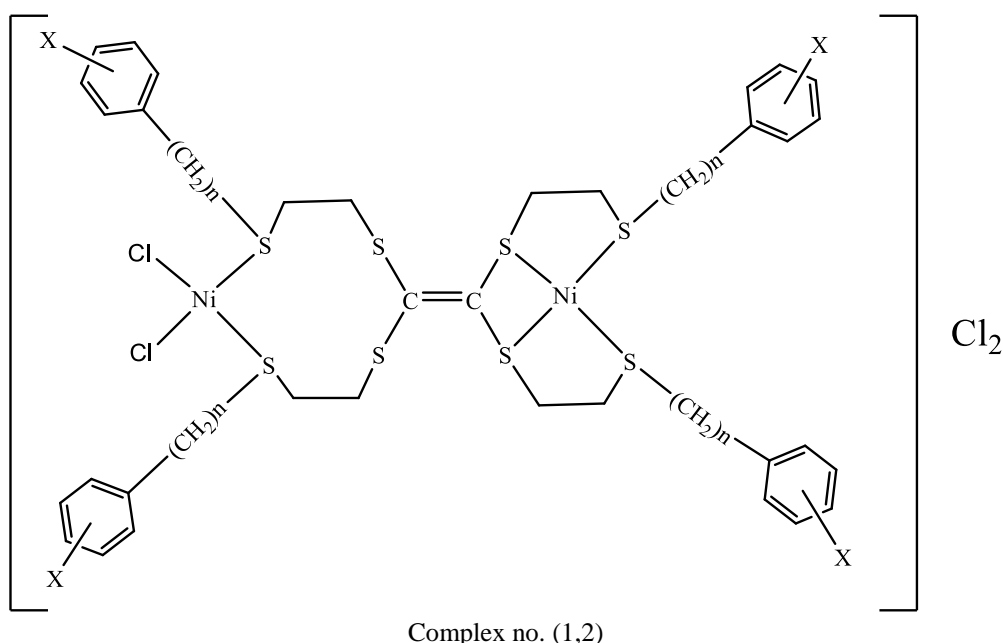


Fig 2a. Suggested structure for nickel complexes

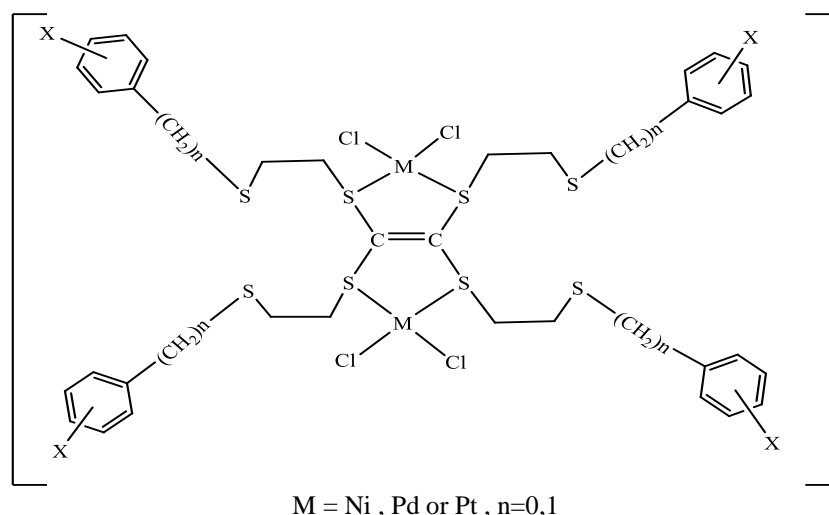


Fig. 2b. Suggested structures for the complexes

Table 1. Some physical properties and elemental analysis of the prepared ligands

| Ligand Seq. | Chemical formula | M. p (°C) | Color | Yield | Analysis found / (calc.) | | | |
|----------------|--|-----------|-------------|-------|--------------------------|----------------|----------------|------------------|
| | | | | | C% | H% | N% | S% |
| L ¹ | C ₃₈ H ₄₄ S ₈ | 231-233 | Beige | 65 | 59.71 (60.31) | 5.42 (5.82) | --- | 33.64 (33.86) |
| L ² | C ₃₈ H ₄₄ S ₈ | 285-288 | Pale yellow | 67 | 60.20 (60.31) | 5.61 (5.82) | --- | 32.90 (33.86) |
| L ³ | C ₃₄ H ₃₂ S ₈ Cl ₄ | 255-258 | White | 63 | 48.46 (48.68) | 3.64 (3.81) | --- | 30.23 (30.54) |
| L ⁴ | C ₃₄ H ₄₀ N ₄ S ₈ | 130 d | Light brown | 72 | 53.99 (53.68) | 5.51 (5.26) | 7.86 (7.36) | 32.74 (33.68) |

d= decomposition

Table 2. Analytical data and physical properties of the complexes

| No. | Complexes | M. p (°C) | Colour | Yield | Analysis found / (calc.) | | | | | Λ_M Ohm ⁻¹ .cm ² .mol ⁻¹ | μ_{eff} B.M |
|-----|---|-----------|-------------|-------|--------------------------|----------------|----------------|------------------|------------------|--|--------------------|
| | | | | | C% | H% | N% | S% | M% | | |
| 1 | [Ni ₂ L ¹ Cl ₂]Cl ₂ | 156 d | Brown | 96 | 44.30 (44.51) | 4.15 (4.29) | --- | 24.76 (24.98) | 11.18 (11.56) | 138 | 3.65 |
| 2 | [Ni ₂ L ² Cl ₂]Cl ₂ | 218 d | Light brown | 51 | 44.75 (44.90) | 4.26 (4.33) | --- | 24.87 (25.21) | 11.00 (11.56) | 121 | 3.15 |
| 3 | [Ni ₂ L ³ Cl ₂] | 150 - 152 | Light brown | 50 | 42.35 (42.70) | 3.22 (3.34) | --- | 25.92 (26.79) | 9.59 (10.70) | 14 | 3.53 |
| 4 | [Ni ₂ L ⁴ Cl ₄].2H ₂ O | 307 - 309 | Light brown | 65 | 38.67 (40.02) | 4.17 (3.92) | 5.30 (5.49) | 24.26 (25.11) | 11.65 (11.52) | 29 | 3.58 |
| 5 | [Pd ₂ L ¹ Cl ₄] | 140-142 | Brown | 94 | 40.06 (41.05) | 3.67 (3.96) | --- | 22.18 (23.04) | 18.21 (19.15) | 20 | Dia |
| 6 | [Pd ₂ L ² Cl ₄] | 182 d | Dark brown | 60 | 40.76 (41.05) | 3.81 (3.96) | --- | 22.91 (23.04) | 17.70 (19.10) | 55 | Dia |
| 7 | [Pd ₂ L ³ Cl ₄] | 200 d | Dark brown | 95 | 33.91 (34.20) | 2.77 (2.68) | --- | 21.61 (21.46) | 16.12 (17.84) | 22 | Dia |
| 8 | [Pd ₂ L ⁴ Cl ₄] | 260 d | Dark brown | 68 | 36.01 (36.62) | 3.70 (3.59) | 4.49 (5.02) | 22.59 (22.98) | 18.71 (19.08) | 50 | Dia |
| 9 | [Pt ₂ L ¹ Cl ₄].2H ₂ O | 135 d | Orange | 78 | 34.43 (35.39) | 3.32 (3.41) | --- | 19.33 (19.87) | --- | 10 | Dia |
| 10 | [Pt ₂ L ² Cl ₄] | 117 - 119 | Black | 72 | 35.23 (35.39) | 3.53 (3.41) | --- | 19.48 (19.87) | --- | 39 | Dia |
| 11 | [Pt ₂ L ³ Cl ₄] | 170 - 172 | Brown | 63 | 28.92 (29.77) | 2.43 (2.33) | --- | 18.79 (18.68) | --- | 71 | Dia |
| 12 | [Pt ₂ L ⁴ Cl ₄] | 142-145 | Olive green | 62 | 32.01 (31.57) | 3.61 (3.09) | 4.37 (4.33) | 20.20 (19.81) | --- | 41 | Dia |

d= decomposition, a= platinum cathode is not available

Table 3. Infrared, electronic spectra of the free ligands and their metal complexes

| Compound | ν (C=C) | ν (C-S) | ν (M-S) | ν (NH ₂) | ν (M-Cl) | U.V./Visible |
|----------------|-------------|-------------|-------------|--------------------------|--------------|--------------------------------------|
| seq. | | | | | | Band maxima |
| | | | | | | λ_{\max} (cm ⁻¹) |
| L ¹ | 1653(m) | 857(m) | ---- | ---- | ---- | 34246,37593 |
| L ² | 1647(m) | 839(m) | ---- | ---- | ---- | 35211 |
| L ³ | 1655(m) | 849(m) | ---- | ---- | ---- | 35714,40983 |
| L ⁴ | 1618(s) | 829(w) | ---- | 3343(b) | ---- | 32467 |
| 1 | 1662(m) | 829(m) | 362(w) | ---- | 305(w) | 12919, 32679 |
| | | | | | 325(w) | |
| 2 | 1655(m) | 829(m) | 365(w) | ---- | 300(m) | 14450 |
| | | | | | 326(m) | |
| 3 | 1655(m) | 831(m) | 352(w) | ---- | 297(m) | 14492,28571 |
| | | | | | 315(w) | |
| 4 | 1620(m) | 877(w) | 360(w) | 3327(b) | 294(w) | 14409 ,33333 |
| | | | | | 320(m) | |
| 5 | 1662(w) | 822(w) | 370(w) | ---- | 295(m) | 24630 |
| | | | | | 325(m) | |
| 6 | 1653(m) | 822(s) | 352(w) | ---- | 305(m) | 22727 |
| | | | | | 325(m) | |
| 7 | 1662(m) | 820(w) | 350(w) | ---- | 295(m) | 24038 |
| | | | | | 322(w) | |
| 8 | 1624(m) | 872(w) | 350(w) | 3347(b) | 297(w) | 23980 |
| | | | | | 315(m) | |
| 9 | 1661(m) | 835(w) | 355(w) | ---- | 300(m) | 24038 |
| | | | | | 325(w) | |
| 10 | 1653(m) | 830(w) | 375(w) | ---- | 290(w) | 23474 |
| | | | | | 315(w) | |
| 11 | 1653(m) | 835(w) | 360(w) | ---- | 280(w) | 25000 |
| | | | | | 305(w) | |
| 12 | 1613(w) | 870(w) | 370(w) | 3339(b) | 297(w) | 25641 |
| | | | | | 310(w) | |

References

- N. H. Pilkington and R. Robson. *Aust. J. Chem.* 23, 2225-2236 (1970).
 J. G. Hughes and R. Robson, *Inorg. Chim. Acta* , 35, 87-92 , (1979) .
 S. Brooker, *Coord. Chem. Rev.*, 222 , 35-56 , (2001) .

- C. K. McKenzie and R. Robson, *Inorg. Chem.* 26, 3615 – 3621, (1987).
A. Christensen, C. Mayer, F. Jensen, A. D. Bond and C. J. McKenzie, *Dalton Trans*, 108 – 120, (2008).
J. D. G. Correia, A. Domingos, I. Santos and H. Spies, *J. Chem. Soc. Dalton Trans*, 2245 – 2250, (2001).
T. Kniess, C. Fernandes, I. Santos, W. Kraus and H. Spies, *Inorg. Chim. Acta*, 348, 237 – 241 (2003).
S.J. Iob and J.R. Mansfield, *Can J. Chem.*, 74, 1377 – 1390, (1996).
R. M. Olk, B. Olk, W. Dietzsch, R. Kirmse and E. Hoyer, *Coord. Chem. Rev.*, 117, 99, (1992).
P. Cassox, L. Valade, H. Kobayashi, A. Kobayashi, R. A. Clark and A. Underhill, *Coord. Chem. Rev.*, 110, 115, (1991).
J. Becher, A. Hazell, C. J. McKenzie and C. Vestergaard, *Polyhedron*, 19, 665 – 672, (2000).
J. A. W. Ilis, M. Lutz, A.L. Spek and E. Boaman, *J. Chem. Dalton Trans*, 1275, (2002).
J. A. W. Verhagen, M. Beretta, A. L. Spek and E. Bouwman, *Inorg-Chim. Acta*, 357, 2687 – 2693, (2004).
C. Bing, W. F. F. Tzeng, C. M. Che., H. Y. Chao, K.K. Cheung and S. M. Peng, *J. Chem. Soc. Dalton, Trans.*, 1017, (1999).
N. H. Buttrus, E. A. Abdalrazaq and A. K. AL-Sger, *Int. J. Chem. Sci.* 5(3), 1111 – 1120, (2007).
N. H. Buttrus, S. N. Mohammed, A. A-Subah and E. Abdalrazaq – *Asian J. Chem.* 23(a), 4886-4891, (2013).
N. H. Buttrus and F.Saeed, *Res. J. Chem. Sci.*, 2(6), 43 – 49, (2012).
W.J. Geary, *Coord. Chem. Rev.*, 7, 8, (1971).
N. H. Buttrus, A. K. Hussain and T. A. K. AL-Allaf, *Asian. Chem.*, 15(3), 1671, (2003).
L. J. AL-Hayly, N. H. Buttrus, F. Taraq and T. A. K. AL-Allaf, *J.J. Appl. Sci.* 17(1), 64-70, (2005).
T. A. K. AL-Allaf, I. A. Mustafa and S. F. AL-Mukhtar, *Transition Met. Chem.*, (8), 1, (1993).
N. H. Buttrus, *Mu'tah J. Res. and Studies* 12(3), 225, (1997).
N. M. Buttrus, S. A. Ahmed and W. M. Jameel, *Res. J. Chem. Sci.*, 3(11), 47-54, (2013).
R. G. McDonald, M. J. Riley and M. A. Hithman, *Inorg. Chem.*, 28, 752, (1989).

Author Information

A.M. Ameen

Dept. of Chem., College of Basic Education
Mosul/IRAQ
Contact E-mail: anwermameen@yahoo.com

N. H. Buttrus

Dept. of Chem., College of Science
University of Mosul
Mosul/IRAQ

Omar K. Hassan

Dept. of Chem., College of Basic Education
Mosul/IRAQ

Determination of the Effect of Age of Broiler Breeders on General Performance, Egg Interior-Exterior Quality and Some Incubation Features

Hakan YILDIRIM
Mustafa Kemal University

Zekeriye AKCIMEN
Mustafa Kemal University

Abstract: In this study, the effect of age on the performance of broiler breeders, egg interior-exterior quality and hatching characteristics were determined. The study was conducted on a total of 6900 broiler on Ross 308 genotype. In addition to this, the rate of male-females was 1/10, and 690 cocks were used. Broilers were divided into 3 treatment groups (23-34, 35-49, 50-61 weeks). Under each age treatment 4 replicates and 575 birds with similar live weights were coincidentally placed. The study continued for a total of 39 weeks, starting at 23 weeks of age and up to 61 weeks of age. During the experiment, 1170 eggs were collected on the same day each week for the purpose of determining 30 egg internal-external quality characteristics. In the study, the effect of age on egg yield, feed consumption, feed conversion ratio, live weight, egg weight, shell thickness, shell weight, shape index, yolk index, white index, Haugh unit, fertilization rate, infertile egg ratio, hatchability of fertile egg, embryo deaths, hatching efficiency, number of double yolked egg, number of thin shelled egg, number of non-hatching egg was significant ($P < 0.05$), while the effect on shell breaking resistance and number of dirty eggs was not significant ($P > 0.05$). According to the findings of the study, age was found to be an effective factor on performance, egg quality and hatching characteristics.

Keywords: Broiler, Parent stock, Performance, Hatchability, Egg quality

Introduction

In broiler breeder rearing, due to the developments in genotype, rearing systems, nutrition and health, annual egg production per animal has reached to 183 units. Approximately 176 of this amount of hatching eggs can be used as hatching (Anonymous, 2019). This figure shows that 96% of breeding eggs produced can be evaluated as hatching. The increase in egg production makes the importance of egg quality more pronounced.

Therefore, genotype, flock age, cultivation system, feeding, health, storage, transportation and operation technology affecting egg quality should be planned well (Türkoğlu and Sarıca, 2009).

In breeding poultry farming, genetic and environmental factors (maintenance feed, in-house environmental conditions, instrument equipment, etc.) and technological developments are the main factors in increasing egg production. With the increase in the number of breeding eggs, increasing the quality of the eggs is the main target. This situation requires more studies on increasing egg quality. There are many factors affecting egg quality before and after ovulation. An egg that has been spawned has the highest quality.

The main aim in poultry farming is to increase the egg yield and to create a marketing system for the delivery of high quality eggs to the hatchery. (Abdallah et al., 1993; Elibol et al., 2000; Atasoy et al., 2001; Simsek et al., 2009).

In the poultry sector, the entire grand parent stock (large parental) chick needs are met from abroad through imports. Parent stock chicks and breeding hatching eggs are also supplied from abroad and some of them are produced in our country.

- This is an Open Access article distributed under the terms of the Creative Commons Attribution-Noncommercial 4.0 Unported License, permitting all non-commercial use, distribution, and reproduction in any medium, provided the original work is properly cited.

- Selection and peer-review under responsibility of the Organizing Committee of the Conference

In parental flocks, important issues such as egg quality monitoring and nutritional problems, some diseases, fertility problems, in-house care feeding conditions and incubation results can be controlled (Staldeman and Owen, 1996; Coleman, 1999). As a result, it is possible to determine the current problems in the flock and to take measures in the early period.

Obtaining quality chicks from parents depends on the production of high quality eggs. The production of high quality hatching eggs is a condition related to correct application of breeding rules as well as the genotypes of parents. Although the conditions of good breeding are provided, the egg weight increases with the increase in the age of the breeder but this increase is not realized in the amount of egg shell. As a result, one of the reasons for the deterioration of egg quality characteristics is the progression of age (Wilson, 1991).

Physical structure changes in breeders due to advancing age is one of the reasons of negative changes in internal and external quality of eggs. It is a fact that the negative changes in egg quality characteristics will negatively affect the incubation results. Therefore, it is inevitable that undesirable results will also arise on the quality of chicks (Söğüt and Sarı, 2009; Nacar and Uluocak, 1995). Most importantly, the hatchability of incubation is affected negatively. In addition to providing suitable incubation conditions to ensure a successful chick output, eggs must have the desired quality characteristics.

For the quality of chicks to be used in broiler breeding, hatching criteria (temperature, humidity, conversion etc.) are not enough to be applied alone; however genotype, age, live weight, egg external quality characteristics (egg weight, shell quality, thickness, color, shape index etc.) and internal quality characteristics (Haugh unit, white and yellow index) are also known to be based on factors such as (Elibol et al., 2000; Nacar and Uluocak, 1995; Simsek et al., 2009; Wilson, 1991).

Decrease in the performance values of the female parents and decrease in the internal and external quality of the eggs can occur. As the hens age, the decrease in egg yield and increase in live weight is an expected result.

Although the results of the studies on feed consumption and feed conversion ratio vary, it is known that the. There is a direct relationship between hen age and egg weight. Egg weight increases with age. The accepted opinion is that hatching is better in medium-weight eggs (Wilson, 1991; Narushin and Ramanov, 2002; Seker et al., 2004). There is a linear relationship between egg weight and incubation.

It has been reported that the hatchability of fertil egg obtained from eggs between 46-50 g and 66-74 g is 8-10.5% lower than those between 50-66 g. The 10 g increase in egg weight reduces the hatching yield by 10.7%, while the decrease in egg weight by 10 g causes a decrease of 3.9%. A similar relationship was reported in Japanese quail eggs (Narushin and Ramanov, 2002).

The proportion of abnormally shaped eggs increases in aging chickens. For a successful incubation, the shape index should be between 72-76% in the eggs. The hatching of normal shaped eggs was reported as 87.2%, 48.9% in defective eggs, 68.1% in eggs with defect in air space and 70.25% in cleaned eggs (Kamanlı et al., 2010; Elibol, 2009; Narushin and Ramanov, 2002).

Witt and Schwalbach (2004) investigated the effect of hatching egg weight on hatching results of hens in different genotypes. The results showed that the hatchability and the daily chick weight increased with the increase of the weight of the hatching eggs of the New Hampshire and Rhode Island Red breed.

In their study, Zglobica and Wezyk (1995) reported that eggs with normal shape in Isa Brown genotypes have higher output power than eggs without normal shape. However, they reported very low hatching from very round eggs.

Sarıca et al. (2010) compared the egg characteristics of native genotypes developed by the use of foreign lines (white laying lines and brown laying lines). As a result of the evaluations of the foreign white genotype eggs up to the age of 76 weeks, it was reported that the eggs were better in terms of internal and external quality characteristics compared to domestic hybrids.

In this study, The effects of different age groups on performance of broiler breeders, eggs internal-external quality and some incubation characteristics were investigated.

Method

This research was carried out in broiler houses belonging to a poultry company in Hatay province. Trial animals were obtained from breeding flock of Ross 308 chicks of daily age. The study was carried out at the age of 23 weeks with a total of 6900 hens; however, 690 cocks were used.

Male and female animals were reared in different houses and were placed according to 1/10 cock-hens ratio at the age of maturity. The pellet feed used in the research was obtained from the factory which is in its own integration.

Table 1. shows the nutrient content and time of use of feeds.

Table 1. Energy and crude protein values of commercial feeds used in the experiment

| Feed material | Age (week) | Energy (Kcal/Kg-ME) | Crude Protein (%) |
|--------------------------|--------------|---------------------|-------------------|
| Chick starter feed | 0-3 | 2750 | 20 |
| Chick growing feed | 4-6 | 2750 | 18 |
| Chicken development feed | 7-23 | 2650 | 14 |
| Layer feed | 24 | 2720 | 15 |
| Rooster feed | 24 and after | 2600 | 12 |

The study was carried out in open poultry houses with 15m × 32m × 3m (width, height, height), floor area 480 m², curtain, natural ventilation and deep litter. Since the placement of the trial set is located in the east-west direction, more suitable ventilation is provided.

In the research, channeled chain feeders were used. Feeding was carried out in the first 2 weeks on the ground, from the third week on the chain feeders and from the 5th week on the fully automatic channel chain feeders. Ducted chain feeders were placed and used as two rows of 64 m per house.

In this study, the water type bowls with 0.6 cm/hen water area were used. In the first week the chicks were given water in the floor type water bowls, and from the second week on, bell-type waterers were used. The water level in the drinking water was kept 0.5 cm high. It was then gradually increased to approximately 1.25 cm at the end of the first week. In order to reduce the contamination, the line height in the drinkers was increased regularly according to the growth rate of the chickens.

In the study, metal nests were preferred for easy cleaning and avoiding the damage of the parasites. 10 cm thick sawdust with moisture absorption feature is used as abutment material. The nests were placed side by side and two floors. The top of the pads is inclined. This prevents the roosting and circulation of chickens. The nesting-box has a width of 30 cm, a depth of 35 cm and a height of 35 cm. A nest box was used for each 4 chickens. The eggs were collected 6 times manually from the nests.

In the research, it was used in artificial lighting in addition to daylight. 60 watt yellow light emitting bulbs were used in lighting. The bulb range is set to reduce 4 watts of light per square meter. In total, 24 ampoules were used in three rows of 3 m transverse and longitudinal. Natural lighting was applied during the growing period. In addition to daylight until the 23rd week, 2 hours, 14 hours of total illumination was applied. When egg yield reached 10%, 15 hours lighting was performed. In the peak egg yield, the lighting was increased by 1 hour and the lighting was applied as 16 hours.

Since broiler breeder hens are kept in the same coop for a long time, the selection of litter is very important. In order to provide thermal insulation, a mixture of 10-15 cm thick, 60% wood shavings and 40% paddy was laid on the poultry house.

Egg measurements were performed with a digital caliper with a sensitivity of ± 0.01 mm.

The incubators belonging to the farm were used. The incubator has a capacity of 56,700 eggs, with a height of 3.5 m and a height of 4.3 m, with a height of 2.35 m. The hatching section has a capacity of 19,200 eggs with a width of 2.1 m and a height of 3.5 m with a height of 2.35 m.

The experiment was conducted on a total of 6900 broiler breeder hens. In addition, male female ratio was calculated as 1/10 and 690 cocks were used in total. The trial was based on 3 age factors (23-34, 35-49, 50-61

weeks). Each factor was created 4 replicates. In each repetition, 575 chickens with similar live weight were randomly placed.

The experimental design is shown in Table 2.

Table 2. Experimental plan

| Treatment groups | Groups (week) | N | Replicate |
|------------------|---------------|-----|-----------|
| 1 | 23-34 | 575 | 4 |
| 2 | 35-49 | 575 | 4 |
| 3 | 50-61 | 575 | 4 |

The study started when animals were 23 weeks old and continued for a total of 39 weeks until 61 weeks of age. During the trial, 390 eggs of each age group and 1170 eggs in total were collected and their internal and external quality characteristics were determined. However, the same amount of eggs were collected and incubated to determine the incubation characteristics.

Performance characteristics (live weight, egg yield, feed consumption, feed efficiency ratio) of the breeder hens were determined, and the external quality characteristics of the eggs obtained from each laying period (egg weight, shell weight, shell thickness, shell fracture resistance, shape index) in laboratory environment It has been identified.

At the same time, internal quality characteristics (index index, yellow index, Haugh unit) were determined. Eggs were collected by hand 6 times a day. Collected eggs are divided into hatching and non-hatching eggs. Non-hatching eggs are classified as abnormal, dirty, broken and double yolked eggs. Abnormal egg expression refers to the eggs which are deformed, and the dirty eggs are eggs that are contaminated with faeces.

The total number of eggs obtained from the experimental groups daily is divided into the number of chickens. The result is multiplied by 100 and the egg yield is determined as a percentage. Abnormal eggs, dirty eggs, broken eggs and double yolked eggs divided by the total number of eggs and multiplied by 100, the rates of non-hatching eggs were determined separately. The results obtained daily were recorded during the study.

Daily feeding was performed during the trial. The chickens used in the experiment were fed the same time each day. Feed consumption was determined on a daily basis and evaluated weekly. The feed conversion rate was calculated according to the following formula.

Feed conversion ratio: $\text{Feed consumption (g)} / \text{Egg weight (g)} \times \text{Egg yield (\%)}$

The chickens were randomly selected from each treatment group by starting from the 23rd week and weighed 16 times once every 14 days. The weighing was carried out with a precision 6 hours after feeding.

In the trial, egg weights were determined by weighing 30 eggs every week from 23rd weeks to 61st weeks according to age groups. ± 0.01 grams sensitive electronic scales were used in the weighing of eggs.

In order to determine the weight of the shell, the shells of the weighed eggs were stored in a drying cabinet at 70 °C for 24 hours after breaking. It is then weighed on a precision scale of ± 0.01 g.

The thickness of the shell was measured with a 0.01 mm sensitive digital caliper. The shell thickness was measured by taking 3 samples from both ends and equatorial regions of the egg. Then the shell thickness was determined by taking the average.

5% egg samples were taken from the treatment groups each month, and after standing at room temperature for 24 hours, the fracture resistance was measured by measuring instrument (kg/cm^2). For the measurement of this parameter, Çukurova University Laboratory of Animal Science was used.

The width and length of the eggs were measured by digital calipers and the shape index was calculated with the help of the following formula.

Shape Index = $\text{Egg Width (mm)} / \text{Egg Length (mm)} \times 100$

The eggs were broken and their white height, white length and white width were measured by digital compass. white index calculated by the following formula.

$$\text{White Index} = \text{Albumin height (mm)} / [\text{White length (mm)} + \text{white width (mm)}] / 2 \times 100$$

Yolk height, yolk width and length are measured with digital caliper in broken eggs. The yolk index was also calculated by the following formula:

$$\text{Yolk Index} = \text{Yolk height (mm)} / \text{Yolk diameter (mm)} \times 100 \text{ (Efil and Sarica, 1997).}$$

The Haugh unit was calculated using the following formula (Stadelman, 1986).

$$\text{HB} = 100 \log (h + 7.57 - 1.7 G^{0.37})$$

HB = Haugh unit

h = white height (mm)

G = Egg weight

Incubation characteristics were calculated by the following formulas.

$$\text{Hatchability} = (\text{Number of chick} / \text{Number of eggs placed in machine}) \times 100$$

$$\text{Hatching rate} = (\text{Number of hatches} / \text{Number of fertil eggs placed on machine}) \times 100$$

$$\text{Fertility rate} = (\text{Number of eggs with fertilization} / \text{Number of eggs placed on machine}) \times 100$$

$$\text{Embryo Deaths} = (\text{Number of embryonic deaths} / \text{Number of eggs placed in machine}) \times 100$$

The experiment was designed according to the trial plan of coincidence plots. The data were analyzed by using SPSS-21 package program according to variance analysis method (Kinnear and Gray, 1994). Duncan multiple comparison test was used to compare the averages of experiment groups (Bek and Efe, 1999). The mathematical model of the experiment is as follows.

$$Y_{ij} = \mu + a_i + e_{ij}$$

Y_{ij} = i. ovulation period, j. observation value (internal-external quality characteristics and incubation characteristics)

μ = Population average,

a_i = The effect of ovulation period (1st, 2nd, 3rd period),

e_{ij} = chance-dependent error

Results and Discussion

In this study, age of sexual maturity, egg production, feed consumption, feed conversion rate and live weight characteristics were investigated.

One of the important factors affecting performance and egg quality criteria in chickens is the age factor. Groups started to spawn at 23rd week and continued until 61st week. The peak yield was reached at the age of 30 weeks and it's yield was 89%. Egg yield continued over 80% for 15 weeks, but as the age progressed, egg yield decreased. As the parent stocks get older, the egg quality decreases as well as the egg quality (Roberts and Nolan, 1997). The egg yields obtained from these groups during ovulation period are given in Table 3. Significant differences were found between the ages of the groups and the egg yields ($P < 0.05$).

During the ovulation period, it was started with a daily feed rate of 110 g/hen, the feed rate was increased as the egg production increased and the feed was given as 158 g/hen in the peak yield. In the same way, the amount of feed was reduced as the egg yield decreased at later ages and feed was given as 145 g/chicken at the age of 61 weeks. The average daily feed consumption was calculated as 1825.42 kg/house in the first period (23-34 weeks), 1926.78 kg/house in the medium term (35-49 weeks) and the average 2060.92 kg/house in the last period (50-61).

The average daily feed intake and feed conversion rates of the groups from the beginning of ovulation to the age of 61 weeks are given in Table 3.

Table 3. Average egg production, egg weight, feed consumption and feed conversion ratio according to age groups

| Groups (week) | N | Egg yield (%) | Egg weight (g) | Feed consumption (g/hen) | Feed conversion rates |
|---------------|------|-------------------------|-------------------------|--------------------------|-------------------------|
| 23-34 | 2300 | 65.87±0.06 ^a | 52.13±0.40 ^a | 148.98±1.02 ^a | 4.34±0.044 ^a |
| 35-49 | 2300 | 80.35±0.04 ^b | 62.18±0.62 ^b | 157.29±1.13 ^b | 3.15±0.017 ^b |
| 50-61 | 2300 | 71.01±0.01 ^a | 69.59±0.36 ^c | 168.24±1.25 ^c | 3.41±0.028 ^c |

*: There is statistical variability between figures shown in different letters in the same column (P<0.05)

When the weekly feed consumption values of the table were analyzed, it was seen that there was a significant difference between the average feed consumption and feed conversion rates between the age groups (P <0.05). As the age of the chickens progressed, an increase was observed in live weight, while the consumption of feed increased due to the need for living. On the other hand, the feed conversion rate has deteriorated.

The weighing of the hens was carried out every 14 days by taking 3% of each treatment group. Accordingly, a total of 69 animals were used in each weighing from each treatment group. According to this, live weight values were calculated as 3394.24 g in the 1st age group (23-34 weeks), 3734.50 g in the 2nd age group (35-49 weeks) and 3981.93 g in the 3rd age group (50-61 weeks). There was a significant difference between the age groups in terms of live weight values (P <0.05).

A linear relationship between live weight and age. There was also an increase in live weight as the age increased. The chickens used in the study started to ovulation with an average of 2883 g. At the age of 61 weeks in which ovulation ended, the chickens weighed 4274 g.

In our study, egg weight, shape index and shell properties were examined as external characteristics of eggs. Characteristics such as white index, yolk index and Haugh unit were also investigated under the title of egg internal quality.

The mean data on egg weight are shown in Table 3. according to age groups. The lowest value of egg weight was determined as 52.13 g in the first age group (23-34 weeks) and the highest value was 69.59 g in the 3rd age group (50-61 weeks). As seen, a statistically significant difference was found between age groups in terms of egg weight (P <0.05). This result Van Den Brand et al., 2004; Petek et al., 2009's has been consistent with the study.

The findings related to the shape index are shown in Table 4. When we examine the table, we see that the difference between the groups is statistically significant (P <0.05). The highest value in terms of shape index was found to be 75.71 in the 3rd age group.

Zita et al. (2009), 3 different age period taking into account their studies on egg quality, egg weight and shape index were reported to be statistically significant (P <0.05). However, Sekeroglu et al. (2014), in the study of the effects of different age stages on the quality of eggs in egg chickens, the effect of age on the shape index was found to be insignificant. According to these statements, we can say that there is not exactly a linear relationship between age and shape index.

Table 4.. Egg shape index depending on age

| Groups (week) | N | Shape index |
|---------------|-----|-------------------------|
| 23-34 | 390 | 75.55±0.45 ^a |
| 35-49 | 390 | 72.08±2.16 ^b |
| 50-61 | 390 | 75.71±0.29 ^a |

*: There is statistical variability between figures shown in different letters in the same column (P<0.05)

The egg shell thickness, shell weight and shell fracture resistance averages of age groups are shown in Table 5. While the mean values between shell thickness and shell weight were found to be statistically significant (P <0.05), the difference between the mean values of the shell fracture resistance was insignificant (P>0.05).

Table 5. Age-dependent egg shell thickness, egg shell weight and shell breaking resistance

| Groups (week) | N | Egg shell thickness (mm) | Egg shell weight (g) | Break resistance (kg/cm ²) |
|---------------|-----|-----------------------------|-------------------------|---|
| 23-34 | 390 | 0.39±0.005 ^a | 4.96±0.75 ^a | 2.68±0.121 ^a |
| 35-49 | 390 | 0.28±0.005 ^b | 5.89±0.74 ^b | 2.75±0.131 ^a |
| 50-61 | 390 | 0.35±0.005 ^c | 6.08±0.50 ^c | 2.64±0.122 ^a |

*: There is statistical variability between figures shown in different letters in the same column (P<0.05)

In our study, a linear relationship between age and shell weight was found. As the age increased, the shell weight increased. In general, this is an expected situation and the increase in egg size also increases in the shell. In other words, there is a positive correlation between egg weight and shell weight (Poyraz, 1989).

The thickness of the shell decreases depending on the age. Although the increase in egg weight is seen to be directly proportional to the increase in the amount of the shell, this is due to the fact that the increase in the amount of shell is not sufficient to maintain the egg shell thickness. Therefore, due to the increase in egg weight in old hens, the crust becomes thinner and weaker (Yannakopoulos and Tserveni-Gousi, 1986; Narayanankutty et al., 1989; Nagarajan et al., 1991). The herd age affects the white, yolk and shell ratios as well as the egg weight. While the rate of yolk increases in the eggs of old herds, the white ratio and shell rate decrease (Flethcher et al., 1983).

The egg shell quality deteriorates as the hen ages. It was observed that the ability to synthesize crust decreased with increasing age and the shells were thinner and weaker towards the end of the ovulation period (Flethcher et al. 1983; Akbaş et al. 1996).

Nagarajan et al. (1991) and Basmacıoğlu (1999) reported that egg shell thickness decreased with age. Izat et al. (1985) stated that the thickness of the crust decreased with increasing age, but this decrease was not statistically significant.

In this study, as the age of the flocks progressed, the shell thickness was reduced, the shell fracture resistance decreased and significant negative correlations were found among these examined properties. The same relationship was also found between the egg weight-shell thickness-fracture resistance.

In addition, some research results showed a positive correlation between egg weight and shell thickness and weight (Poyraz 1989; Narayana et al. 1991; Işcan and Akcan 1995; Özçelik 2002).

According to the research, yolk index, white index and Haugh unit are given in Table 6.

Table 6. Yellow index, white index and haugh unit averages depending on age groups

| Groups (week) | N | Yolk index | White index | Haugh unit |
|---------------|-----|-------------------------|-------------------------|-------------------------|
| 23-34 | 390 | 52.72±0.34 ^a | 13.32±0.30 ^a | 91.37±0.73 ^a |
| 35-49 | 390 | 47.44±0.43 ^b | 9.23±0.29 ^b | 80.89±0.97 ^b |
| 50-61 | 390 | 51.12±0.29 ^c | 9.94±0.22 ^b | 82.60±0.74 ^b |

*: There is statistical variability between figures shown in different letters in the same column (P<0.05)

The difference between yolk index values was found to be statistically significant among age groups (P<0.05). Besides, the difference between age groups in terms of white index values was found to be statistically significant (P<0.05).

On the other hand, the white index values in the 2nd and 3rd groups were 9.23 and 9.94, respectively. Haugh unit averages decreased with age and it was found to be 91.37, 80.89 and 82.60 in the 1st, 2nd and 3rd age groups, respectively.

Petek et al. (2009) found that the effect of the hosting system and animal age on the Haugh unit was significant (P<0.01). However, their effect on white index and yolk index was statistically insignificant (P>0.01). Studies using foreign and domestic genotypes were similar in age-related changes. On the other hand, differences in white index, yolk index, Haugh unit and yolk color were found to be significant (P<0.01) (Sarica et al., 2010).

The fertility, hatchability of fertil egg, embryo death, infertile egg rate and hatchability in different age groups are shown in Table 7. The effect of age on the fertility, embryo deaths, fertilization rate and hatchability were found to be statistically significant among the groups (P <0.05).

Table 7. According to age groups, fertility, hatchability of fertil egg, embryo mortality, infertile egg ratio and hatchability averages

| Groups (week) | N | Fertility (%) | Hatchability of fertil egg (%) | Embryo mortality (%) | Infertile egg (%) | Hatchability (%) |
|---------------|-----|-------------------------|--------------------------------|-------------------------|-------------------------|-------------------------|
| 23-34 | 390 | 86.88±1.53 ^a | 88.16±0.015 ^a | 11.84±1.05 ^a | 13.12±1.53 ^a | 75.04±2.46 ^a |
| 35-49 | 390 | 92.08±0.25 ^a | 95.03±0.004 ^b | 4.97±0.34 ^b | 7.92±0.38 ^b | 87.11±0.25 ^b |
| 50-61 | 390 | 82.87±2.40 ^b | 90.27±0.014 ^a | 9.73±1.15 ^a | 17.13±1.83 ^a | 73.14±2.40 ^a |

*: There is statistical variability between figures shown in different letters in the same column (P<0.05)

According to Table 7, it is seen that the statistical difference between groups is important in terms of fertility rate (P <0.05). The highest fertility rate was in the second age group. This can be explained by the peak yield period. There was also a statistical difference between the groups in the hatchability of fertil eggs (P <0.05). However, the highest value was found to be in the 2nd age group as 95.03. The highest values for embryo deaths and fertilization rates were 11.84% and 17.13% in 1st and 3rd age groups, respectively. The results of hatchery yield were found to be the highest in the second age group.

The age of the breeder flock is an important parameter to be considered in the management of incubation. There is a close relationship between the age of the breeder flock and the hatching and embryonic deaths (Elibol et al., 2000). Zglobica and Wezyk (1995) stated that with the increase in chicken age, there is a difference in hatching in fertil eggs. However, they found that the hatching decreased with the increase of age. At the same time there is a high positive relationship between age and egg weight (North and Bell 1990). As the egg weight increases, the hatching decreases (Altan et al. 1995; Narushin and Romanov 2002).

Table 8. shows the ratio of double yolked eggs, thin shelled eggs (cracked, broken), dirty eggs and abnormal eggs that can not be incubated in the eggs collected during the ovulation period. In the treatment groups, the differences between the double yolked eggs, the thin shelled eggs and the abnormal eggs were found to be statistically significant (P <0.05), the difference between the number of dirty eggs was insignificant (P >0.05).

Table 8. The rates of double yolked egg, broken eggs, abnormal eggs and dirty eggs between age groups

| Groups (week) | N | Double yolked egg ratio (%) | Broken egg ratio (%) | Abnormal egg ratio (%) | Dirty egg ratio (%) |
|---------------|-----|-----------------------------|------------------------|------------------------|------------------------|
| 23-34 | 390 | 3.14±0.81 ^a | 0.76±0.02 ^a | 1.29±0.18 ^a | 1.11±0.39 ^a |
| 35-49 | 390 | 0.44±0.07 ^b | 0.67±0.04 ^a | 1.09±0.16 ^a | 0.81±0.11 ^a |
| 50-61 | 390 | 0.09±0.04 ^b | 0.92±0.08 ^b | 1.91±0.25 ^b | 1.02±0.20 ^a |

*: There is statistical variability between figures shown in different letters in the same column (P<0.05)

It was observed that the rate of double yolked egg decreased as the age progressed and it was determined as 3.14%, 0.44% and 0.09% in the 1st, 2nd and 3rd treatment groups, respectively.

Broken egg rates increased with advancing age and were found to be 0.76%, 0.67% and 0.92% in the 1st, 2nd and 3rd age groups, respectively. We can explain this situation as a result of thinning of the egg shell with the progression of the animal age and hence the deterioration of the egg shell quality.

The number of abnormal eggs increased with age. It is possible to explain the reason for this by age-related negative changes in animal physiology. For example, the genetic or environmental effects on the egg shell during egg formation may have a negative effect on the structure of the egg shell.

Although no statistically significant difference was found between the treatment groups at the rate of dirty eggs, a numerical decrease was recorded. This is due to the fact that, with the age, the number of laying on the ground is increased, but because of the hardness of the litter structure, the eggs are less polluted.

Conclusion

The differences between age and performance characteristics were statistically significant (P <0.05). Egg yield was found to be highest as 80.35% in the second age group (35-49 weeks) and egg yield decreased with the progression of age. It was observed that egg peak yield reached 30 weeks. Egg production continued for more than 80% over 15 weeks (27-42 weeks). In this study, egg yield was obtained over Ross-308 yield averages. It was determined that egg yield would increase in better maintenance and feeding conditions.

Feed consumption increased as the age of the animal progressed. The highest feed consumption values were found in the 3rd age group (50-61 weeks). In this age group, it was found that a daily average of 168.24 g of feed was given per animal.

The feed conversion rate was found to be the highest in the 2nd age group (35-49 weeks) with a feed rate of 3.15. As age progressed, an increase in live weight was observed due to increased feed consumption.

A double yolked egg is an undesirable condition in enterprises that produce breeding eggs. The number of double yolked eggs decreased with the progression of age, and in the last weeks of the experiment, no double yolked egg was encountered.

With the increase in age, the number of broken eggs increased due to the deterioration of the shell quality. The highest rate of broken eggs was found in the 3th age group (50-61 weeks) with a rate of 0.92%.

Similarly, the number of abnormal eggs increased with the progression of age and the highest rate of abnormal egg (1.91%) occurred in the 3rd age group (50-61 weeks).

The difference between age and dirty egg ratio was not statistically significant ($P>0.05$). The change in the number of dirty eggs has been found to be related to the humidity of the material used in the nest base, not with age.

The changes in egg weight, shape index, shell thickness and shell weight parameters were found to be statistically significant with the progression of chicken age ($P<0.05$). The change in shell fracture resistance parameter was insignificant ($P>0.05$).

As the ages of breeder hens changed, the egg weight increased. Egg weights were found to be 52.13 g, 62.18 g and 69.59 g in the 1st, 2nd and 3rd age groups, respectively. If the shape index of the eggs is smaller than 72, it is called long and it is determined to be round if it is greater than 76. In our experiment, shape index changed with age and it was found to be between 72-76 in 3 age factor.

The thickness of the shell was the lowest in the 2nd age group (35-49 weeks). This can be explained by the fact that the 2nd age group (35-49 weeks) has reached the peak period of egg production. The fracture resistance was 2.68 kg/cm², 2.75 kg/cm² and 2.64 kg/cm² in the 1st, 2nd and 3rd age periods, respectively.

Recommendations

It is expected that performance values will decrease with increasing age. However, performance decreases can be slowed down by increasing the age by selecting the most suitable genotype for the environment and applying better maintenance and feeding conditions. Thus, the number of eggs obtained per animal can be increased.

With the increase in flock age, egg weight increased and egg shell quality deteriorated. In order to slow the increase in egg weight with increasing age, the feed content and feed programs of breeder chickens are very important.

With the balanced and regular feeding of breeding animals, the rate of increase in egg weight can be slowed down and more hatching eggs can be obtained by this slowdown. Since breeding flocks stay in the same house for a long time, the selection of litter should be done well in order to reduce the animal welfare as well as the pollution in the eggs.

The moisture content of the litter material used in the nesting-box can be adjusted well to reduce the number of dirty eggs, thus increasing the number of hatching eggs. In addition to flock care and management, more chicks can be obtained with the measures taken depending on the quality of the eggs and the enterprises can increase the income.

As a result, superior eggs with internal and external quality characteristics should be obtained to increase hatchability. Also the age of the breeder flock must be taken into account.

Acknowledgements or Notes

This study was carried out from the MSc thesis titled EFFECTS OF AGE DETERMINATION OF BROILER BREEDERS ON GENERAL PERFORMANCE, INTERIOR-EXTERIOR QUALITY and SOME INCUBATION FEATURES by Sciences institute of Hatay Mustafa Kemal University.

We would like to thank “Beyza Piliç A.Ş.” for providing and assistance the opportunity to this research.

References

- Abdallah, A. G., Harms, R. H. ve Elhusseiny, O.. 1993. Performance of Hens Laying Eggs with Heavy or Light Shell Weight When Fed Diets with Different Calcium and Phosphorus Levels. *Poultry Science*. 72 (10). 1881-1891.
- Akbaş, Y., Ö. Altan ve Ç. Koçak. 1995. Tavuk Yaşının Tavuk Yumurtasının İç Ve Dış Kalite Özellikleri Üzerine Etkileri. *Türk Veterinerlik Ve Hayvancılık Dergisi*, 20: 455-460.
- Altan, Ö. and İ. OĞUZ. 1995. Japon Bildircinlarında (Coturnix Coturnix Japonica) Yaşın Ve Yumurtlama Zamanının Kimi Yumurta Özellikleri Üzerine Etkileri. Tr. *Journal Of Veterinary And Animal Science*, 19: 405- 408.
- Anonymous, 2019. <http://eu.aviagen.com/tech-center/download/1054/308SF-PS-EU-PO-EN-16.pdf> date: 26.05.201908:06
- Atasoy, F., Onbaşlar, E. ve Apaydın, S.. 2001. Denizli ve ticari tavuk sürülerinde yumurta kalite özelliklerinin karşılaştırılması. *Lalahan Hay. Araş. Ens. D.* 41 (2): 89. 100.
- Basmacıoğlu, H. 1999. Yumurta Tavuklarında Yumurtanın Kolesterol İçeriği İle Diğer Bazı Özelliklerine Etki Eden Etkenler Üzerinde Bir Araştırma. Doktora Tezi, *Ege Üniversitesi Fen Bilimleri Enst., Bornova, İzmir*, s.1-94.
- Bek, Y. ve Efe, E. 1999. Araştırma Deneme Metodları 1. *Çukurova Üniversitesi, Ziraat Fakültesi, Ofset ve Teksir Atölyesi, Adana*, 395s.
- Coleman, M. 1999. Quality Control İn The Hatchery, The Fresh Egg Break Out Part 1. *Mac Associates. Incubator Co. Usa*.
- Efil, H. ve Sarıca, M.. 1997. Yumurtada kalite tanımında güçlükler ve son gelişmeler. *OMİ Ziraat Fakültesi Dergisi*. 12 (3): 141. 150.
- Elibol, O. 2009. Embriyo gelişimi ve kuluçka. *Tavukçuluk Bilimi, Yetiştirme, Besleme, Hastalıklar. (Ed. M.Türkoğlu, M. Sarıca) Bey Ofset Matbaacılık*, 3. Basım, s., 588.
- Elibol, O., Türkoglu, M. ve Erol, H. 2000. “Bir Broiler Damızlık Sürüsünde Farklı Yaşlarda Üretilen Yumurtalarda Yumurta Ağırlığı ve Kuluçka Yerlesim Düzeninin Kuluçka Sonuçlarına Etkisi”. *Tavukçuluk Araştırma Dergisi* 2(1):17-24.
- Fletcher, D.L., Britton, W.M., Pesti, G.M., Rahn, A.P., Savage, S.I., 1983. The relationship of layer flock of age and egg weight on egg component yields and solid content. *Poultry Sci.* 62:1800.
- Izat, A.L., Gardner, F.A., Mellar, D.B., 1985. Effects of age bird on season of the year on egg quality. 1.Shell quality. *Poultry Sci.* 64:1900.
- İşcan, K.M. ve A. Akcan. 1995. Broiler parent yumurtalarında yumurta ağırlığı, yumurta özgül ağırlığı ve bazı yumurta kısımları arasındaki ilişkiler. *Hayvancılık Araştırma Dergisi*, 5: 49-52.
- Kamanlı, S., Durmuş, İ., Demir, S. 2010. Hatching characteristics of abnormal eggs. *Asian Journal of Animal and Veterinary Advances*, 5(4): 271-274.
- Kinnear, P.R., ve Gray, C.D.,1994. SPSS for Windows. Department of Psychology Univ. of Aberdeen, UK.
- Nacar, H., Uluocak, AN., 1995. Etlik Bildircin Üretiminde Anaç Yaşının Etkileri. *Uluslar Arası Tavukçuluk Fuarı ve Konferansı* 24-27 Mayıs 1995 İstanbul. 81-89
- Nagarajan, S., D. Narahari, I.A. Jayaprasad and D. Thyagarajan, 1991. Influence of Stocking Density And Layer Age On Production Traits And Egg Quality İn Japanese Quail. *Brit. Poult. Sci.*, 32:243-248.
- Narayana, R., S.K. Varma and U.D. Gupta. 1991. Inheritance Of Plasma Protein, Cholesterol And Glucose And Their Association With Egg- Quality Traits İn İnbred Lines Of White Leghorn. *Indian Journal Of Animal Sciences*, 61(4): 445-448.
- Narayanankutty, K., A. Jalaludeen and A. Ramakrishnan. 1989. Effect Of Age On Quality Characteristics Of Japanese Quail (*Coturnix Coturnix japonica*) Eggs. *Cherion*, 18(2): 97-98.
- North, M.O. and Bell, D.D. 1990. Commercial Chicken Production. Manuel 4th Edition. Ogunshile, G. and N. Sparks. 1995. Effect Of Broiler Egg Weight On Hatchability. *Wpsc Assoc. Proceedings Of Spring Meeting Scarborough*, 22-23 March.
- Narushin, V.G., and Romanov, M.N. 2002. Egg physical characteristics and hatchability. *World's Poultry Science Journal*, 58(3):297-303.

- Özçelik, M. 2002. Japon Bildircını Yumurtalarında Bazı Dış Ve İç Kalite Özellikleri Arasındaki Fenotipik Korelasyonlar. *Ankara Üniv. Veteriner Fakültesi Dergisi*, 49: 67-72.
- Petek. M., Alpay. F., Gezen. S. S. ve Çıbık. R.. 2009. Ticari Yumurtacı Tavuklarda Barındırma Sistemi ve Yaşın Erken Dönem Yumurta Verimi ve Kalitesi Üzerine Etkileri. *Kafkas Üniversitesi Veteriner Fakültesi Dergisi*.
- Poyraz Ö (1989). Tavuk Yetiştirme ve Üretim Teknikleri. AÜ Vet Fak Yayınları, Ankara.
- Roberts, J. and J. Nolan. 1997. Egg and egg shell quality in five strains of laying hen and the effect of calcium source and hen age. Proc. *The 13th and 7th European Symposium on the quality of poultry meat and on the quality of eggs and egg products*. Poznan, Poland, Sept. 21-26
- Sarıca. M., Yamak. U. S., Boz. M. A.. 2010. Changes in egg quality parameters due to age in laying hens from two commercial and three local layer genotypes. *Journal of Poultry Research*. 9 (1).
- Şeker, İ., Kul, S., Bayraktar, M. 2004. Effects of parental age and hatching egg weight of Japanese quails on hatchability and chick weight. *International Journal of Poultry Science*, 3(4):259-265.
- Söğüt, B., Sarı, M., 2009. Bildircınlarda (*Coturnix coturnix japonica*) Anaç Yaşının ve Yumurtlama Zamanının Yumurta Özellikleri Üzerine Etkisi: 2. Yumurta İç Kalite Özellikleri Üzerine Etkisi. *YYU Veteriner Fakültesi Dergisi*, 2009, 20 (2),49-53:
- Stadelman, W.J., 1986. The preservation of quality in shell eggs. In W.J. Stadelman. O.J. Cotteril (Eds), *Egg science and technology. Avi PUBLISHING Com Inc Westport, Connecticut, U.S.A.*
- Stadelman W.J. and J. Owen. 1996. *Egg Science and Technology. Haworth Press Inc New York.*
- Şimşek, Ü.G., Gürses, M., Yıldız, N., 2009. Farklı Anaç Yaşına ve Ovipozisyon Zamanına Sahip Kuluçkalık Yumurtalarda Lamba Kontrolüyle Ayıklama İşleminin Etlik Piliç Damızlıklarında Kuluçka sonuçları Üzerine Etkisi. *F.Ü.Sağ.Bil.Vet.Derg.* 2009; 23 (3): 147- 151
- Türkoğlu, M., Sarıca, M., 2009. *Tavukçuluk Bilimi. Yetiştirme, Besleme, Hastalıklar*. Sayfa: 268-271.
- Van Den Brand. H., Parmentier. H. ve Kemp. B.. 2004. Effects of housing system (outdoor vs cages) and age of laying hens on egg characteristics. *Br Poult Sci*. 45 (6). 745-752.
- Wilson HR., 1991 Interrelationship of egg size, chick size, posthatching growth and hatchability. *World's Poult Sci J* ; 47: 5-20.
- Witt, F.D.E. and L.M.J. Schwalbach. 2004. The Effect Of Egg Weight On The Hatchability And Growth Performance Of New Hampshire And Rhode Island Red Chicks. *South African J. Animal Science*, 34(2): 62-64.
- Yannakopoulos AL, Tserveni-Gousi AS (1986). Quality Characteristics of Quail Eggs. *British Poultry Sci*, 27(2): 171-176.
- Zglobica, A. and S. Wezyk. 1995. Relationship Between External Egg Quality Traits And Hatchability Of Laying Hens. *Roczniki Naukowe Zootechniki*, 22: 113-123.
- Zita. L., Tümová. E. ve Štolc. L.. 2009. Effects of Genotype. Age and Their Interaction on Egg Quality in Brown-Egg Laying Hens. *Acta Veterinaria Brno*. 78 (1). 85-91.

Author Information

Hakan Yıldırım

Hatay Mustafa Kemal University
Agriculture Faculty Animal Science
HATAY/TURKEY
Contact E-mail: hakanvld@gmail.com

Zekeriye Akcimen

Hatay Mustafa Kemal University
Agriculture Faculty Animal Science
HATAY/TURKEY

The Interaction of a Charged Particle in the Generalized Woods-Saxon Potential

Orhan BAYRAK
 Akdeniz University

Abstract: An analytical solution of any given potential model presenting particle interaction is hot topic in physics. There are few potential models that can be analytically solved in literature. The analytically solvable potential models are the infinite and the finite well, the harmonic oscillator, the Coulomb and the Kratzer potential for any angular momentum quantum number. In this study, we examine the interaction of charged particle in the generalized Woods-Saxon Potential with an approximation to the effective potential by using the Hypergeometric function with physical boundary conditions and continuity requirement of the wave function. We obtain the bound state energy eigenvalues and corresponding wavefunction in closed form and discuss the effect of the potential parameters on the energy eigenvalues and corresponding eigenfunctions.

Keywords: Analytical solutions, Generalized Woods-Saxon potential, Charged particles

Introduction

Analytical solution of the generalized Woods-Saxon potential for the Schrödinger equation has a very important place in determining interaction of the particle in case of the bound, quasi-bound and scattering states (Zaichenko & Ol'Khovskii 1976; You et. al., 2002; Guo & Sheng, 2005; Panella et. al., 2010; Alpdoğan et. al., 2013; Bayrak&Aciksoz, 2015; Lütfüoğlu et. al., 2016; Lütfüoğlu 2018; Lütfüoğlu et. al. 2018). The generalized Woods-Saxon potential is given by (Satchler 1983),

$$V_N(r) = -\frac{V_0}{1 + \exp\left(\frac{r-R}{a}\right)} + a \frac{d}{dr} \left(\frac{W_0}{1 + \exp\left(\frac{r-R}{a}\right)} \right) \quad (1)$$

where V_0 and W_0 are depths of the potential. R and a are the nuclear radius and surface thickness of the nucleus. The second term in Equation (1) is the surface term of the Woods-Saxon potential and crucial role for surface interaction of the nuclei (Satchler, 1983). In Figure 1, we plot the effective potential constituted the nuclear potential, Coulomb and centrifugal barrier potentials. It is seen that the surface potential in Equation (1) changes shape of the effective potential at the surface region. Depending on the sign of W_0 parameter, the nuclear potential is repulsive or attractive at the surface region.

There no an analytical solution of the generalized Woods-Saxon potential for the case of charged particles. We need to use an approximation for the Coulomb and centrifugal potentials. In literature, there are some approximation scheme. If we use Taylor expansion for the centrifugal potential and suggest an exponential potential as well as equating both of them, we obtained the parameter of the suggested exponential potential. This approximation firstly used by Pekeris for the analysis of the Rotation-Vibration Coupling in Diatomic Molecules (Pekeris, 1934). The second approximation for the Coulomb and Centrifugal potentials is called Greene-Aldrich approximation (Greene&Aldrich, 1976). Greene-Aldrich approximation is given by Equation (3). This approximation is convenient for small δ parameter. We use this approximation for the Coulomb and Centrifugal potentials in our calculations. Another approximation is suggested by Jia et. al. in the obtaining bound state energy eigenvalues and corresponding wave function of the Hulthen potential (Jia et. al., 2008).

- This is an Open Access article distributed under the terms of the Creative Commons Attribution-Noncommercial 4.0 Unported License, permitting all non-commercial use, distribution, and reproduction in any medium, provided the original work is properly cited.

- Selection and peer-review under responsibility of the Organizing Committee of the Conference

In next section, we present method and calculation procedure. The brief discussion for obtained numerical results are given in Results and Discussion section. Then, we give a conclusion.

Method

In order to describe behavior of a proton orbiting around ^{56}Fe nucleus, we have to determine the effective potential between interacting nuclei. By transforming the Schrödinger equation with $R(r) = \frac{\chi(r)}{r}$ we obtain,

$$\left[\frac{d^2}{dr^2} + \frac{2\mu}{\hbar^2} (E - V_{\text{eff}}(r)) \right] \chi(r) = 0, \quad V_{\text{eff}}(r) = V_N(r) - V_C(r) - \frac{l(l+1)\hbar^2}{2\mu r^2} \quad (2)$$

where $V_N(r)$ and $V_C(r)$ are the nuclear and Coulomb potentials. The last term in Equation (2) is the centrifugal potential. The reduced mass of interacting particle is $\mu = \frac{m_1 m_2}{m_1 + m_2}$. Here, m_1 and m_2 are atomic mass of interacting particles. In the calculation we use point charge interaction between projectile and target nuclei. The Coulomb potential is $V_C(r) = \frac{Z_1 Z_2 e^2}{r}$. Here, Z_1 and Z_2 are proton numbers of the projectile proton and target ^{56}Fe . The effective potential is shown in Figure 1.

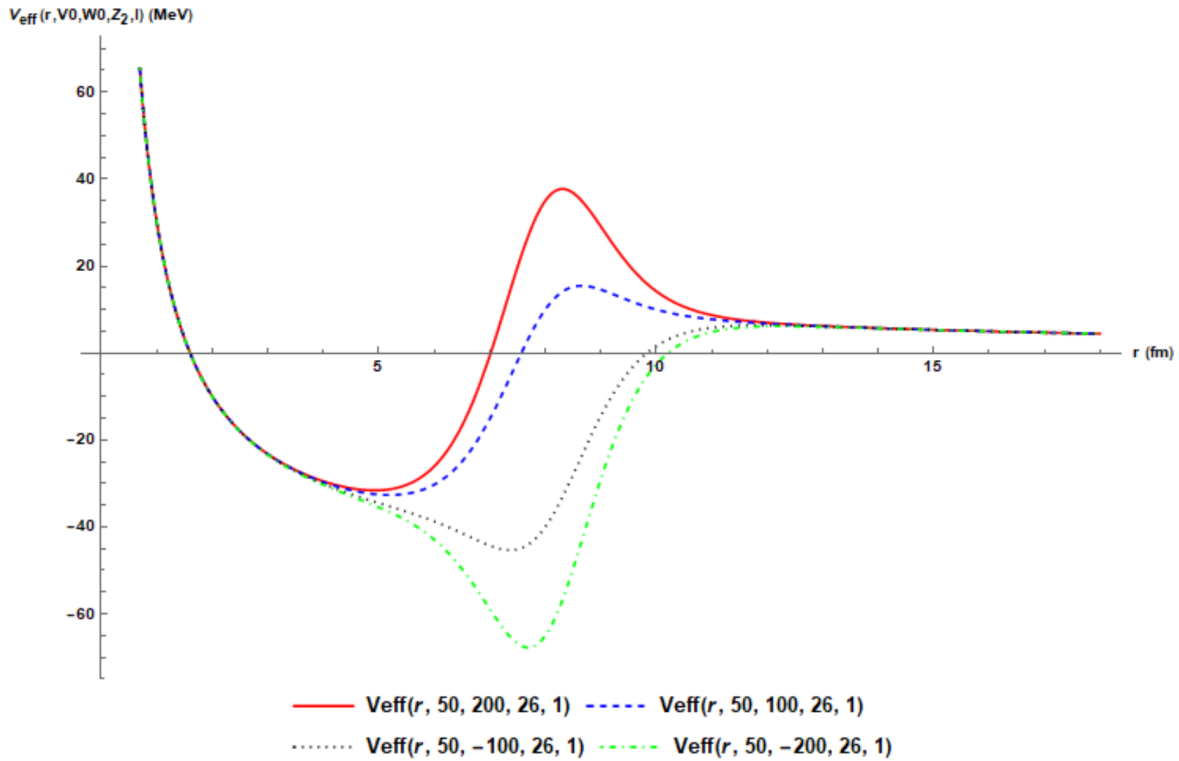


Figure 1. The effective potentials in Equation (1) which are the superposition of the nuclear, Coulomb and centrifugal barrier potentials for several nuclear parameters. The parameters in the effective potential can be given by the function as $V_{\text{eff}}(r, V_0, W_0, Z_2, l)$. We take $Z_1=1$, $R = 8$, $a = 0.65$

There is no analytical solution of the generalize Woods-Saxon potential with Coulomb potential for any angular momentum quantum number. We use an approximation for the Coulomb potential and centrifugal potential in Equation (2). The approximation is (Greene&Aldrich, 1976),

$$\frac{1}{r^2} = \frac{\delta^2 e^{-2\delta r}}{(1 + e^{-\delta r})^2} \quad \text{and} \quad \frac{1}{r} = \frac{\delta e^{-\delta r}}{1 + e^{-\delta r}} \quad (3)$$

where δ is screening parameter. Transforming Equation (2) with $x = \frac{1}{1 + e^{\frac{r-R}{a}}}$ we can easily obtain,

$$\chi''(x) + \frac{1-2x}{x(1-x)} \chi'(x) + \frac{1}{x^2(1-x)^2} \left[-\varepsilon^2 + \alpha^2 x + \beta^2 x(1-x) - \gamma^2 x - \Lambda^2 x^2 \right] \chi(x) = 0 \quad (4)$$

where,

$$-\varepsilon^2 = \frac{2\mu}{\hbar^2} a^2 E_n, \beta^2 = -\frac{2\mu}{\hbar^2} a^2 W_0, \alpha^2 = \frac{2\mu}{\hbar^2} a^2 V_0, \gamma^2 = \frac{2\mu}{\hbar^2} a^2 Z_1 Z_2 e^2 \delta, \Lambda^2 = a^2 \delta^2 L(L+1) \quad (5)$$

Investigating the singular points of Equation (4), we purpose an asymptotic wave function as $\chi(x) = x^\varepsilon (1-x)^\mu f(x)$ with $\mu^2 = \varepsilon^2 - \alpha^2 + \gamma^2 + \Lambda^2$ and insert into Equation (4). We obtain a Hypergeometric differential equation. Comparing between obtained differential equation with the Hypergeometric differential equation we can obtain the wave function as,

$$\chi(x) = x^\varepsilon (1-x)^\mu {}_2F_1 \left(\frac{1}{2} \left(1 + 2\varepsilon + 2\mu \pm \sqrt{1 + 4\beta^2} \right), \frac{1}{2} \left(1 + 2\varepsilon + 2\mu \pm \sqrt{1 + 4\beta^2} \right); 1 + 2\varepsilon; x \right) \quad (6)$$

The wave function should satisfy the boundary conditions, namely, $\chi(r \rightarrow 0, x \rightarrow 1) = 0$. Therefore, the wave function explicitly analysis near the $x \cong 1$ by using following relation (Flügge, 1994),

$${}_2F_1(a, b; c; y) = \frac{\Gamma(c)\Gamma(c-a-b)}{\Gamma(c-a)\Gamma(c-b)} {}_2F_1(a, b; a+b-c+1; 1-y) + \frac{\Gamma(c)\Gamma(a+b+c)}{\Gamma(a)\Gamma(b)} (1-y)^{c-a-b} {}_2F_1(c-a, c-b; c-a-b+1; 1-y) \quad (7)$$

As a result, the energy eigenvalue equation is obtained

$$\frac{\Gamma(a_1 + b_1 - c_1)\Gamma(c_1 - a_1)\Gamma(c_1 - a_1)}{\Gamma(c_1 - a_1 - b_1)\Gamma(a_1)\Gamma(b_1)} \left(1 + e^{\frac{R}{a}} \right)^{-2\mu} = -1 \quad (8)$$

where,

$$a_1 = \frac{1}{2} \left(1 + 2\varepsilon + 2\mu \pm \sqrt{1 + 4\beta^2 + 4\Lambda^2} \right), b_1 = \frac{1}{2} \left(1 + 2\varepsilon + 2\mu \mp \sqrt{1 + 4\beta^2 + 4\Lambda^2} \right) \\ c_1 = 1 + 2\varepsilon$$

This equation is called a “transcendental equation”. The energy eigenvalues in Equation (8) are independent from function of r . Since the energy eigenvalues is not obtained increasing r with step h for the given boundary conditions, obtained energy eigenvalues in Equation (8) are analytical results. But the energy eigenvalues cannot be extracted form Equation (8), we should be used any root finding method such as Bisection, Newton-Raphson etc.

Results and Discussion

We calculate the bound state energy eigenvalues of proton- ^{56}Fe system with Equation (8) which is obtained for the effective potential in Equation (2) by using the approximation in Equation (3) to the Coulomb and Centrifugal potentials. In calculation we take $R = 4 \text{ fm}$, $a = 0.4 \text{ fm}$, $\delta = 0.01 \text{ fm}$, $Z_1 = 1$, $Z_2 = 26$ and change other potential parameters. The variation of the energy eigenvalues with the potential parameters are calculated by using Bisection method which is a method to calculate roots of a function (Table 1).

Table 1. Variation of the bound state energy eigenvalues for several potential parameters. In calculation we take potential parameter as $V_0=60$ MeV, $W_0=30$ MeV, $l=0$ and $n=0$. We keep the other parameter constant by calculating energy eigenvalues E_{nl} as a function of a parameter

| V_0 (MeV) | E_{00} (MeV) | W_0 (MeV) | E_{00} (MeV) | n | E_{n0} (MeV) |
|-------------|----------------|-------------|----------------|---|----------------|
| 0 | - | 0 | -48.35 | 0 | -49.17 |
| 20 | -12.75 | 20 | -48.88 | 1 | -21.67 |
| 40 | -30.44 | 40 | -49.48 | 2 | - |
| 60 | -49.17 | 60 | -50.15 | 3 | - |
| 80 | -68.30 | 80 | -50.91 | 3 | - |

When we increase depth of the potential V_0 by keeping other potential parameters constant, we see that the energy increases. While the depth of the surface term W_0 in the effective potential increases, the depth of the effective potential also increases. In this way, the energy eigenvalues increase for the ground state. We calculate excited state of ^{56}Fe nucleus by the constant potential parameters. We see that increasing quantum number n, the energy eigenvalues decrease and after $n>2$, the proton could be unbound or quasi-bound in last column in Table 1. This station could be calculated by changing the boundary conditions.

Conclusion

We investigate the energy eigenvalues and corresponding wave function of the generalized Woods-Saxon potential with taking into account of the Coulomb potential and centrifugal barrier potentials. There is no analytical solution of the generalized Woods-Saxon potential with Coulomb and/or Centrifugal potential. In order to overcome this issue, we use the approximation to the Coulomb and Centrifugal potentials and obtain the approximate analytical solution for the energy eigenvalues and corresponding wave function. An application we calculate the energy eigenvalues of the proton orbiting around ^{56}Fe nucleus. Then we quantitatively investigate how energy eigenvalues is related to the potential parameters. This potential model could be important in order to investigate nuclear structure of the nuclei.

Acknowledgements

This work was supported by the scientific research projects units of Akdeniz University.

References

- Alpdoğan, S., Aydoğdu, O., Havare, A., (2013). Relativistic spinless particles in the generalized asymmetric Woods-Saxon potential. *J. Phys. A: Math. Theor.*, 46:015301.
- Bayrak, O., Aciksoz, E., (2015). Corrected analytical solution of the generalized Woods-Saxon potential for arbitrary states. *Phys. Scripta*, 95:015302.
- Greene, R. L., Aldrich, C., (1976). Variational wave functions for a screened Coulomb potential. *Phys. Rev. A*, 14:2363.
- Guo, J. Y. and Sheng, Z.Q., (2005). Solution of the Dirac equation for the Woods-Saxon potential with spin and pseudospin symmetry. *Phys. Lett. A*, 338(2): 90-96.
- Jia, C.-S., Liu, J.-Y., Wang, P.-Quan., (2008). A new approximation scheme for the centrifugal term and the Hulthén potential. *Physics Letters A* 372:(27-30) 4779.
- Lütfüoğlu, B. C. (2018). An investigation of the bound-state solutions of the Klein-Gordon equation for the generalized Woods-Saxon potential in symmetry and pseudo-spin symmetry limits. *Eur. Phys. J. Plus*, 133(8): 309.
- Lütfüoğlu, B. C., Akdeniz, F., Bayrak, O., (2016). Scattering, bound and quasi-bound states of the generalized symmetric Woods-Saxon potential. *J. of Math. Phys.*, 57(3): 032103.
- Lütfüoğlu, B. C., Lipovsky, J. and Kriz, J., (2018). Scattering of Klein-Gordon particles in the background of mixed scalar-vector generalized symmetric Woods-Saxon potential. *Eur. Phys. J. plus*, 133(1): 17.
- Panella, O., Biondini, S. and Arda, A. 2010. New exact solution of the one-dimensional Dirac equation for the Woods-Saxon potential within the effective mass case. *J. Phys. A: Math. Theor.*,43(32): 325302.
- Pekeris, C. L., (1934). The Rotation-Vibration Coupling in Diatomic Molecules. *Phys. Rev.* 45:98

Satchler, G. R. (1983). *Direct Nuclear Reactions*. Oxford, Clarendon Press.

You, G. J., Zheng, F. X., Xin, X. F., (2002). solution of the relativistic Dirac-Woods-Saxon problem. *Phys. Rev. A*, 66(6): 062105.

Zaichenko, A. K. and Ol'Khovskii, V. S., (1976). Analytic solutions of the scattering by potentials of the Eckart class. *Theo. And Math. Phys.*, 27(2): 475-477.

Author Information

Orhan Bayrak

Akdeniz University

Akdeniz University, Dumlupınar Boulevard, 07058 Campus,

Antalya / TURKEY

Contact E-mail: bayrak@akdeniz.edu.tr

Investigation of Electronic Properties of Substituted Pyrimidine Derivatives with Density Functional Theory

Erdem ERGAN

Yuzuncu Yil University

Esvet AKBAS

Yuzuncu Yil University

Abstract: Quantum chemical calculations are widely used in the reactivity of organic compounds. The configuration in the methodology reached a point where the reasonably predicted properties could be obtained from the density functional theory (DFT) calculations. The geometry and molecular orbitals of organic compounds are characterized by their activities. The electronic properties of the compounds are related to the frontier orbital energy of highest occupied molecular orbital energy (E_{HOMO}), lowest unoccupied molecular orbital energy (E_{LUMO}), and energy gap ($\Delta E_{\text{LUMO-HOMO}}$). In this study, compounds of pyrimidine have been researched the electronic properties using density functional theory.

Keywords: Pyrimidine compounds, DFT, HOMO, LUMO

Introduction

Substituted pyrimidines attracted synthetic organic chemistry interest very much because of their biological and chemotherapeutic importance. The pyrimidine compounds and related fused heterocycles are interesting classes of heterocyclic compounds that exhibit a wide spectrum of biological activities such as anticancer, antiviral, antioxidant, antibacterial, anxiolytic, antidepressant, anti-inflammatory and analgesic activities (Addepalli, at al., 2018; Gokhale, at al., 2017).

Quantum chemical calculations are widely used in the reactivity of organic compounds. The configuration in the methodology reached a point where the reasonably predicted properties could be obtained from the density functional theory (DFT) calculations. The geometry and molecular orbitals of organic compounds are characterized by their activities. The properties of the components, the highest molecular orbital energy (E_{HOMO}), the lowest empty molecular orbital energy (E_{LUMO}) and energy deficit ($\Delta E = E_{\text{LUMO}} - E_{\text{HOMO}}$) are related to the use of the boundary orbital (Kanmazalp, 2017).

The high E_{HOMO} value has a molecule tendency to give electrons, while a low E_{LUMO} value indicates the ability of the molecule to accept electrons. The difference between E_{LUMO} and E_{HOMO} energies is called energy gap. Larger values of the energy gap will provide low reactivity to a chemical interaction and inhibition efficiency. But the lower values of the ΔE will render good reactivity to a chemical interaction and inhibition efficiency (Karzazi, at al., 2014).

Method

Calculation Analysis

The quantum chemical parameters of the earlier synthesized pyrimidine compounds **1-5** (Taslami, at al., 2018) (Fig. 1.) have been investigated as electronic properties using density functional theory. Full geometry optimizations of pyrimidine derivatives were performed using DFT based on Beck's three parameter exchange

- This is an Open Access article distributed under the terms of the Creative Commons Attribution-Noncommercial 4.0 Unported License, permitting all non-commercial use, distribution, and reproduction in any medium, provided the original work is properly cited.

- Selection and peer-review under responsibility of the Organizing Committee of the Conference

functional and Lee–Yang–Parr nonlocal correlation functional (B3LYP) and the 6-31G (d, p) orbital basis sets in Gaussian09 program (Becke, 1993; Lee, et al., 1988; Frisch, et al., 2009).

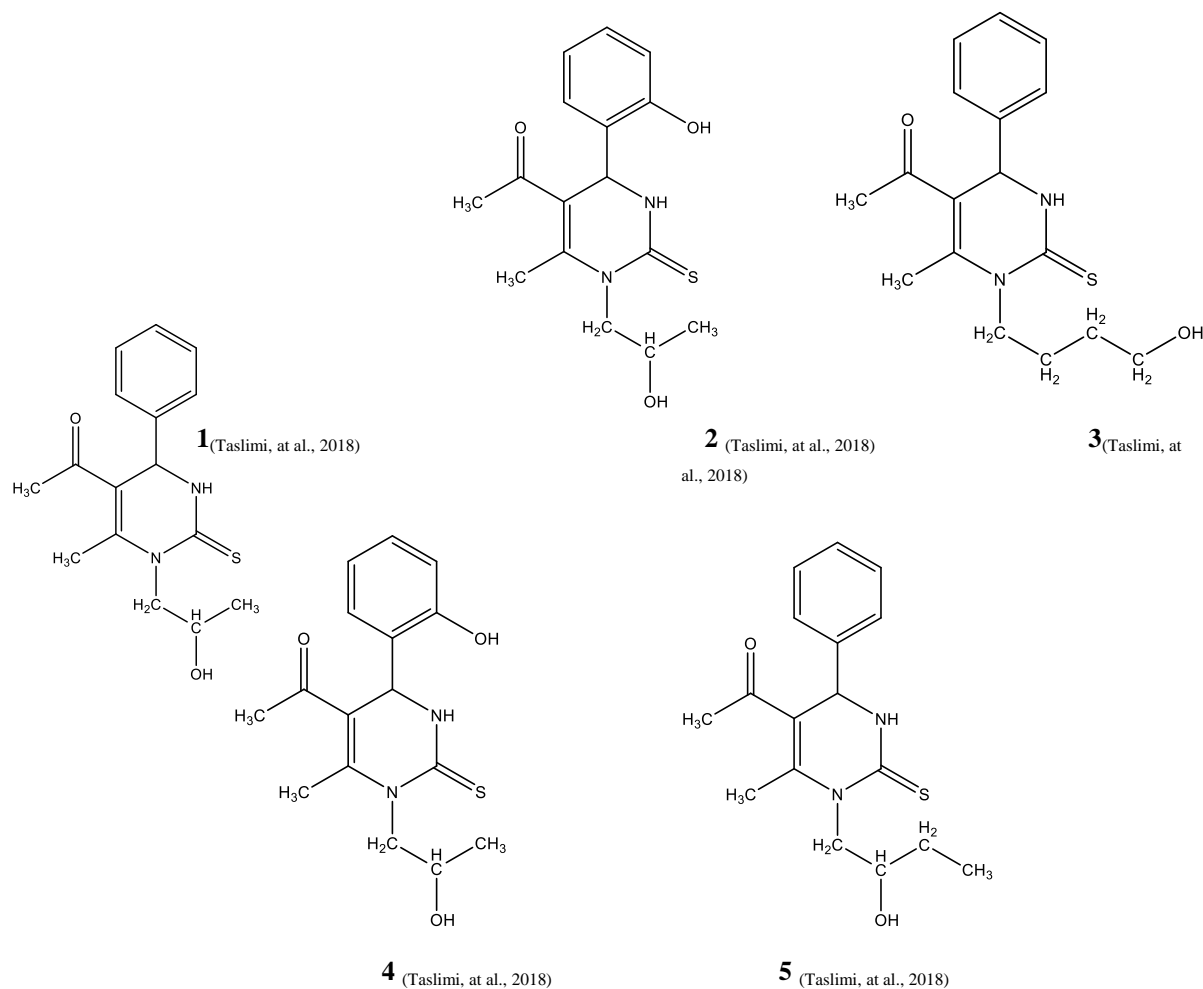


Figure 1. Molecular structures of the compounds

Results and Discussion

The highest occupied molecular orbital (HOMO) energy and the lowest unoccupied molecular orbital (LUMO) energy and the energy gap of HOMO and LUMO are calculated at the B3LYP/6–31G(d,p) level in order to evaluate the energetic behavior of earlier synthesized molecules 1-5. The energies and pictorial illustration of HOMO and LUMO frontier molecular orbitals are shown in Fig. 9. The positive and negative phases are represented in red and green color, respectively. It is very important to know the energy gap of synthesized molecules and see the contribution of functional groups on frontier molecular orbitals because HOMO and LUMO play an important role in the electrical and optical properties, as well as in UV–vis spectra and chemical reactions (Cinar, et al., 2011). The bio- and chemical-activity of the molecules depend on the eigen value of HOMO which represents the ability to donate an electron, LUMO which represents the ability to obtain an electron as an electron acceptor and $\Delta E_{\text{HOMO-LUMO}}$ energy gap (Shukla, et al., 2014). If the molecules have a large energy gap, they are more stable molecules in terms of a chemical activity. The graphs show that HOMOs are generally formed in the pyrimidine ring and that LUMOs are localized in the benzoyl group attached to the pyrimidine ring shown in Figure 2.

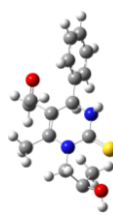
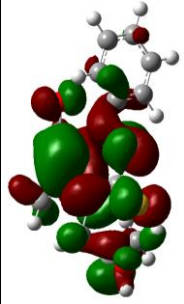
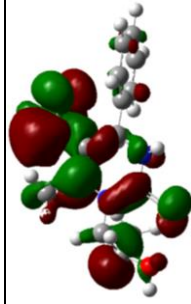
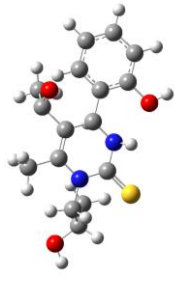
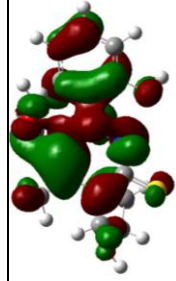
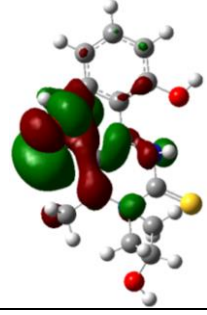
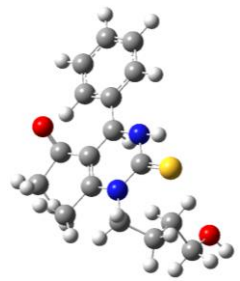
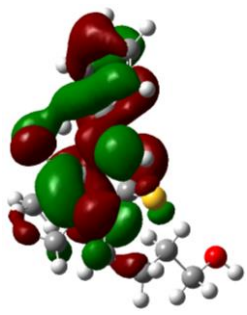
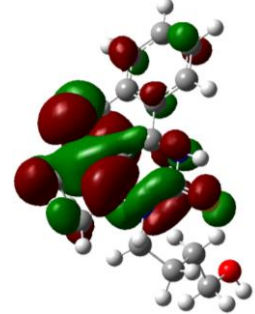
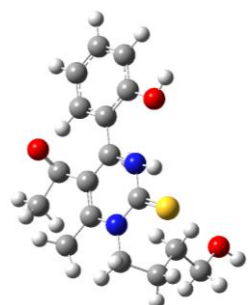
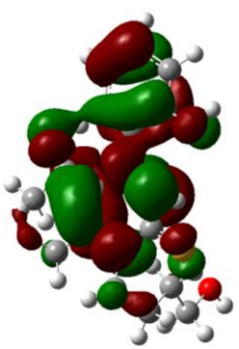
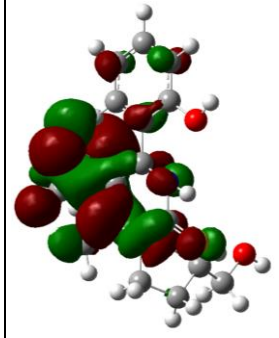
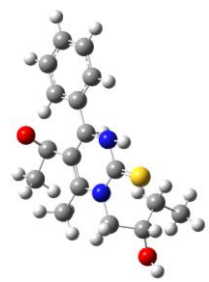
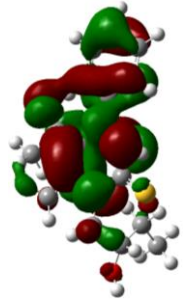
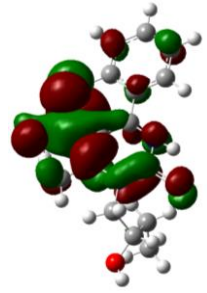
| Compounds | Molecular structure | HOMO | LUMO |
|-----------|---|--|---|
| 1 |  |  |  |
| 2 |  |  |  |
| 3 |  |  |  |
| 4 |  |  |  |
| 5 |  |  |  |

Figure 2. The optimized structures of molecules 1-5 obtained at B3LYP/6-31 G (d, p)

By using HOMO and LUMO energy values for a molecule, the global chemical reactivity descriptors of molecules such as hardness (η), chemical potential (μ), softness (S), electronegativity (χ) and electrophilicity index (ω) have been defined. Where A is the ionization potential and I is the electron affinity of the molecule. All the calculated values of ionization potential, electron affinity, hardness, potential, softness and electrophilicity index are shown in Table 1.

Table 1. Calculated quantum chemical parameters of the studied molecules

| Compounds | 1 | 2 | 3 | 4 | 5 |
|--|---------|---------|---------|---------|---------|
| E_{HOMO} (eV) | -5.0956 | -5.0080 | -5.0056 | -4.8347 | -5.0507 |
| E_{LUMO} (eV) | -2.0836 | -2.5565 | -2.6012 | -2.5312 | -2.6325 |
| Ionization potential: I (eV) | 5.0956 | 5.0080 | 5.0056 | 4.8347 | 5.0507 |
| Electron affinity: A (eV) | 2.0836 | 2.5565 | 2.6012 | 2.5312 | 2.6325 |
| Electronegativity: χ (eV) | 3.5896 | 3.7823 | 3.8034 | 3.6830 | 3.8416 |
| Chemical hardness: η (eV) | 3.012 | 2.4515 | 2.4044 | 2.3035 | 2.4182 |
| Chemical softness: S | 0.3320 | 0.4079 | 0.4159 | 0.4341 | 0.4135 |
| Dipole moment: $\mu_{\text{(debye)}}$ | 3.6072 | 1.5520 | 6.2170 | 4.6906 | 4.6787 |
| Electrophilicity index: (ω) | 2.1600 | 0.4913 | 8.0376 | 4.7757 | 4.5261 |
| Transferred electrons fraction: (ΔN) | 0.5661 | 0.6563 | 0.6647 | 0.7200 | 0.6530 |
| Energy gap: $\Delta E = E_{\text{LUMO}} - E_{\text{HOMO}}$ (eV) | 3.012 | 2.4515 | 2.4044 | 2.3035 | 2.4182 |
| $\Delta E_{\text{back donation}}$ | -0.753 | -0.6129 | -0.6011 | -0.5759 | -0.6046 |

As presented in Table 1, the compound which have the lowest energetic gap is the compound 4 ($\Delta E = 2.3035$ eV). This lower gap allows it to be the softest molecule. The compound that have the highest energy gap is the compound 1 ($\Delta E = 3.012$ eV). The compound that has the highest HOMO energy is the compound 4 ($E_{\text{HOMO}} = -4.8347$ eV). This higher energy allows it to be the best electron donor. The compound that has the lowest LUMO energy is the compound 5 ($E_{\text{LUMO}} = -2.6325$ eV) which signifies that it can be the best electron acceptor.

The two properties like I (potential ionization) and A (affinity) are so important, the determination of these two properties allow us to calculate the absolute electro negativity (χ) and the absolute hardness (η). These two parameters are related to the one-electron orbital energies of the HOMO and LUMO respectively. Compound 4 has lowest value of the potential ionization ($I = 4.8347$ eV), so that will be the better electron donor. Compound 5 has the largest value of the affinity ($A = 2.6325$ eV), so it is the better electron acceptor. The chemical reactivity varies with the structural of molecules.

Chemical hardness (softness) value of compound 4 ($\eta = 2.3035$ eV, $S = 0.4341$ eV) is lesser (greater) among all the molecules. Thus, compound 4 is found to be more reactive than all the compounds. Compound 5 possesses higher electro negativity value ($\chi = 3.8416$ eV) than all compounds so; it is the best electron acceptor. The value of ω for compound 3 ($\omega = 8.0376$ eV) indicates that it is the stronger electrophiles than all compounds.

Compound 4 has the smaller frontier orbital gap so, it is more polarizable and is associated with a high chemical reactivity, low kinetic stability and is also termed as soft molecule.

Molecular Electrostatic Potential (MEP) Surface

MEP is a protocol of mapping electrostatic potential onto the iso electron density surface. Red color shows electron rich regions which are partially negatively charged. Blue color shows electron deficient regions which are partially positively charged. Light blue shows slightly electron deficient regions. Yellow color shows slightly electron rich regions and green color represents neutral regions. The MEPs have been used for interpreting and predicting relative reactivities of sites for electrophilic and nucleophilic attack, investigation of biological recognition, hydrogen bonding interactions, studies of zeolite, molecular cluster and crystal behavior and the correlation and prediction of a wide range of macroscopic properties (Ravikumar at al., 2008). In this study, 3D plots of MEP for 1-5 have been drew in Figure. 3.

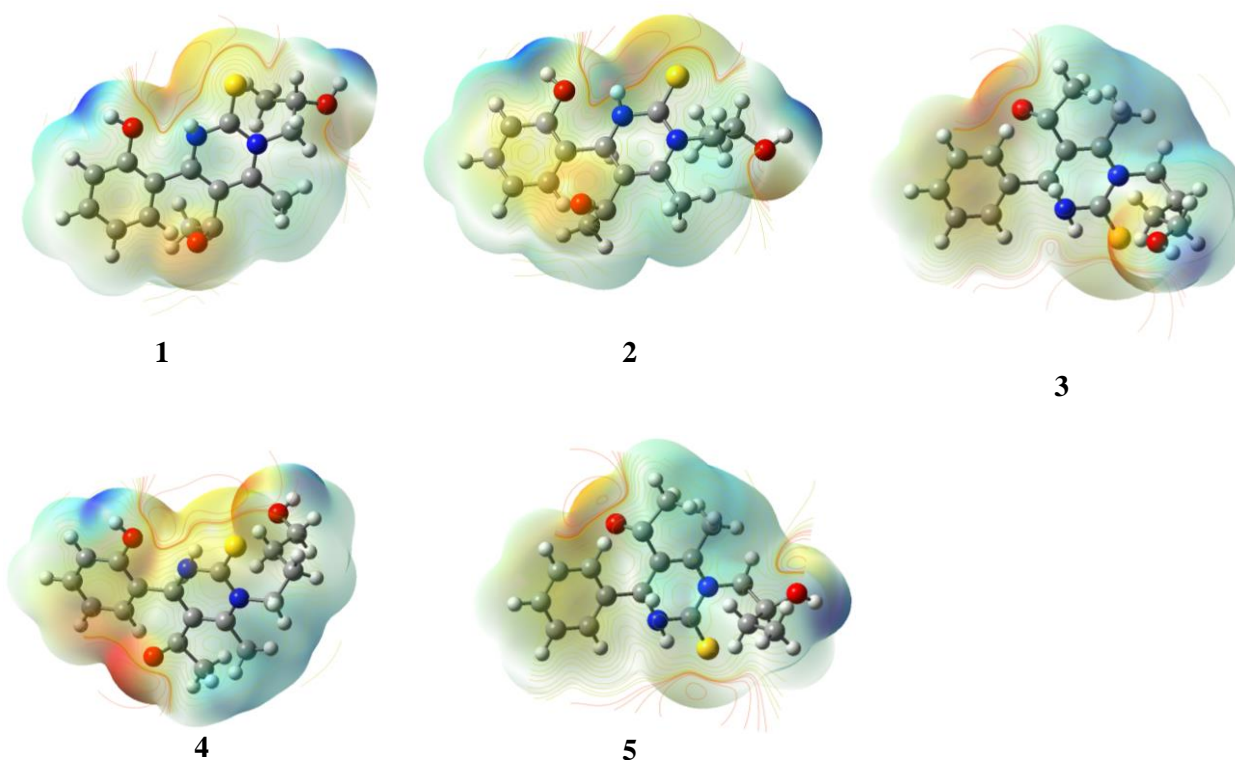


Fig. 3. Molecular electrostatic potential for 1-5

Conclusion

The calculated HOMO–LUMO energy gaps showed that eventual charge transfer took place within the compound. The predicted MEPs revealed the negative regions of the molecules, subjected to the electrophilic attack of these compounds and positive regions of the molecules which are attacked by nucleophiles. To sumup, the calculated data, molecular orbital diagrams and Molecular Electrostatic Potential (MEP) maps provided information about the electronic properties of pyrimidine compounds.

References

- Addepalli, Y., Yang, X., Zhou, M., Reddy, D. P., Zhang, S.L., Wang, Z., He, Y. (2018). Synthesis and anticancer activity evaluation of novel azacalix[2]arene[2]pyrimidines. *Eur. J. Med. Chem.*, 151, 214-225.
- Becke, A.D. (1993) A new mixing of Hartree–Fock and local density-functional theories. *The Journal of Chemical Physics*, 98, 1372.
- Cinar, M., Coruh, A., Karabacak, M. (2011). FT-IR, UV–vis, ^1H and ^{13}C NMR spectra and the equilibrium structure of organic dye molecule disperse red 1 acrylate: A combined experimental and theoretical analysis *Spectrochim. Acta A*, 83, 561–569.
- Frisch, M.J., Trucks, G.W., Schlegel, H.B., Scuseria, G.E., Robb, M.A., Cheeseman, J.R., Scalmani, G., Barone, V., Mennucci, B., Petersson, G.A., Nakatsuji, H., Caricato, M., Li, X., Hratchian, H.P., Izmaylov, A.F., Bloino, J., Zheng, G., Sonnenberg, J.L., Hada, M., Ehara, M., Toyota, K., Fukuda, R., Hasegawa, J., Ishida, M., Nakajima, T., Honda, Y., Kitao, O., Nakai, H., Vreven, T., Montgomery, J.A., Jr., Peralta, J.E., Ogliaro, F., Bearpark, M., Heyd, J.J., Brothers, E., Kudin, K.N., Staroverov, V.N., Kobayashi, R., Normand, J., Raghavachari, K., Rendell, A., Burant, J.C., Iyengar, S.S., Tomasi, J., Cossi, M., Rega, N., Millam, N.J., Klene, M., Knox, J.E., Cross, J.B., Bakken, V., Adamo, C., Jaramillo, J., Gomperts, R., Stratmann, R.E., Yazyev, O., Austin, A. J., Cammi, R., Pomelli, C., Ochterski, J. W., Martin, R.L., Morokuma, K., Zakrzewski, V.G., Voth, G.A., Salvador, P., Dannenberg, J.J., Dapprich, S., Daniels,

- A.D., Farkas, Ö., Foresman, J.B., Ortiz, J.V., Cioslowski, J., Fox, D.J. (2009). Gaussian, Inc., Wallingford CT.
- Gokhale, N., Dalimba, U., Kumsi, M. (2017). Facile synthesis of indole-pyrimidine hybrids and evaluation of their anticancer and antimicrobial activity *J. Saudi Chem. Soc.*, 21, 761-775.
- Kanmazalp, S.D. (2017). Investigation of Theoretical Calculations of 2-(1-Phenylethylideneamino)guanidine Compound: NBO, NLO, HOMO-LUMO and MEP Analysis by DFT Method. *Karaelmas Science and Engineering Journal*, 7(2), 491-496.
- Karzazi, Y., Belghiti, M.E.A., Dafali, A., Hammouti, B. (2014). A theoretical investigation on the corrosion inhibition of mild steel by piperidine derivatives in hydrochloric acid solution. *Journal of Chemical and Pharmaceutical Research*, 6(4), 689.
- Lee, C., Yang, W., Parr, R.G. (1988) Development of the Colle-Salvetti correlation-energy formula into a functional of the electron density. *Physical Review B*, 37(2), 785.
- Ravikumar, C., Joe, I.H., Jayakumar, V.S. (2008). Charge transfer interactions and nonlinear optical properties of push-pull chromophore benzaldehyde phenylhydrazone: A vibrational approach. *Chem. Phys. Lett.*, 460, 552-558.
- Shukla, V.K., Al-Abdullah, E.S., El-Emam, A.A., Sachan, A.K., Pathak, S.K., Kumar, A., Prasad, O., Bishnoi, A., Sinha, L. (2014). Spectroscopic (FT-IR, FT-Raman, and UV-visible) and quantum chemical studies on molecular geometry, Frontier molecular orbitals, NBO, NLO and thermodynamic properties of 1-acetyldole. *Spectrochim. Acta A*, 133, 626-638.
- Taslimi, P., Sujayev, A., Turkan, F., Garibov, E., Huyut, Z., Farzaliyev, V., Mamedova, S., Gulçin, İ. (2018). Synthesis and investigation of the conversion reactions of pyrimidine-thiones with nucleophilic reagent and evaluation of their acetylcholinesterase, carbonic anhydrase inhibition, and antioxidant activities. *Journal of Biochemical and Molecular Toxicology*, 32(2), 1-12.

Author Information

Erdem Ergan

Van Yuzuncu Yil University,
Van Vocational School Of Security,
Department of property protection and security,
65080 Van/Turkey
Contact E-mail: erdemergan@yyu.edu.tr

Esvet Akbas

Van Yuzuncu Yil University,
Faculty of Science, Department of Chemistry,
65080 Van / Turkey

Domestic Battery Charge Unit Design and Production for Military Vehicle

Ahmet AKTAS
Dumlupinar University

Abstract: As a result of increased research and development expenditures on the branding of domestic products used in the defense industry in our country, speed is given. The defense industry constitutes a large share of the inventory of military vehicles in land vehicles. At the same time, military vehicles are exported to many units of the armed forces. Domestic production of other hardware components used in these vehicles will reduce external dependency. As a result of developments in electronic communication and electro-optical technologies, such devices are widely used in fixed point surveillance and command-control tasks. With this study, original and locally designed and prototype production of battery charging units have been realized in order to meet the energy needs of the electronic systems in the fixed point services of military land vehicles from the network. Manufactured in accordance with military standards, the battery charger unit is designed to extend the cycle life of the battery by controlling its temperature. With the battery charging unit realized, defense contributes to my country economically and strategically by decreasing the external dependency by using indigenous and original resources in the industry.

Keywords: Defense industry, Battery charge, Control systems, Power electronics

Introduction

The new generation of modern military vehicles now carries many electronic and power-driven components. Previously, military vehicles were used for combat and support vehicles. These vehicles needed power for long-running radios and electronic systems. Military vehicles today include sensors, communications units, drivers and powerful weapon systems that require more energy than a conventional lead-acid battery can provide [Bogosyan, S.].

Especially during surveillance, batteries with low energy storage capacity can supply energy to demanding electrical units for a short time. This requires regular charging of the batteries [Masrur, M. A.].

New generation military armored vehicles should function as mobile power plants. Modern combat and hybrid vehicles must be capable of generating significant amounts of electrical power to provide full technology support. To meet the needs of today's vehicles, power electronics designers reassessed the built-in energy architecture. The sensor, control and communication systems of each vehicle are constantly improving [Lee, S.].

In military vehicles, 28 V batteries are commonly used with two 12 V lead-acid batteries, which are usually placed in series for military vehicles. The batteries were initially used only for loads such as lighting and ignition. However, as the complexity of vehicle systems increases, the batteries should be able to provide more power [Antoniou, A. I.].

In this study, a battery charging circuit design and production of 28 V, 60 A and 1700 W for military vehicles was realized. The battery charging circuit is designed and manufactured to meet military standards. The system was designed in Matlab/Simulink program and the results were given.

Battery Charge Circuit

Matlab/Simulink block diagram of 28 V/60 A rectifier design is given in Figure 1. In the rectifier design, the system grid input voltage is simulated to be 220 V/50 Hz. Then 311 V DC bus voltage with the full bridge rectifier diodes is obtained. The DC bus voltage is passed through the R-L filter and then supply to the mosfet switching elements. The drive signal S3_g is applied to the mosfet switching elements S2 and S3. The drive signal S1_g is applied to the mosfet switching elements S1 and S4. The transformer in the rectifier simulation design has one primary input and two secondary outputs. The primary voltage of the transformer is 311 V and the secondary voltage is 36 V. By combining the ends of the secondary windings, 0V of the output voltage is obtained. The other end is transferred to the filter circuit by diodes and the power stage of the system design is completed.

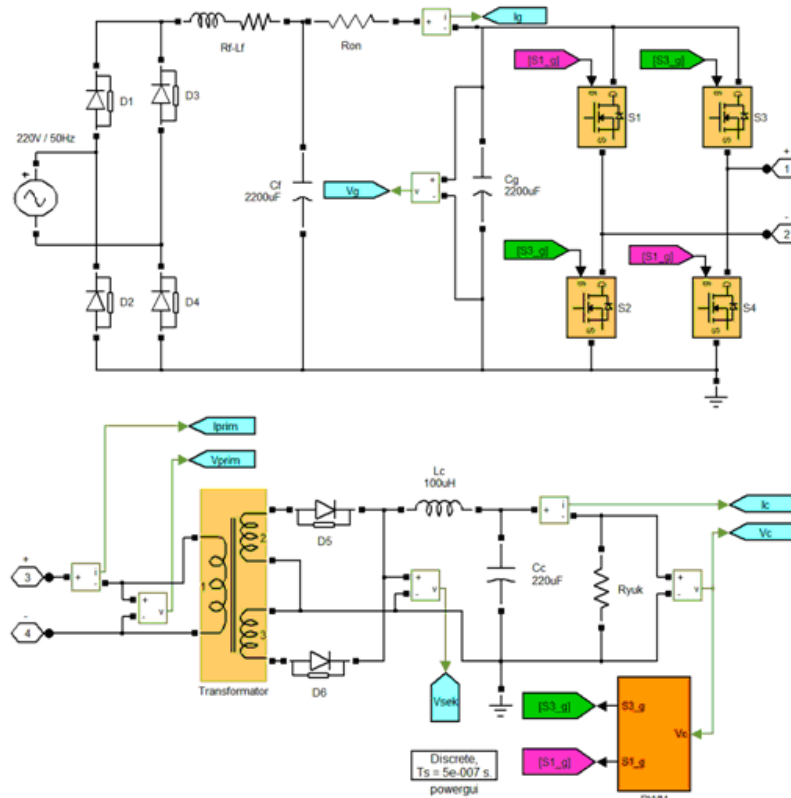


Figure 1. Battery charge circuit Matlab/Simulink block diagram

Figure 2 gives a detailed diagram of the block controlling the voltage at the rectifier output. The difference between the reference voltage value 28 V and the voltage reading at the sensor output is input to the PI controller. The PI controller produces the output by comparing the measured and reference voltage values. The switching signal is generated by comparing the error value of the PI output with the triangular wave of 55 kHz. The generated switching signal is compared with the clock generator to change the signal so that the switching elements are not simultaneously transmitting. The switching signals are then applied crosswise such that S1-S4 and S3-S2.

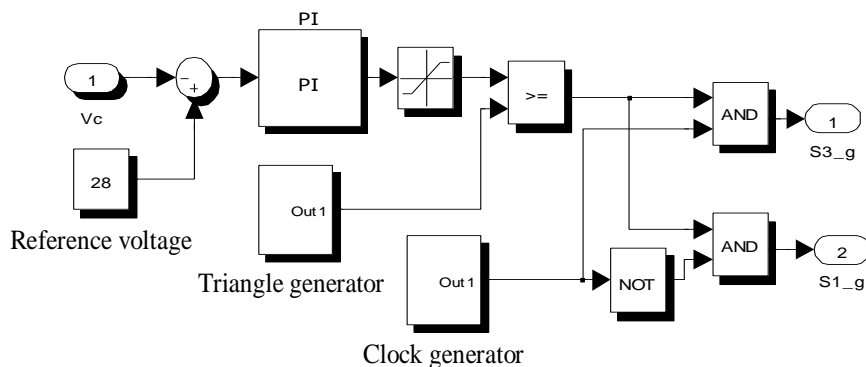


Figure 2. DC bus voltage control block diagram

Simulation Results under 60A Load

Figure 3 shows the DC bus voltage of 311 V. The DC bus voltage is provided by the full bridge rectifier circuit at the mains input. Figure 4 shows the DC bus current under 60A load. The DC bus current requires current from the grid at an average of 6 A.

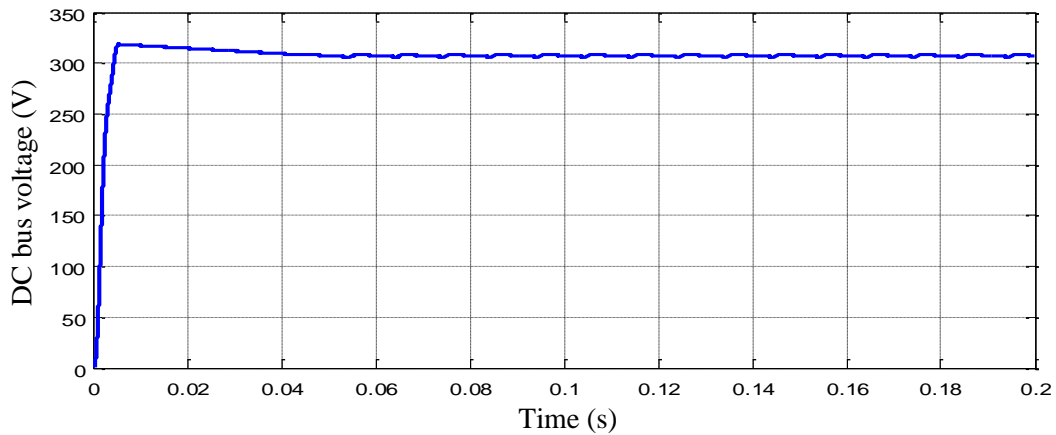


Figure 3. DC bus voltage under 60A load

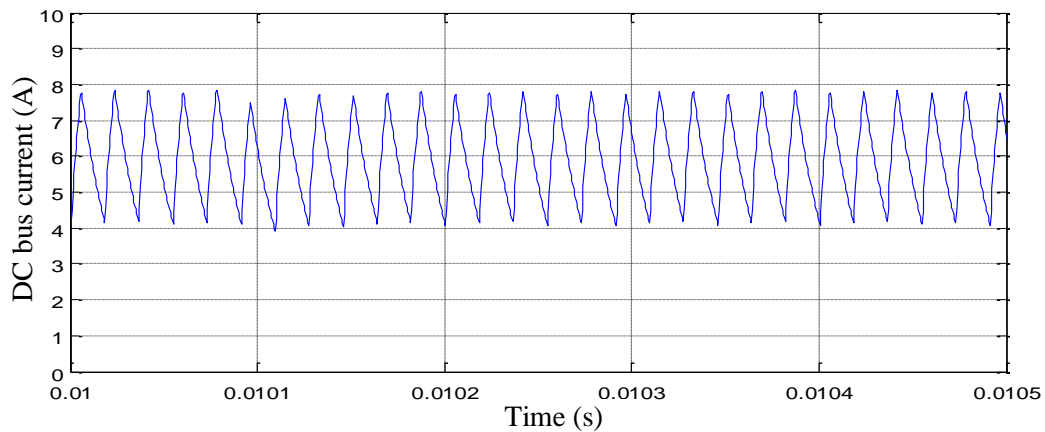


Figure 4. DC bus current under 60A load

Figure 5 shows the winding voltage at the primary terminals of the transformer under load 60A. Figure 6 shows the current change in the primary windings of the transformer for the same load current value. Figure 7 shows the secondary voltage change of the transformer in detail.

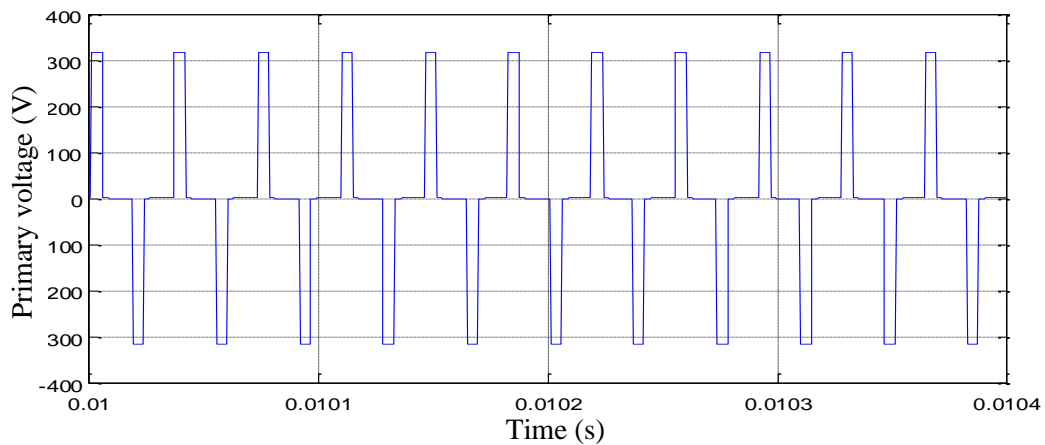


Figure 5. Transformer primary voltage under 60A load

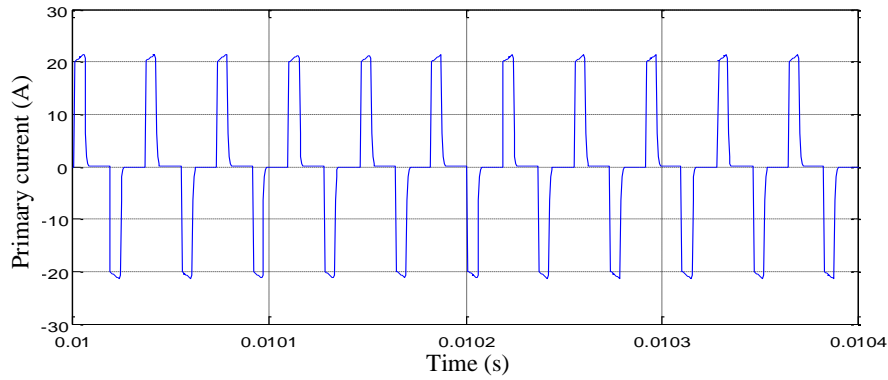


Figure 6. Transformer primary current under 60A load

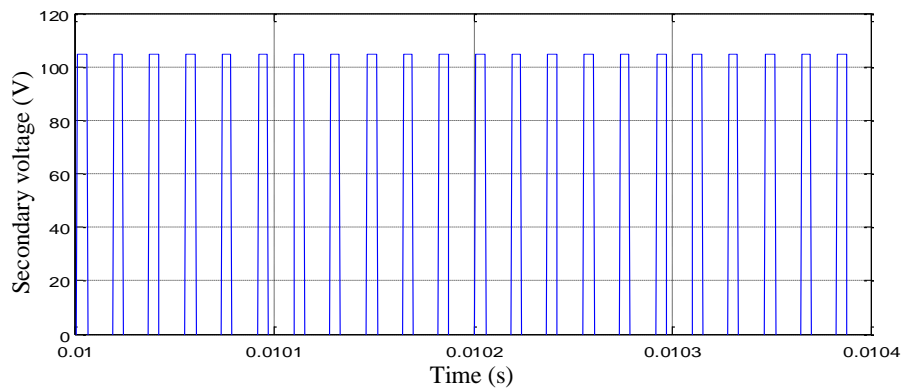


Figure 7. Transformer secondary voltage under 60A load

Figure 8 shows the change of rectifier output voltage. It is understood that rectifier output is fixed at 28 V. At the first time, the rise value is set to 0.01 s by the PI controller and drawn to the desired reference voltage. Figure 9 shows the rectifier output current value. 60 A is continuously supplied to the load connected to the system.

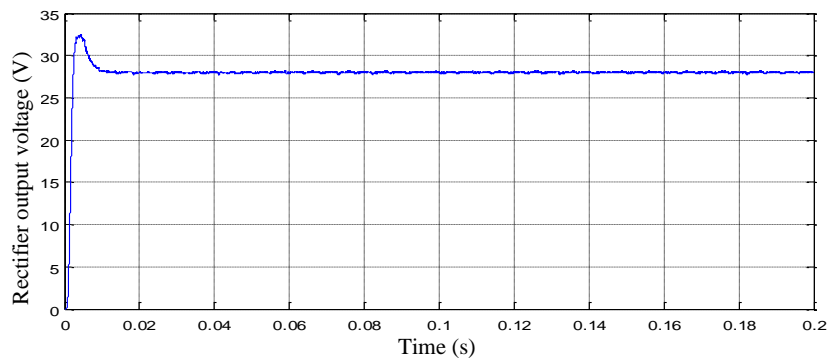


Figure 8. Rectifier output voltage under 60A load

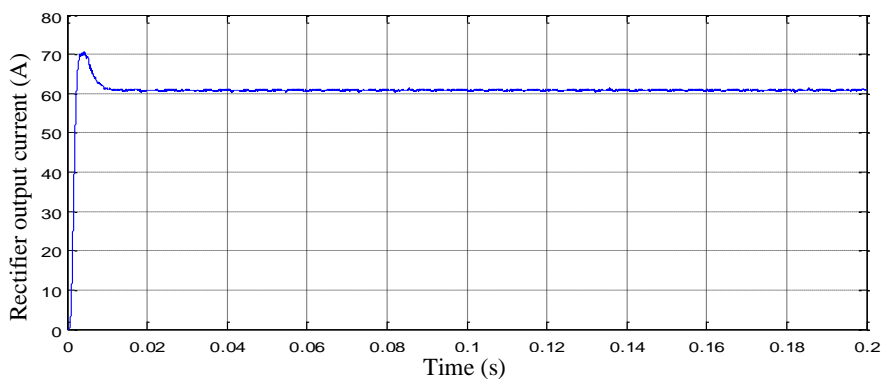


Figure 9. Rectifier output current under 60A load

Figure 10 shows the waveforms of the 55 kHz triangle wave generator. This waveform generated by the triangle wave generator is compared with the error in the PI controller output given in Figure 11. As a result of this comparison, when the PI error value is greater than the triangular wave, the comparator generates 0 when the value is smaller. This signal change produced by comparison is given in Figure 14. Figure 14 shows the output of the clock, comparator, S1_g and S3_g switching signals in detail. The frequency of the block signal is selected as half of the switching frequency.

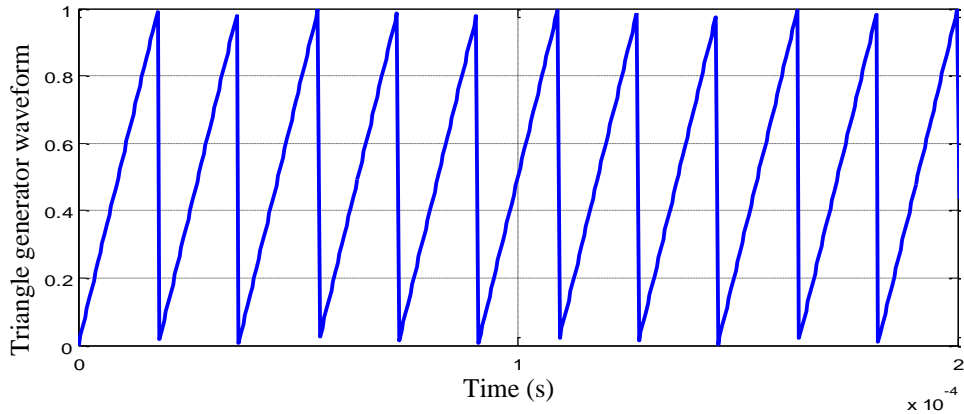


Figure 10. Triangle generator waveform under 60A load

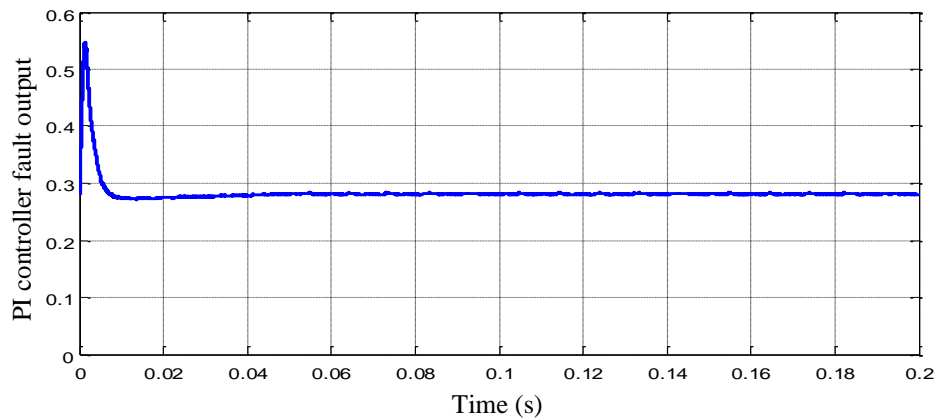


Figure 11. PI controller fault output under 60A load

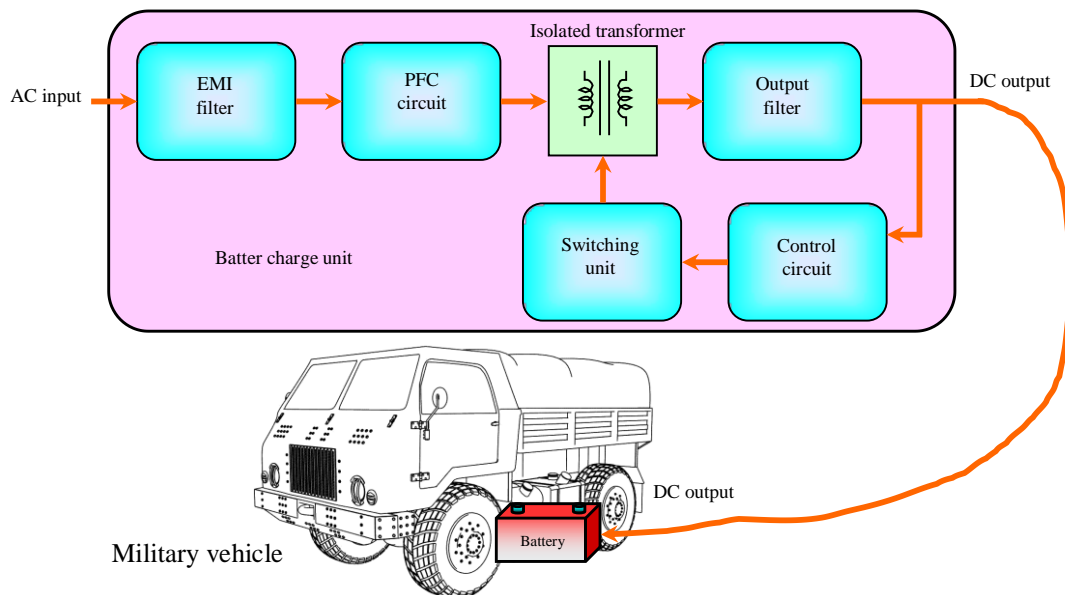


Figure 12. Diagram of military vehicle battery charge circuit

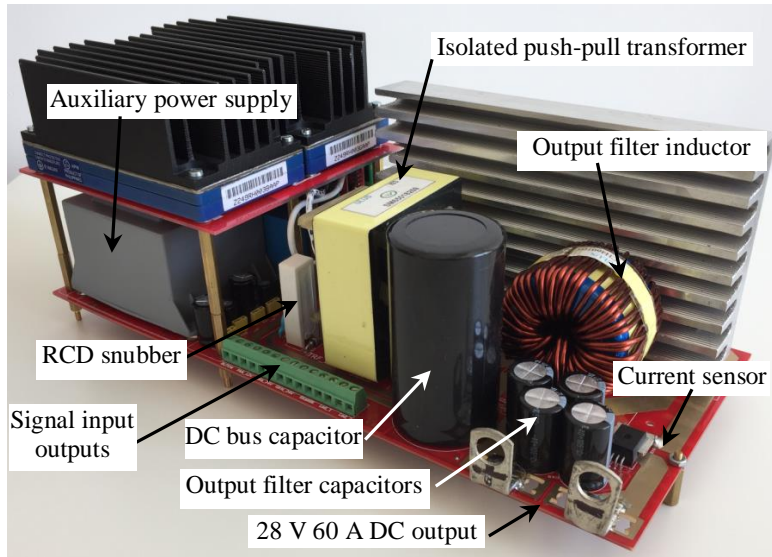


Figure 13. Photograph of battery charge circuit

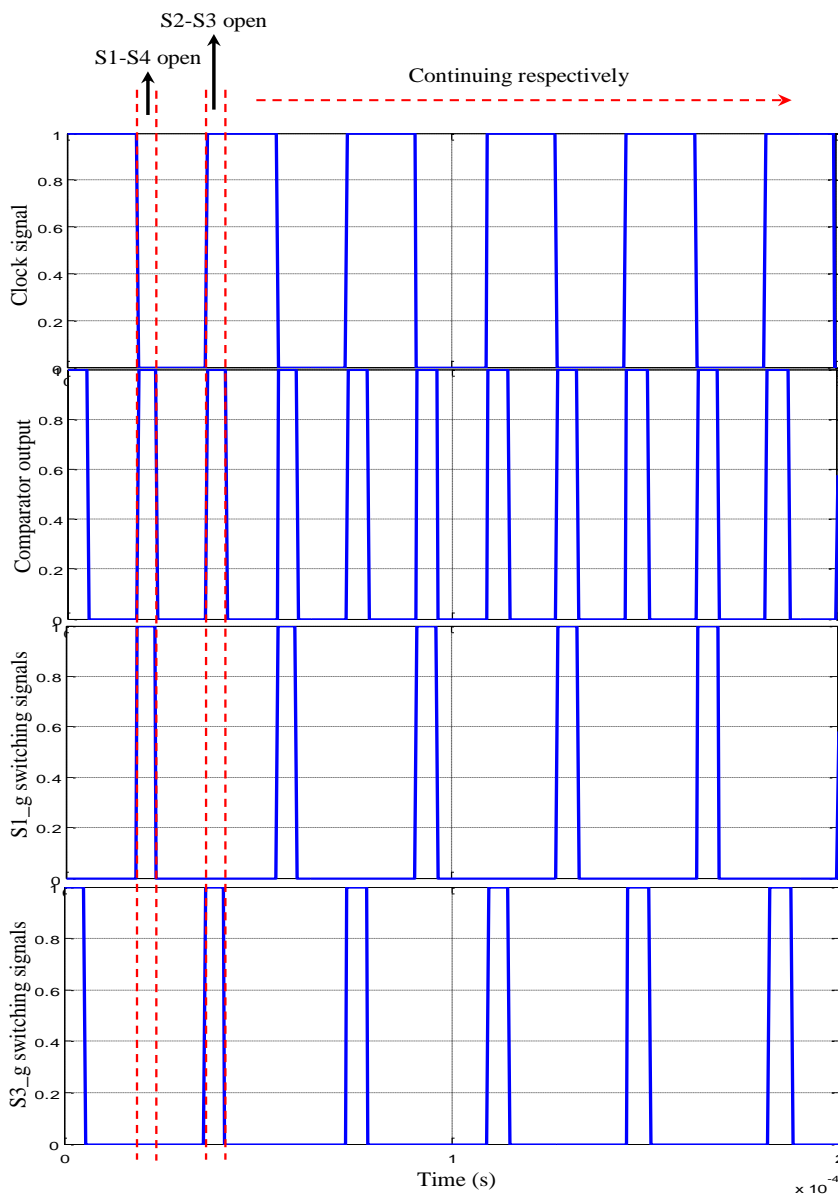


Figure 14. Comparator, S1_g and S3_g switching signals under 60A load

Conclusion

In this study, the battery charge circuit used in military vehicles was simulated with Matlab/Simulink program. The results of the circuit which has been designed with simulation program under full load are given. It is seen that the output of the battery charging circuit remains at the desired constant voltage under full load. PI voltage controller is used in the designed circuit to ensure stable operation of the system. The system designed according to the simulation results was produced.

Acknowledgments

This study was supported by within Tekom Electric and Electronic Company.

References

- Bogosyan, S., Gokasan, M., and Goering, D. J., A Novel Model Validation and Estimation Approach for Hybrid Serial Electric Vehicles, *IEEE Trans Veh Technol*, vol. 56, pp. 1485-1497, 2007.
- Masrur, M. A., Skowronska, A. G., Hancock, J., Kolhoff, S. W., McGrew, D. Z., Vandiver, J. C. , and Gatherer, J., Military-Based Vehicle-to-Grid and Vehicle-to-Vehicle Microgrid-System Architecture and Implementation, *IEEE Trans on Transp Electf*, vol. 4, pp. 157-171, 2018.
- Lee, S., and Kim, J., Implementation methodology of powertrain for series-hybrid military vehicles applications equipped with hybrid energy storage, *Energy*, vol. 120, pp. 229-240, 2017.
- Antoniou, A. I., Komyathy, J., Bench, J., and Emadi, A., Modeling and Simulation of Various Hybrid-Electric Configurations of the High-Mobility Multipurpose Wheeled Vehicle (HMMWV), *IEEE Trans Veh Technol*, vol. 56, pp. 459-465, 2007.

Author Information

Ahmet Aktas

Kütahya Dumlupınar Üniversitesi,
Simav Teknoloji Fakültesi,
Elektrik Elektronik Mühendisliği Bölümü, 43500,
Simav/KÜTAHYA
Contact E-mail: ahmet_aktas_1987@hotmail.com

ParEncrypt: A Two-phased Encryption for Improved Security

Haneya KHAN

University of Texas at Dallas

Asim SIDDIQUI

University of Texas at Dallas

Fariha ISLAM

University of Texas at Dallas

Elham HAMID

University of Texas at Dallas

Ebru CELIKEL CANKAYA

University of Texas at Dallas

Abstract: The idea of encrypting text is alluring still as it is the most convenient and straightforward means to shuffle text so as to make it unintelligible to unintended third parties. We design and develop a novel symmetric encryption algorithm ParEncrypt that implements a cascaded structure of known encryption approaches: It first employs Feistel cipher to scramble the plaintext, then applies a further step of substitution implemented via left and right parentheses into the intermediate output to finalize the encryption. This two-phased encryption provides enhanced security with the cost of slower paced performance. We provide performance comparison of our design with common benchmark encryption algorithms and see that ParEncrypt outperforms all others with respect to the level of security. Additionally, our scheme offers an additional benefit as our special way of encryption provides a significant level of compression.

Keywords: Encryption, Lossless compression, Data security

Introduction

Security has become one of the most critical parts of the technological world. The increasing use of technology in almost every aspect of life mandates security and privacy of personal and sensitive data. One of the most basic, yet useful, forms of security are encryption algorithms. Various different types of encryption algorithms exist today, each with different properties and uses. Different subsets include symmetric key algorithms, asymmetric key algorithms, block ciphers, stream ciphers, etc.

Symmetric key algorithms are on subset of encryption algorithms and use a single private key to encrypt and decrypt sensitive data. Existing implementations include AES, DES, Blowfish, etc.

We propose a new symmetric key encryption scheme. We base our scheme on the Feistel cipher model, a symmetric key algorithm model, and introduce a nested implementation of it that produces a uniform ciphertext. We then evaluate the performance of our proposed encryption scheme and compare it to the performance of similar existing algorithms. Finally, we consider further work that can be done to better both the security and performance of our scheme.

Related Work

Research in the field of encryption nowadays is typically associated with the application of existing algorithms. For novel encryption algorithm research, much of it is done with a specific purpose in mind building off widely adopted cryptographic tools including the Advanced Encryption Standard, Rivest-Shamir-Adleman cryptosystem, and MD5 message-digest algorithm.

The authors of [1] seek to build a new encryption algorithm named DTT which utilizes computationally simple shifting procedures and “bitxor” to obfuscate messages. The algorithm itself incorporates environmental factors including temperature and time that strengthen it against cryptanalysis. The goal of the algorithm is to prevent hackers from decrypting the message as it fails based on time and temperature. The simple shifting procedure is a key part of the Feistel Network Structure incorporated in our scheme, Nested.

Double-chaining encryption is another approach on improving existing encryption algorithms. In [2], a double chaining encryption algorithm is constructed with fixed 16-byte blocks. It functions similarly to Cipher Block Chaining mode commonly used in AES but does it in two steps instead of a single one. It performs Cipher Block Chaining once before reversing the order of blocks and performing it again. Because of the increased overhead, the number of rounds is shortened to 4. This is similar to our algorithm, as we reduced the number of rounds in order to compensate for the increased processing in each round. A key difference is that they double the chaining process where as we double the encryption itself.

Another work [3], develops an order-revealing encryption algorithm, which builds upon Order-Preserving Encryption (OPE) that supports comparisons over encrypted values. This algorithm is useful for encrypted databases, and data that is stored as it provides security and quick comparisons. A key weakness in OPE encrypted databases is the vulnerability to “inference attacks” which the Order-Revealing Encryption (ORE) algorithm strengthens against. Additionally, the ORE scheme speeds up the process significantly as it is over 60 times faster than conventional OPE schemes. Furthermore, OPE solutions were limited by the constraint that both the ciphertext and plaintext needed to be numbered and ordered. On the contrary, the proposed ORE scheme is not limited by the order constraint, and instead relies on pseudorandom functions in a tuple of three algorithms. The benefit is that searches can be executed on encrypted data which does not sacrifice functionality for security.

Other encryption schemes seek to meet with new demands of technologies. The authors of [4] design a broadcast encryption scheme for verifying subscribers. They propose a new public-key cryptosystem by using efficient and computationally inexpensive public key cryptosystem Number Theory Research Unit (NTRU). The NTRU cryptosystem relies on a triple of integer parameters and four sets of polynomials with integer coefficients. Key Creation is achieved by randomly choosing two polynomials in a set which satisfies invertible modularity. For encryption, the encoder selects a public key and a random polynomial to compute cipher text. Decryption utilizes precomputed polynomial and inverts the encryption process. The algorithm is then applied to a broadcast encryption scheme that can detect traitors or pirate decoders. Upon detection it can revoke some users availability without redistributing a new secret key. The cryptosystem is computationally light with a logarithmic time complexity.

A growing area where integrity and confidentiality are key is in cloud computing. Researchers in [5] seek to optimize Fully Homomorphic Encryption for the purpose of securing cloud data from exploitation during computation. They use Rivest-Shamir-Adleman (RSA) to improve performance and Diffie-Hellman Algorithm for secure channel establishment in the Fully Homomorphic Encryption Scheme. The authors utilize inbuilt functions of MATLAB for implementation. Comparison between the RSA and Diffie-Hellman Algorithms is thorough and RSA is found to significantly cut down on execution time and probability of attacks at the cost of being less robust.

The advent of cloud computing has been in tandem with the development of the Internet of Things (IoT). One work [6], seeks to improve on the lightweight encryption algorithm (LEA) standardized in Korean IoT devices. The current LEA clock encryption algorithm is vulnerable to side-channel analysis attack. A masking technique is used to counter this vulnerability at the cost of performance. The authors develop and implement a new LEA block encryption algorithm which introduces a dummy operation of 4 bytes. This dummy operation does little to add to space overhead and increases each triple of 4 bytes to a quadruple of 4 bytes. It requires only a single operation to restore the original plain text value. Moreover, it protects against power consumption wave pattern outputs, so the secret key cannot be guessed easily. Upon testing, it was found to be roughly 17 times faster than existing masking algorithm that prevents against side-channel attack.

The authors of [7] don't really develop their own encryption algorithm. Rather they test the effectiveness of Attribute Based Encryption (ABE) which doesn't encrypt the whole data but attributes of the data. A key limitation in ABE is that the decryption process is expensive. They propose modifications to ABE which simplifies the process using digital signature and hash functions. The purpose of including these steps is to make it more robust against attackers. The secret key is generated using the input of the asymmetric public key into a hash function. Encryption takes in the public key and secret key and creates a digital signature. This only occurs if the encryption of the hash function matches with the access structure. Decryption is more complex. It takes an input of the public key, private key, secret key and access structure. If the private key matches the access structure, it will decrypt the hash function before checking the access structure.

Others incorporate a multitude of security mechanisms in designing a cryptosystem such as in [8]. The authors devise a mixed encryption algorithm utilizing the heterogenous capabilities of the networking components of IoT devices. The proposed solution combines AES for faster encryption speeds, ECC for digital signature and key management, MD5 to integrate it all together, forming a hybrid encryption algorithm. It uses the hard math problem elliptic curve to generate both the public and private key. Because the hybrid cipher algorithm is easy to calculate and key distribution easier to manage, it is seen as a potential solution to protect the authenticity and integrity during transmission for IoT devices. Nested is similar as it builds upon adopted security mechanisms.

ParEncrypt: Nested Encryption in Two Phases

In this section, we describe the design and implementation of our encryption scheme ParEncrypt. In essence, we propose a two phase encryption that cascades Feistel cipher in the first phase with substitution cipher to follow in the second phase. The symmetric scheme takes plaintext and a key as input, and then produces a double encrypted, uniform ciphertext in two steps, as shown in Figure 1; first, it doubly encrypts the inputted plaintext based on the Feistel cipher model using the inputted key, producing a ciphertext, and then second, it further encrypts the ciphertext into a series of left and right parentheses to obscure any patterns in the ciphertext. Moreover, the scheme is designed for the Unicode character set.

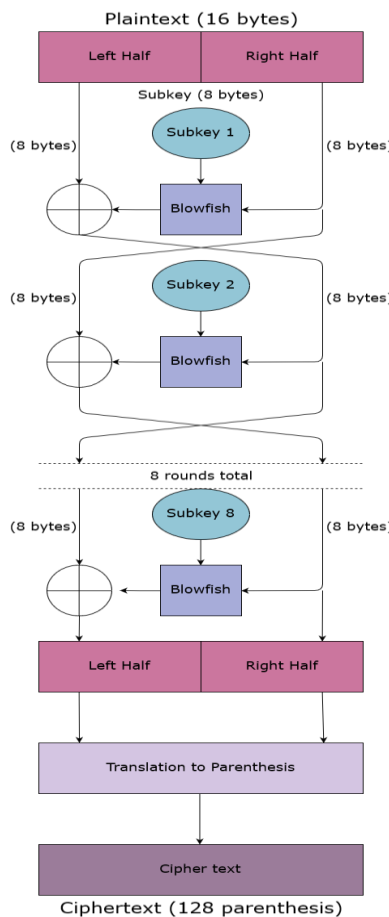


Figure 1. Encryption process diagram for ParEncrypt

Phase I: The Feistel Cipher

The first part of the scheme employs the Feistel cipher model that most existing and effective encryption algorithms, such as DES, are based on. We chose this block cipher model due to its iterative use of both substitution and permutation rounds that make it very difficult to break.

The algorithm uses a 16-char key (128 bits) for encryption. We chose a larger key size to prevent brute force attacks from breaking the cipher. The plaintext is split into 16-char (128-bit) blocks and incomplete blocks are padded so that the size of the blocks also cannot be used to break the cipher.

The scheme then employs eight rounds of substitutions and permutations on each block. Usually, 16 rounds are performed; however, we halved this due to other alterations we made so that the performance would not be degraded.

The Feistel cipher uses an internal function, the F function, for the substitutions and permutations. Generally, the F function is simply a one-way function; however, to increase security, we use the Blowfish cipher as the F function. Although the blowfish cipher is reversible, it is also based on the Feistel cipher and is very secure. This allows for the double encryption as the algorithm is essentially using nested Feistel ciphers. This is the main reason why we use 8 rounds instead of 16 rounds - to balance security against time. We use an existing, open-source implementation of the Blowfish cipher as this is not the focus of our algorithm - it is simply the F function inside it [9].

In the Feistel cipher, a different key is used for each round and is generally a variation of the original inputted key. For the subkeys, instead of a simple shift left or right, we shifted inwards: the two outer bits moved to the middle for every round. Finally, the blocks are appended together to produce a double encrypted ciphertext.

Phase II: Uniform Encryption

The second step in the scheme further enciphers the already encrypted text once more into a series of left and right parentheses. The characters in the encrypted text produced by the first step are broken into binary and then replaced with the left and right parentheses. We do this to hide any patterns in the original ciphertext that can be used to break the cipher.

Decryption

To decrypt the ciphertext, the algorithm simply performs the encryption steps in reverse order. First, the parenthesis is converted back into the ciphertext character. Then, the Feistel cipher algorithm runs with the subkeys in reverse order. Since the algorithm is symmetric, the same key is used to encrypt and decrypt.

Pseudocode

Our encryption scheme ParEncrypt can be summarized as a pseudocode as follows:

1. The *input* to the algorithm is a *16-char key* and the *plaintext* to encrypt.
2. The text is then split into *16-char blocks* and incomplete blocks are padded.
3. Each block is passed into the *Feistel cipher*, which permutes for *8 rounds*.

The *F function*, which is the encryption scheme used for each round, is the Blowfish cipher. *Subkeys* are the original key shifted in for each round.

4. The blocks are then appended together and passed into the *second encryption method*, which converts the ciphered text into *parentheses*.
5. The *output* is the *doubly encrypted, uniform ciphertext*.

Results

Our experiments record the execution time of encrypting and decrypting various sizes of plaintext and ciphertext using ParEncrypt. We compare our runtimes to those of existing algorithms. Figure 2 shows a sample run of our scheme.

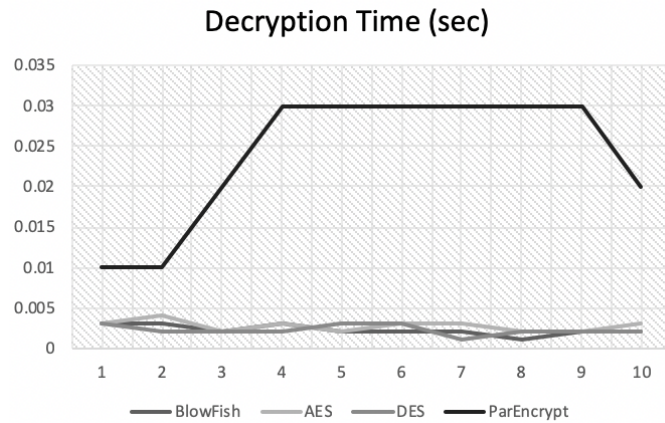


Figure 4. Decryption Runtime of ParEncrypt vs. Existing Schemes

The figures above illustrate the disparities in encryption and decryption time between our encryption scheme and other existing algorithms. As illustrated by the graphs, our encryption scheme performs much slower than Blowfish, AES, and DES, as expected. Our scheme performs a double encryption, whereas the other three simply encrypt once. There is a trade-off between security and performance, and our scheme prioritizes security.

Conclusion

In this work, we propose a novel symmetric encryption scheme that cascades two conventional encryption approaches in two phases: The Feistel cipher and substitution cipher. Our algorithm is simple, yet powerful and outperforms the security provided by conventional encryption schemes that we compare with. The unavoidable trade-off remains still that ParEncrypt performs slower than any one-phase counterpart, as expected. Yet another benefit of ParEncrypt is that it offers a significant level of compression.

As part of future work, we plan to make a comprehensive comparison of ParEncrypt with benchmark encryption tools such as AES and DES to reveal its security level among the others. Additionally, we plan to elaborate ParEncrypt's fringe benefit: lossless compression. Though not perfect, our scheme does provide a level of compression which serves as an added benefit. We will explore ways to improve this level of compression to make it comparable to other tools.

We also plan on running our encryption algorithm on standard corpora from different source languages so as to investigate language specific discrepancies. Moreover, we plan on expanding our implementation by replacing each of the two phases with various alternatives, such as DES or AES for phase one, and transposition cipher for phase 2, etc.

Acknowledgements

The authors would like to thank to students Teena Jagan and Rohit Ravi for their help in the initial design of this project.

References

- D. Kahil, M. A. Lebdeh, M. S. E. Dine and A. E. Rafhi, "Innovation of a secured transmitter/ receiver chain by creating a new encryption algorithm," 2017 Sensors Networks Smart and Emerging Technologies (SENSET), Beirut, 2017, pp. 1-3. doi: 10.1109/SENSET.2017.8125037
- D. H. Kurniawan and R. Munir, "Double Chaining Algorithm: A secure symmetric-key encryption algorithm," 2016 International Conference On Advanced Informatics: Concepts, Theory And Application (ICAICTA), George Town, 2016, pp. 1-6. doi: 10.1109/ICAICTA.2016.7803097
- Lewi, K., & Wu, D. J. (2016, October). Order-revealing encryption: New constructions, applications, and lower bounds. In Proceedings of the 2016 ACM SIGSAC Conference on Computer and Communications Security (pp. 1167-1178). ACM.

- Zhang, W., Lü, X., & Li, H. (2010). Efficient broadcast encryption scheme based on number theory research unit. *Wuhan University Journal of Natural Sciences*, 15(3), 247–250. <https://doi.org/10.1007/s11859-010-0313-7>
- Negi, A., & Goyal, A. (2018). Optimizing Fully Homomorphic Encryption Algorithm using RSA and Diffie-Hellman Approach in Cloud Computing.
- J. Choi and Y. Kim, "An improved LEA block encryption algorithm to prevent side-channel attack in the IoT system," 2016 Asia-Pacific Signal and Information Processing Association Annual Summit and Conference (APSIPA), Jeju, 2016, pp. 1-4.
- Kumar, N. S., Lakshmi, G. R., & Balamurugan, B. (2015). Enhanced attribute based encryption for cloud computing. *Procedia Computer Science*, 46, 689-696.
- M. Xin, "A Mixed Encryption Algorithm Used in Internet of Things Security Transmission System," 2015 International Conference on Cyber-Enabled Distributed Computing and Knowledge Discovery, Xi'an, 2015, pp. 62-65. doi: 10.1109/CyberC.2015.9
- "Blowfish," Blowfish on GitHub. Michael Gilfix, Jun-2018. <https://gist.github.com/eigenein/a56ce4d572484a582e14>

Author Information

Haneya Khan

University of Texas at Dallas
Department of Computer Science
800 W Campbell Rd.
Richardson, TX 75080 USA
Contact E-mail: hkk150030@utdallas.edu

Asim Siddiqui

University of Texas at Dallas
Department of Computer Science
800 W Campbell Rd.
Richardson, TX 75080 USA

Fariha Islam

University of Texas at Dallas
Department of Computer Science
800 W Campbell Rd.
Richardson, TX 75080 USA

Elham Hamid

University of Texas at Dallas
Department of Computer Science
800 W Campbell Rd.
Richardson, TX 75080 USA

Ebru Celikel Cankaya

University of Texas at Dallas
Department of Computer Science
800 W Campbell Rd.
Richardson, TX 75080 USA

Impact of the Chemical Mutagenesis on Biomass and Productivity of some Micro Green Algae

Rasha Kareem Mohammed AL-SAEDI
Baghdad University

Ali Muaed NAJEM
Baghdad University

Ibrahim Jabber ABED
Baghdad University

Abstract: Mutant microalgae *Nanochloropsis oculata*. and *Chlorella* sp included in this study exhibited a high potential for energetic lipid storage as well as high growth rates comparing to the un mutants (standard), therefore, considered promising candidates for advancing the biofuel production. In addition to the exponentially increase in biomass carbohydrates, proteins and fatty acids remarkably increased after these strains were mutated by ethyl methane sulphonate (EMS), while total lipids decreased. Biochemical compositional analysis was carried out by using gas chromatography to find out concentrations of five major fatty acids: Palmitic acid, Lenolenic acid, Stearic acid, Oleic acid and Linoleic acid. In mutant *N. oculata* and *Chlorella* sp. Lenolenic acid is the fatty acid with high percentage (11.7 and 4.8 %) respectively compared with un- mutant (0.241 and 1.824) %. Five fatty acids were selected to assess effect of the mutation, which revealed that initial concentrations of all the fatty acids before the mutation were multiplied about 48, 16, 14, 7 and 6 fold of Lenolenic, Palmitic, Oleic, Stearic and Linoleic acids respectively in *N. oculata*, while slightly changes occurred in the concentrations of *Chlorella* sp fatty acids.

Keywords: EMS, Microalgae, Biofuel, Mutant

Introduction

There are many potential advantages of using biofuel, the emissions from such fuels are far lower than those of fossil fuels and biofuels crucially biodegrade much faster also non-toxic comparing to the catastrophic impacts on atmosphere and biosphere result from biofuel are far less than the horror accompanies from continuing urge of using fossil fuel, although one drawback needs work in fossil fuels is that burning it releases nitrogen oxide into the air (Muto et al., 2013). Micro green algae are known as the oldest life forms, they are the large and diverse group of aquatic organisms that lack the complex cell structures found in higher plants, moreover the algae presence and populated approximately all types of environments, some species thriving in freshwater, others in saline conditions, hot springs, and seawater (Brennan and Owende, 2010). The current depletion of world oil resources and pollution of our planet create a dilemma intriguing minds of scientists to confront this dilemma, therefore, efforts have been made to produce an ecologically pure fuel based on renewable bioresources (biofuel) and the treatments of biological waste through anaerobic digestion have many benefits; biogas leads not only to cleaner and healthier environment but also produces a renewable energy sources such as methane (Balat and Balat, 2009).

Micro-algae have received considerable interest as a potential feedstock for biofuel production because they have higher CO₂ fixation rates than terrestrial plants and can thus utilize CO₂ from flue gas to produce biomass depending on the species and cultivation conditions, they can produce useful quantities of polysaccharides and triacylglycerides, which are raw materials for producing bioethanol and biodiesel (Chien-Ya et al., 2011). Microalgae synthesize fatty acids as building blocks to form various lipid compounds, such as polarized

- This is an Open Access article distributed under the terms of the Creative Commons Attribution-NonCommercial 4.0 Unported License, permitting all non-commercial use, distribution, and reproduction in any medium, provided the original work is properly cited.

- Selection and peer-review under responsibility of the Organizing Committee of the Conference

structural and functional lipid such as phospholipid and glycolipid together with neutral lipids such as monoglyceride, diglyceride, and triglyceride, free fatty acid, hydrocarbon and pigment. Limited polarized lipid is located in organelle membrane within the cell, such as lactide in the chloroplast.

Triglyceride is a neutral lipid stored in the vacuole inside the cell. High C18:0 and C18:1 content inside microalgae is the precondition in biodiesel production for their oxidative stability and high adaptation ability potential for industrial-scale production (Olofsson et al., 2012). C16:0 is also proposed as the suitable fatty acid in renewable biodiesel production. Both are rarely found in *Nannochloropsis* sp. cells, these microalgae species are become a potential biofuel material species. Researchers on microalgae mutated by ethyl methane sulfonate are still rare. Chemical mutagens induced mutagenesis may be particularly biased in some cases, as they may increase the mutation levels, particularly in some genomic regions with high GC-content. It is expected that some mutagenesis experiments may not result in desired phenotypes due to limited mutant pools. Therefore, it is important to understand the biases before selection of a chemical mutagen for mutagenesis experiments. Ethyl methanesulfonate (EMS) is another popular chemical mutagen that has been proven to be effective and efficient in mutagenesis (Jabeen and Mirza, 2004).

Successful mutagenesis has been performed using EMS to create algal mutants with increased lipid accumulation, for example *Chlamydomonas reinhardtii* was randomly mutagenized by EMS for enhanced lipid production (Chaturvedi. and Fujita, 2006). Chemical mutagenesis has long been employed to improve the biomass of microalgae lipid productivity such as *Nannochloropsis* sp. and *Chlorella* sp. (Doan and Obbard, 2012; Shin et al., 2016). It has been demonstrated that the attenuation of the light-harvesting property by mutation could improve the photosynthesis efficiency of microalgae by decreasing the cell shading effect, allowing an increase in biomass and lipid productivities (Polle et al., 2002). Chemical mutagenesis method using ethyl methane sulphonate (EMS) which was used in this research is relatively new and complicated. This study, aims to demonstrate impact of chemical mutagenesis to generate mutant in two water surface- floating microalgae to identify proximate cell composition (carbohydrate, fatty acid, and protein) in *Nannochloropsis oculata*. and *Chlorella* sp.

Materials and Methods

Isolation and Purification of Algae

The microalgae samples were collected from the water canals around the University of Baghdad- Al-Jadriah, uni-algal cultures of *Chlorella* sp and *N. oculata* were obtained using serial dilution method with 1ml of sample inoculated into 9 ml of Chu-10 nutrient solution. The procedures were repeated with microscopic examination until one species of both microalgae were obtained.

Chu-10 Media Preparation

Stock solution (250 mL) from the following salts were prepared: MgSO₄.7H₂O, K₂HPO₄, NaNO₃, CaCl₂, FeCl₃, EDTA-Na, NaCl, Na₂CO₃, MnCl₂.4H₂O, (NH₄)₆Mo₇O₂₄.4H₂O, ZnSO₄.7H₂O, CuSO₄.5H₂O, CoCl₂.6H₂O, H₃BO₃, and Na₂SiO₃. 2.5 ml of each stock were taken and completed the volume to one liter of distilled water according to Kassim and Salman (1999), while the medium was autoclaved and used to culture *Chlorella* sp. and *N. oculata*

Chemical Mutagenesis

Preparation of Ethyl Methane Sulphonate (EMS)

EMS with 0.5 % (v/v) in 100 ml phosphate buffer solution at (pH7) was prepared (Rasha and Kadium, 2017).

EMS Mutagenesis

Cell suspensions of both microalgae *N. oculata* and *Chlorella* sp. in exponential phase at 10⁷ cells/ml were subjected to random mutagenesis via exposure to EMS concentration (Himedia-India) 0.5% for 1 hour in darkness at room temperature with vigorous agitation at 300 rpm. Following incubation, treated cultures were

centrifuged at 8000 rpm for 10 min., pellets were then washed twice with the autoclaved solution of 10% (w/v) sodium thiosulfate to remove excess EMS. Micro algae were re-suspended into 10 ml sterile Chu-10 medium and kept in darkness overnight to grow for further selection. After three weeks incubation at a temperature 25 °C (Kawaroe et al., 2015).

Estimation of Micro Algal Biomass

The growth rate was estimated according to Mackinney, G. (1941) as an indirect method for chlorophyll estimation. The pigments can be completely extractable in acetone and exhibit characteristic absorbance at 663 nm wavelength. 10 ml of microalgae cultures were centrifuged at 5000 rpm for 10 minutes. The pellet was re-suspended in 80% acetone and vortexed thoroughly. The tubes were incubated in water bath at 60 °C in dark for 1 hr. with occasional shaking. After 1 hr. incubation, the suspension was centrifuged again and the supernatant was stored in dark. The procedure was repeated for the pellet to ensure complete chlorophyll extraction. An absorbance of the supernatant was read at 663 nm in UV-Vis spectrophotometer using 80% acetone as blank. The growth was estimated spectrophotometrically every 2 days, and the curve was plotted using the absorbance versus time.

Evaluation Effects of the Mutation on Major Biochemical Composition

Carbohydrates Extraction

The carbohydrates were extracted using anthrone method Raunkjær, et al. (1994), which is a simple colorimetric method based on a reaction between the carbohydrates and anthrone reagent developing a green color. A solution with 0.1 of anthrone was prepared in 75% H₂SO₄; the reagent must be prepared freshly at the day of measurement. Glucose standard curve was prepared with final concentration 100 mg/L. 100 mg of freeze-dried algal biomass was weighed and transferred to COD tube and placed on ice, 2 mL of 75% H₂SO₄ were added to the samples and vortexed thoroughly to mix the acid and the biomass.

Anthrone reagent was added to all the tubes including glucose tubes (4 mL) and vortexed again to ensure the mixing of the reagent with the carbohydrates. Tubes were placed in water bath 100 °C for 15 minutes and then cooled down to room temperature. The absorbance was measured at 625 nm for all the tubes and calibration curve was drawn from the glucose concentration and the total carbohydrates were obtained using this calibration curve.

Lipids Extraction

The lipids were extracted according to Bligh, (1959). For 1 gm of a dried algal sample, 2 mL of methanol and 1 mL of chloroform were added, the mixture was kept at room temperature for 24 hours, and the mixture was then vortexed for 2 minutes. 1 ml of chloroform was added again and mixed well. Then 1.8 ml of distilled water was added. The mixture was vortexed again for 2 minutes followed by centrifugation for 10 min at 2000 rpm. Upper layer was discarded and the lower layer was filtered with Whatman No. 1 filter paper. The vial was weighed and recorded as (weight 1). The vial was put in a water bath until evaporation; the vial was weighed again and expressed as (weight 2). The lipid yield was calculated as w_2-w_1 and the result was expressed as % dcw gm/ L.

Results and Discussion

Estimation of Microalgal Biomass

Optical density is used as a convenient indirect measurement of biomass concentration in microalgal cell suspensions. The absorbance of light by a suspension can be related directly to chlorophyll concentration using a suitable standard curve. However, inaccuracies can be introduced when the pigment content of the cells changes. Mutant *Chlorella* sp. and *N. oculata* reached stationary phase after 17 day comparing to the un-mutated culturing in Chu-10 media under light intensity 167.48 $\mu\text{E m}^{-2}\text{s}^{-1}$ and temperature (24±2) and initial pH 7 with continuous shaking. The growth curve is shown in (Figures 1, 2, 3, 4). Under the pre mentioned culture conditions and during 17 day of culturing pigment content of the un- mutated *Chlorella* sp. varied between 0.055 and 1.329 g/l while mutated *Chlorella* sp. varied between 0.076 and 1.462 g/l. In un-mutated *N. oculata* pigment

content varied between 0.094 and 0.848 g/l, while 0.024 and 0.977 g/l in the mutated. The highest O.D₆₆₃ reading was in 17 days about 1.462 g/l in the mutated *Chlorella sp.* while the highest O.D₆₆₃ reading of mutated *N. oculata* was 0.977g/l as shown in Table 1.

Evaluation Effects of the Mutation on Major Biochemical Composition

As with biomass, lipid content was also measured, lipid content decreased after mutation in both algae. Protein concentration in mutated *N. oculata* was higher than that in mutated *Chlorella sp.* and un mutated *N. oculata*, in bottom line production of protein decreased after mutation in *C. kesslari* while increased in *N. oculata* Highest carbohydrates contents occurred in mutated *Chlorella sp.* comparing to its concentration in mutated *N. oculata* Mutation caused increased in carbohydrates in both algae. A summary production of lipids and carbohydrates increased after mutation in *Chlorella sp.* except protein production decreased comparing to their production levels in *N. oculata* as shown in Figure 5.

Table 1. The growth rate of *N. oculata* and *Chlorella sp.* Cultivation before and after the treatment with 0.5% EMS.

| Duration Day | O.D ₆₆₃ reading for <i>Chlorella sp.</i> | | O.D ₆₆₃ reading for <i>N. oculata</i> | |
|--------------|---|-------|--|-------|
| | Before | After | Before | After |
| Zero | 0.055 | 0.076 | 0.094 | 0.024 |
| 2 | 0.102 | 0.124 | 0.053 | 0.127 |
| 4 | 0.068 | 0.185 | 0.053 | 0.158 |
| 6 | 0.091 | 0.226 | 0.093 | 0.143 |
| 8 | 0.272 | 0.42 | 0.187 | 0.234 |
| 10 | 0.359 | 0.483 | 0.233 | 0.209 |
| 12 | 0.595 | 0.866 | 0.63 | 0.458 |
| 17 | 1.32 | 1.462 | 0.848 | 0.977 |

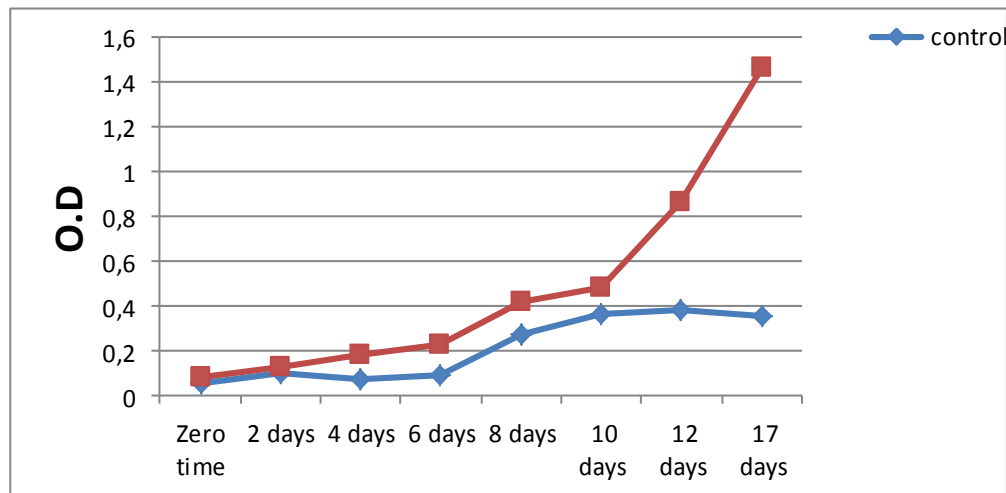


Figure 1. Variations in biomass between mutant *Chlorella sp.* and the control (un mutant)

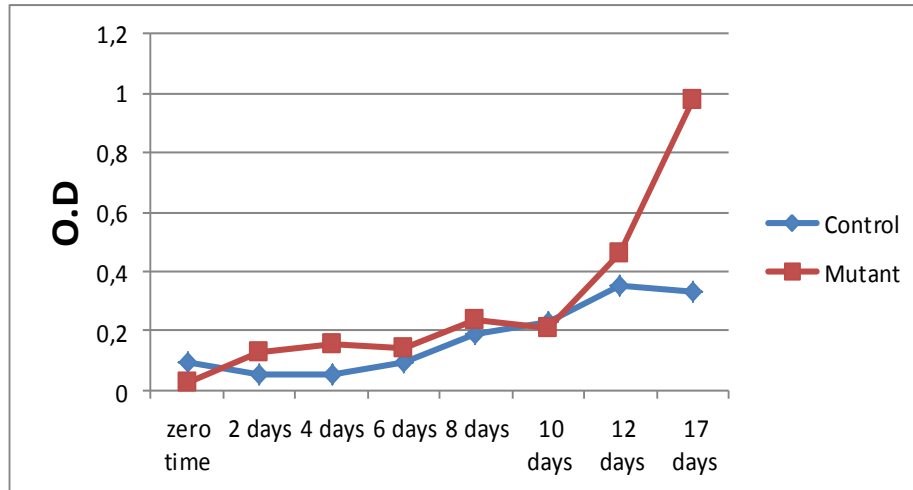


Figure 2. Variations in biomass between mutant *N. oculata* and the control (un mutant)

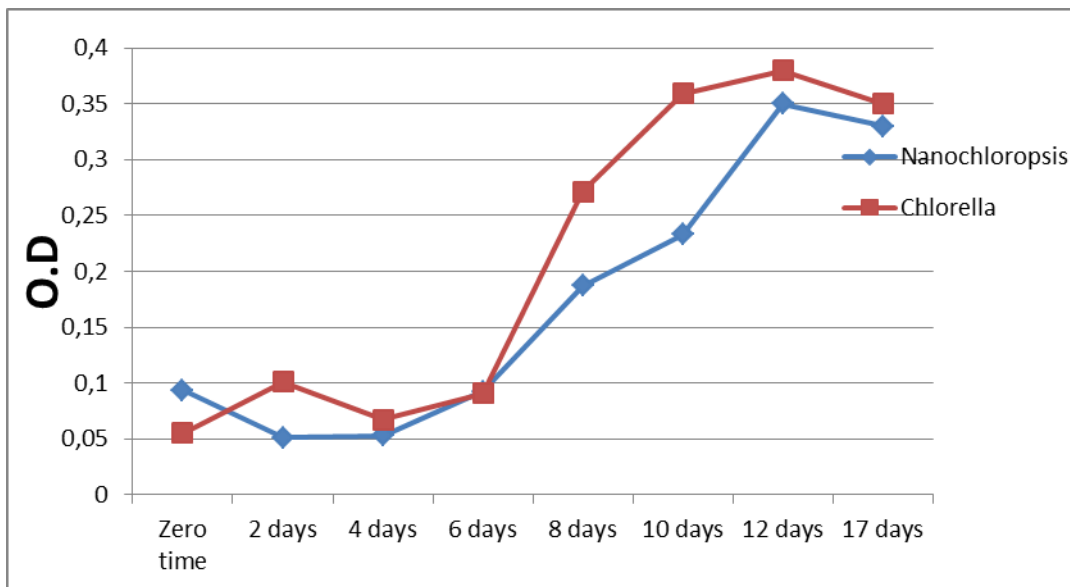


Figure 3. Variations in biomass between *N. oculata* and *Chlorella sp* before mutagenicity

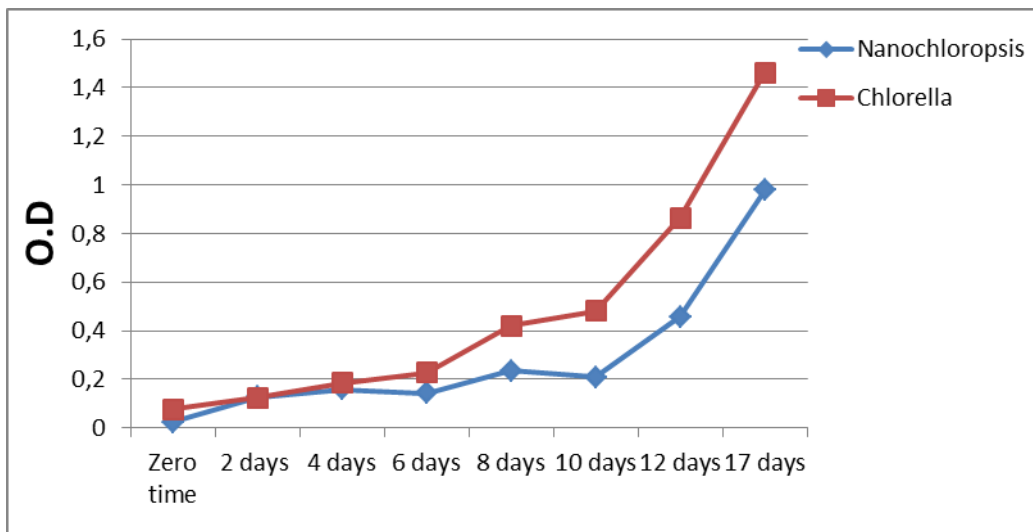


Figure 4. Variations in biomass between *N. oculata* and *Chlorella sp* after mutagenicity

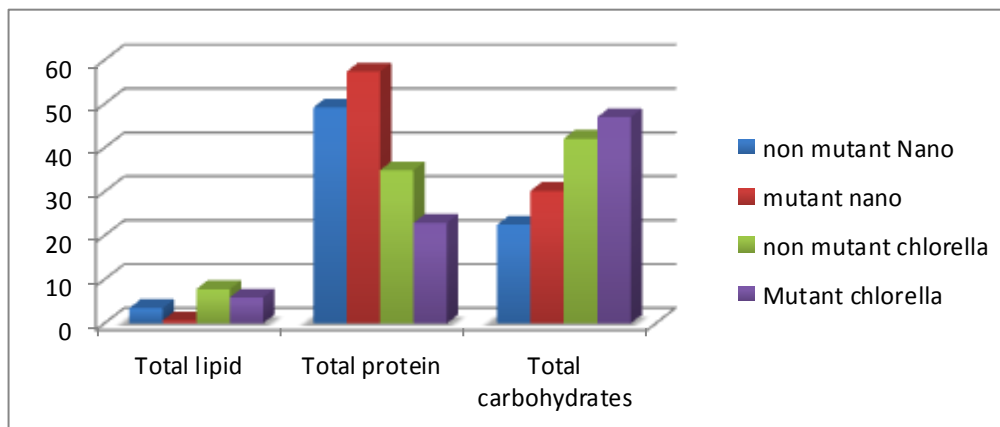


Figure 5. Variations in chemical composition (Lipids, proteins and carbohydrates) between mutant and un mutant *Chlorella sp* and *N. oculata*

Fatty Acids

Biochemical compositional analysis was carried out by using gas chromatography to find out concentrations of five major fatty acids: Palmitic acid, Lenolenic acid, Stearic acid, Oleic acid and Linoleic acid. In mutant *N. oculata* and *Chlorella sp*. Lenolenic acid is the fatty acid with high percentage (11.7 and 4.8 %) respectively compared with un- mutant (0.241 and 1.824) % as shown in table 2. These results showed that fatty acids increased in mutant algae 11 folds than un- mutant. In other hand mutant *N. oculata* showed increased in all fatty acids percentage that detected compared with mutant *Chlorella sp*. as shown in Table (2).

Table 2: Variations in fatty acids concentrations (%) between mutant and the control (un -mutant) *Chlorella sp* and *N. oculata*.

| Algae | Palmitic acid | Lenolenic acid | Stearic acid | Oleic acid | Linoleic acid |
|--|---------------|----------------|--------------|------------|---------------|
| Un-mutant <i>Nanochloropsis</i> | 0.19 | 0.241 | 1.08 | 0.29 | 1.03 |
| Mutant <i>Nanochloropsis</i> | 3.1 | 11.7 | 8.17 | 4.13 | 6.01 |
| Un-mutant <i>C. kesslari</i> | 0.574 | 1.824 | 1.04 | 0.621 | 0.94 |
| mutant <i>C. kesslari</i> | 0.61 | 4.8 | 0.83 | 0.437 | 0.82 |

Discussion

Ong et al. (2010) stated that *C. kesslari* mutated with 0.1 M EMS and cultivated in higher temperature from the original species has higher specific growth rate, this came along with the results of this study, on the other hand *Nannochloropsis sp.* treated with the same EMS concentration gave higher growth rate value comparing with the un mutated. Also, higher lipid productivity of the mutated species cultivated with high temperature is higher compared to its original form. Results range between 0.6 - 1.2 g/l for mutated *Chlorella sp.* with 0.1 M EMS and 0.4 - 0.9 g/l for un mutated with 40°C cultivation temperature.

A few notable studies in this scientific field such as Chaturvedi and Fujita (2006) which included EPA fatty acid compound of mutated *Nannochloropsis sp.*, also Doan and Obbard (2012) figured out that lipid compound of *Nannochloropsis* increased after the mutation From another research conducted by Chaturvedi and Fujita (2006), it is proven that EPA type fatty acid can be boosted by applying mutagenesis on *Nannochloropsis oculata*. Research by Doan and Obbard (2012) that tested lipid content increase of *Nannochloropsis sp.*, mutated microalgae species can produce more fatty acid compared to its original state, both in exponential and stationery phase.

In this research EMS used to mutagenize *Chlorella sp.* and *N. oculata* cells because it is a powerful and easy technique to generate a number of mutants, and we can create a number of candidate mutants that are from various types of random mutations by modulating AT to G-C in DNAs on microalgae genome as described in many successful reports in several microorganisms (Kim et al., 2006; Sandesh et al., 2008; Lee et al., 2014). For instance, *Chlamydomonas reinhardtii* mutants (ADP glucose pyrophosphorylase mutated) exhibited 10-fold increase of TAG accumulation compared to wild type by using EMS mutagenesis (Radakovits et al., 2010 and work et al., 2010).

Other EMS application was also used in other eukaryotic organism such as *Saccharomyces cerevisiae*, *Cyclotella sp.* and *Arthrospira platensis* (cyanobacterium) to find a higher bioethanol producer (Mobini-Dehkordi et al., 2008). Fatty acids (FAs) are one of the primary metabolites of microalgae, which enrich their utility both in the form of food and fuels. Palmitic acid (C16:0) and oleic acid (C18:1n9c) were found to be dominant among the members of Cyanophyceae whereas members of Chlorophyceae were rich in palmitic acid (C16:0), oleic acid (C18:1n9c) and linoleic acid (C18:2n6). (Sahu et al., 2013). *Nannochloropsis sp.* have attracted sustained interest from algal biofuels researchers owing to their rapid growth, high amounts of triacylglycerol (TAG) and high-value polyunsaturated fatty acid (FA) and their successful cultivation at large scale using natural sunlight by multiple institutes and companies (Ajjawi et al., 2017; Wei H et al., 2017; Zienkiewicz et al., 2017).

References

- Ajjawi, I., Verruto, J., Aqui, M., Soriaga, L. B., Coppersmith, J., & Kwok, K., et al. (2017, Jun 19). Lipid production in *Nannochloropsis gaditana* is doubled by decreasing expression of a single transcriptional regulator. *National Biotechnology*. 35, 647–652.
- Balat, M., & Balat, H. (2009, May19). Biogas as a renewable energy source – a review. *Journal of Energy Sources, Part A: Recovery, Utilization, and Environmental Effects*, 31, 1280-1293.
- Bligh, E.G., & Dyer, W.J. (1959, August). A rapid method of total lipid extraction and purification. *Canadian Journal of Biochemistry and Physiology*, 37(8):911-917.
- Brennan, L., & Owende, P. (2010). Biofuels from microalgae—A review of technologies for production, processing, and extractions of biofuels and co-products. *Renewable and Sustainable Energy Review*, 14,557–577.
- Chaturvedi, R., & Fujita, Y. (2006, September 14). Isolation of enhanced eicosapentaenoic acid producing mutants of *Nannochloropsis oculata* ST-6 using ethyl methane sulfonate induced mutagenesis techniques and their characterization at mRNA transcript level. *Phycological Research*, 54(3),208- 219.
- Chien-Ya, K., Sheng-Yi, C., Huang, T., Dai, L., Hsu, L., & Lin, C. (2012, January 24). Ability of a mutant strain of the microalgae *Chlorella sp.* to capture carbon dioxide for biogas upgrading. *Journal of Applied Energy* 93,176-183. ELSEVIER.
- Doan, T.T.Y., & Obbard, J.P. (2012). Enhanced intracellular lipid in *Nannochloropsis sp.* via random mutagenesis and flow cytometric cell sorting. *Algal Research* 1, 17–21.
- Jabeen, N., & Mirza, B. (2004). Ethyl methane sulphonate induces morphological mutations in *Casipicum annum*. *International Journal of Agriculture and Biology*, 6 (2), 340-345.
- Kassim, T., Al-Saadi, H., & Salman, N. (1999). Production of some phyto-and zooplankton and their use as live food for fish larva. *Iraqi Journal of Agriculture and Processing*, 2,188-201.
- Kawaroe, M., Agus, O.S., Junkwan, H., & Dina, A. (2015). Chemical mutagenesis of microalgae *Nannochloropsis sp.* using EMS (ethyl Methanesulfonate). *British Journal of Applied Science & Technology* 8(5), 494-505.
- Kim, Y., Schumaker, K.S., & Zhu, J.K. (2006). EMS mutagenesis of *Arabidopsis* methods. *Mol. Biol.*, 323(6), 101–3.
- Lee, B., Choi, G.G., Choi, Y.E., Sung, M., Park, M. S., & Yang, J .W. (2014, June). Enhancement of lipid productivity by ethyl methane sulfonate-mediated random mutagenesis and proteomic analysis in *Chlamydomonas reinhardtii*. *Korean Journal of Chemical Engineering*, 31(6), 1036–1042.
- Mackinney G (1941, March 13). Absorption of light by chlorophyll solutions. *Journal of biological Chemistry* 140 (2):315-322.
- Mendoza, H., de la Jara, A., Freijanes, K., Carmona, L., Ramos, A.A., de Sousa Duarte, V., & Serafim Varela, J.C. (2008, October 15). Characterization of *Dunaliella salina* strains by flow cytometry: a new approach to select carotenoid hyperproducing strains. *Electronic Journal of Biotechnology*, 11(4), 1-13.
- Mobini-Dehkordi, M., Nahvi, I., Zarkesh-Esfahani, H., Ghaedi, K., Tavassoli, M., & Akada, R. (2008). Isolation of a novel mutant strain of *Saccharomyces cerevisiae* by an ethyl methane sulfonate-induced mutagenesis approach as a high producer of bioethanol. *Journal of Bioscience and Bioengineering*, 105(4), 403–408.

- Muto, M., Fukuda, Y., Nemoto, M., Yoshino, T., Matsunaga, T., & Tanaka, T. (2013, February). Establishment of a genetic transformation system for the marine pennate diatom *Fistulifera* sp. strain JPCC DA0580-a high triglyceride producer. *Mar. Biotechnology*, 15(1), 48–55.
- Olofsson, M., Lamela, T., Nilsson, E., Bergé, J.P., Pino, V., Uronen, P., & Legrand, C. (2012, May 21). Seasonal variation of lipids and fatty acids of the microalgae *Nannochloropsis oculata* grown in outdoor large-scale photobioreactors. *Energies*, 5, 1577-1592.
- Ong, S.C., Kao, C.Y., Chiu, S.Y., Tsai, M.T., & Lin, C.S. (2010, April). Characterization of the thermaltolerant mutants of *Chlorella* sp. with high growth rate and application in outdoor photobioreactor cultivation. *Bioresearch Technology* 101, 2880–2883.
- Polle, J.E., Kanakagiri, S., Jin, E., Masuda, T., & Melis, A. (2002, December). Truncated chlorophyll antenna size of the photosystems—A practical method to improve microalgal productivity and hydrogen production in mass culture. *International Journal of Hydrogen. Energy* 27(11-12), 1257–1264.
- Radakovits, R., Jinkerson, R.E., Darzins, A., & Posewitz, M.C. (2010, April). Genetic engineering of algae for enhanced biofuel production. *Eukaryot. Cell*, 9(40), 486–501.
- Rasha, K.M., & Kadium, M. I. (2017, March). Cytological effect of mutagenic agents and NaCl on mitotic division in two Iraqi rice (*Oryza sativa* L.) genotypes. *Journal of Al-Nahrain University* 20 (1), 116-122.
- Raunkjær, K., Hvitved-Jacobsen, T., & Nielsen, P.H. (1994, February). Measurement of pools of protein, carbohydrate and lipid in domestic wastewater. *Water research*. 28(2), 251-262.
- Sahu, A., Pancha, I., Jain, D., Paliwal, C., Ghosh, T., Patidar, S., Bhattacharya, S., & Mishra, S. (2013, February 28). Fatty acids as biomarkers of microalgae. *Phytochemistry*. 89:53-8.
- Sandesh, B., Kamath, R., Vidhyavathi, R. S., & Ravishankar, G.A. (2008, December). Enhancement of carotenoids by mutation and stress induced carotenogenic genes in *Haematococcus pluvialis* mutants. *Bioresource Technology*, 99(18), 8667 –8673.
- Shin, W.S., Lee, B., Jeong, B.R., Chang, Y.K., & Kwon, J.H. (2016). Truncated light-harvesting chlorophyll antenna size in *Chlorella vulgaris* improves biomass productivity. *Journal of Applied Phycology* 28, 3193–3202.
- Wei, H., Shi, Y., Ma, X., Pan, Y., Hu, H., Li, Y. et al. (2017, July). A type-I diacylglycerol acyltransferase modulates triacylglycerol biosynthesis and fatty acid composition in the oleaginous microalga, *Nannochloropsis oceanica*. *Biotechnology Biofuels* 10:174.
- Work, V.H., Radakovits, R., Jinkerson, R.E., Meuser, J.E., Elliott, L.G., Vinyard, D.J., Laurens, L.M.L., Dismukes, G.C., & Posewitz, M.C. (2010, August). Increased lipid accumulation in the *Chlamydomonas reinhardtii* sta7-10 starchless isoamylase mutant and increased carbohydrate synthesis in complemented strains. *Eukaryot Cell* 9 (8), 1251–61.
- Zienkiewicz, K., Zienkiewicz, A., Poliner, E., Du, Z. Y., Vollheyde, K., Herrfurth, C., et al. (2017, January 3). *Nannochloropsis*, a rich source of diacylglycerol acyltransferases for engineering of triacylglycerol content in different hosts. *Biotechnology for Biofuels* 10:8.

Author information

Rasha Kareem Mohammed Al-Saedi
Baghdad University
Al-Jadriya, Baghdad, Iraq
Contact E-mail: rasha.alsaedi80@gmail.com

Ali Muaed Najem
Baghdad University
Al-Jadriya, Baghdad, Iraq

Ibrahim Jabber Abed
Baghdad University
Al-Jadriya, Baghdad, Iraq

Synthesis and Characterization of Novel 1-(Morpholin-4-yl-methyl)-3-alkyl(aryl)-4-[3-ethoxy-4-(2-furylcarbonyloxy)-benzylidenamino]-4,5-dihydro-1*H*-1,2,4-triazol-5-ones

Onur AKYILDIRIM

Kafkas University

Haydar YUKSEK

Kafkas University

Sevda MANAP

Kafkas University

Abstract: In this study, six novel 1-(morpholin-4-yl-methyl)-3-alkyl(aryl)-4-[3-ethoxy-4-(2-furylcarbonyloxy)-benzylidenamino]-4,5-dihydro-1*H*-1,2,4-triazol-5-one (2) compounds were synthesized from a reaction of type 1 compounds with formaldehyde and morpholine. The finally part contains that synthesis of new compounds. The structures of these novel compounds were characterized by using, IR, ¹H NMR and ¹³C NMR spectral data.

Keywords: Schiff bases, Mannich bases, Synthesis, Characterization

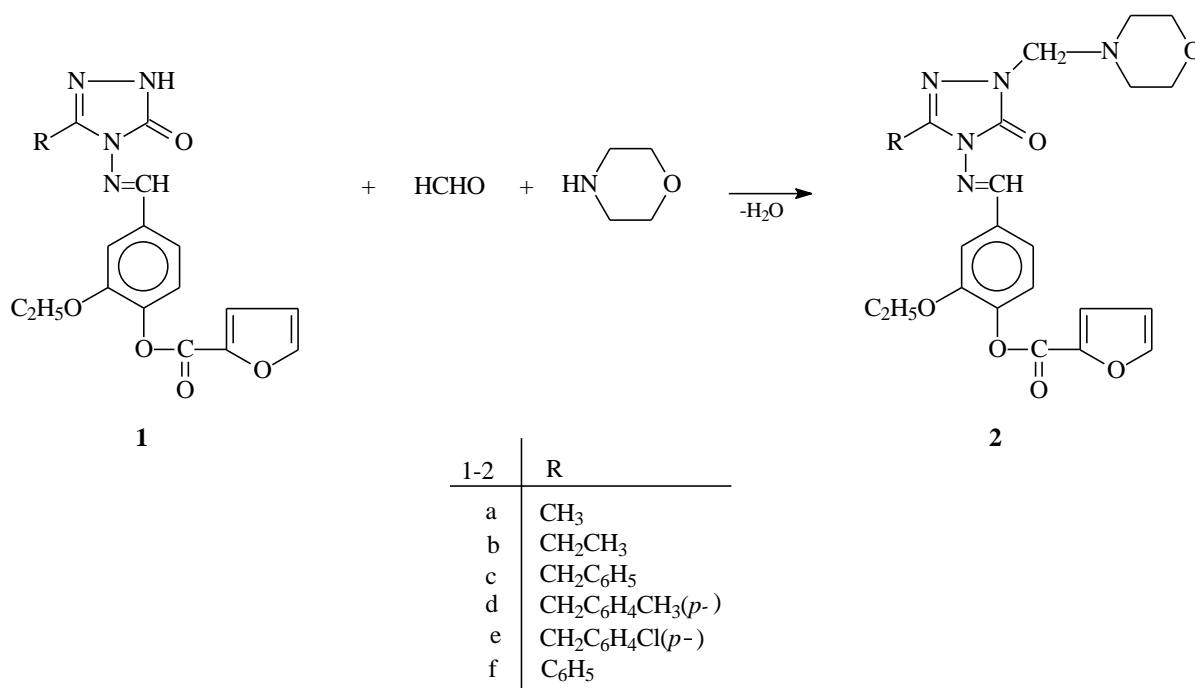
Introduction

1,2,4-triazole nucleus is one of the active ingredients found in many standard drugs and is known to increase the pharmacological activity of the molecules. Compounds containing the morpholine moiety are effective in contributing to the net biological activity of a system. It has been found that some of the compounds having 1,2,4-triazole ring have antimicrobial activity against various microorganisms (Demirbas et al., 2009).

In a recent study, pyrimidine alkyne-derived Mannich bases were synthesized and their neuroprotection and neurotoxicity activities were evaluated (Triloknadh et al., 2018). Mannich bases containing 5-mercapto-1,2,4-triazole derivative were synthesized and screened for a panel of 60 cell lines derived from seven cancer types, such as lung, colon, melanoma, renal, ovarian, CNS and leukemia, for their anticancer activity (Holla et al., 2003). Some Mannich bases carrying morpholine fragment showed good anti-inflammatory and analgesic activity (Nithinchandra et al., 2012). The antimicrobial activities of the triazole compounds containing Mannich base were screened; some have shown good or moderate activity against tested microorganisms (Bektaş et al., 2010). Anti-lipase and anti-urease activities of some 1,2,4-triazole derived compounds were investigated. Some of these have shown moderate to good lipase inhibitory effects (Bekircan et al., 2014). Some heterocyclic compounds containing morpholine showed good and moderate antimicrobial activity (Bayrak et al., 2009).

A series of compounds containing 1,2,4-triazole and morpholine were synthesized. Some of them showed significant anti-inflammatory activity. They have also been tested for analgesic activities and gastric ulceration studies. Important analgesic activity was detected in the compounds containing morpholine rings without causing any stomach irritation. Most of the compounds were found to exhibit moderate antimicrobial activity (Alam et al., 2012). Recently, some 1,2,4-triazole derived compounds have been tested for antimicrobial and anti-lipase inhibitory activities (Ozdemir et al., 2017).

In the present study, six novel compounds 1-(morpholin-4-yl-methyl)-3-alkyl(aryl)-4-[3-ethoxy-4-(2-furylcarbonyloxy)-benzylidenamino]-4,5-dihydro-1H-1,2,4-triazol-5-ones (2a-f) were synthesized from the reactions of 3-alkyl(aryl)-4-[3-ethoxy-4-(2-furylcarbonyloxy)-benzylidenamino]-4,5-dihydro-1H-1,2,4-triazol-5-ones (1a-f) with formaldehyde and morpholine (Scheme 1).



Scheme 1

Method

Chemicals and Apparatus

Chemical reagents and all solvents used in this study were purchased from Merck AG, Aldrich and Fluka. Melting point was determined in open glass capillary using a Stuart melting point SMP30 apparatus and is uncorrected. The IR spectra were obtained on an ALPHA-P BRUKER FT-IR spectrometer. ¹H and ¹³C NMR spectra were recorded in deuterated dimethyl sulfoxide with TMS as internal standard using a Bruker Ultrashield Plus Biospin spectrometer at 400 MHz and 100 MHz, respectively.

Synthesis of Compounds 2: The General Procedure

The corresponding compound 1 (0.01 mol) was dissolved in ethanol (40 mL) and was treated with morpholine (0.01 mol) and formaldehyde (37%) (0.02 mol) and then the mixture was refluxed for 2 h and filtered. The filtrate evaporated *in vacuo*, and the crude product was recrystallized from ethanol to afford compound 2.

Results and Discussion

1-(Morpholin-4-yl-methyl)-3-methyl-4-[3-ethoxy-4-(2-furylcarbonyloxy)-benzylidenamino]-4,5-dihydro-1H-1,2,4-triazol-5-one (2a)

Yield: 3.18 g (70%), m.p. 146 °C. IR (KBr, *v*, cm⁻¹): 1741, 1704 (C=O), 1573 (C=N), 1505, 1463 (C=C), 1298 (COO), 1159 (C-O, furan), 856 (1,4-disubstituted benzenoid ring) cm⁻¹; ¹H NMR (400MHz, DMSO-d₆): δ 1.24 (t, 3H, OCH₂CH₃, *J* = 6.80 Hz), 2.33 (s, 3H, CH₃), 2.59 (t, 4H, CH₂NCH₂, *J* = 4.40 Hz), 3.56 (t, 4H, CH₂OCH₂, *J* = 4.40 Hz), 4.14 (q, 2H, OCH₂CH₃, *J* = 6.80 Hz), 4.54 (s, 2H, NCH₂N), 6.82 (dd, 1H, Ar-H, *J* = 3.60, 1.60 Hz), 7.38 (d, 1H, Ar-H, *J* = 8.40 Hz), 7.50 (dd, 1H, Ar-H, *J* = 8.40, 1.60 Hz), 7.59 (dd, 1H, Ar-H, *J* = 3.60, 0.80 Hz), 7.64 (d, 1H, Ar-H, *J* = 1.60 Hz), 8.12 (dd, 1H, Ar-H, *J* = 1.60, 0.80 Hz), 9.71 (s, 1H, N=CH); ¹³C NMR (100 MHz, DMSO-d₆): δ 10.94 (CH₃), 14.38 (OCH₂CH₃), 49.97 (CH₂NCH₂), 64.34 (OCH₂CH₃), 65.93

(NCH₂N), 66.03 (CH₂OCH₂), 112.70 (CH), 112.76 (CH), 120.33 (CH), 120.70 (CH), 123.62 (CH), 132.56 (C), 141.46 (C), 142.66 (C), 148.75 (CH), 150.53 (arom-C), 143.15 (triazol C₃), 150.22 (triazol C₅), 153.63 (N=CH), 155.48 (COO).

1-(Morpholin-4-yl-methyl)-3-ethyl-4-[3-ethoxy-4-(2-furylcarbonyloxy)-benzylidenamino]-4,5-dihydro-1H-1,2,4-triazol-5-one (2b)

Yield: 3.90 g (83.33%), m.p. 142 °C. IR (KBr, ν , cm⁻¹): 1731, 1691 (C=O), 1575 (C=N), 1509, 1471 (C=C), 1282 (COO), 1165 (C-O, furan), 859 (1,4-disubstituted benzenoid ring) cm⁻¹; ¹H NMR (400MHz, DMSO-d₆): δ 1.22-1.26 (m, 6H, 2CH₂CH₃), 2.59 (t, 4H, CH₂NCH₂, J = 4.40 Hz), 2.73 (q, 2H, CH₂CH₃, J = 7.20 Hz), 3.57 (t, 4H, CH₂OCH₂, J = 4.40 Hz), 4.14 (q, 2H, OCH₂CH₃, J = 7.20 Hz), 4.55 (s, 2H, NCH₂N), 6.81 (dd, 1H, Ar-H, J = 3.60, 1.60 Hz), 7.38 (d, 1H, Ar-H, J = 8.40 Hz), 7.50 (dd, 1H, Ar-H, J = 8.40, 1.60 Hz), 7.60 (dd, 1H, Ar-H, J = 3.60, 0.80 Hz), 7.63 (d, 1H, Ar-H, J = 1.60 Hz), 8.12 (dd, 1H, Ar-H, J = 1.60, 0.80 Hz), 9.71 (s, 1H, N=CH); ¹³C NMR (100 MHz, DMSO-d₆): δ 9.99 (CH₂CH₃), 14.37 (OCH₂CH₃), 18.39 (CH₂CH₃), 49.99 (CH₂NCH₂), 64.32 (OCH₂CH₃), 65.98 (NCH₂N), 66.04 (CH₂OCH₂), 112.74 (2CH), 120.32 (CH), 120.59 (CH), 123.65 (CH), 132.60 (C), 141.45 (C), 142.67 (C), 148.75 (CH), 150.58 (arom-C), 146.86 (triazol C₃), 150.35 (triazol C₅), 153.60 (N=CH), 155.48 (COO).

1-(Morpholin-4-yl-methyl)-3-benzyl-4-[3-ethoxy-4-(2-furylcarbonyloxy)-benzylidenamino]-4,5-dihydro-1H-1,2,4-triazol-5-one (2c)

Yield: 3.75 g (70.68%), m.p. 105 °C. IR (KBr, ν , cm⁻¹): 1744, 1700 (C=O), 1573 (C=N), 1500, 1432 (C=C), 1290 (COO), 1159 (C-O, furan), 856 (1,4-disubstituted benzenoid ring), 772 and 694 (monosubstituted benzenoid ring) cm⁻¹; ¹H NMR (400MHz, DMSO-d₆): δ 1.26 (t, 3H, OCH₂CH₃, J = 6.80 Hz), 2.61 (t, 4H, CH₂NCH₂, J = 4.40 Hz), 3.58 (t, 4H, CH₂OCH₂, J = 4.40 Hz), 4.09 (s, 2H, CH₂Ph), 4.11 (q, 2H, OCH₂CH₃, J = 6.80 Hz), 4.59 (s, 2H, NCH₂N), 6.82 (dd, 1H, Ar-H, J = 3.60, 1.60 Hz), 7.24-7.25 (m, 1H, Ar-H), 7.31-7.37 (m, 5H, Ar-H), 7.42 (dd, 1H, Ar-H, J = 8.00, 1.60 Hz), 7.53 (d, 1H, Ar-H, J = 1.60 Hz), 7.59 (d, 1H, Ar-H, J = 3.20 Hz), 8.12 (dd, 1H, Ar-H, J = 1.60, 0.80 Hz), 9.67 (s, 1H, N=CH); ¹³C NMR (100 MHz, DMSO-d₆): δ 14.36 (OCH₂CH₃), 31.04 (CH₂Ph), 50.01 (CH₂NCH₂), 64.25 (OCH₂CH₃), 66.06 (NCH₂N + CH₂OCH₂), 111.84 (CH), 112.76 (CH), 120.33 (CH), 121.23 (CH), 123.60 (CH), 132.52 (C), 141.47 (C), 142.65 (C), 148.75 (CH), 150.52 (arom-C), 126.78 (CH), 128.51 (2CH), 128.66 (2CH), 135.72 (C₃-arom-C), 144.91 (triazol C₃), 150.24 (triazol C₅), 153.00 (N=CH), 155.47 (COO).

1-(Morpholin-4-yl-methyl)-3-p-methylbenzyl-4-[3-ethoxy-4-(2-furylcarbonyloxy)-benzylidenamino]-4,5-dihydro-1H-1,2,4-triazol-5-one (2d)

Yield: 4.15 g (76.27%), m.p. 154 °C. IR (KBr, ν , cm⁻¹): 1741, 1703 (C=O), 1573 (C=N), 1507, 1468 (C=C), 1291 (COO), 1156 (C-O, furan), 858 (1,4-disubstituted benzenoid ring) cm⁻¹; ¹H NMR (400MHz, DMSO-d₆): δ 1.26 (t, 3H, OCH₂CH₃, J = 6.80 Hz), 2.25 (s, 3H, PhCH₃), 2.60 (t, 4H, CH₂NCH₂, J = 4.40 Hz), 3.57 (t, 4H, CH₂OCH₂, J = 4.40 Hz), 4.06 (s, 2H, CH₂Ph), 4.12 (q, 2H, OCH₂CH₃, J = 6.80 Hz), 4.59 (s, 2H, NCH₂N), 6.82 (dd, 1H, Ar-H, J = 3.60, 1.60 Hz), 7.12 (d, 2H, Ar-H, J = 7.60 Hz), 7.23 (d, 2H, Ar-H, J = 8.00 Hz), 7.36 (d, 1H, Ar-H, J = 8.00 Hz), 7.42 (m, 1H, Ar-H), 7.53 (d, 1H, Ar-H, J = 1.60 Hz), 7.59 (dd, 1H, Ar-H, J = 3.60, 0.80 Hz), 8.12 (dd, 1H, Ar-H, J = 1.60, 0.80 Hz), 9.66 (s, 1H, N=CH); ¹³C NMR (100 MHz, DMSO-d₆): δ 14.37 (OCH₂CH₃), 20.57 (PhCH₃), 30.65 (CH₂Ph), 50.01 (CH₂NCH₂), 64.23 (OCH₂CH₃), 66.04 (NCH₂N + CH₂OCH₂), 111.83 (CH), 112.76 (CH), 120.34 (CH), 121.25 (CH), 123.61 (CH), 132.59 (C), 141.47 (C), 142.66 (C), 148.75 (CH), 150.52 (arom-C), 128.49 (2CH), 129.00 (2CH), 132.54 (C), 135.87 (C₃-arom-C), 146.06 (triazol C₃), 150.24 (triazol C₅), 152.97 (N=CH), 155.48 (COO).

1-(Morpholin-4-yl-methyl)-3-p-chlorobenzyl-4-[3-ethoxy-4-(2-furylcarbonyloxy)-benzylidenamino]-4,5-dihydro-1H-1,2,4-triazol-5-one (2e)

Yield: 4.24 g (75%), m.p. 129 °C. IR (KBr, ν , cm⁻¹): 1735, 1704 (C=O), 1595 (C=N), 1493, 1469 (C=C), 1297 (COO), 1161 (C-O, furan), 853 (1,4-disubstituted benzenoid ring) cm⁻¹; ¹H NMR (400MHz, DMSO-d₆): δ 1.26 (t, 3H, OCH₂CH₃, J = 6.80 Hz), 2.60 (t, 4H, CH₂NCH₂, J = 4.40 Hz), 3.57 (t, 4H, CH₂OCH₂, J = 4.40 Hz), 4.11 (q, 2H, OCH₂CH₃, J = 6.80 Hz), 4.14 (s, 2H, CH₂Ph), 4.58 (s, 2H, NCH₂N), 6.82 (dd, 1H, Ar-H, J = 3.60, 2.00 Hz), 7.37 (d, 1H, Ar-H, J = 8.00 Hz), 7.41-7.44 (m, 5H, Ar-H), 7.51 (d, 1H, Ar-H, J = 2.00 Hz), 7.59 (dd, 1H,

Ar-H, $J = 3.60, 0.80$ Hz), 8.12 (dd, 1H, Ar-H, $J = 1.60, 0.80$ Hz), 9.67 (s, 1H, N=CH); ^{13}C NMR (100 MHz, DMSO- d_6): δ 14.36 (OCH₂CH₃), 30.37 (CH₂Ph), 49.99 (CH₂NCH₂), 64.25 (OCH₂CH₃), 66.04 (CH₂OCH₂), 66.11 (NCH₂N), 111.89 (CH), 112.75 (CH), 120.33 (CH), 121.24 (CH), 123.61 (CH), 132.48 (C), 141.51 (C), 142.66 (C), 148.75 (CH), 150.54 (arom-C), 128.45 (2CH), 130.71 (2CH), 131.48 (C), 134.72 (C₃-arom-C), 144.57 (triazol C₃), 150.23 (triazol C₅), 153.16 (N=CH), 155.47 (COO).

1-(Morpholin-4-yl-methyl)-3-phenyl-4-[3-ethoxy-4-(2-furylcarbonyloxy)-benzylidenamino]-4,5-dihydro-1H-1,2,4-triazol-5-one (2f)

Yield: 4.91 g (95.12%), m.p. 191 °C. IR (KBr, ν , cm^{-1}): 1733, 1697 (C=O), 1574 (C=N), 1499, 1469 (C=C), 1280 (COO), 1133 (C-O, furan), 856 (1,4-disubstituted benzenoid ring) cm^{-1} ; ^1H NMR (400MHz, DMSO- d_6): δ 1.24 (t, 3H, OCH₂CH₃, $J = 6.80$ Hz), 2.67 (t, 4H, CH₂NCH₂, $J = 4.40$ Hz), 3.59 (t, 4H, CH₂OCH₂, $J = 4.40$ Hz), 4.12 (q, 2H, OCH₂CH₃, $J = 6.80$ Hz), 4.71 (s, 2H, NCH₂N), 6.82 (dd, 1H, Ar-H, $J = 3.60, 1.60$ Hz), 7.39 (d, 1H, Ar-H, $J = 8.00$ Hz), 7.47 (m, 1H, Ar-H), 7.55-7.57 (m, 3H, Ar-H), 7.60 (dd, 1H, Ar-H, $J = 3.60, 0.80$ Hz), 7.62 (d, 1H, Ar-H, $J = 1.60$ Hz), 7.93-7.95 (m, 2H, Ar-H), 8.12 (dd, 1H, Ar-H, $J = 1.60, 0.80$ Hz), 9.66 (s, 1H, N=CH); ^{13}C NMR (100 MHz, DMSO- d_6): δ 14.33 (OCH₂CH₃), 49.98 (CH₂NCH₂), 64.23 (OCH₂CH₃), 66.07 (CH₂OCH₂), 112.60 (CH), 112.76 (CH), 120.37 (CH), 120.98 (CH), 123.76 (CH), 132.42 (C), 141.63 (C), 142.64 (C), 148.76 (CH), 150.57 (arom-C), 126.12 (C), 128.17 (2CH), 128.54 (2CH), 130.37 (C₃-arom-C), 143.23 (triazol C₃), 150.40 (triazol C₅), 156.08 (N=CH), 155.47 (COO).

Conclusion

In this study, the structures of six novel 1-(morpholin-4-yl-methyl)-3-alkyl(aryl)-4-[3-ethoxy-4-(2-furylcarbonyloxy)-benzylidenamino]-4,5-dihydro-1H-1,2,4-triazol-5-ones (2a-f) were characterized with IR, ^1H NMR and ^{13}C NMR spectral data and these were in parallel with previously published reports. *In vitro* antioxidant and antimicrobial properties of these novel compounds are currently under investigation and will be reported in the near future.

Acknowledgements

This study was supported by the Kafkas University Scientific Research Projects Coordination (Project Number 2018-FM-86).

References

- Alam, M. M., Nazreen, S., Haider, S., Shafi, S., Yar, M. S., Hamid, H., & Alam., M. S. (2012). Synthesis of some new *S*-Alkylated 1,2,4-triazoles, their Mannich bases and their biological activities. *Archiv der Pharmazie-Chemistry in Life Sciences*, 345, 203–214. <http://doi.org/10.1002/ardp.201100128>
- Bayrak, H., Demirbas, A., Karaoglu, S. A., Demirbas, N. (2009). Synthesis of some new 1,2,4-triazoles, their Mannich and Schiff bases and evaluation of their antimicrobial activities. *European Journal of Medicinal Chemistry*, 44, 1057-1066. <http://doi.org/10.1016/j.ejmech.2008.06.019>
- Bekircan, O., Menteşe, E., Ülker, S., & Kucuk., C. (2014). Synthesis of some new 1,2,4-triazole derivatives starting from 3-(4-chlorophenyl)-5-(4-methoxybenzyl)-4H-1,2,4-triazol with anti-lipase and anti-urease activities. *Archiv der Pharmazie-Chemistry in Life Sciences*, 347, 387–397. <http://doi.org/10.1002/ardp.201300344>
- Bektaş, H., Karaali, N., Şahin, D., Demirbaş, A., Karaoglu, Ş. A., Demirbaş, N. (2010). Synthesis and antimicrobial activities of some new 1,2,4-triazole derivatives. *Molecules*, 15, 2427-2438. <http://doi.org/10.3390/molecules15042427>
- Demirbas, A., Sahin, D., Demirbas, N., Karaoglu, S. A. (2009). Synthesis of some new 1,3,4-thiadiazol-2-ylmethyl-1,2,4-triazole derivatives and investigation of their antimicrobial activities. *European Journal of Medicinal Chemistry*, 44, 2896–2903. <http://doi.org/10.1016/j.ejmech.2008.12.005>
- Holla, B. S., Veerendra, B., Shivananda, M. K., Poojary, B. (2003). Synthesis characterization and anticancer activity studies on some Mannich bases derived from 1,2,4-triazoles. *European Journal of Medicinal Chemistry*, 38, 759–767. [http://doi.org/10.1016/S0223-5234\(03\)00128-4](http://doi.org/10.1016/S0223-5234(03)00128-4)
- Nithinchandra, Kalluraya, B., Aamir, S., Shabaraya, A. R. (2012). Regioselective reaction: Synthesis, characterization and pharmacological activity of some new Mannich and Schiff bases containing

sydnone. *European Journal of Medicinal Chemistry*, 54, 597-604.
<http://doi.org/10.1016/j.ejmech.2012.06.011>

Ozdemir, Y., Gultekin, E., & Bekircan, O. (2017). Synthesis and biological significances of new heterocyclic compounds containing 5-(4-chlorobenzyl)-3-(4-chlorophenyl)-1H-1,2,4-triazol ring. *Journal of The Chemical Society of Pakistan*, 39, 1055–1067. <http://doi.org/10.1002/ardp.201300344>

Triloknadh, S., Rao, C. V., Nagaraju, K., Krishna, N. H., Ramaiah, C. V., Rajendra, W., Trinath, D., Suneetha, Y. (2018). Design, synthesis, neuroprotective, antibacterial activities and docking studies of novel thieno[2,3-*d*]pyrimidine-alkyne Mannich base and oxadiazole hybrids. *Bioorganic & Medicinal Chemistry Letters*, 28, 1663–1669. <http://doi.org/10.1016/j.bmcl.2018.03.030>

Author Information

Onur Akyildirim

Kafkas University,
Faculty of Engineering and Architecture
Department of Chemical Engineering
Kars, Turkey
Contact E-mail: onurakyildirim@gmail.com

Haydar Yuksek

Kafkas University,
Faculty of Science and Letters
Department of Chemistry
Kars, Turkey

Sevda Manap

Kafkas University,
Faculty of Science and Letters
Department of Chemistry
Kars, Turkey

Theoretical Studies of the Molecular Structure, Conformational and Nonlinear Optical Properties of (2-Benzyloxy-Pyrimidin-5-Yl) Boronic Acid

Guventurk UGURLU
Kafkas University

Abstract: In this study, ab initio Hartree-Fock (HF) and Density Functional Theory (DFT), using Becke-3-Lee-Yang-Parr (B3LYP) hybrid density functional, calculations have been performed to characterize the ground state geometrical energy, the dipole moment (μ), polarizability (α), the hyperpolarizability (β) of (2-benzyloxy-pyrimidin-5-yl) boronic acid molecule. The ^1H and ^{13}C NMR chemical shifts were calculated by GIAO approach by using B3LYP/6-311+G (2d, p) and HF/6-31G (d) level of theory. The potential energy surface of title molecule has been investigated as a function dihedral angles (C3-B-O1-H1 and C3-B-O2-H2). Also, using the calculated the highest occupied molecular orbital energies (E_{HOMO}) and the lowest unoccupied molecular orbital energies (E_{LUMO}), electronic properties of the studied molecules such as energy gap ΔE_{g} ($E_{\text{LUMO}}-E_{\text{HOMO}}$), chemical potential μ , electrophilic index ω , ionization potential IP, electron affinity EA, electronegativity χ , molecular softness S , molecular hardness η were obtained. The dipole moment title molecule are calculated at 1.20 Debye at DFT/B3LYP/6-311++G (d, p) and 1.58 Debye at HF/6-311++G (d, p), respectively. Structural parameters of title molecules compared with the experimental data in the literature. All computational studies have been performed with the Gaussian 09W program.

Keywords: (2-benzyloxy-pyrimidin-5-yl) boronic acid molecule, Density functional theory, Hyperpolarizability polarizability

Introduction

Boronic acids (Lulinski et al. 2007; Maly et al. 2006) have recently attracted a wide range of researches due to their applications in organic synthesis biology and even lithium-ion batteries (Wang, et al., 2008; Bebeda, et al., 2015). The structural parameters of phenylboronic acid were investigated experimentally (Rettig and Trotte, 1977). Heterocyclic boronic acid have found application as Suzuki-Miyaura cross-coupling partners. However, pyrimidylboronic acids have been largely neglected, although some derivatives were synthesized (Clapham et al., 2007; Durka et al., 2012; Liao et al., 1964; Saygili et al., 2004). Crystal structure of (2-benzyloxy-pyrimidin-5-yl) boronic acid molecule were determined experimentally using X-ray structure analysis and spectroscopic methods (Durka et al., (20014). In this work, molecular structure, dipole moment, relative energies, rotational barriers, polarizability, first static hyper polarizability, potential energy scan, the electronic structure and HOMO-LUMO energies of above-mentioned molecule have been studied. ^1H NMR and ^{13}C NMR chemical shifts calculations have been performed. The molecular structure using numbering scheme of the (2-benzyloxy-pyrimidin-5-yl) boronic acid molecule is given in Figure 1.

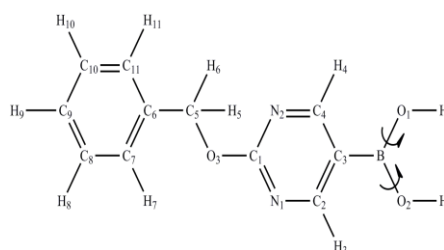


Figure 1. Molecular structure of (2-Benzyloxy-Pyrimidin-5-yl) Boronic Acid numbering scheme

- This is an Open Access article distributed under the terms of the Creative Commons Attribution-NonCommercial 4.0 Unported License, permitting all non-commercial use, distribution, and reproduction in any medium, provided the original work is properly cited.

- Selection and peer-review under responsibility of the Organizing Committee of the Conference

Method

Theoretical calculations on the isolated (2-Benzyloxy-Pyrimidin-5-yl) Boronic Acid molecule were performed by the aid of Gaussian 09W program package and Gauss view 5.0 molecular visualization programs (Frisch et al., 2010; Dennington et al., 2009) in the gas phase. The geometric parameters of 3-bromo-4-(2-pyridyl) thiophene molecule in the equilibrium state were optimized at HF (Moller et al., 1934) and DFT with Becke's three parameter hybrid functional (B3) (Becke et al., 1988) and combined with gradient corrected correlation functional of Lee–Yang–Parr (LYP) (Lee et al., 1988; Becke, 1993) and employing 6-311++G (d,p) basis set (Francl et al., 1982; Rassolov et al., 2001). After optimization, at all optimized structures of the title compounds obtained B3LYP/6-311++G (d,p) and HF/6-311++G (d,p) level of theory, dipole moment (μ), polarizability (α), hyperpolarizability (β) based on finite field approach and energy differences of ELUMO –EHOMO were calculated in the same as level of theory. The ^1H and ^{13}C NMR chemical shifts were calculated by GIAO approach by using B3LYP/6-311+G (2d, p) and HF/6-31G (d) level of theory (McLean et al., 1980; Krishnan et al., 1980).

Results and Discussion

The potential energy surface of (2-Benzyloxy-Pyrimidin-5-yl) Boronic Acid molecule has been investigated as a function dihedral angles (C3-B-O1-H1 and C3-B-O2-H2). The optimized geometry and Molecular electrostatic potential (MEP) surface values of (2-Benzyloxy-Pyrimidin-5-yl) Boronic Acid molecule obtained B3LYP/6-311++G (d, p) level are presented Figure 2 (a) and (b)

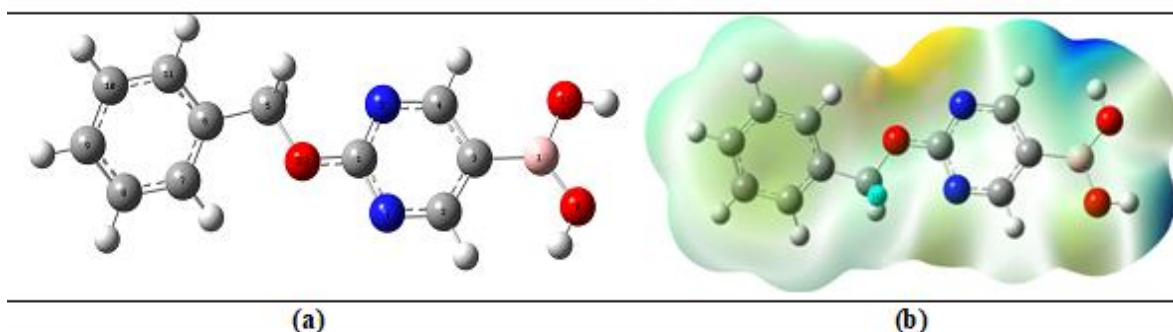


Figure 2. (a)The optimized geometry, (b) Molecular electrostatic (MEP) potential surface (PES) of (2-Benzyloxy-Pyrimidin-5-yl) Boronic Acid molecule

Potential Energy surface (PES) and electrostatic potential curves of (2-Benzyloxy-Pyrimidin-5-yl) Boronic Acid molecule obtained B3LYP/6-311++G (d, p) level are presented Figure 3 (a) and (b)

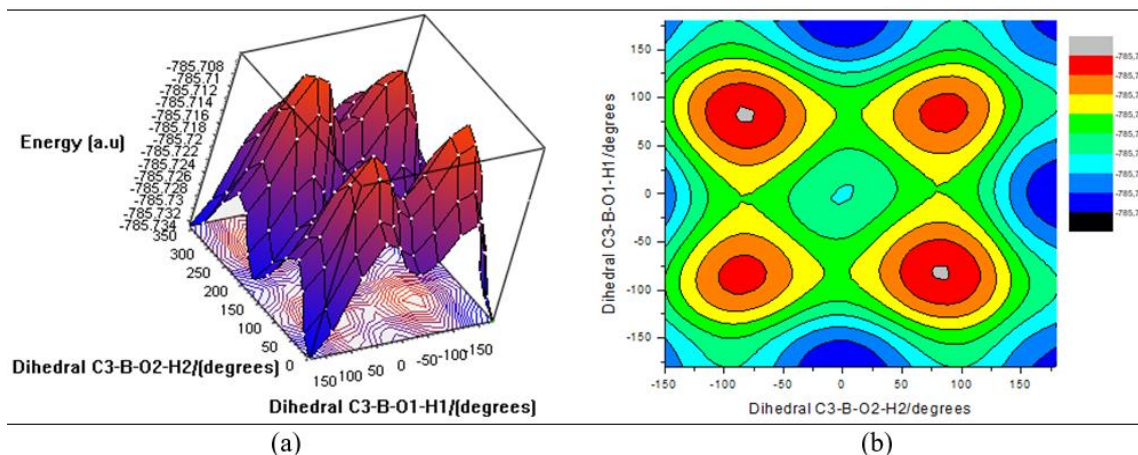


Figure 3. (a) Potential Energy surface (PES) (b) electrostatic potential curves of (2-Benzyloxy-Pyrimidin-5-yl) Boronic Acid molecule obtained B3LYP/6-311++G (d, p) level

The calculated values of the electronic, dipole moment, polarizability, hyperpolarizability, HOMO, LUMO energy and energy gap (ΔE_g) at the ground-state equilibrium geometry of (2-Benzyloxy-Pyrimidin-5-yl) Boronic Acid are listed in Table 1. As seen from Table 1, dipole moment values of obtained B3LYP/6-311++G (d, p) level is lower than that of HF/6-311++G (d, p) level.

Table 1. The electronic, HOMO, LUMO energy, dipole moment, polarizability, hyperpolarizability, and energy gap (ΔE_g) of (2-Benzyloxy-Pyrimidin-5-yl) Boronic Acid molecule

| B3LYP/6-311++G(d, p) | | | | | | |
|-----------------------------|---------------|----------------|---------------|-------------|-------------|-------------------|
| Electronic Energy (a.u) | μ (Debye) | α (a.u) | β (a.u) | EHOMO (a.u) | ELUMO (a.u) | ΔE_g (eV) |
| -786.160372266 | 1.20 | 169.18 | 652.41 | -0.254716 | -0.058358 | 5.34 |
| HF/6-311++G(d,p) | | | | | | |
| -781.461269575 | 1.58 | 150.98 | 247,21 | -0.330525 | 0.036124 | 9.98 |

The X-ray crystal structures for studied molecule is available in the literature and (Durka et al., (20014) and the calculated parameter studied molecule of both at the B3LYP/6-311++G (d, p) and HF/6-311++G (d, p) methods in the ground state are tabulated in the Table 2.

Table 2. Selected structural parameters of (2-Benzyloxy-Pyrimidin-5-Yl) Boronic Acid molecule

| Atoms | DFT | HF | Exp. | HF | Exp ^a . | DFT | HF |
|-----------------------------|---------------------------|--------|--------------|-----------|--------------------|-------------------------|-------------|
| | Bond length/ \AA | | | Atoms | | Bond angle/($^\circ$) | |
| C1-N1 | 1.3387 | 1.3227 | 1.3375 (15) | O3-C1-N2 | 119.2 | 119.1 | 118.63 (10) |
| C1-N2 | 1.3352 | 1.3165 | 1.3336 (15) | N1-C1-N2 | 126.8 | 126.5 | 127.51 (11) |
| C2-C3 | 1.4034 | 1.395 | 1.3957 (17) | C3-C2-N1 | 124.4 | 124.4 | |
| C2-N1 | 1.3268 | 1.3102 | 1.3407 (16) | C2-C3-C4 | 113.8 | 113.2 | 114.36 (11) |
| C3-C4 | 1.3999 | 1.3894 | 1.3898 (16) | C2-C3-B | 124.7 | 125.3 | 125.58 (11) |
| C3-B | 1.5608 | 1.5641 | 1.5775 (19) | C4-C3-B | 121.5 | 121.4 | 120.05 (10) |
| C4-N2 | 1.3346 | 1.32 | 1.3415 (16) | C3-C4-N2 | 123.7 | 123.7 | |
| C5-C6 | 1.5074 | 1.5099 | 1.5028 (18) | C6-C5-O3 | 108.7 | 109.1 | 110.46 (10) |
| C5-O3 | 1.4423 | 1.4137 | 1.4412 (14) | C7-C6-C11 | 119.1 | 119.1 | 119.14 (11) |
| C6-C7 | 1.3979 | 1.3867 | 1.3898 (17) | C6-C7-C8 | 120.3 | 120.2 | 119.86 (11) |
| C6-C11 | 1.3973 | 1.3901 | 1.3972 (16) | C8-C9-C10 | 119.6 | 119.5 | 119.09 (12) |
| C7-C8 | 1.393 | 1.3874 | 1.3912 (18) | C1-O3-C5 | 118.3 | 119.8 | |
| C8-C9 | 1.3945 | 1.3837 | 1.3870 (18) | B-O1-H | 112.6 | 113.6 | 121.3 (12) |
| C9-C10 | 1.3933 | 1.3864 | 1.3933 (19) | B-O2-H | 115.8 | 117.2 | 117.4 (12) |
| C10-C11 | 1.3939 | 1.3836 | 1.3856 (18) | C3-B-O1 | 117.9 | 117.9 | 123.67 (11) |
| O1-B | 1.3664 | 1.3542 | 1.3475 (16) | C3-B-O2 | 124.6 | 124.5 | 116.12 (11) |
| O2-B | 1.3728 | 1.3601 | 1.3602 (16) | O3-C1-N1 | 114.0 | 114.3 | 113.86 (10) |
| Dihedral angle/($^\circ$) | | | | | | | |
| | DFT | HF | Exp. | | - | - | |
| N1-C1-O3-C5 | -178.2 | -178.5 | -175.72 (10) | | - | - | |
| N2-C1-O3-C5 | 1.9 | 1.6 | 4.30 (16) | | - | - | |
| C2-C3-B-O1 | -179.7 | 179.8 | -175.21 (12) | | - | - | |
| C2-C3-B-O2 | 0.3 | -0.2 | 3.78 (17) | | - | - | |
| C4-C3-B-O1 | 0.4 | -0.2 | 3.3 (2) | | - | - | |
| C4-C3-B-O2 | -179.6 | 179.8 | -177.72 (12) | | - | - | |
| O3-C5-C6-C7 | -35.2 | -19.0 | -8.77 (17) | | - | - | |
| O3-C5-C6-C11 | 147.5 | 162.9 | 173.27 (10) | | - | - | |
| N1-C1-O3-C5 | -178.2 | -178.5 | -175.72 (10) | | - | - | |

(^a ref Durka et al. 2014)

The pictures of HOMO and LUMO obtained at the B3LYP/6-311++G (d, p) of (2-Benzyloxy-Pyrimidin-5-yl) Boronic Acid molecule at the B3LYP/6-311++G (d, p) is given in Figure 4.

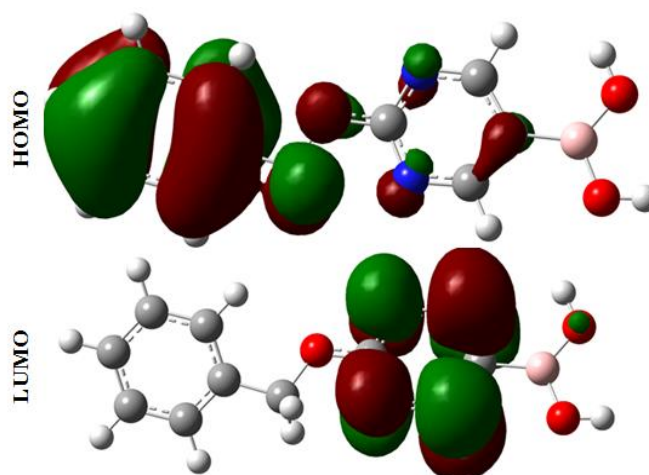


Figure 4. The pictures of HOMO and LUMO of (2-Benzyloxy-Pyrimidin-5-yl) Boronic Acid molecule

^1H and ^{13}C NMR values of (2-Benzyloxy-Pyrimidin-5-yl) Boronic Acid molecule has been calculated and given in Tables 3.

Table 3. NMR chemical shifts of (2-Benzyloxy-Pyrimidin-5-yl) Boronic Acid molecule

| B3LYP/6-311++(2d,p) | | HF/6-31(d) | |
|---------------------|------|------------|------|
| Atoms | Gas | Atoms | Gas |
| C1 | 174. | H4 | 9.38 |
| C4 | 172. | H3 | 8.82 |
| C2 | 168. | H7 | 8.12 |
| C6 | 143. | H8 | 7.65 |
| C8 | 133. | H10 | 7.61 |
| C10 | 132. | H9 | 7.54 |
| C9 | 132. | H11 | 7.52 |
| C7 | 131. | H5 | 5.73 |
| C11 | 130. | H6 | 5.26 |
| C3 | 118. | H2 | 4.19 |
| C5 | 74.3 | H1 | 3.50 |

Conclusion

The ground state geometrical parameter, energy, dipole moment, polarizability, hyperpolarizability, E_{HOMO} , E_{LUMO} , ΔE_g of (2-Benzyloxy-Pyrimidin-5-yl) Boronic Acid molecule are examined both HF/6-311++G (d,p) and B3LYP/6-311++G(d,p) level of the theory. The ^1H and ^{13}C NMR chemical shifts were calculated by GIAO approach by using B3LYP/6-311+G (2d, p) and HF/6-31G (d) level of theory. The potential energy surface of title molecule has been investigated as a function dihedral angles (C3-B-O1-H1 and C3-B-O2-H2). The dipole moment title molecule are calculated at 1.20 Debye at DFT/B3LYP/6-311++G (d, p) and 1.58 Debye at HF/6-311++G (d, p), respectively. Structural parameters of title molecules compared with the experimental data in the literature. The structural parameters of title molecules indicates that results of HF/6-311++G (d, p), and B3LYP/6-311++G (d,p) level of the theory are in a good agreement with experimental data for (2-Benzyloxy-Pyrimidin-5-yl) Boronic acid molecule.

References

- Bebeda, A.W., van Ree, T. (2015) Conformational performance and electrochemical performance of ethyleneoxy phenyl boronate electrolyte additives. Arab. J.Sci. Eng 40 28141-2851
- Becke, A. D. (1988) Density-functional exchange-energy approximation with correct asymptotic behavior. Physical Review A, 38(6), 3098–3100
- Becke, A. D., 1993. Density-Functional Thermochemistry .3. The Role of Exact Exchange. J. Chem. Phys., 98 (7): 5648-5652

- Clapham, K.M., Smith, A.E., Batsanov, A.S., McIntyre, L., Pountney, A., Bryce, M.R., & Tarbit, B. (2007) 3-New pyrimidylboronic acids and functionalized heteroarylpyrimidines by Suzuki cross-coupling reactions. *European Journal Of Organic Chemistry* 34,5712-5716
- Dennington, R., Keith T., Millam, J. (2009). Semichem Inc., GaussView, Version 5, Shawnee Mission KS,
- Durka, K., Klis, T., & Serwatowski, J. (2014) Crystal structure of (2-benzyloxyppyrimidin-5-yl)boronic acid, *Acta Cryst. E70*, o1259–o1260
- Durka, K., Katarzyna Jarzemska., K. N., Kamiński, R., Luliński, S., Serwatowski, J., & Woźniak, K., (2012) Structural and Energetic Landscape of Fluorinated 1,4-Phenylenediboronic Acids. *Cryst. Growth Des.* 12 3720-373
- Francl, M.M., Pietro, W.J., Hehre, W.J., Binkley, J.S., Gordon, M.S., DeFrees, D.J., Pople, J.A, (1982). Self-consistent molecular orbital methods. XXIII. A polarization-type basis set for second-row elements. *Chem. Phys*, 77 3654-3665
- Frisch M J, Trucks G W, Schlegel H B, Scuseria G E, Robb M A, Cheeseman J R, Scalmani G, Barone V, Mennucci B, Petersson G A, Nakatsuji H, Caricato M, Li X, Hratchian H P, Izmaylov A F, Bloino J, Zheng G, Sonnenberg J L, Hada M, Ehara M, Toyota K, Fukuda R, Hasegawa J, Ishida, M, Nakajima T, Honda Y, Kitao O, Nakai H, Vreven T, Montgomery J A, Vreven T J, Peralta J E, Ogliaro F, Bearpark M, Heyd J. J, Brothers E, Kudin N, Staroverov V N, Kobayashi R, Normand J, Raghavachari K, Rendell A, Burant J C, Iyengar S S, Tomasi J, Cossi M, Rega N, Millam J M, Klene, M, Knox J E, Cross J B, Bakken V, Adamo C, Jaramillo J, Gomperts R, Stratmann R E, Yazyev O, Austin A J, Cammi R, Pomelli C J, Ochterski W, Martin L R, Morokuma K, Zakrzewski V G, Voth G A, Salvador P, Dannenberg J J, Dapprich S, Daniels A D, Farkas O, Foresman J B, Ortiz J V, Cioslowski J, Fox D J, 2009. Gaussian Inc., (Wallingford, CT).
- Krishnan, R., Binkley, J. S., Seeger, R. and Pople, J. A, (1980). Self-consistent molecular-orbital methods. 20. basis set for correlated wave-functions. *J. Chem. Phys.* 72: 650–654.
- Lee, C. T., Yang, W. T., Parr, R. G. (1988). Development of the colle-salvetti correlation-energy formula into a functional of the electron density. *Physical Review B*, 37, 785-789.
- Liao, T. K., Podrebarac, E. G., & Cheng C.C. (1964) Boron-Substituted Pyrimidines *J. Am. Chem. Soc.* 1869-1870
- Lulisnki, S., Madura, I., Serwatowski, J., Szatyłowicz, H., & Zachara, J, (2007) A tautomeric equilibrium between functionalized 2-formylphenylboronic acids and corresponding 1,3-dihydro-1,3-dihydroxybenzo[c][2,1]oxaboroles *New J. Chem.*, 31, 144-154
- Maly, K. E., Maris, T., and Wuest, J. D. (2006) wo-dimensional hydrogen-bonded networks in crystals of diboronic acids *Ctyst Eng Comm.* 8, 33-35
- McLean, A.D., Chandler, G.S. (1980). Contracted Gaussian basis sets for molecular calculations. I. Second row atoms, Z= 11–18. *J Chem Phys*, 72:5639–5648
- Moller, C., Plesset, M. S. (1934). Note on an approximation treatment for many- electron systems. *Phys. Rev.*, 46 618-622.
- Rassolov, V-A., Ratner, M-A., Pople, J-A., Redfern, P-C., Curtiss, L-A., (2001). 6–31G* basis set for third-row atoms. *J Comp Chem.*, 22:976–984.
- Rettig, S.J., Trotte, C.J. (1977) Crystal and molecular structure of phenylboronic acid. *Can. J. Chem.* Vol. 55. 3071-3075
- Saygili, N., Batsanova A. S., & Bryce, M., R. (2004) 5-Pyrimidylboronic acid and 2-methoxy-5-pyrimidylboronic acid: new heteroarylpyrimidine derivatives via Suzuki cross-coupling reactions *Organic & Biomolecular Chemistry* Issue 6, 852-857
- Sowmya, D. V., Teja, G. L., Padmaja, A., Prasad, V. K., Padmavathi, V, (2018) Green approach for the synthesis of thiophenyl pyrazoles and isoxazoles by adopting 1,3-dipolar cycloaddition methodology and their antimicrobial activity. *Eur. J. Med. Chem.* 143; 891-898.
- Wang, B., Qu, Q.T., Xia, Q., Wu, Y.P., Gan, C.L., van Ree, T. (2008) Effects of 3,5-bis(trifluoromethyl)benzeneboronic acid as an additive on electrochemical performance of propylene carbonate based electrolytes for lithium ion batteries. *Electrochim. Acta.* 54, 816-820

Author Information

Guventurk Ugurlu

Kafkas University,
Faculty of Science and Letter, Department of Physics,
36100 Kars, Turkey
Contact E-mail: gugurlu@kafkas.edu.tr

Vitamin D Status And Parathyroid Hormone In Albanians

Merita RUMANO

University of Tirana

Anila MITRE

University of Tirana

Elvisa RUMANO

University of Medicine

Abstract: Vitamin D is a fat soluble organic compound, acting like a hormone and playing a crucial role in calcium homeostasis in the human body. Both vitamin D and parathyroid hormone are essential in calcium metabolism. This paper aims the assessment of the current situation of vitamin D status and parathyroid hormone in Albanians, during the period of time from 2009 to 2014. All the individuals involved in this study were taken under examination through blood sampling (10 ml/person) to check for the present value of vitamin D and PTH as well as other parameters, such as calcium, phosphate, etc. PTH and vitamin D levels were measured by electrochemiluminescence immunoassay, while total calcium and phosphate values were measured by Turbidimetry method on Coobas 6000 system. The values of 25(OH) D and PTH were correlated with age, gender and electrolytes. From the results, we notice a high prevalence of vitamin D insufficiency in the group with primary hyperparathyroidism (18.15±8.75 ng/ml), low levels of vitamin D in the group with secondary hyperparathyroidism (15.71±4.45 ng/ml) and in the group with hypoparathyroidism (15.83±9.31 ng/ml). We noticed also a negative correlation between 25(OH) D and PTH levels. In conclusion, we can say that, from this study, it is noticed a high prevalence of vitamin D deficiency in Albanians, and we can recommend regular blood tests at a certain age, in order to prevent other diseases linked to low levels or insufficiency of vitamin D.

Keywords: 25-(OH)₂-D Vitamin, Parathyroids, PTH, Hypoparathyroidism, Hyperparathyroidism

Introduction

Vitamin D is a fat soluble organic compound, acting like a hormone and playing a crucial role in calcium homeostasis in the human body. Vitamin D and PTH level affect directly the calcium concentration in serum and in the extracellular level. Calcium homeostasis is largely regulated through an integrated hormonal system that controls calcium transport in the gut, kidney, and bone. It involves two major calcium-regulating hormones and their receptors—PTH and the PTH receptor (PTHR) (Potts JT, Gardella TJ, 2007) and 1,25(OH)₂D and the vitamin D receptor (VDR) (Jurutka PW., et al 2001)—as well as serum ionized calcium and the calcium-sensing receptor (CaR) (Brown EM., 2007). The increased PTH also stimulates the kidney to increase secretion of 1,25(OH)₂D, which activates the VDR in gut to increase calcium absorption, in the parathyroid glands to decrease PTH secretion, and in bone to increase resorption (Peacock M., 2010).

Regarding the vitamin D, the major source of it, is the skin synthesis, contributing to more than 90% of vitamin D serum concentration (Bellavia D., 2016). The precursors of vitamin D in the body are also very important, so diet plays a key role to vitamin D level too. Fortified foods or vitamin D supplementation is considered also. There are many studies about what is considered normal and abnormal vitamin D concentration, vitamin D deficiency, insufficiency, normality or increased.

Although there is a variation of the ideal values to establish adequate levels of vitamin D, many experts agree that levels of 25(OH)D below 20 ng/mL are classified as deficient, levels between 20 and 29 ng/mL as

- This is an Open Access article distributed under the terms of the Creative Commons Attribution-Noncommercial 4.0 Unported License, permitting all non-commercial use, distribution, and reproduction in any medium, provided the original work is properly cited.

- Selection and peer-review under responsibility of the Organizing Committee of the Conference

insufficiency, and those between 30 and 100 ng/mL as sufficiency (Maeda S. S., 2014; Yanoff L. B., et al 2006). Chronic vitamin D inadequacy in adults can result in compensatory hyperparathyroidism, leading to increased bone turnover, enhanced bone loss, and increased risk of fragility fracture (Guilsun K. et al, 2012). It has also been reported that serum 25(OH)D levels decline with age earlier in women than in men and less efficiently prevent compensatory hyperparathyroidism in older adults (Dawson-Hughes B., et al 2005). In this study, we assessed and analyzed the current situation of vitamin D status and parathyroid hormone in Albanians, as well as calcium and phosphates, in the role of the two main electrolytes affecting directly the PTH and vitamin D concentration as a result of the bifunctional mechanism of calcium and PTH homeostasis. Our focus was the albanian population, including patients with parathyroid problems and the healthy population, represented by the control group.

Method

A group of 969 individuals was enrolled in this study during the period of time from 2009 to 2014. 500 individuals were representing the control group, which was chosen randomly. 290 individuals were diagnosed with primary hyperparathyroidism, 115 individuals were dialysis patients suffering from secondary hyperparathyroidism and 64 individuals were diagnosed with hypoparathyroidism. All details of the clinical and biochemical parameters of these patients were recorded. A 10 ml fasting blood sample was collected for the determination of 25-hydroxyvitamin D, PTH, total serum calcium and inorganic phosphates in serum. Serum concentration of 25(OH) D and PTH were measured by the Electrochemiluminescence immunoassay and serum calcium and inorganic phosphate were measured by colorimetric methods on Coobas 6000 system. The reference values of vitamin D, used in this study are as follows: <20 ng/ml (deficiency), 20-29 ng/ml (insufficiency), 30-100 ng/ml (sufficiency) and >100 ng/ml (increased). The reference value of PTH was from 15-65 mg/dl (normal), the reference value for serum calcium, was 8.6-10.2 mg/dl and for serum phosphate it was 2.6-4.5 mg/dl.

Datas were expressed as mean±standard deviation and median. Statistical analysis is done using the nonparametric test of Spearman correlation. Significance level was set for the values of $p < 0.000$.

Results and Discussion

The focus of our study was the Albanian population. We have included the healthy population (represented by the control group) and a group of individuals diagnosed with different parathyroid problems, such as: primary hyperparathyroidism, secondary hyperparathyroidism and hypoparathyroidism. The first group, control group is represented by 500 "healthy" individuals; the second group is represented by 405 individuals with hyperparathyroidism, of whom 290 with primary hyperparathyroidism and 115 dialysis patients diagnosed with secondary hyperparathyroidism. The fourth group is represented by 64 patients with hypoparathyroidism.

Control Group

78 individuals from the control group (15.6%), have resulted with primary hyperparathyroidism problems and 9 individuals (1.8%), with hypoparathyroidism. PTH values within this group range from 3.16 mg/dl to 206 mg/dl. The average value of PTH in the subgroup with increased PTH levels is 82.12 (\pm 23.98) mg/dl, while for the subgroup with low PTH level is 8.03 (\pm 3.74) mg/dl. Calcium in the subgroup with increased PTH reaches the values from 7.91 to 12.1 mg/dl, with an average value of 9.62 (\pm 0.78) mg/dl.

Regarding vitamin D concentration, we noticed that in the group with low PTH value, the values range from 13 to 48.8 ng/ml, with an average value of 19.02 (\pm 11.28) ng/ml, while in the group with increased PTH, vitamin D has a range of 7.8-35.4 ng/ml, with an average value of 20.96 (\pm 5.49) ng/ml. Considering the reference values of vitamin D, concentrations lower than 30 ng/ml are considered insufficient. In many recent studies, various authors find that the concentration of vitamin D in the serum is insufficient at levels lower than 30 ng/ml (Arnold J. et al., 2007; Dawson-Hughes B et al 2005).

From the examination of the control group, we noticed that parathyroid problems are present in the asymptomatic population and their diagnosis is randomly performed during routine analyzes. This is also seen in studies conducted in other countries, highlighting the large number of randomly diagnosed cases during routine analysis.

Parathyroid Problems Group

In this group with parathyroid problems, we analysed three main groups, suffering from primary hyperparathyroidism, secondary parathyroidism and hypoparathyroidism. There is a strong correlation as we will see between parathyroid problems, PTH and vitamin D concentration in these groups.

A total number of 290 individuals suffering with primary hyperparathyroidism, was observed and evaluated for PTH and vitamin D levels. Analysis of PTH, resulted in very high values, ranging from 60.51 to 1845 pg/ml and an average of 272.23 (± 330.289). On the other hand analysis of vitamin D, resulted in low levels of vitamin D with an average of 18.15 (± 8.75) ng/ml, ranging from 3.56 to 39.10 ng/ml. Low levels of phosphates in the blood and high levels of calcium are present in this group. The age of these individuals varies from 18 to 85 years old, with an average of 46.7 (± 10.97). Most of these individuals are presented to the physician with bone disorders, in 75-80% of cases, fatigue and weakness, as well as muscle pain in 65-70% of cases. Other problems faced in these individuals are nephrocalcinosis in 14% of cases and renal calculi in 42% of cases.

Analyzing the distribution of PTH values, we noticed a higher frequency for PTH values from 60.5 pg/ml to 200 pg/ml. These individuals manifest the first signs of hyperparathyroidism. Most of them manifest high calcium values and normal PTH levels, or vice versa with high levels of PTH and normal calcium concentration, which is explained with two different stages of the disease development, as well as with the bifunctional calcium relationship, where calcium and PTH interact to regulate each other's concentration (Arnold J. et al., 2007).

Vitamin D concentration, is higher in this group compared to a group characterized by secondary hyperparathyroidism or hypoparathyroidism. It is explained with the certain relationship of parathyroid hormone and vitamin D, where PTH promotes the maturation of vitamin D and its conversion into biologically active form, in the proximal tubule of nephrons. The main function of vitamin D, is to increase calcium absorption from the intestine, through interaction with vitamin D receptor (VDR), expressed in the distal as well as in the proximal intestine (Veldurthy V. et al 2016).

Taking into consideration the age groups, most of the cases, (116 cases, of which 80 are female and 36 males) suffering from primary hyperparathyroidism problems are encountered in the age group from 40-50 years old. In this study and other studies also, it is observed that women in this group of age, are almost twice affected compared to the men of the same age (G. Pryia et al 2008, Dina M Elaraj, MD Orlo H Clark, MD, 2008, Ghada El et al., 2012).

The correlation between variables: PTH level, sex, age, calcium level, phosphorus level and vitamin D level is expressed by Spearman correlation coefficient, which indicates a highly significant correlation between PTH level and calcium, phosphorus, vitamin D, age ($p < 0.01$) and sex ($p < 0.05$). There is a poor correlation between PTH level and vitamin D concentration ($r = -0.275$, $p < 0.000$), which confirms that with the increase in PTH level there is a decrease in vitamin D concentration. It is theoretically expected that the high levels of PTH will affect and stimulate the maturation of vitamin D in the kidney. There is an exceptions to the case when primary hyperparathyroidism has not been treated for a long time and nephrocalcinosis or renal calculi, gradually lead to chronic renal failure, a condition which subsequently leads to vitamin D deficiency in these individuals due to the dysfunction of this mechanism. Results comparable to those of our work were also obtained from other studies performed on primary hyperparathyroidism and its relation to vitamin D (Ghada El. et al 2013; Shoni J.S. 2013).

In the group with secondary hyperparathyroidism, the level of vitamin D, due to chronic renal impairment comes down to 4.65 (a value considered absent) up to 34.20 ng/mL with an average value of 15.72 (± 4.454) ng/ml, which, according to some studies, is considered inadequate (Arnold J. et al., 2007).

The chronic renal impairment function, on the other hand, causes these patients to be hypocalcemic in most cases. In these individuals, the low level of vitamin D has a direct impact on the reduction of serum calcium (Arnold et al., 2007; Malberti F. et al 1999). Reduced vitamin D levels also decrease the absorption of calcium into the intestine.

Received data show a modest correlation between PTH level and vitamin D concentration ($r = -0.479$, $p < 0.01$), which proves that PTH level increase is associated with decreased vitamin D. Possibly this is caused by the decrease of the activity of the α -1 hydroxylase enzyme in the kidney, which is responsible for the maturation of vitamin D in the kidneys.

In the group with hypoparathyroidism, the low values up to the absence of PTH (from 0.50 to 14.98 pg/ml, with an average value of 9.52 (± 4.03)), are associated with hypocalcemia, with an average of serum calcium of 7.28 (± 0.60) mg/dl, hyperphosphatemia, with mean serum phosphates of 5.04 (1.03) mg/dl and low vitamin D levels, average 15.8 (± 9.31) ng/ml. Taking into consideration the total number of cases diagnosed with hypoparathyroidism in this study, we notice that women are more affected than men, 36 in total compared to males 28 in total.

Mostly, these individuals visit the doctor due to a variety of symptoms, like weakness and different neuromuscular disorders such as: muscular cramps, tremors and muscular spasms, mainly as a result of hypocalcemia. After measuring PTH concentration in the serum of all these individuals, it resulted in low PTH values below 15 mg/dl.

The correlation between PTH, calcium, phosphorus and vitamin D in the group of individuals with secondary hyperparathyroidism, expressed by the Pearson correlation coefficient, indicates a highly significant correlation between these parameters. We found a modest correlation between PTH level and vitamin D concentrations ($r = 0.494$, $p = 0.000$), indicating that increased PTH levels are associated with increased vitamin D concentration. This as a result of the direct impact of PTH on α -1 hydroxylase enzyme activity in the kidneys.

Significant correlation exist between the vitamin D level and the calcium level ($r = 0.520$, $p = 0.000$), which proves that increased vitamin D concentration, causes the increase of calcium in serum.

We found also a poor correlation ($r = -0.313$, $p < 0.05$) between increased vitamin D level and low phosphorus concentration. It can happen due to the insufficiency of PTH, which increases the excretion of kidney phosphorus but also due to the low concentration (insufficiency) of vitamin D, which stimulates the absorption of phosphorus from the nephrons.

Insufficiency of vitamin D results more problematic in secondary hyperparathyroidism and hypoparathyroidism compared with primary hyperparathyroidism. In secondary hyperparathyroidism it comes as a result of the chronic fall in renal function and in the hypoparathyroidism group it is a result of PTH insufficiency. According to other studies, there is a high prevalence of vitamin D deficiency in other populations around the globe, including countries with a sunny environment (Ning Z. et al 2016., Cashman K. D. 2016., Holick M. F. and Chen T. C., 2008).

Conclusion

This study demonstrated a high vitamin D insufficiency level in the group with parathyroid problems as well as in the control group. We found parathyroid problems even in the control group, accompanied by low levels of vitamin D or insufficiency and high levels of PTH and more rarely low levels of PTH. Insufficiency of vitamin D and high values of PTH are characteristic for primary hyperparathyroidism, accompanied by hypercalcemia and hypophosphatemia in general. Low levels of vitamin D and very high values of PTH (10-100 times higher than the reference value) characterize secondary hyperparathyroidism. Hypocalcemia and hyperphosphatemia must be considered too in this group. There are met low levels of vitamin D, low levels of PTH, hypocalcemia and high levels of phosphates in hypoparathyroidism also. The clinical spectrum of individuals with parathyroid problems varies between the subgroups involved in the study, but also within the group depending on their age or their life style.

Recommendations

We recommend regular blood tests, in order to prevent parathyroid problems and other diseases linked to low levels or insufficiency of vitamin D.

References

Arnold J. Felsenfeld, Mariano Rodriguez, Escolastico Aguilera-Tejero. "Dynamics of Parathyroid Hormone Secretion in Health and Secondary Hyperparathyroidism" In –Depth Review; Clin J Am Soc Nephrol 2: 1283-1305, 2007.

- Bellavia D., Costa V., De Luca A., et al. Vitamin D level between calcium-phosphorus homeostasis and immune system: new perspective in osteoporosis. *Current Osteoporosis Reports*. 2016;1–12. doi: 10.1007/s11914-016-0331-2. [PubMed] [CrossRef] [Google Scholar]
- Brown EM: The calcium-sensing receptor: physiology, pathophysiology and CaR-based therapeutics. *Subcell Biochem* 45: 139–167, 2007 CrossRefPubMedGoogle Scholar
- Cashman K. D., Dowling K. G., Škrabáková Z. et al., “Vitamin D deficiency in Europe: pandemic?” *American Journal of Clinical Nutrition*, vol. 103, no. 4, pp. 1033–1044, 2016. View at Publisher · View at Google Scholar · View at Scopus
- Dawson-Huges B, Haeney RP, Holick MF, Lips P, Meunier PJ, Vieth R: Estimates of optional vitamin D status. *Osteoporosis Int* 16: 713-716, 2005.
- Guilsun Kim1*, Ki Won Oh2*, Eun-Hee Jang3, Mee-Kyoung Kim3, et al. Relationship between Vitamin D, Parathyroid Hormone, and Bone Mineral Density in Elderly Koreans. *J Korean Med Sci* 2012; 27: 636-643
- Jurutka PW, Whitfield GK, Hsieh JC, Thompson PD, Haussler CA, Haussler MR: Molecular nature of the vitamin D receptor and its role in regulation of gene expression. *Rev Endocr Metab Disord* 2: 203–216, 2001 CrossRefPubMedGoogle Scholar
- Maeda S. S., Borba V. Z. C., Camargo M. B. R., et al. Recommendations of the Brazilian Society of Endocrinology and Metabology (SBEM) for the diagnosis and treatment of hypovitaminosis D. *Arquivos Brasileiros de Endocrinologia e Metabologia*. 2014;58(5):411–433. doi: 10.1590/0004-2730000003388. [PubMed] [CrossRef] [Google Scholar]
- Ning Z., Song S., Miao L. et al., “High prevalence of vitamin D deficiency in urban health checkup population,” *Clinical Nutrition*, vol. 35, no. 4, pp. 859–863, 2016. View at Publisher · View at Google Scholar · View at Scopus
- Peacock M. Calcium metabolism in health and disease. *Clin J Am Soc Nephrol*. 2010 Jan;5 Suppl 1:S23-30. doi: 10.2215/CJN.05910809.
- Potts JT, Gardella TJ: Progress, paradox, and potential: Parathyroid hormone research over five decades. *Ann N Y Acad Sci* 1117: 196–208, 2007 CrossRefPubMedGoogle Scholar
- Holick M. F. and Chen T. C., “Vitamin D deficiency: a worldwide problem with health consequences,” *American Journal of Clinical Nutrition*, vol. 87, no. 4, pp. 1080S–1086S, 2008. View at Google Scholar · View at Scopus
- Veldurthy V., Wei R., Oz L., Dhawan P., Jeon Y. H., and Christakos S., “Vitamin D, calcium homeostasis and aging,” *Bone Research*, vol. 4, Article ID 16041, 2016. View at Publisher · View at Google Scholar
- Yanoff L. B., Parikh S. J., Spitalnik A., et al. The prevalence of hypovitaminosis D and secondary hyperparathyroidism in obese Black Americans. *Clinical Endocrinology*. 2006;64(5):523–529. doi: 10.1111/j.1365-2265.2006.02502.x. [PMC free article] [PubMed] [CrossRef] [Google Scholar]

Author Information

Merita Rumano

University of Tirana
Bulevardi "ZOG I- rë", No.2, 1001
Tirana, Albania
Contact E-mail:meritarumano@yahoo.com

Anila Mitre

University of Tirana
Bulevardi "ZOG I- rë", No.2, 1001
Tirana, Albania

Elvisa Rumano

University of Medicine
Tirana, Albania

Preparation of Gelatin and Chitosan Hydrogels Beads

Mehlika PULAT
Gazi University

Abstract: In this study, a series of gelatin and chitosan hydrogel beads were prepared via covalently crosslinking of these polymers. At the first step, three types of gelatin beads were obtained by dropping polymer solution into Glutaraldehyde (GA)-oil emulsion. While the concentration of polymer solution was varied from 7% to 14%, the concentration of crosslinking solution kept constant. Secondly, two types of chitosan beads were prepared by ionic gelation interaction procedure using Sodium Tripolyphosphate (TPP) as crosslinker. 1% of polymer solution was dropped into TPP solutions at different concentrations. At the last step, the different series of gelatin hydrogels were prepared by cutting the crosslinked polymer roads to form beads. Swelling behaviors of all the hydrogel beads were studied by changing time at constant temperature and pH. Swelling percentages (S%) increased with time initially, and then remained constant at close to 24 h. In general, it was determined that the gelatin hydrogel beads were much more swellable than the chitosan beads.

Keywords: Gelatin, Chitosan, Hydrogel, Glutaraldehyde

Introduction

Hydrogels are three-dimensionally cross-linked hydrophilic polymers that can absorb and retain large amounts of water up to thousands of times of their own weight. The hydrophilic property is due to presence of chemical residues such as -OH, -COOH, -NH₂, -CONH₂, -SO₃H and others with in molecular structure. Hydrogels have been extensively studied and preferred for a large number of industrial fields [Pulat and Asil, 2009]. Because of their excellent characteristics, they can also be used for a large number of applications in the medical field such as controlled drug release matrices, enzyme and yeast cell immobilization, blood-contacting applications, and others. Hydrogels are also very useful in production of agricultural and horticultural materials [Pulat and Yoltay, 2016].

Most of the synthetic polymers used to prepare hydrogels causes some problems because of their long degradation times and degradation products. Natural polymers are a good choice to overcome this issue [Pulat and Akalın, 2013].

Gelatin is a biodegradable natural polymer with extensive industrial, pharmaceutical, and biomedical uses that has been employed for coatings and microencapsulating various drugs, and for preparing biodegradable hydrogels [Pulat and Akalın, 2013]. As gelatin is an animal protein, it is obtained by thermal denaturation or physical and chemical degradation of collagen; the most widespread protein in the body occurs in most connective tissues as skin, tendon, and bone [Kushibiki et al. 2003, Gilsenan and Ross-Murphy, 2001] (Figure 1). Since it is soluble in aqueous solutions, the materials for long-term applications must be submitted to crosslinking, which improves both thermal and mechanical stability of gelatin [Bigi et al, 2001].

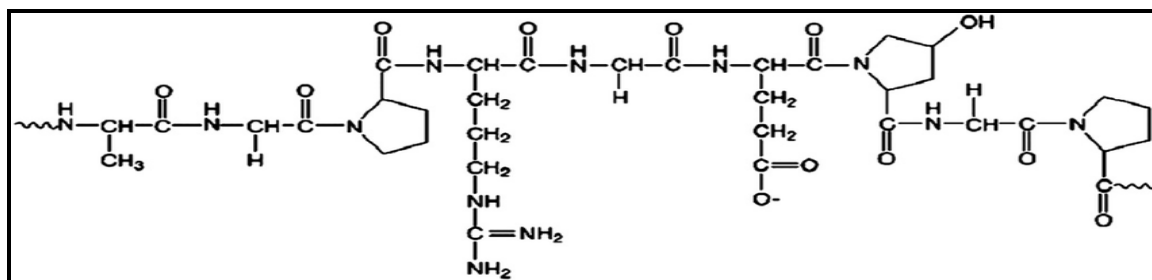


Figure 1. Molecular formula of gelatin

Chitosan (Cs) is a natural polymer obtained through the alkaline deacetylation of chitin (Figure 2). The hydrophilicity of Cs, due to the presence of amine and hydroxyl functional groups in its repeat unit, makes the polymer soluble in dilute acidic solutions and yields to a rubbery hydrogel in water [Pulat M. et al., 2011]. The propensity of CS to absorb water and swell into a soft rubbery material makes it a good matrix material for incorporating hydrophilic drugs.

It exhibits excellent biological properties such as biodegradation in the human body and immunological, antibacterial, and wound-healing activity. Cs has also been found to be a good candidate as a support material for gene delivery, cell culture, and tissue engineering [MacLeod et al. 1999]. Moreover, Cs has antacid and anti-ulcer activity, and can prevent or weaken drug-induced irritations in the stomach. In addition, this cationic biopolymer has been reported to improve transport across biological barriers [Kotze' A F et al,1999]. From a biomedical point of view, Cs has demonstrated high activity as wound healing activators or accelerators, and now is used in human and veterinary medications. Several researchers have reported on the mechanism of the activation of wound healing considering the activation of polymorphonuclear cells, protective effects against microorganisms, or the promotion of granulocyte tissue formation with angiogenesis. Finally, Cs is very abundant and its production is both environmentally safe and of low cost. These interesting properties make Cs an ideal candidate for use in controlled drug release formulations.

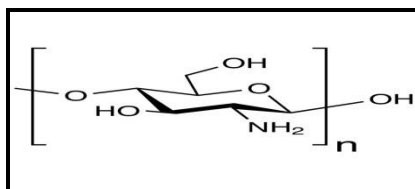


Figure 2. Molecular formula of Cs

The purpose of this study is to develop a series of gelatin and chitosan hydrogels in bead form. Hydrogels will be prepared by crosslinking of gelatin with glutaraldehyde (GA) and Cs with sodium *tripolyphosphate* (TPP). It is aimed that to obtain utilizable hydrogels at different swelling values.

Methods

Preparing of Hydrogel Beads

A series of Cs (Aldrich) beads were obtained by ionotropic gelation method (Nitsae M. et al, 2016). 1% of Cs solution was prepared in 5% of acetic acid (Merck) solution. This solution was added drop wise into TPP solutions of 1% and 3%. The mixture was gently stirred with a speed of 60 rpm for 1h. The formed beads were collected by filtration and immersed in distilled water in order to remove unreacted ingredients. After purification, the beads were dried in oven at 40 °C.

Aqueous gelatin (Fluka, Type B, 280-Bloom) solutions were prepared at 7%, 10% and 14% concentrations and added drop wise into emulsion bath including GA as crosslinker and oil. This bath was prepared using 20 mL of oil and 5 mL of GA solution. The mixture was gently stirred with a speed of 60 rpm for 1h. The formed beads were collected by filtration and immersed in distilled water in order to remove unparticipated ingredients. After purification, the beads were dried in oven at 40 °C. The schematic representation was given in Figure 3.

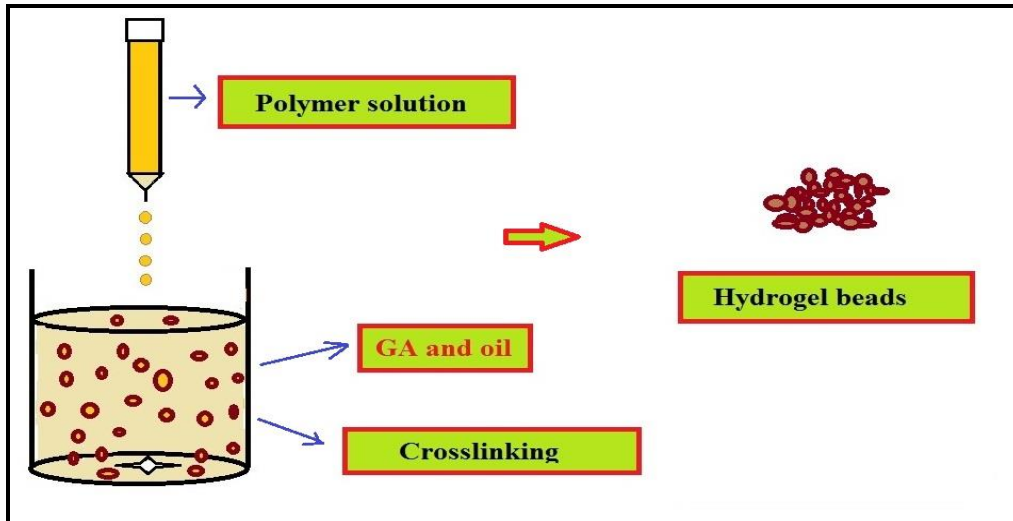


Figure 3. Preparation of hydrogel beads by dropping gelation

Another series of gelatin hydrogel beads were prepared by directly mixing of gelatin and GA solutions in a glass tube. The steps of procedure were presented in Figure 4. Four types of gelatin hydrogels were obtained by using the polymer and crosslinker solutions at different concentration as given in Table 1. Crosslinking reaction was preceded for 24 h at room temperature in a glass tube. The fresh hydrogel rods were taken from the tube and were cut into pieces 0.5 cm long. After the discs were left overnight at room conditions, they were washed several times with distilled water to remove unreacted chemicals [Blanco M.D. et al, 2003].

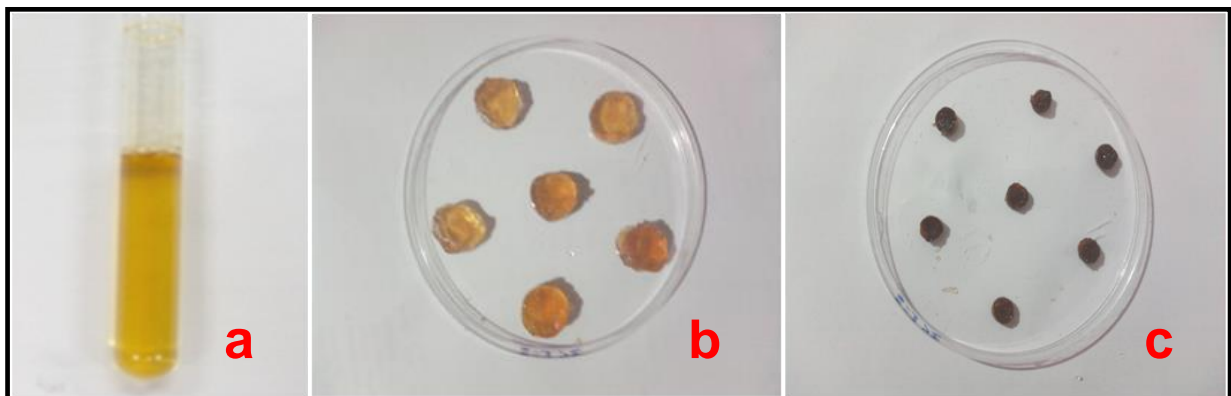


Figure 4. The preparation of gelatin hydrogel beads in tube (a), swollen (b) and dry (c) beads

The abbreviations and preparing conditions of all hydrogels were summarized in Table 1.

Table 1. Preparing conditions of the hydrogels

| HYDROGEL | Gelatin (%) | GA (%) | Chitosan (%) | TPP (%) | C/P |
|----------|--------------------|---------------|--------------|---------|-----|
| C-1 | - | - | 1 | 1 | 1.0 |
| C-2 | - | - | 1 | 3 | 3.0 |
| G-1 | 7 | 25 | - | - | 3.6 |
| G-2 | 10 | 25 | - | - | 2.5 |
| G-3 | 14 | 25 | - | - | 1.8 |
| | Gelatin (g) | GA (g) | | | |
| G-4 | 1.0 | 0.4 | - | - | 0.4 |
| G-5 | 1.0 | 2.0 | - | - | 2.0 |
| G-6 | 1.5 | 0.4 | - | - | 0.3 |
| G-7 | 1.5 | 2.0 | - | - | 1.3 |

Swelling Tests

Swelling tests of hydrogel beads were gravimetrically carried out. The dried discs were left to swell in a Britton-Robinson buffer (BRB) solution (pH = 7.0) at 30°C. Swollen gels, removed from the swelling medium at regular intervals, were dried superficially with a filter paper, weighed, and placed into the same bath. The measurements were performed until a constant weight was reached for each sample. The swelling percentage (S% values) was calculated with the following equation [Pulat and Asil 2009, Chen et al, 2005]:

$$\text{Swelling (\%)} = \frac{M_w - M_d}{M_d} \times 100 \quad (1)$$

where M_w is the wet weight of the sample and M_d is the dry weight of the sample before swelling. Reproducible results for all swelling studies were obtained with triplicate measurements.

Results and Discussion

Cs beads were prepared by ionotropic gelation method based on the interaction of oppositely charged macromolecules. Ionotropic gelation involves simply the interaction of an ionic polymer with oppositely charged ion to initiate cross linking [Sapana A et al., 2014]. TPP has often been used to prepare chitosan particles because TPP is nontoxic, multivalent and able to form gels through ionic interactions. Cs gel beads were obtained by the fixation of its amine groups with TPP (ionic crosslinker). The negative charged TPP ions can react with positive charged chitosan via electrostatic attraction to form ionic crosslinked networks. A schematic mechanism about ionic crosslinking of Cs was presented in Figure 5.

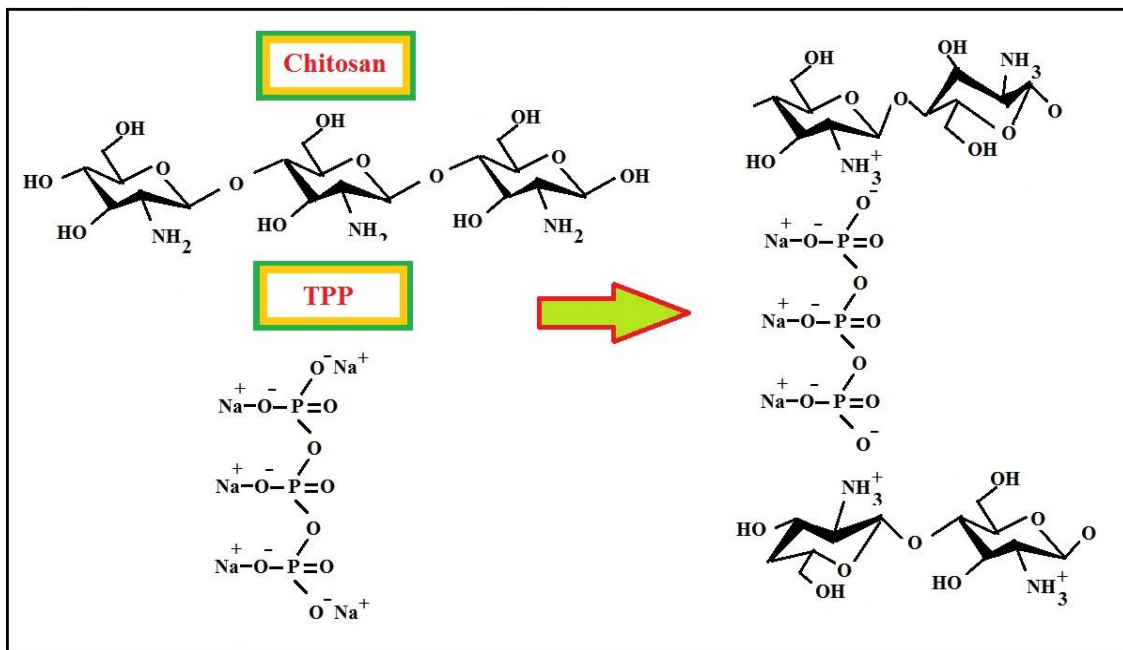


Figure 5. Ionic crosslinking mechanism of Cs with TPP

Gelatin beads were prepared by covalently crosslinking of polymer with GA. A schematic mechanism about ionic crosslinking of Na-Alg was presented in Figure 6.

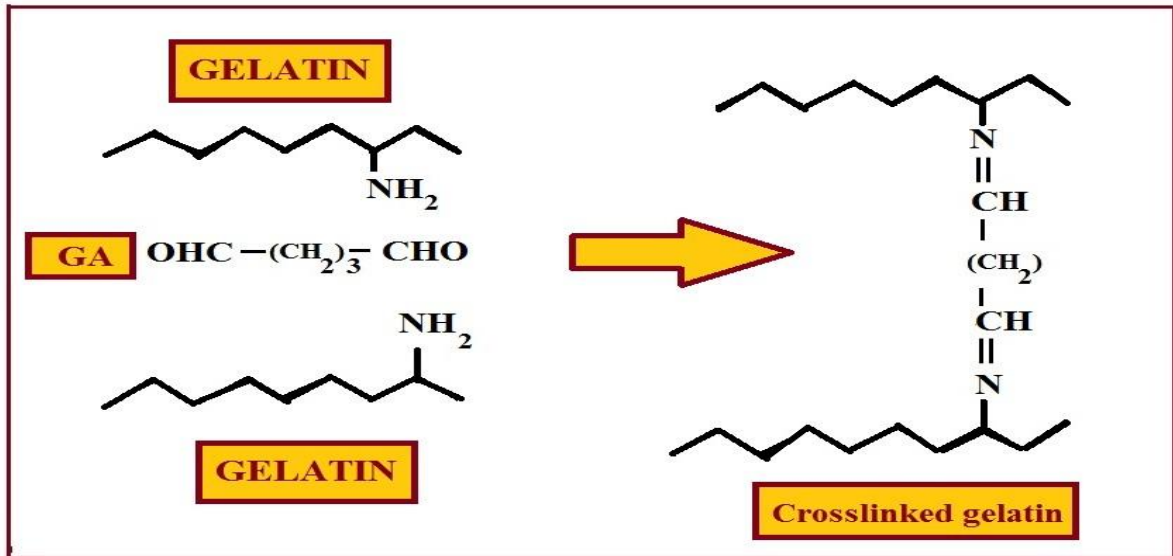


Figure 6. Crosslinking mechanism of gelatin with GA

Swelling Results

All of the swelling percentages belong to hydrogel beads were calculated from Equation 1. The photographs of dry and swollen hydrogels were presented in Figure 4.

The swelling variations of Cs beads with time at pH 7.0 and 30°C were shown in Figure 7. The swelling increased with time initially and then remained constant at close to 12 h. S% values were determined to be 135% for the most swollen hydrogel C-1, and 115 % for the least swollen hydrogel C-2. Swelling values were directly connected with composition, monomer ratio, ionic charge content, polymerization route, type and density of cross-linker, and so forth [El-Sherbiny *et al.*, 2005]. At this part of the work, hydrogels were prepared by changing crosslinker (C) amount while the polymer (P) amount was kept constant. As C/P ratio increased from C-1 to C-2, S% values decreased. This behavior is attributed to the fact that the network chains became inflexible at higher crosslinker density and thus, fewer amounts of water molecules penetrated the hydrogel structure.

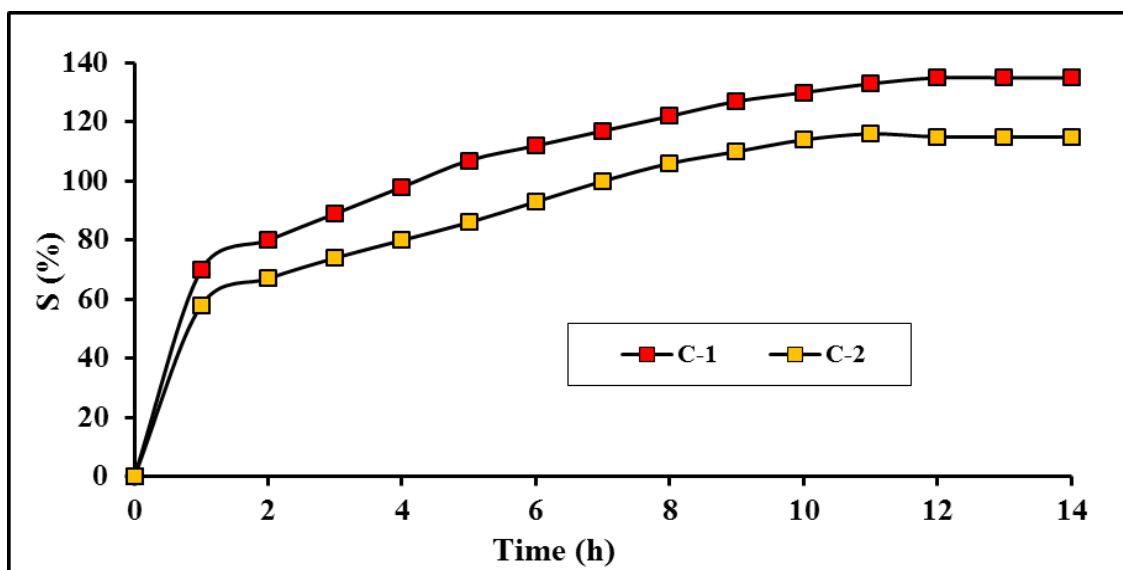


Figure 7. The variations of S% values belongs to chitosan beads with time (30°C; pH=7.0)

Swelling behaviors of the gelatin beads obtained by dropping were followed explained at experimental part. The variation of S% values with time was presented in Figure 8. The swelling increased with time initially and then remained constant at close to 24 h. S% values were determined to be 433% for the most swollen hydrogel G-1,

and 290 % for the least swollen hydrogel G-3. At this part of work, gelatin hydrogel beads were prepared by changing crosslinker amount while the polymer amount was kept constant. G-1 beads include the least amount of gelatin than G-2 and G-3. So, having relatively more crosslinker causes the less swelling value. G-3 beads were the most swollen hydrogel prepared from 14% of gelatin solution.

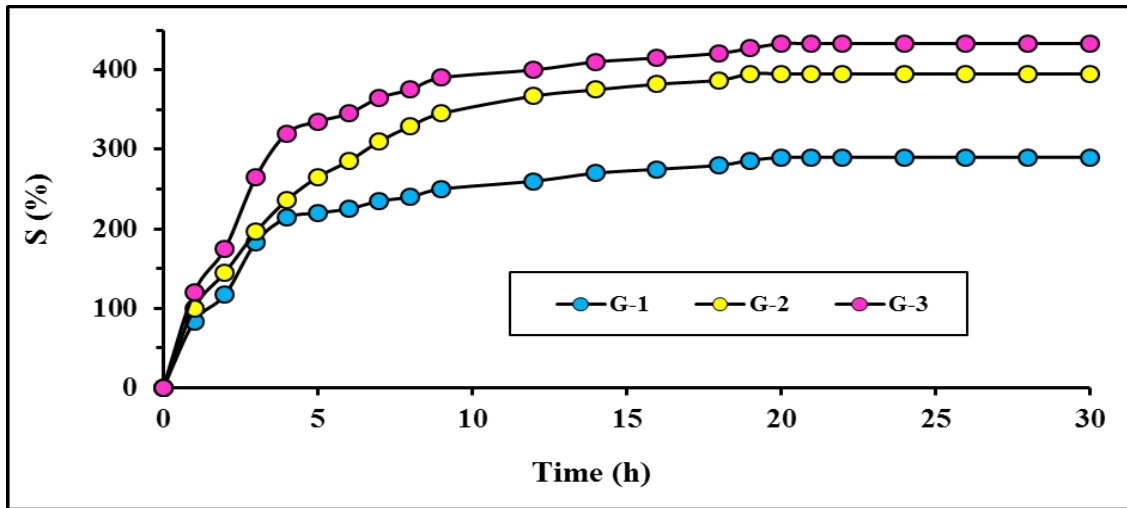


Figure 8. The variations of S% values belongs to gelatin beads with time (30°C; pH=7.0)

The last part of swelling experiment was carried out for the gelatin beads prepared in the glass tube. The variations of S% were given in Figure 9. The swelling increased with time initially and then remained constant at close to 24 h. S% values were determined to be 419% for the most swollen hydrogel G-4, and 304% for the least swollen hydrogel G-5. At this part of work, gelatin hydrogel beads were prepared by changing both crosslinker and polymer amounts. G-4 and G-5 hydrogels were obtained by using same amount of polymer despite varying amounts of crosslinker. C/P rates changed from 0.4 to 2.0 caused decreasing of S% values from 419 to 304. G-6 and G-7 hydrogels were prepared by changing C/P rates from 0.3 to 1.3. As the rates increases, S% values decreased from 385 to 347. All of the swelling values are compatible with their polymer/crosslinker contents.

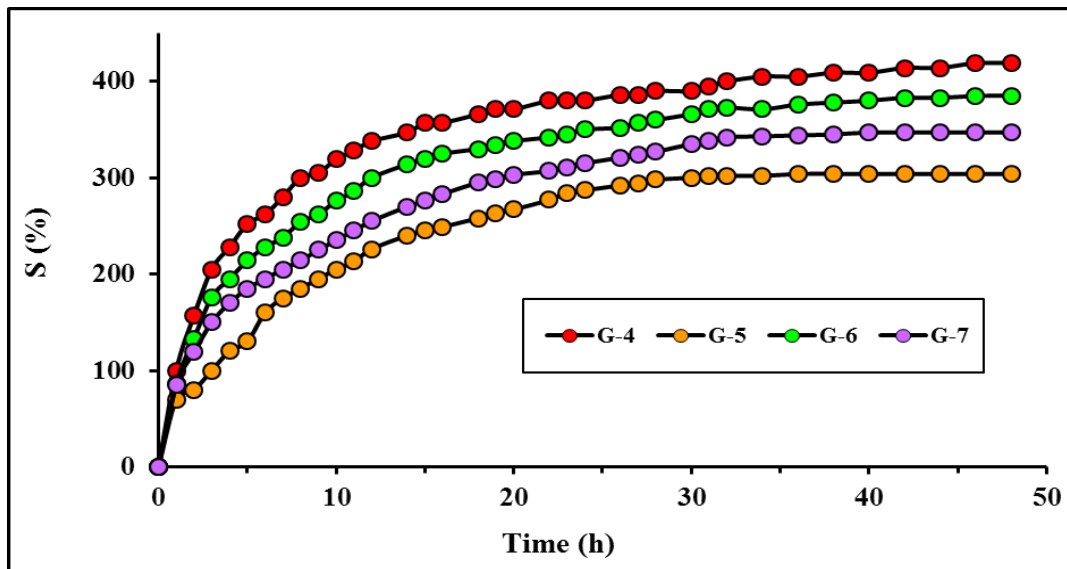


Figure 9. The variations of S% values belongs to gelatin beads with time (prepared in glass tube, 30°C; pH=7.0)

Conclusion

The results of the present work indicate that the beads type of hydrogels could be prepared by using gelatin and chitosan natural polymers. GA and TPP are good choices to obtain various hydrogels having different swelling values.

References

- Bigi A., Cojazzi G., Panzavolta S., Rubini K., Roveri N. (2001). Mechanical and thermal properties of gelatin films at different degrees of glutaraldehyde crosslinking. *Biomat.* 22, 763-768.
- Blanco M.D., Bernardo M.V., Teijon C., Sastre R.L., Teijon J.M.: Transdermal application of bupivacaine-loaded p (AAm-co-mm itacon) hydrogels. *Int. J. Pharm.* 255,99-107 (2003).
- Chen K., Ku Y., Lin H., Yan T., Sheu D., Chen T., Lin F. (2005). Preparation and characterization of pH-sensitive poly (N-vinyl 2-pyrrolidone/itaconic acid) copolymer hydrogels. *Mat. Chem. Phys.* 91, 484-489.
- El-Sherbiny I.M., Lins R.J., Abdel-Bary E.M., Harding D.R.K.(2005). Preparation, characterization, swelling and in vitro drug release behaviour of poly(N-AG-chitosan) interpolymeric pH and therm.-responsive hydrogels. *Europ. Polym. J.* 41, 2584-2591.
- Gilsenan P, Ross-Murphy S. 2001. Shear creep of gelatin gels from mammalian and piscine collagens. *International Journal of Biological Macromolecules* 29: 53–61.
- Kotze A F, et all. (1999). Chitosan for enhanced intestinal permeability: prospects for derivatives soluble in neutral and basic environments. *Eur J Pharma Sci.* 7:2, 145-151.
- Kushibiki T, Tomoshige R, Fukunaka Y, Kakemi M, Tabataa Y. (2003). In vivo release and gene expression of plasmid DNA by hydrogels of gelatin with different cationization extents. *Journal of Control Release* 90: 207–216.
- Macleod GS, et.all.(1999). Selective drug delivery to the colon using pectin, chitosan, hydroxypropyl methylcellulose film coated tablets. *Int J Pharm.* 187:251–257.
- Nitsae M., Madjid A., Hakim L. and Sabarudin A., (2016). Preparation of chitosan beads using tripolyphosphate and ethylene glycol diglycidyl ether as crosslinker for Cr(vi) adsorption. *Chemistry & chemical Technology*, Vol. 10, No. 1., 105-113.
- Pulat M, Tan N, Onurdag FK. (2011). Swelling Dynamics of IPN Hydrogels Including Acrylamide-Acrylic Acid-Chitosan and Evaluation of their Potential for Controlled Release of Piperacillin-Tazobactam, *Journal of Applied Polymer Science*, Vol. 120, 441–450.
- Pulat M., Asil D. (2009). Fluconazole release through semi-ipn hydrogels based on chitosan, AA, and citraconic acid. *J. Appl. Polym. Sci.* 113, 2613-2619.
- Pulat M., Yoltay N. (2016). Smart fertilizers: preparation and characterization of gelatin-based hydrogels for controlled release of MAP and AN fertilizers, *Agrochimica*, 60:4, 249-261.
- Pulat M., Akalin G.O. (2013). Preparation and characterization of gelatin hydrogel support for immobilization of *C. Rugosa* lipase. *Artif. Cells Nanomed. Biotechnol.* 41, 145-151.
- Sapana P Ahirrao, Paraag S Gide, B Shrivastav, and Pankaj Sharma. Iontropic Gelation: (2014). A Promising Cross Linking Technique for Hydrogels. *research and reviews: journal of pharmaceutics and nanotechnology*, 2 :1, 1-6.

Author Information

Mehlika Pulat

Department of Chemistry, Faculty of Sciences,
Gazi University, Teknikokullar,
Ankara/Turkey
Contact E-mail: mpulat@gazi.edu.tr

A New Potential Model for Cluster Decay of the Heavy Nuclei

Orhan BAYRAK
Akdeniz University

Abstract: We calculate cluster decay half-life of the heavy nuclei by using the WKB barrier potential model. In this model, the cluster is already preformed in the parent nucleus and orbiting around the daughter nucleus before tunneling through a potential barrier between the cluster and daughter nuclei. In this paper, we purpose the Morse potential describing interactions between the cluster and daughter nuclei in order to calculate the cluster decay half-life of the heavy nuclei. The Morse potential model is used frequently the vibrational and rotational energy spectrum of diatomic molecules and atomic scattering process. Similar calculation for Morse potential is used the vibrational and rotational energy spectrum of the nucleus and there is also experimental evidence that the nucleus has a molecular structure. Since the nucleus has a molecular structure, we use the Morse potential in order to describe the interactions between the cluster and daughter nuclei and show that the Morse potential is a convenient model in order to explain cluster decay half-life of the heavy nuclei.

Keywords: Cluster decay, Morse potential, WKB method, Decay half-life

Introduction

Investigating the cluster decay of a heavy nucleus is a convenient way in order to probe the experimental observable of the nucleus for both nuclear structure and reactions. In literature, some studies have been carried out for the idea that light or heavy nuclei are clustered as alpha or heavier cluster. Pei and Xu (2007) used a mean-field-type cluster potential to model decay of alpha particle from ^{10}Be , ^{20}Ne and ^{12}C parent nuclei by using the WKB (Wentzel-Kramers-Brillouin) method. It was calculated the alpha decay widths for the excited states of ^{10}Be , ^{20}Ne and ^{12}C parent nuclei and compared the experimental data. Xu et al. (2010) analyzed the decay mechanisms of the ^8Be and ^{12}C cluster from the ^{24}Mg nucleus within the framework of the Woods-Saxon potential model and calculated the decay widths for the excited rotational band levels of the ^{24}Mg nucleus. Another phenomenological model is the proximity potential and has extensive application in the explaining the cluster decay mechanism of the heavy nuclei (Santhosh, 2012; Zheng, 2013; Zhang, 2016). The proximity potential model was also applied to the alpha and clustering mechanisms of super-heavy nuclei ($^{294-326}122$) (Santhosh, 2009). Soylu et al. (2012) examined the effect of deformation on decay half-lives in the cluster decay processes of parent nuclei by using Woods-Saxon square potential with deforming nuclear radius. The decay half-life of ^{14}C , ^{20}O , ^{23}F , $^{24-26}\text{Ne}$, $^{28-30}\text{Mg}$ and ^{32}Si cluster from heavy nuclei were investigated by using the generalized liquid drop model formula for heavy nuclei (Royer, 2001). Another model in the explaining nuclear decay observable is the microscopic model. Microscopic density-dependent double folding potential model, which takes into account the M3Y nucleon-nucleon interaction, was used in order to investigate the clustering mechanisms of heavy nuclei (Ren, 2004; Delion, 2007; Adel, 2017).

In this paper, taking into account that the nucleus is a molecular structure (Oertzen et. al. (2006), we suggest the Morse potential in order to explain the cluster decay observable of heavy nuclei. In next section, we present model and calculation procedure. The brief discussion for obtained numerical results are given in Results and Discussion section. Then, we give a conclusion.

Method

According to the cluster model, the cluster is already preformed in the parent nucleus and orbiting around the daughter nucleus before tunneling through a potential barrier constituted between the cluster and daughter nuclei. The effective potential between the cluster and daughter nuclei is

$$V_{eff}(r) = V_L(r) + V_N(r) + V_C(r),$$

where $V_L(r)$, $V_N(r)$ and $V_C(r)$ are the centrifugal, nuclear and Coulomb potentials, respectively. In the calculation, modified version of the centrifugal potential is used (Langer, 1937) and the Coulomb potential consists of the point charged cluster and uniformly charged spherical daughter nucleus with radius R_C (Satchler, 1983). The nuclear potential is the Morse potential and given as follows (Morse, 1929; Bayrak et. al., 2006),

$$V_N(r) = D_e(e^{-a(r-r_e)} - 2e^{-a(r-re)}),$$

where D_e , a and r_e are dissociation energy, a control parameter and the equilibrium distance (bound length) between nuclei.

The Alpha decay width is

$$\Gamma = P_c F \frac{\hbar^2}{4\mu} T,$$

where P_c , F and T are the form factor, normalization factor and decay probability of the cluster nucleus from the parent nucleus respectively (Xu et. al., 2008). In literature, the form factor P_c is found to vary in the range of $P_c = 0,005 - 1$ (Bai et. al., 2019). In the calculation, we take $P_c = 1$. Normalization factor F (Xu et. al., 2008) is,

$$F = \left(\int_{r_1}^{r_2} dr \frac{1}{k(r)} \right)^{-1},$$

where r_1 and r_2 are the inner and outer turning points and calculated from root of equation $V_{eff}(r) = Q$ and $k(r) = \sqrt{\frac{2\mu}{\hbar^2} |V_{eff}(r) - Q|}$. Here μ and Q are the reduced mass of the cluster and daughter nucleus and reaction energy, respectively (Xu et. al., 2008). Decay probability can be calculated by WKB methods as follows,

$$T = \exp\left(-2 \int_{r_2}^{r_3} k(r) dr\right),$$

where r_3 is the outermost turning point. The cluster decay half-life can be calculated from $T_{1/2} = \hbar \ln 2 / \Gamma$ (Xu et. al., 2008). In order to eliminate the uncertainty in the depth of the potential we can use the Bohr-Sommerfeld formula in following form (Xu et. al., 2008),

$$\int_{r_1}^{r_2} k(r) dr = (G - L + 1) \frac{\pi}{2}$$

where G and L are the global and angular momentum quantum numbers. In the calculation we take $G = 5Ac$ and $L = 0$ (Buck et. al., 1996). Here Ac is atomic mass number of cluster nucleus.

Results and Discussion

We systematically calculate the cluster decay half-life of Ra, Th, U and Pu nuclei by using WKB method within the framework of the Bohr-Sommerfeld quantization formula. In the calculation we use the Morse potential for the nuclear potential. In order to eliminate uncertainty in depth of the nuclear potential, we take into account the clustering effect by using the Bohr-Sommerfeld quantization formula. In the calculation the equilibrium distance is taken as $r_e = 1.1 \text{ fm}$. In order to obtain a best fit for the experimental data, we search optimum control parameter and find in the range of 0.59-0.61 fm for variation of atomic mass number of parent nucleus A. After considering variation of parameter a with A, we develop a formula as follow,

$$a = 8618.71 - 6.24252 A + 990966.93/A - 174267.854/\sqrt{A}$$

We calculate decay half- life of the Ra, Th, U and Pu parent nuclei with the same potential parameters.

Table 1. Comparison of theoretical and experimental half-lives (Buck et. al., 1996)

| Decay | Q(MeV) | $T_{1/2}$ (Square Well) (s) | $T_{1/2}$ (cosh) | $T_{1/2}$ (Mixed Woods-Saxon) (s) | $T_{1/2}$ (Present Study) (s) | $T_{1/2}$ (Experimental Data) (s) |
|---|--------|-----------------------------|-----------------------|-----------------------------------|-------------------------------|-----------------------------------|
| $^{222}_{88}\text{Ra} \rightarrow ^{208}_{82}\text{Pb} + ^{14}_6\text{C}$ | 33.158 | 1.28×10^{11} | 1.38×10^{11} | 1.93×10^{11} | 0.98×10^{11} | $(1.01 \pm 0.14) \times 10^{11}$ |
| $^{224}_{88}\text{Ra} \rightarrow ^{210}_{82}\text{Pb} + ^{14}_6\text{C}$ | 30.639 | 5.31×10^{15} | 7.36×10^{15} | 1.30×10^{16} | 10.83×10^{15} | $(8.25 \pm 2.22) \times 10^{15}$ |
| $^{226}_{88}\text{Ra} \rightarrow ^{212}_{82}\text{Pb} + ^{14}_6\text{C}$ | 28.316 | 4.07×10^{20} | 7.06×10^{20} | 1.21×10^{21} | 2.77×10^{21} | $(2.21 \pm 0.96) \times 10^{21}$ |
| $^{228}_{90}\text{Th} \rightarrow ^{208}_{82}\text{Pb} + ^{20}_8\text{O}$ | 44.867 | 3.95×10^{21} | 5.64×10^{21} | 5.78×10^{21} | 6.95×10^{20} | $(5.29 \pm 1.01) \times 10^{20}$ |
| $^{230}_{90}\text{Th} \rightarrow ^{206}_{80}\text{Hg} + ^{24}_{10}\text{Ne}$ | 57.954 | 3.73×10^{24} | 5.16×10^{24} | 4.83×10^{24} | 1.44×10^{24} | $(4.10 \pm 0.95) \times 10^{24}$ |
| $^{232}_{92}\text{U} \rightarrow ^{208}_{82}\text{Pb} + ^{24}_{10}\text{Ne}$ | 62.492 | 5.77×10^{20} | 5.68×10^{20} | 4.75×10^{20} | 5.79×10^{20} | $(2.50 \pm 0.30) \times 10^{20}$ |
| $^{234}_{92}\text{U} \rightarrow ^{206}_{80}\text{Hg} + ^{28}_{12}\text{Mg}$ | 74.349 | 2.30×10^{25} | 2.51×10^{25} | 2.13×10^{25} | 8.84×10^{25} | $(5.50 \pm 1.00) \times 10^{25}$ |
| $^{236}_{94}\text{Pu} \rightarrow ^{208}_{82}\text{Pb} + ^{28}_{12}\text{Mg}$ | 79.896 | 2.72×10^{21} | 1.95×10^{21} | 1.42×10^{21} | 4.46×10^{21} | 4.7×10^{21} |
| $^{238}_{94}\text{Pu} \rightarrow ^{206}_{80}\text{Hg} + ^{32}_{14}\text{Si}$ | 91.474 | 6.79×10^{25} | 5.64×10^{25} | 4.19×10^{25} | 2.26×10^{25} | $(1.89 \pm 0.68) \times 10^{25}$ |

In Table 1, we compare the cluster decay half-lives obtained the Morse potential with the experimental data. We also compare other potential models (the square well, cosh potentials) in literature (Buck et. al., 1996). In the calculation, we see that the Morse potential is also a convenient model in the explaining cluster decay half-lives of heavy nuclei (Table 1).

Conclusion

We systematically explain the cluster decay half-lives of Ra, Th, U and Pu nuclei within the framework of the Bohr-Sommerfeld quantization by using WKB method. We compare our result with experimental data and obtain good agreement between our result and experimental data. We see that the Morse potential is also good model in the explaining the decay mechanism of heavy nuclei. But, in order to increase the reliability of our model potential, we have to extent the calculations for the Morse potential to all cluster decay experimental half-lives data of heavy nuclei. These calculations are in progress.

Acknowledgements

This work was supported by the scientific research projects units of Akdeniz University.

References

- Adel, A. and Alharbi, T. (2017). Cluster decay half-lives of trans-lead nuclei based on a finite-range nucleon–nucleon interaction. *Nuclear Physics A*, 958:187–201.
- Bai, D., Ren, Z., Röpkke, G. (2019). α clustering from the quartet model. *Phys. Rev. C*, 99, 034305 (2019).
- Bayrak, O., Boztosun, I., (2006). Arbitrary ℓ -state solutions of the rotating Morse potential by the asymptotic iteration method. *J. Phys. A: Math. Gen.* 39, 6955.
- Buck, B., Merchant, A.C., Perez, S. M. (1996). Exotic Cluster States in Actinide Nuclei. *Phys. Review Lett.*, 76, 380-383.
- Delion, D. S. et al., (2007). Evidence for α clustering in heavy and super heavy nuclei. *Phys. Rev. C*, 6, 044318.
- Langer, R. E., (1937). On the Connection Formulas and the Solutions of the Wave Equation. *Phys. Rev.*, 51, 669.
- Morse, Philip M., (1929). Diatomic Molecules According to the Wave Mechanics. II. Vibrational Levels. *Phys. Rev.* 34, 57.
- Pei, J. C. and Xu, F. R., (2007). Helium-cluster decay widths of molecular states in beryllium and carbon isotopes. *Physics Letters B*, 650, 224–228.
- Ren, Z., Xu, C. and Wang, Z., (2004). New perspective on complex cluster radioactivity of heavy nuclei. *Phys. Rev. C*, 70, 034304.
- Royer, G. and Moustabchir, R., (2001). Light nucleus emission within a generalized liquid-drop model and quasimolecular shapes. *Nuclear Physics A*, 683, 182–206.
- Santhosh, K. P., and Biju, R. K., (2009). Alpha decay, cluster decay and spontaneous fission in $^{294-326}_{122}$ isotopes. *J. Phys. G: Nucl. Part. Phys.*, 36, 015107.
- Santhosh, K. P., Priyanka, B. and Unnikrishnan, M. S., (2012). Cluster decay half-lives of trans-lead nuclei within the Coulomb and proximity potential model. *Nuclear Physics A*, 889, 29–50.
- Satchler, G. R. (1983). *Direct Nuclear Reactions*. Oxford, Clarendon Press.
- Soylu, A. et al. (2012). Role of the cluster deformations in explaining the exotic decay half-lives. *Eur. Phys. J. A*, 48, 128.
- Oertzen, W. von, Freer, M., Enyo, Y. K., (2006). Nuclear clusters and nuclear molecules. *Physics Reports*, 432, 43 – 113
- Xu, C. and Ren, Z., (2008). Alpha Decay Half-Lives of Ground and Isometric States of Exotic Nuclei Around Closed Shells. *Phys. Rev. C*, 78, 057302.
- Xu, C., et al., (2010). Molecular structure of highly excited resonant states in ^{24}Mg and the corresponding $8\text{Be} + 16\text{O}$ and $12\text{C} + 12\text{C}$ decays. *Phys. Rev. C*, 81, 054319.
- Zheng, L. et al., (2013). Calculation of half-lives of cluster decay by using proximity potential with a new universal function. *Nuclear Physics A*, 915, 70–77.
- Zhang, G. L., et al. (2016). Comparative studies for different proximity potentials applied to large cluster radioactivity of nuclei. *Nuclear Physics A*, 951, 86–96.

Author Information

Orhan Bayrak

Akdeniz University
Akdeniz University, Dumlupınar Boulevard,
07058 Campus, Antalya / TURKEY
Contact E-mail: bayrak@akdeniz.edu.tr

Upconversion Emission Properties of Nb₂O₅ Modified Tellurite-Based Glasses Activated with Rare Earth Ions

Huseyin ERTAP
Kafkas University

Gokhan BILIR
Kafkas University

Lidong MA
Boston College

Baldassare DI BARTOLO
Boston College

Abstract: The upconversion emission properties of Nb₂O₅ modified tellurite-based glasses activated with Er³⁺, Tm³⁺, Ho³⁺, and Yb³⁺ ions were studied. The glass samples were obtained using melt-quenching method. The optical absorption spectra of the samples were collected in the 400-1100 nm wavelength range at room temperature. The forbidden gap of the glasses were determined using the absorption spectra of the samples. The upconversion emission of samples were obtained under the 975 nm laser excitation and recorded in the 350-900 nm wavelength range. Three primary colors were simultaneously obtained from the samples under the 975 nm excitation. The CIE-1931 coordinates and the correlated color temperatures of obtained upconversion emissions were also determined using the upconversion emission spectra.

Keywords: Tellurite glasses, Nb₂O₅, Rare earth ions, Upconversion

Introduction

Rare earth ions (RE) activated heavy metal oxide glasses, like tellurite and antimony-based glasses, have been subject to a special interest in last few decades due to their low phonon energies among other oxide glass systems which increases the quantum efficiency from excited states of RE ions via decreasing the non-radiative energy losses due to the phonon vibrations in these matrices and provides the possibility of developing more efficient photonic devices. On the other hand, the upconversion (UC) mechanisms of the RE ions activated glasses are also attract special attention because they are possessing some superior properties compared to bulk crystals like longer lifetime of REs in glasses and their ability to contain considerable amount of RE ions without inducing crystallization (Bilir, 2017).

Tellurite glasses emerge for the many excellent properties for photonics applications, like low melting temperature (~750°C), chemical and thermal stability, high dielectric constant, wide transparency region (0.3 – 7 μm). They also exhibit phonon energies of about 780 cm⁻¹ and high refractive index (2.1 to 2.3) which are excellent properties for UC purposes because of decreasing the non-radiative energy losses due to the phonon vibrations and increasing the local field correction at the dopant site, respectively (Bilir, et al., 2016; Bilir&Ozen, 2011; Bilir, 2015; Bilir, et al., 2011; Burtan-Gwizdala, et al., 2017; El-Mallawany, 2002).

Since TeO₂ is a conditional glass former and is the most stable oxide form of the tellurium, it cannot able to form glassy matrix easily by itself. Network modifiers should be added into the system to obtain tellurite glasses. In this context, we added Niobium Oxide (Nb₂O₅) into the system to obtain tellurite glasses. We also

- This is an Open Access article distributed under the terms of the Creative Commons Attribution-Noncommercial 4.0 Unported License, permitting all non-commercial use, distribution, and reproduction in any medium, provided the original work is properly cited.

- Selection and peer-review under responsibility of the Organizing Committee of the Conference

added Er^{3+} , Tm^{3+} , Ho^{3+} and Yb^{3+} ions into the system to investigate the UC emission properties of the glasses. To do so, we measured the optical absorption, and the UC emission spectra of samples.

Method

The glass samples with the compositions $0.1\text{Nb}_2\text{O}_5 + (0.9-x-y-z)\text{TeO}_2 + x\text{Er}_2\text{O}_3 + y\text{Tm}_2\text{O}_3 + z\text{Yb}_2\text{O}_3$ ($x = 0.005$, $y = 0.003$, and $z = 0.03$), and $0.1\text{Nb}_2\text{O}_5 + (0.9-x-y-z)\text{TeO}_2 + x\text{Tm}_2\text{O}_3 + y\text{Ho}_2\text{O}_3 + z\text{Yb}_2\text{O}_3$ ($x = 0.005$, $y = 0.007$, and $z = 0.03$) were synthesized by melting the ultrapure (99.99%) TeO_2 , Nb_2O_5 , Er_2O_3 , Tm_2O_3 , and Yb_2O_3 powders which is followed by rapid quenching of the glass melts. 7g of batches were prepared using a high precision scale, mixed in an agate mortar, and transferred into a platinum crucible with a lid. The mixture put into an electric furnace and heated up to $850\text{ }^\circ\text{C}$ for an hour. The obtained glass melts, then, were poured onto a preheated ($250\text{ }^\circ\text{C}$) stainless steel mold. After that, the glass samples were thermally treated below their glass transition temperature (at about $250\text{ }^\circ\text{C}$) for an hour to reduce thermal stresses due to the high synthesis temperatures. The obtained as-cast glass samples were polished to form two parallel shiny surfaces for optical measurements.

The optical absorption characteristics of the samples were determined using a Perkin Elmer Lambda 25 UV-Vis spectrophotometer in the 300 – 1100 nm wavelength range. The UC luminescence spectra of the samples were collected using a Sheamann model laser diode operated at 975 nm as an excitation source and an Ocean Optics USB4000-VIS-NIR spectrophotometer for the detection of the luminescence signal. A short pass filter with a 950 nm cut off wavelength was used to avoid the spurious modes of the laser and the harmonics of the emission. All optical measurements were conducted under ambient conditions.

Results and Discussion

Glass samples were successfully synthesized using the melt quenching technique. The optical absorption spectra of the samples, in the 300 – 1100 nm wavelength range are given in Figure 1 with the corresponding transitions of the doped RE ions. As seen from Figure, several characteristic group of ground state transitions were observed due to the $4f^n$ electronic configuration of the RE ions. The increase in the spectra below the 450 nm is due to the forbidden energy gap of glass samples. The calculated direct and indirect band gap values using the Davis – Mott theory (Davis&Mott, 1970) were found to be 2.856 eV and 2.504 eV for the $\text{Er}^{3+}\text{-Tm}^{3+}\text{-Yb}^{3+}$ activated sample, and 2.866 eV and 2.582 eV for the $\text{Tm}^{3+}\text{-Ho}^{3+}\text{-Yb}^{3+}$ activated sample, respectively.

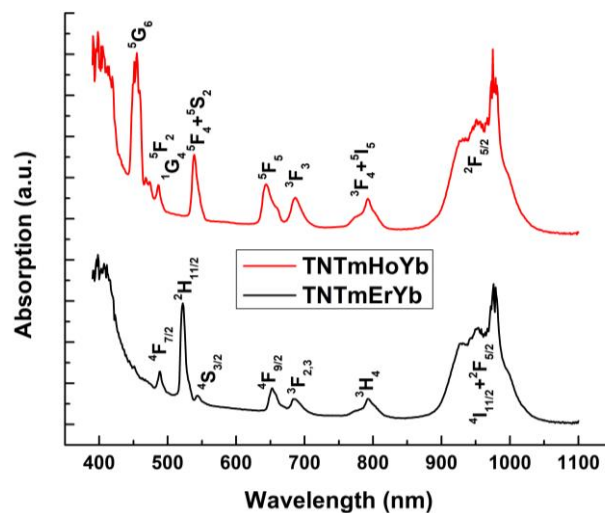


Figure 1. Absorption spectra of the glass samples

The upconversion emission spectra of samples which is collected under 975 nm excitation in the 350 – 900 nm wavelength range are given in Figure 2. The insets are the energy level diagrams of the RE ions which show the possible mechanisms responsible for the appearance of different UV-Visible emissions upon 975 nm laser diode excitation. As seen from Figure, five upconversion bands in the blue (476 nm), green (524 nm and 546 nm), red (655 nm), and near-infrared (808 nm) spectral regions for the $\text{Er}^{3+}\text{-Tm}^{3+}\text{-Yb}^{3+}$ activated sample and three upconversion emission bands in the green (547 nm), red (660 nm), and near-infrared (804 nm) for the $\text{Tm}^{3+}\text{-}$

Ho³⁺-Yb³⁺ activated sample have been observed. The observed upconversion emission bands can be easily assigned to the transitions from upper populated levels to the lower energy levels of the RE ions. In Er³⁺-Tm³⁺-Yb³⁺ activated case, the emission bands are due to the ¹D₂→³F₄, ¹G₄→³H₆ transitions of Tm³⁺, the ¹D₂→³F₄, ¹G₄→³H₆ transitions of Tm³⁺, ²H_{11/2}, ⁴S_{3/2}→⁴I_{15/2} transitions of Er³⁺, ⁴F_{9/2}→⁴I_{15/2}, ¹G₄→³F₄ transitions of Er³⁺ and Tm³⁺, and ¹G₄→³H₅, ³H₄→³H₆ transitions of Tm³⁺, respectively. The upconversion emission bands in the Tm³⁺-Ho³⁺-Yb³⁺ activated sample assigned to the ⁵S₂→⁵F₄, ⁵F₄→⁵I₈ transitions of Ho³⁺, the ¹G₄→³F₄, ⁵F₅→⁵I₈ transitions of Tm³⁺ and Ho³⁺, and ¹G₄→³H₅, ³H₄→³H₆ transitions of Tm³⁺, respectively.

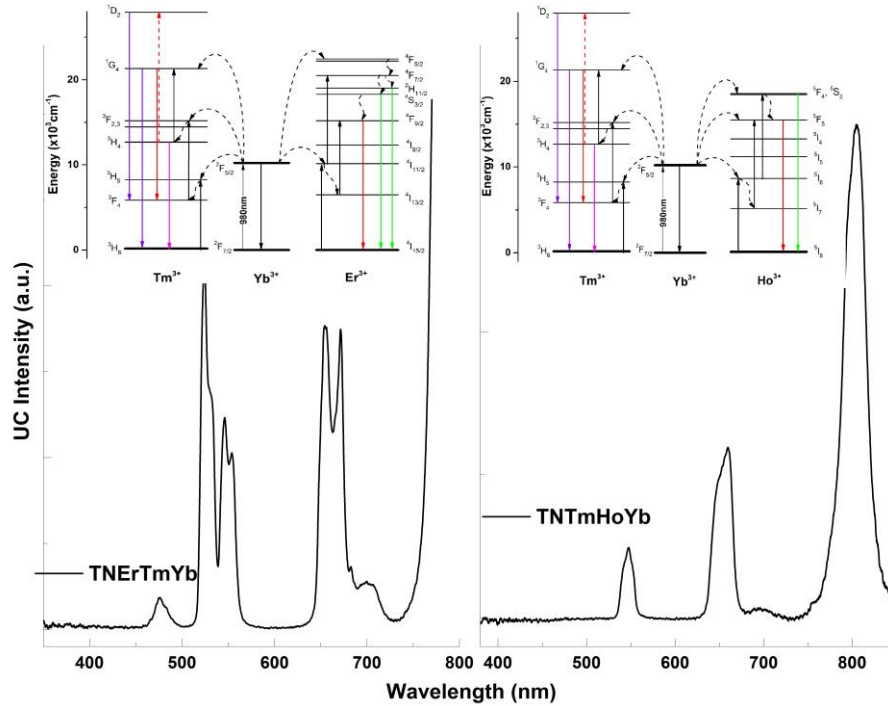


Figure 2. Upconversion emission spectra of samples. Insets show the energy level diagrams

The responsible mechanism to obtain UC emissions is mostly Energy Transfer (ET) process from ytterbium ions to the other RE ions because of Yb³⁺ ions having the highest concentration and its high absorption cross-section in the wavelength of the excitation source. To better understand the mechanisms behind the upconversion emissions, the band intensities dependence on the pumping excitation power were measured (the power law; $I \propto P^n$, where n is the number of excitation photons involved in process) was employed to determine the how many excitation photons included in the upconversion mechanisms. The n values were found as 2.42, 2.14, 1.78, and 1.65 for blue, green, red and IR emission in the Er³⁺-Tm³⁺-Yb³⁺ activated sample and 1.87, 1.78, and 1.68 for green, red, and IR emissions in the Tm³⁺-Ho³⁺-Yb³⁺ activated sample, respectively.

The CIE 1031 color coordinates of the samples were also determined to estimate the color of the visible emissions and results are given Figure 3. It is clearly seen from figure that the visible upconversion emissions from Er³⁺-Tm³⁺-Yb³⁺ activated sample lie in the reddish-orange region to greenish region of the CIE diagram, while those of the Tm³⁺-Ho³⁺-Yb³⁺ activated sample lie in the reddish-orange region of the CIE 1931 diagram.

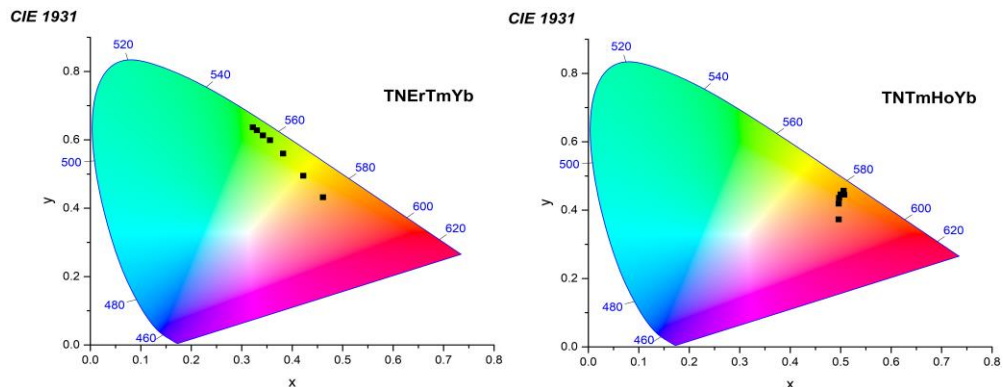


Figure 3. CIE 1931 coordinates of obtained upconversion visible emissions

Conclusion

Nb₂O₅ modified tellurite glasses triply doped with different type of RE ions were successfully synthesized using traditional melting and quenching method. The upconversion emission properties of samples were determined. The primary colors were simultaneously obtained from samples and the possible mechanisms responsible for the upconversion visible emissions were explained in the light of energy level diagrams and the power law, which gives number of excitation photons involved in the upconversion mechanisms.

Acknowledgements

This research has been supported by the Coordination Office of the Scientific Research Projects of Kafkas University under the project numbered 2017-FM-57.

References

- Bilir, G. (2017). Intense upconverted white light emission from Tm³⁺-Er³⁺+Yb³⁺ doped zinc tungsten tellurite glasses. *SDU J. Nat. Appl. Sci.*, 21, 768-790.
- Bilir, G., Kaya, A., Cinkaya, H., Eryürek, G. (2016). Spectroscopic investigation of zinc tellurite glasses doped with Yb³⁺ and Er³⁺ ions. *Spectrochim. Acta A Mol. Biomol. Spectrosc.*, 165, 183-190.
- Bilir, G., Ozen, G. (2011). Optical absorption and emission properties of Nd³⁺ in TeO₂-WO₃ and TeO₂-WO₃-CdO glasses. *Physica B.*, 406, 4007-4013.
- Bilir, G. (2015). Synthesis and Spectroscopy of Nd³⁺ doped tellurite-based glasses. *Int. J. Appl. Glass Sci.*, 6, 397-405.
- Bilir, G., Mustafaoğlu, N., Ozen, G., Di Bartolo, B. (2011). Characterization of emission properties of Er³⁺ ions in TeO₂-CdF₂-WO₃ glasses. *Spectrochim. Acta A Mol. Biomol. Spectrosc.*, 83, 314-321.
- Burtan-Gwizdala, B et al. (2017). Spectroscopic properties of Er³⁺-doped fluorotellurite glasses containing various modifiers. *Opt. Mater.*, 73, 509-516.
- Davis, F. A., Mott, N. F. (1970). Conduction in non-crystalline systems V. Conductivity, optical absorption and photoconductivity in amorphous semiconductors. *Philos. Mag.*, 22, 903-922.
- El-Mallawany, R. A. H. (2002). Tellurite Glasses Handbook: Physical Properties and Data. (New York: CRC Press)

Author Information

Hüseyin Ertap
Kafkas University
36100 Kars / TURKEY
Contact E-mail: huseyinertap@gmail.com

Gökhan Bilir
Kafkas University
36100 Kars / TURKEY

Lidong MA
Boston College
MA 02467, USA

Baldassare Di Bartolo
Boston College
MA 02467, USA

Theoretical Investigation of Nmr, Conformational, Vibrational and Electronic Structure of 3-Bromo-4-(2-Pyridyl) Thiophene

Guventurk UGURLU
Kafkas University

Abstract: Compounds containing thiophene and pyridine rings very much attention due to their biological activity. The molecular geometry, vibration frequencies, dipole moment (μ), polarizability (α), hyperpolarizability (β) of 3-Bromo-4-(2-pyridyl) thiophene have been calculated at ab initio Hartree Fock (HF) and Density Functional Theory (DFT / B3LYP) with 6-311++G (d, p) basis set. The highest occupied molecular orbital (HOMO), the lowest unoccupied molecular orbital (LUMO) of title molecule has been computed and their respective gap (ΔE_g) have been examined. The gauge independent atomic orbital (GIAO) ^1H - and ^{13}C -NMR chemical shifts values of studied molecule in the ground state in both gas phase and in solution of chloroform and dimethyl sulfoxide have been investigated using the HF and DFT/B3LYP employing different basis sets. In addition, the potential energy curve of the molecule as a function of the dihedral angle (N-C3-C6-C7) have been carried out using the 6-31G basis set in both methods. The results of vibrational parameters were analyzed by VEDA 4 software. The ^1H chemical shifts values of the molecule, which were calculated by both methods, were compared with the data in the literature and there was a good agreement between the structural parameters.

Keywords: 3-Bromo-4-(2-pyridyl) thiophene, HF, DFT, Vibration frequencies, Polarizability (α)

Introduction

Many compounds containing pyridine and thiophene continue to attract the interest of researchers due to their biological properties. Thiophenes with broad spectrum of biological activity and many derivatives has important features such as potential analgesics (Başoğlu et al. 2017), anticonvulsant (Kulandasamy et al. 2009), antiinflammatory (Mohareb et al. 2015), antibacterial (Khalil et al. 2009), antipyretic Amr et al. 2010), antitumor (Abdel-Rahman et al. 2017), antiparasitic (Jose et al. 2007), antimicrobial (Sowmya et al. 2018), antihistaminik (Viswanatha et al. 208). Theoretical study has been played a crucial role in designing and development of novel materials for nonlinear optics. The physical and chemical properties of a substance are strongly related to both its geometrical and electronic structures. In this work, molecular structure, dipole moment, relative energies, rotational barriers, polarizability, first static hyper polarizability, potential energy scan, the electronic structure and HOMO-LUMO energies of title molecule have been studied. ^1H NMR and ^{13}C NMR chemical shifts calculations have been performed.

Method

Theoretical calculations on the isolated 3-bromo-4-(2-pyridyl) thiophene molecule were performed by the aid of Gaussian 09W program package and Gauss view 5.0 molecular visualization programs (Frisch et al., 2010; Dennington et al., 2009) in the gas phase. The geometric parameters of 3-bromo-4-(2-pyridyl) thiophene molecule in the equilibrium state were optimized at HF (Moller et al., 1934) and DFT with Becke's three parameter hybrid functional (B3) (Becke et al., 1988) and combined with gradient corrected correlation functional of Lee–Yang–Parr (LYP) (Lee et al., 1988; Becke, 1993) and employing 6-311++G (d,p) basis set (Francl et al., 1982; Rassolov et al., 2001). After optimization, at all optimized structures of the title compounds obtained B3LYP/6-311++G (d,p) and HF/6-311++G (d,p) level of theory, dipole moment (μ), polarizability (α), hyperpolarizability (β) based on finite field approach and energy differences of ELUMO –EHOMO were

- This is an Open Access article distributed under the terms of the Creative Commons Attribution-Noncommercial 4.0 Unported License, permitting all non-commercial use, distribution, and reproduction in any medium, provided the original work is properly cited.

- Selection and peer-review under responsibility of the Organizing Committee of the Conference

calculated in the same as level of theory. The ¹H and ¹³C NMR chemical shifts were calculated by GIAO approach by using B3LYP/6-311+G (2d, p) and HF/6-31G (d) level of theory (McLean et al., 1980; Krishnan et al., 1980).

Results and Discussion

Molecular Structure

The calculated values of the electronic, dipole moment, polarizability, hyperpolarizability, HOMO, LUMO energy and energy gap (ΔE_g) at the ground-state equilibrium geometry of studied molecules are listed in Table 1.

Table 1. The electronic, HOMO, LUMO energy, dipole moment, polarizability, hyperpolarizability, and energy gap (ΔE_g) of 3-Bromo-4-(2-pyridyl) thiophene

| B3LYP/6-311++G (d, p) | | | | | | |
|-------------------------|---------------|----------------|---------------|-------------------------|-------------------------|--------------|
| Electronic energy (a.u) | μ (Debye) | α (a.u) | β (a.u) | E_{HOMO} (a.u) | E_{LUMO} (a.u) | ΔE_g |
| -3373.76496133 | 1.47 | 149.86 | 415.83 | -0.243436 | -0.055208 | 5.12 |
| HF /6-311++G(d, p) | | | | | | |
| -3368.72657919 | 1.87 | 138.14 | 129.68 | -0.323695 | 0.036273 | 9.80 |

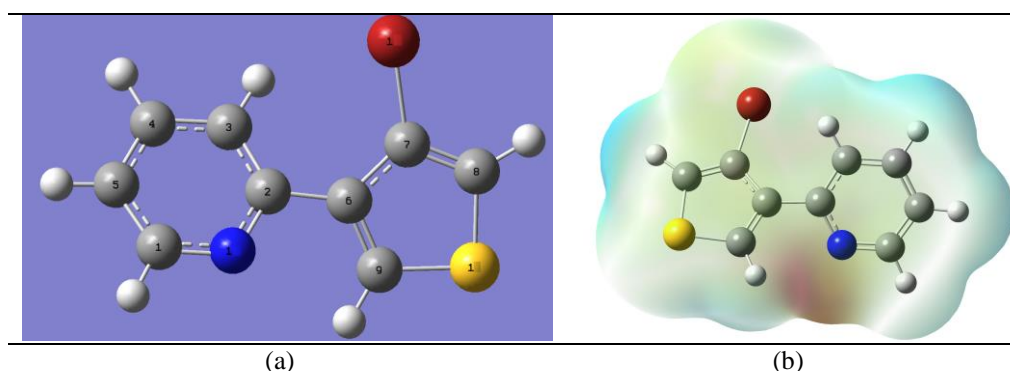


Figure 1. (a)The optimized geometry, (b) Molecular electrostatic (MEP) potential surface (PES) of 3-Bromo-4-(2-pyridyl) thiophene molecule

Table 2. Selected structural parameters of 3-Bromo-4-(2-pyridyl) thiophene

| Atoms | DFT | HF | Atoms | DFT | HF |
|-------|---------------------------|--------|------------------------------|-------------------------|---------|
| | Bond length/ \AA | | | Bond angle/($^\circ$) | |
| C1-N | 1.333 | 1.319 | N-C2-C3 | 121.79 | 122.12 |
| C1-C5 | 1.3933 | 1.383 | N-C2-C6 | 115.58 | 115.91 |
| N-C2 | 1.345 | 1.3234 | C3-C2-C6 | 122.57 | 121.89 |
| C2-C3 | 1.4015 | 1.3908 | C2-C6-C7 | 128.97 | 128.07 |
| C2-C6 | 1.4822 | 1.4884 | C2-C6-C9 | 120.93 | 121.60 |
| C3-C4 | 1.3902 | 1.3811 | C7-C6-C9 | 110.10 | 110.32 |
| C6-C7 | 1.4406 | 1.4462 | C6-C7-Br | 125.58 | 125.18 |
| C6-C9 | 1.3727 | 1.349 | C8-S-C9 | 91.53 | 91.34 |
| C7-C8 | 1.3627 | 1.342 | Dihedral angle /($^\circ$) | | |
| C7-Br | 1.9105 | 1.8925 | N-C2-C6-C7 | -146.88 | -138.42 |
| C8-S | 1.7298 | 1.7194 | N-C2-C6-C9 | 33.23 | 41.83 |
| C9-S | 1.7223 | 1.7161 | C3-C2-C6-C7 | 36.07 | 44.64 |
| - | - | - | C3-C2-C6-C9 | -143.82 | -135.11 |
| - | - | - | C2-C6-C7-Br | 4.57 | 4.27 |
| - | - | - | C9-C6-C7-Br | -175.53 | -175.95 |

The optimized geometry and Molecular electrostatic potential (MEP) surface values of 3-Bromo-4-(2-pyridyl) thiophene molecule obtained B3LYP/6-311++G (d, p) level are presented Figure 1 (a) and (b). The calculated parameter studied molecule of both at the B3LYP/6-311++G (d, p) and HF/6-311++G (d, p) methods in the

ground state are tabulated in the Table 2. The pictures of HOMO and LUMO obtained at the B3LYP/6-311++G (d, p) of 3-Bromo-4-(2-pyridyl) thiophene at the B3LYP/6-311++G (d, p) is given in Figure 2.

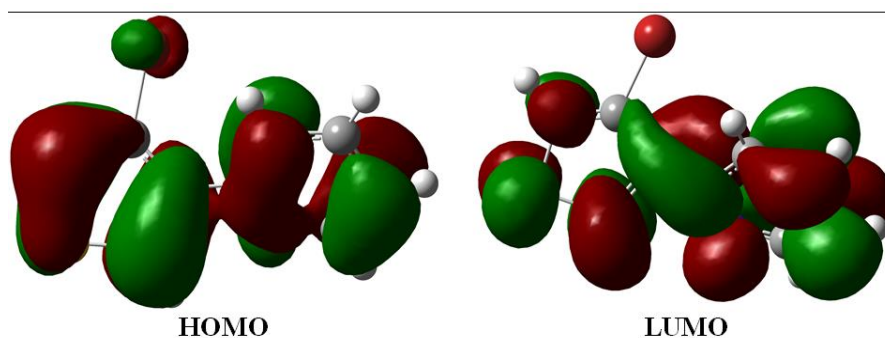


Figure 2. The pictures of HOMO and LUMO of 3-Bromo-4-(2-pyridyl) thiophene

Vibrational Frequencies

The 18 atoms and the number of the normal vibrations is 48. The calculated the IR and Raman spectrums are given in Figure 3.

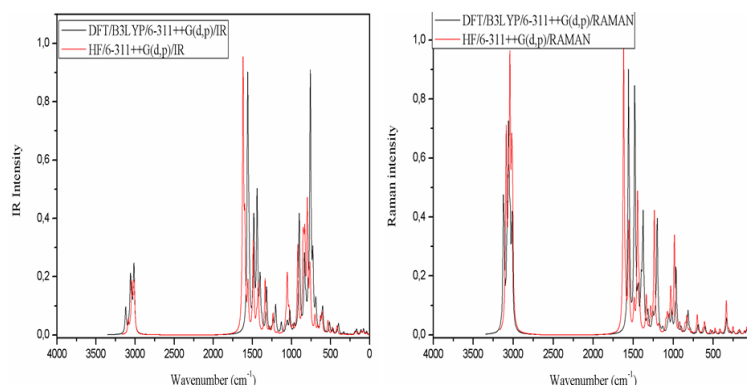


Figure 3. IR and Raman spectrums of 3-Bromo-4-(2-pyridyl) thiophene molecule

NMR Spectral Analysis

Table 3. NMR chemical shifts for 3-Bromo-4-(2-pyridyl) thiophene molecule

| Atoms | B3LYP/6-311+G(2d,p) | | | Exp ^a | B3LYP/6-311++G (d,p) | | |
|-------|---------------------|--------|-------------------|------------------|----------------------|--------|-------------------|
| | Gas | DMSO | CHCl ₃ | | Gas | DMSO | CHCl ₃ |
| C2 | 160.50 | 161.07 | 161.10 | - | 161.38 | 161.37 | 161.39 |
| C1 | 155.52 | 157.16 | 156.85 | - | 156.92 | 157.98 | 157.66 |
| C6 | 148.00 | 149.06 | 148.93 | - | 149.02 | 149.47 | 149.34 |
| C4 | 139.71 | 143.07 | 142.17 | - | 141.04 | 143.82 | 142.90 |
| C9 | 138.83 | 140.23 | 140.01 | - | 141.34 | 142.11 | 141.91 |
| C8 | 133.15 | 136.77 | 135.80 | - | 135.08 | 138.19 | 137.19 |
| C7 | 132.10 | 132.14 | 132.27 | - | 132.98 | 132.39 | 132.52 |
| C3 | 126.46 | 128.25 | 127.84 | - | 128.12 | 129.33 | 128.91 |
| C5 | 125.30 | 128.25 | 127.48 | - | 126.86 | 129.23 | 128.45 |
| C1H | 8.95 | 9.00 | 8.99 | 8.68 | 8.90 | 8.94 | 8.93 |
| C9H | 8.22 | 8.32 | 8.29 | 7.71 | 8.19 | 8.28 | 8.25 |
| C3H | 8.20 | 8.31 | 8.28 | 7.77 | 8.12 | 8.24 | 8.19 |
| C4H | 7.85 | 8.15 | 8.06 | 7.48 | 7.82 | 8.11 | 8.02 |
| C8H | 7.34 | 7.63 | 7.52 | 7.39 | 7.19 | 7.49 | 7.40 |
| C5H | 7.30 | 7.61 | 7.52 | 7.27 | 7.26 | 7.56 | 7.46 |

The calculated values of ^1H - and ^{13}C -NMR chemical shifts values of 3-Bromo-4-(2-pyridyl) thiophene molecule in the ground state in both gas phase and in solution of chloroform and dimethyl sulfoxide were given in Table 3.

Conclusion

In this paper, the ground state geometrical energy dipole moment, polarizability, hyperpolarizability, E_{HOMO} , E_{LUMO} , ΔE_g , ^1H and ^{13}C NMR chemical shifts of 3-Bromo-4-(2-pyridyl) thiophene molecule are examined both HF/6-311++G (d,p) and B3LYP/6-311++G(d,p) level of the theory. Comparison of the calculated and the experimental ^1H and ^{13}C NMR values indicates that results of HF/ 6-31G (d) and B3LYP/6-311++G (d,p) level of the theory are in a good agreement with experimental data for 3-Bromo-4-(2-pyridyl) thiophene molecule.

References

- Abdel-Rahman, S. A., El-Gohary. N, S., El-Bendary, E. R., El-Ashry, S. M., Shaaban, M. I. (2017). Synthesis, antimicrobial, anti-quorum-sensing, antitumor and cytotoxic activities of new series of cyclopenta(hepta)[b]thiophene and fused cyclohepta[b]thiophene analogs, *Eur. J. Med. Chem.* 140; 200-211.
- Amr, A. E., Sherif, M. H., Assay, M. G., Al-Omar, M. A., Ragab, I. (2010). Antiarrhythmic, serotonin antagonist and antianxiety activities of novel substituted thiophene derivatives synthesized from 2-amino-4,5,6,7-tetrahydroN-phenylbenzo[b]thiophene-3-carboxamide. *Eur. J. Med. Chem.* 45; 5935-5942.
- Başoğlu, A., Dirkmann, S., Golpayegani, N. Z., Silke Vortherms, S., Tentrop, J., Nowotnik, D., Prinz, H., Frohlich, R., Müller, K. (2017). Structure-activity relationships of the tricyclic quinone skeleton and the oxadiazole substituent. *Eur. J. Med. Chem.* 134; 119-132.
- Becke, A. D. (1988) Density-functional exchange-energy approximation with correct asymptotic behavior. *Physical Review A*, 38(6), 3098–3100
- Becke, A. D., 1993. Density-Functional Thermochemistry .3. The Role of Exact Exchange. *J. Chem. Phys.*, 98 (7): 5648-5652
- Dennington, R., Keith T., Millam, J. (2009). Semichem Inc., GaussView, Version 5, Shawnee Mission KS,
- Francl, M.M., Pietro, W.J., Hehre, W.J., Binkley, J.S., Gordon, M.S., DeFrees, D.J., Pople, J.A, (1982). Self-consistent molecular orbital methods. XXIII. A polarization-type basis set for second-row elements. *Chem. Phys*, 77 3654-3665
- Frisch M J, Trucks G W, Schlegel H B, Scuseria G E, Robb M A, Cheeseman J R, Scalmani G, Barone V, Mennucci B, Petersson G A, Nakatsuji H, Caricato M, Li X, Hratchian H P, Izmaylov A F, Bloino J, Zheng G, Sonnenberg J L, Hada M, Ehara M, Toyota K, Fukuda R, Hasegawa J, Ishida, M, Nakajima T, Honda Y, Kitao O, Nakai H, Vreven T, Montgomery J A, Vreven T J, Peralta J E, Ogliaro F, Bearpark M, Heyd J. J, Brothers E, Kudin N, Staroverov V N, Kobayashi R, Normand J, Raghavachari K, Rendell A, Burant J C, Iyengar S S, Tomasi J, Cossi M, Rega N, Millam J M, Klene, M, Knox J E, Cross J B, Bakken V, Adamo C, Jaramillo J, Gomperts R, Stratmann R E, Yazyev O, Austin A J, Cammi R, Pomelli C J, Ochterski W, Martin L R, Morokuma K, Zakrzewski V G, Voth G A, Salvador P, Dannenberg J J, Dapprich S, Daniels A D, Farkas O, Foresman J B, Ortiz J V, Cioslowski J, Fox D J, 2009. Gaussian Inc., (Wallingford, CT).
- Jose, L., Gonzalez, J. L., Stephens, C E, Wenzler T, Brun R, Tanius, F.A., Wilson, W. D., Barszcz, T., (2007). Werbovetz, K.A.; Boykin, D.W. Synthesis and antiparasitic evaluation of bis(2,5-[4-guanidinophenyl]thiophenes). *Eur. J. Med. Chem.* 42; 552-557.
- Khalil A M, Berghot M A, Gouda M A (2009). Synthesis and antibacterial activity of some new thiazole and thiophene derivatives. *Eur. J. Med. Chem.* 44; 4434-4440.
- Kulandasamy, R., Adhikari, A. V., Stables, J. P. (2009). A new class of anticonvulsants possessing 6 Hz activity: 3,4-Dialkyloxy thiophene bishydrazones. *Eur. J. Med. Chem.* 44; 4376-4384.
- Krishnan, R., Binkley, J. S., Seeger, R. and Pople, J. A, (1980). Self-consistent molecular-orbital methods. 20. basis set for correlated wave-functions. *J. Chem.Phys.* 72: 650–654.
- McLean, A.D., Chandler, G.S. (1980). Contracted Gaussian basis sets for molecular calculations. I. Second row atoms, $Z= 11-18$. *J Chem Phys*, 72:5639–5648
- Lee, C. T., Yang, W. T., Parr, R. G. (1988). Development of the colle-salvetti correlation-energy formula into a functional of the electron density. *Physical Review B*, 37, 785-789.

- Mohareb, R. M., Mayssoune, Y., Zaki, M. Y., Nermeen, S., Abbas, N. S. (2015) Synthesis, antiinflammatory and anti-ulcer evaluations of thiazole, thiophene, pyridine and pyran derivatives derived from androstenedione. *Steroids*. 98; 80-91.
- Rassolov, V-A., Ratner, M-A., Pople ,J-A., Redfern, P-C., Curtiss ,L-A., (2001). 6–31G* basis set for third-row atoms. *J Comp Chem.*, 22:976–984.
- Moller, C., Plesset, M. S. (1934). Note on an approximation treatment for many- electron systems. *Phys. Rev.*, 46 618-622.
- Sowmya, D. V., Teja, G. L., Padmaja, A., Prasad, V. K., Padmavathi, V, (2018) Green approach for the synthesis of thiophenyl pyrazoles and isoxazoles by adopting 1,3-dipolar cycloaddition methodology and their antimicrobial activity. *Eur. J. Med. Chem.* 143; 891-898.
- Viswanatha, G. L, Priyadarshini, B. J., Krishnadas, N., Janardhanan, S., Rangappa, S., Hanumanthappa, S. (2012). Synthesis and antihistaminic activity of 3H-benzo[4,5]thieno[2,3d][1,2,3] triazin-4-ones. *Saudi Pharm. J.* 20; 45-52.

Author Information

Guventurk Ugurlu

Kafkas University,
Faculty of Science and Letter, Department of Physics,
36100 Kars, Turkey
Contact E-mail: gugurlu@kafkas.edu.tr

Nonlinear Optical Properties of Tellurite-based Glasses

Gokhan BILIR

Kafkas University

Mustafa YUKSEK

Kafkas University

Ahmet KARATAY

Ankara University

Ayhan ELMALI

Ankara University

Abstract: We have investigated the mechanisms which are contribute to the linear and nonlinear optical behaviors of the heavy metal containing tellurite glasses by using UV-Vis spectrophotometer and open aperture Z-scan experiments. The bandgap values of the studied tellurite glasses with WO_3 , Nb_2O_5 , and ZnO modifiers were found among 2.58 eV and 3.01 eV. The results of the open aperture Z-scan experiments indicated that the studied tellurite glasses modified with different amounts of WO_3 , Nb_2O_5 , and ZnO possessed larger nonlinear absorption coefficients (among 2.62×10^{-7} cm/W and 6.38×10^{-7} cm/W) than the nonlinear absorption coefficients of previously investigated tellurite glasses. When the linear and nonlinear absorption results of the studied modified tellurite glasses considered together, it can be reported that the mechanisms which are contributed to the nonlinear absorption coefficients caused mainly from two photon absorption and two photon assisted free carrier absorption.

Keywords: Tellurite glasses, Z-scan experiments, Nonlinear absorption

Introduction

Because of their wide application area such as: amplifiers, modulators, lasers, sensors, optical limiters, the tellurite glasses still attracting interest (de Araujo et al., 2017). In addition, thermal, mechanical, chemical, and optical properties save several advantages to the tellurite glasses compared to the other glasses (Bilir et al., 2011, Bilir et al., 2011). The new trend to evolve suitable materials for desired application area is achieving by the combination and/or hosting of the some materials. The disadvantages to improve the optical properties of the some materials can be described as: (i) difficulties of the growth of the single crystals, (ii) prone to recrystallization of the inorganic materials and (iii) poor stability of the organic crystal phases at elevated temperatures (Yankov et al., 2012). It is possible to overcome these disadvantages by glassy materials. The tellurite glasses are very good candidates for hosting up to certain amounts of heavy metals and nanoparticles, due to their superior mechanical and chemical properties. On the other hand, the high polarizability is one of the unique property of the tellurite glasses (Tasheva et al., 2017). As well known that the polarization is the basic parameter of the nonlinear response of the materials, and under light of this truth, the tellurite based glasses should exhibit high third order nonlinear optical susceptibility (Yamane et al., 2000, Manning et al., 2012, Komatsu 2015).

In the literature, from the third order nonlinearity, generally the nonlinear refraction properties of the tellurite glasses had been studied (Tasheva et al., 2017, Souza et al., 2006, Kaur et al., 2017, Kim et al., 1993, Kim et al 1995, Castro-Beltran et al., 2011). In this study, we have investigated the linear and nonlinear optical characteristics of the WO_3 , Nb_2O_5 , and ZnO doped tellurite glasses with UV-Vis spectrophotometer and open

- This is an Open Access article distributed under the terms of the Creative Commons Attribution-Noncommercial 4.0 Unported License, permitting all non-commercial use, distribution, and reproduction in any medium, provided the original work is properly cited.

- Selection and peer-review under responsibility of the Organizing Committee of the Conference

aperture Z-scan experiments. As the linear and nonlinear optical results of the studied glasses are considered together, it can be estimated that the nonlinear optical absorption causes from two photon absorption and two photon assisted free carrier absorption mechanisms. In the presence of TPA, the intensity dependent absorption is described by Eq. (1)

$$\alpha(I) = \alpha_0 + \beta I \quad (1)$$

where α_0 is the linear absorption coefficient and β is the nonlinear absorption coefficient. Experimental normalized transmittance data was fitted to Eq. (2) (Bahae et al., 1990)

$$T(z, S = 1) = \frac{1}{\sqrt{\pi} q_0(z, 0)} \int_{-\infty}^{\infty} \ln[1 + q_0(z, 0) e^{-\tau^2}] d\tau \quad (2)$$

where $q_0(z, 0) = \beta I_0 L_{eff} / (1 + z^2/z_0^2)$, z is the position of the sample with respect to the focal position, $z_0 = k\omega_0^2/2$ is the Rayleigh range, ω_0 is the beam radius at focus, I_0 is the intensity of the incident light beam at the focus ($z = 0$), $L_{eff} = [1 - \exp(-\alpha_0 L)]/\alpha_0$ is the effective thickness of the material and L is the sample length.

Method

5 glass systems with the compositions of $(1-x)\text{TeO}_2 + x\text{ZnO}$ ($x=0.15, 0.25, 0.35$), $0.85\text{TeO}_2 + 0.15\text{WO}_3$, and $0.85\text{TeO}_2 + 0.15\text{Nb}_2\text{O}_5$ were synthesized using the conventional melt quenching technique. The oxide powders of each reagents with purities not less than 99.99% were used for the synthesis of glass samples. All the oxide powders with appropriate molar amounts were mixed thoroughly using an agate mortar. The batches of 7g of powders were prepared and were then melted in a platinum crucible in an electric muffle furnace under ambient conditions at temperatures ranges from 800 to 1100C according to the type and the amount of the modifier. The powders were kept at under these temperatures for an hour. Then, the glass melts were poured onto a stainless steel mold. The obtained glasses were thermally treated under their glass transition temperature (250°C) for 2 hours to remove thermal stresses due to the high synthesis temperatures.

The linear absorption spectra of the glass samples were recorded using a Shimadzu-1800 model UV-Vis spectrophotometer under room temperature conditions. The nonlinear absorption characteristics were investigated by open aperture Z-scan experiments., A laser source with 532 nm wavelength, 10 Hz repetition rate and 65 ps pulse duration was used in the open aperture Z-scan experiments. In addition, a 30 cm focal length lens was used to enlarge the Rayleigh range.

Results and Discussion

The linear absorption spectra of the studied glasses which are recorded by UV-Vis spectrophotometer under room temperature conditions are given in Figure 1. As seen from the figure, the absorption edges are changing related to the mole percentage and/or type of network modifiers (WO_3 , Nb_2O_5 , and ZnO).

The differences among the wavelengths at absorption edges can be attributed to the ratio of the non-binding oxygen atoms. The band gaps of the glasses were estimated by the linear extrapolation of the absorption edges to the wavelength axis. The calculated band gaps of the glasses are given in Table 1. It is clearly seen from the table that the increasing of the mole ratio of the ZnO in the tellurite glass causes to the narrowing at the band gap. This result can be attributed to the formation of the dopant states by the ZnO dopant at the bottom of the conduction band of the glass. On the other hand, the increasing of the ratio of the non-bridging oxygen atoms are causing to decrease at the band gap of the modified tellurite glasses.

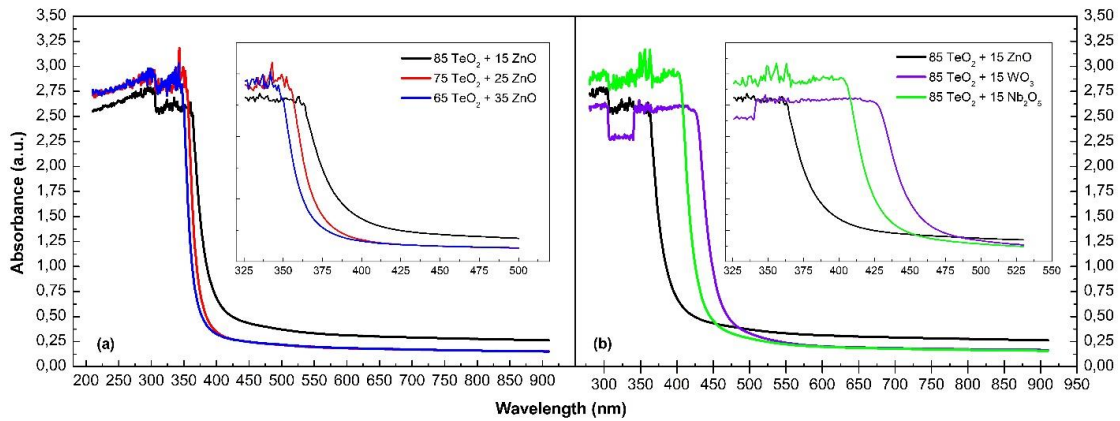


Figure 1. Linear absorption spectra of the studied glasses

The nonlinear absorption traces obtained from the open aperture Z-scan experiments of the studied glasses were shown in Figure 2. The nonlinear absorption coefficients of the modified tellurite glasses were obtained by fitting of the open aperture Z-scan results. The found nonlinear absorption coefficients (β_{eff}) were given in Table 1. As we mentioned above the two photon absorption and two photon assisted free carrier absorption mechanisms contributed to the nonlinear absorption coefficients.

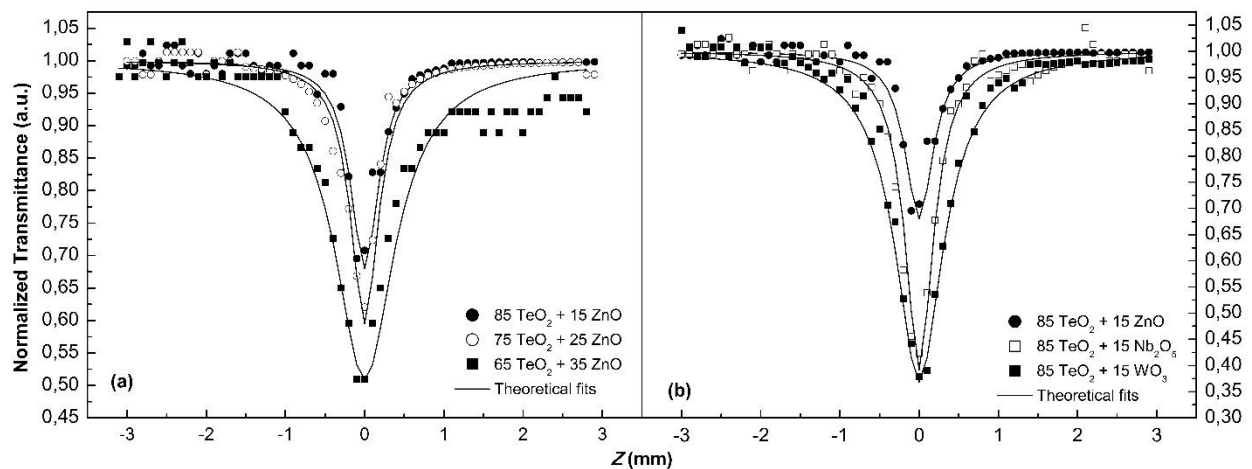


Figure 2. Comparison of the effective nonlinear absorption traces of samples according to (a) amount, and (b) type of the modifiers at 532 nm for 65 ps pulse duration

The narrowing of the band gap of the glasses lead to the increasing of the nonlinear absorption coefficient (Table 1).

Table 1. Comparison of the nonlinear absorption coefficients of the tellurite glasses related to the amount and/or type of the doped network modifiers

| Material | Thickness (cm) | $\alpha_0 (cm^{-1})$ | $\omega_0 (\mu m)$ | $\beta_{eff} (cm/W)$ | Band gap (eV) |
|--|----------------|----------------------|--------------------|-----------------------|---------------|
| 85 mole% TeO ₂ +15 mole% ZnO | 0.5 | 0.688 | 54 | 2.62×10^{-7} | 3.07 |
| 75 mole% TeO ₂ +25 mole% ZnO | | 0.402 | | 3.08×10^{-7} | 3.24 |
| 65 mole% TeO ₂ +35 mole% ZnO | | 0.338 | | 3.67×10^{-7} | 3.32 |
| 85 mole% TeO ₂ +15 mole% Nb ₂ O ₅ | | 0.352 | | 6.24×10^{-7} | 2.85 |
| 85 mole% TeO ₂ +15 mole% WO ₃ | | 0.364 | | 6.38×10^{-7} | 2.73 |

Conclusion

The linear and nonlinear absorption properties of binary tellurite glasses have been investigated using absorption spectrophotometer and open aperture Z-Scan experiments, respectively. The band gap of the glass samples were determined using linear absorption spectra and found to be blue shifted at about 32 nm with the increasing amount of ZnO and red shifted at about 70 nm with the change of the type of the modifier. The linear optical absorption measurements showed the tunability of the band gaps of the glass samples, which has great significance for photonics applications, by changing the type and the amount of the modifiers. As for the nonlinear optical measurements, it was found that the two-photon absorption signals and the response times are relatively fast which is a desired feature for optical switching and photodetector applications.

References

- Bahae, M. S., Said A. A., Wei, T. H., Hagan D. J., Van Stryland, E. W., (1990) Sensitive measurement of optical nonlinearities using a single beam. *IEEE J. Quantum Electron.* 26(4), 760-69.
- Bilir, G., Ozen, G., Tatar, D., Öveçoğlu, M. L., (2011) Judd–Ofelt analysis and near infrared emission properties of the Er³⁺ ions in tellurite glasses containing WO₃ and CdO. *Optics Communications*, 284(3), 863-68.
- Bilir, G., Ozen, G., (2011) Optical absorption and emission properties of Nd³⁺ in TeO₂–WO₃ and TeO₂–WO₃–CdO glasses. *Physica B.* 406(21), 4007-13.
- Castro-Beltran, R., Desirena, H., Ramos-Ortiz, G., De la Rosa, E., Lanty, G., et al. (2011) Third-order nonlinear optical response and photoluminescence characterization of tellurite glasses with different alkali metal oxides as network modifiers. *Journal of Applied Physics*, 110, 083110-7.
- de Araujo, C. B. Kassab, L. R. P., (2017) Linear and nonlinear optical properties of some tellurium oxide glasses. In V. A. G. Rivera, D. Manzani (Eds.), *Technological Advances in Tellurite Glasses* (pp. 15-39) Switzerland: Springer International Publishing.
- Kaur, A., Khanna, A., Aleksandrov, L. I. (2017). Structural, thermal, optical and photo-luminescent properties of barium tellurite glasses doped with rare-earth ions. *Journal of Non-Crystalline Solids*, 476, 67-74.
- Kim, S.-H., Yoko, T. (1995). Nonlinear optical properties of TeO₂ based glasses: MO_x – TeO₂ (M = Sc, Ti, V, Nb, Mo, Ta, and W) binary glasses. *Journal of American Ceramic Society*, 78, 1061-1065.
- Kim, S.-H., Yoko, T., Sakka, S. (1993). Linear and nonlinear optical properties of TeO₂ glass, *Journal of American Ceramic Society*, 76, 2486-2490.
- Komatsu T. (2015). Design and control of crystallization in oxide glasses. *J. Non-Crystalline Solids*, 428, 156-175.
- Manning, S., Heidepriem, H. E., Monro, T. M. (2012). Ternary tellurite glasses for the fabrication of nonlinear optical fibers. *Optical Materials Express*, 2, 140-152.
- Souza, R. F., Alencar M. A. R. C., Hickmann, J. M., Kobayashi, R., Kassab, L. R. P. (2006). Femtosecond nonlinear optical properties of tellurite glasses. *Applied Physics Letters*, 89, 171917-3.
- Tasheva, T. R., Dimitrov, V. V., (2017). Synthesis, structure and nonlinear optical properties of tellurium oxide-bismuth oxide-boron oxide glasses. *Bulgarian Chemical Communications*, 49, 43-48.
- Yamane, M., Asahara, Y. (2000). Glasses for photonics, Cambridge University Press.
- Yankov, G., Dimowa, L., Petrova, N., Tarassov, M., Dimitrov, K., Petrov, T., Shivachev, B. L., (2012). Synthesis, structural and non-linear optical properties of TeO₂–GeO₂–Li₂O glasses. *Optical Materials*, 35, 248-251.

Author Information

Gökhan Bilir

Kafkas University
Department of Physics
36100 Kars / TURKEY
Contact E-mail: gbilir@gmail.com

Mustafa Yuksek

Kafkas University
Department of Electrical&Electronics Engineering
36100 Kars / TURKEY

Ahmet Karatay

Ankara University
Department of Physics Engineering
06100 Ankara / TURKEY

Ayhan Elmali

Ankara University
Department of Physics Engineering
06100 Ankara / TURKEY

Isolation, Identification and Role of Glyphosate-Degrading Bacteria from Soils of Baghdad

Hala M. RADIF
University of Baghdad

Shaymaa Fadhel Abbas ALBAAÏT
University of Baghdad

Abstract: Glyphosate (N-phosphonomethylglycine) is the most commonly used herbicide worldwide. Due to concern regarding its toxicity for non-targeted species in soil, finding glyphosate-degrading microorganisms in soil is important as these bacteria can grow by utilizing glyphosate as a source of carbon. Two bacteria species were isolated from soils of Baghdad. Morphological characteristic and biochemical reactions indicated these species were identified as *Bacillus* and *Serratia marcescens*. These bacterial isolates showed an ability to consume glyphosate as energy and sole carbon source at 20 mM. The growth of bacteria in the media containing glyphosate was determined after two days of incubation at 30 C by measuring turbidity (O.D) at 680 nm. The maximum growth of *Bacillus* in halogenated compound containing media was found to be (O.D=0.3836) after two days of incubation as compared to control media (O.D=0.0170) without halogenated compound. In comparison to *Bacillus*, *Serratia marcescens* showed less growth activity (O.D=0.06) in halogenated compound containing media after two days of incubation as compared to its growth in control media (O.D= 0.03). The maximum chloride ion released due to dehalogenase enzyme activity was higher for *Bacillus* (O.D=1.3199) as compared to *S. marcescens* (O.D= 0.3) with respect to their control media (O.D =0.0491 and 0.04) respectively. This result gives hint regarding the role of dehalogenase present in the bacteria for their affinity to substrate and utilizing it for their growth. For a better understanding of dehalogenase enzyme produced by these two bacterial species, more research has to be explored for their possible use as bioremediation tools in the natural environment.

Keywords: Glyphosate, Soil bacteria, Bio-degradation

Introduction

Glyphosate is a non-selective herbicide having potential to kill both broadleaf plants and grasses. The sodium salt form of glyphosate regulates plants growth and help in ripening fruit instead of inhibiting plant growth (Eker et al., 2006). Glyphosate prevents the plant growth by inhibiting certain enzymes of shikimic acid pathway which is an important pathway necessary for plants and some microorganisms (Tohge et al., 2013). Due to its tight binding with soil, it is not likely to get into groundwater and will remain in soil for up to 6 months depending on the type of climate and soil. It is well established that the half-life of glyphosate present in dead leaves were broken down in 8 or 9 days. In addition, some of glyphosate were absorbed by carrots and lettuce grown in soil containing glyphosate (Diamand and Broon, 2001).

Recently, biological decontamination processes are preferred more as compared to conventional approaches due to the utilization of some microorganisms to degrade and detoxify many toxic xenobiotics, especially pesticides, which is an efficient tool for the decontamination of polluted sites, which in general microorganism does it without producing toxic intermediates in the environment (Ortiz-Hernandez 2013; Javaid et al., 2016).

Some strains of bacteria that are able to degrade carbamate pesticides have been isolated from soil around the world (Hamada et al., 2015). Previous studies have shown that atrazine-degrading bacteria applied as single strains or as consortia can increase degradation of atrazine in soil (Wanget al., 2014), thus, the present study was

- This is an Open Access article distributed under the terms of the Creative Commons Attribution-Noncommercial 4.0 Unported License, permitting all non-commercial use, distribution, and reproduction in any medium, provided the original work is properly cited.

- Selection and peer-review under responsibility of the Organizing Committee of the Conference

undertaken to isolate and characterize glyphosate-degrading bacteria from different untreated soils of Baghdad. Together, the assessment of growth response of these isolates and optimization of some abiotic parameters for the cultivation of isolated strains providing maximal effective condition for the glyphosate degradation.

Method

Determination of Glyphosate Degrading Strains

Fresh samples collected from soil were inoculated into Luria-Bertani (LB) agar plates containing 1.0% tryptone, 0.5% yeast extract, 1.0% NaCl and halogenated compound and then incubated at 30 °C for 16 h. Several colonies were selected from this plate and streaked onto fresh LB agar medium to obtain a pure colony. Pure bacteria colony grown were inoculated in glyphosate liquid broth containing 20 mM concentration of carbon and incubated in shaker (150 rpm, 30 °C). At different time interval, small quantity of liquid medium were taken out to determine the growth of bacteria by measuring turbidity (absorbance value) of broth at 680 nm.

Determination of Chloride Ion Released in Growth Medium

The protocol of Bergman and Sanik (1957) was followed to measure dehalogenase enzyme activity. Bacteria sample (1mL) was added into 100 µL of 0.25 M ammonium ferric sulphate prepared in 9 M nitric acid and mixed thoroughly. After proper mixing, 100 µL of mercuric thiocyanate-saturated ethanol was added and mixed. The color was allowed to develop for 10 min and chloride ion liberation were determined by taking absorbance at 460 nm.

Results

Isolation and Identification of Bacteria

Two different bacteria were isolated and identified by morphological characteristics and biochemical reaction as *Serratia marcescens* and *Bacillus* from different soils of Baghdad. These isolate were able to grow in a culture medium in presence of herbicide glyphosate and utilized it as an energy source.

Bacterial Degradation of Glyphosate Medium

Bacteria were grown in minimal medium that supplied with 20mM Glyphosate at 30 oC. The growth was determined by measuring the optical density at 680nm, the highest growth was (OD average = 0.3836) in *Bacillus* after two days of incubation compared to control (OD average = 0.0170), while the lowest growth was (OD average = 0.06) in *Serratia marcescens* compared with control was (OD average = 0.03).

Chloride Ion Released into Growth Medium

Maximum amount of ion chloride was released by dehalogenase enzyme activity. The ODs averages were about 1.31 and 0.055 compared with control 0.0491 and 0.03 for *Bacillus* and *Serratia marcescens*, respectively.

Discussion

In the present study, two different bacterial species were isolated from soil and identified as *Serratia marcescens* and *Bacillus*. These bacteria are a glyphosate degrading microorganism that could grow by utilizing glyphosate as a sole source of carbon or phosphorus, and able to produce dehalogenase enzyme therefore have potential to degrade halogenated compound. The reduction in microbial population when glyphosate was added to the medium culture can be explained by the mode of action of glyphosate which makes the organisms unable to synthesize essential aromatic amino acids (Kryzsko-Lupicka and Orlik, 1997). Allison et al reported that *Serratia* has faster growth rate (doubling time) than *Rhizobium* Sp and ability to consume 2,2-dichloropropionate as a source of carbon at 20 mM with cell doubling time of 5 h and maximum chloride ion

release of 38 μ mol/ml (Adel et al., 2012; Alison et al., 1983), however, the present work showed that the expression of dehalogenase enzyme in *Serratia* is lower as compared to *Bacillus* because of which *Serratia* releases less amount of halogens causing its slow growth on glyphosate medium. There were some other species which were reported to degrade glyphosate like *Alkaligenes* sp., *Rhizobium* sp., *Agrobacterium* sp., *Bacillus megaterium*, *Flavobacterium* sp. (Talbot et al., 1984) (Peng et al., 2018). In the natural environment, the use of microorganisms for glyphosate as a sole source of energy provides a substantial competitive advantage over other microorganisms in successful removal of herbicide.

Conclusion

This study is the first report on the isolation and characterisation of soil bacterial strains of *Serratia marcescens* and *Bacillus*. from untreated soil in Baghdad that possesses the capacity to degrade glyphosate. In addition, this work provides vital information on the glyphosate degradation and dehalogenase enzyme production by these bacteria.

References

- Abel, E., Ibrahim, N., & Huyop, F. (2012). Identification of *Serratia marcescens* SE1 and determination of its herbicide 2, 2-dichloropropionate (2, 2-DCP) degradation potential. *Malaysian Journal of Microbiology*, 8(4), 259-265.
- Allison, N., Skinner, A. J., & Cooper, R. A. (1983). The dehalogenases of a 2, 2-dichloropropionate-degrading bacterium. *Microbiology*, 129(5), 1283-1293.
- Diamond, E., & Barron, H. (2001). Health and environmental impacts of glyphosate.
- Eker, S., Ozturk, L., Yazici, A., Erenoglu, B., Romheld, V., & Cakmak, I. (2006). Foliar-applied glyphosate substantially reduced uptake and transport of iron and manganese in sunflower (*Helianthus annuus* L.) plants. *Journal of agricultural and food chemistry*, 54(26), 10019-10025.
- Hamada, M., Matar, A., & Bashir, A. (2015). Carbaryl degradation by bacterial isolates from a soil ecosystem of the Gaza Strip. *Brazilian Journal of Microbiology*, 46(4), 1087-1091.
- Javaid, M. K., Ashiq, M., & Tahir, M. (2016). Potential of biological agents in decontamination of agricultural soil. *Scientifica*, 2016.
- Krzyśko-Lupicka, T., & Orlik, A. (1997). The use of glyphosate as the sole source of phosphorus or carbon for the selection of soil-borne fungal strains capable to degrade this herbicide. *Chemosphere*, 34(12), 2601-2605.
- Ortiz-Hernández, M. L., Sánchez-Salinas, E., Dantán-González, E., & Castrejón-Godínez, M. L. (2013). Pesticide biodegradation: mechanisms, genetics and strategies to enhance the process. In *Biodegradation-life of science*. Intech.
- Peng, R. H., Tian, Y. S., Xiong, A. S., Zhao, W., Fu, X. Y., Han, H. J., ... & Yao, Q. H. (2012). A novel 5-enolpyruvylshikimate-3-phosphate synthase from *Rahnella aquatilis* with significantly reduced glyphosate sensitivity. *PloS one*, 7(8), e3
- Talbot, H. W., Johnson, L. M., & Munnecke, D. M. (1984). Glyphosate utilization by *Pseudomonas* sp. and *Alcaligenes* sp. isolated from environmental sources. *Current Microbiology*, 10(5), 255-259.
- Tohge, T., Watanabe, M., Hoefgen, R., & Fernie, A. R. (2013). Shikimate and phenylalanine biosynthesis in the green lineage. *Frontiers in plant science*, 4, 62.
- Wang, J., Zhu, L., Wang, Q., Wang, J., & Xie, H. (2014). Isolation and characterization of atrazine mineralizing *Bacillus subtilis* strain HB-6. *PLoS One*, 9(9), e107270.

Author Information

Hala M. Radif

Department of Biology, College of Science,
University of Baghdad
Al-Jadriya, Baghdad 10070, Iraq
Contact E-mail: dhala8181@gmail.com

Shaymaa Fadhel Abbas Albaayit

Department of Biology, College of Science,
University of Baghdad
Al-Jadriya, Baghdad 10070, Iraq

Optical Properties and Natural Radioactivity Levels of Turkish Natural Glass Obsidian

Gulcin Bilgici CENGIZ
Kafkas University

Ilyas CAGLAR
Kafkas University

Gokhan BILIR
Kafkas University

Abstract: Obsidian is a naturally occurring volcanic glass formed as an igneous rock. It is a kind of aluminosilicate glass containing iron impurities and some tiny particles (particle-dispersed glasses). It can be found in black, gray, brown, blue, and green colors in nature. In recent work, the obsidian specimens in black and brown colors were collected from Sarıkamış which is a small town in Kars province located at the north-east part of Turkey. The obtained specimens were then cut and polished to obtain two parallel surfaces to perform optical measurements. The optical absorption spectra of the samples were collected under ambient environment. The natural radioactivity levels of the specimens were also measured using a gamma spectrometer which uses a NaI(Tl) scintillation detector for the determination of the radioactivity.

Keywords: Obsidian, NaI(Tl) detector, Natural radioactivity

Introduction

The total radiation dose, which all living beings exposed to everyday, is mainly due to the natural radioactivity. There are two main sources of natural radioactivity. These are primordial sources (^{238}U , ^{235}U , ^{232}Th , ^{40}K , ^{87}Rb , and ^{187}Re), which are always available from the beginning of the Earth because of their long lifetimes, and cosmic rays. Therefore, all the natural geographical formations around us can be considered as a source of natural radioactivity (UNSCEAR, 2000, Tzortzis et al., 2003).

The obsidian, one of these formations, is a volcanic glass formed as an igneous rock. It is a kind of aluminosilicate glass containing iron impurities and some tiny particles (particle-dispersed glasses). It is formed when felsic lava extruded from a volcano cools so rapidly which does not allow atoms to re-arrange themselves into a crystalline structure. It is a non-crystalline amorphous material and doesn't have long range order. It can be found in black, gray, brown, blue, and green colors in nature (Chataigner et al., 2014).

In this work, the optical properties and the natural radioactivity levels of obsidian specimens in black and brown colors, which were collected from Sarıkamış, were investigated.

Method

All obsidian specimens were collected from Sarıkamış, which is a small county of Kars province located at the eastern part of Anatolia. The Sarıkamış district stands between $40^{\circ} 18'$ north latitude and $42^{\circ} 31'$ east longitude and an average of 2225 m above sea level. The obsidian samples were collected from near the Mescitli village, which is 14 kilometers away from the Sarıkamış town center.

- This is an Open Access article distributed under the terms of the Creative Commons Attribution-Noncommercial 4.0 Unported License, permitting all non-commercial use, distribution, and reproduction in any medium, provided the original work is properly cited.

- Selection and peer-review under responsibility of the Organizing Committee of the Conference

The obtained samples were cut and polished using a Microcut model cutting and polishing machine to obtain two parallel surfaces to perform optical absorption measurements. The optical absorption characteristics of the samples were determined using a Perkin Elmer Lambda 25 UV-Vis spectrophotometer in the 300–1100 nm wavelength range.

The collected samples were crushed, homogenized, sieved through a 1 mm mesh sieve, weighed and transferred into an airtight cylindrical plastic container with 65 mm diameter and 50 mm height. Then, each were sealed and stored for about 40 days before counting to achieve equilibrium for ^{238}U and ^{232}Th with their respective progeny. The radioactivity analysis of naturally occurring radionuclides (^{226}Ra , ^{232}Th , and ^{40}K) were performed on obsidian samples using gamma spectrometry system with NaI(Tl) detector which shielded by 5 cm thick lead on all sides to avoid the natural gamma radiation contribution.

The obtained gamma ray spectra were analyzed using a PC based multichannel analyzer (MCA) system and Maestro software. The energy calibration and relative efficiency calibration of the gamma spectrometry system were carried out using a standard reference material (IAEA-375). Each sample was acquired for 100.000 seconds to obtain good statistics in the evaluation of gamma peaks.

Results and Discussion

The optical absorption spectra of brown and black obsidian samples were measured in the 200–1100 nm wavelength range under ambient conditions and the results are given in Figure 1. The samples with different colors were prepared in 1.2 mm thicknesses using a cutting and polishing machine to perform optical absorption measurements. The rapid increase of the absorption below 400 nm seen in the absorption spectrum of the black obsidian can be easily assigned to the forbidden gap of the sample. However, although some absorption characters appear in the absorption spectrum of the brown obsidian, no clear rapid absorption due to the forbidden band gap of the sample was observed.

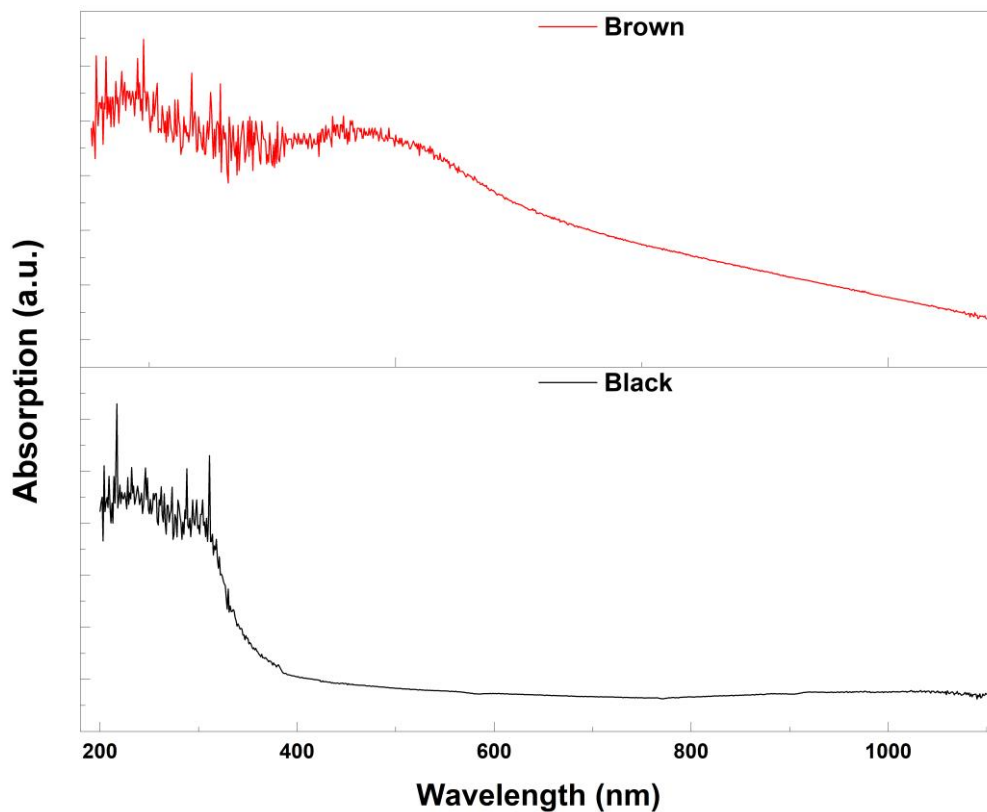


Figure 1. Absorption spectra of obsidian samples with different colors

The activity concentrations of ^{238}U (^{226}Ra) and ^{232}Th were determined from 1764.5 keV gamma peak of ^{214}Bi and 2614 keV gamma peak of ^{208}Tl , respectively. The activity of ^{40}K was directly measured using its own 1460.8 keV gamma peak.

The activity concentrations of the natural radionuclides in the each samples were calculated through the following formula (El-Farrash et al., 2012)

$$A = \frac{C}{\epsilon_{\gamma} P_{\gamma} T_m m_s} \quad (1)$$

where A is the activity of the radionuclides in Bq kg^{-1} , C is the net count (background subtracted) under the γ -ray peak, ϵ_{γ} is full energy peak efficiency of detector at particular γ -ray energy, P_{γ} is the γ -ray emission probability per decay, T_m is the counting time in second and m_s is the weight of the sample in g. The results obtained from equation 1 were corrected for gamma ray self-attenuation effects to obtain accurate values for the activity concentrations. The self-attenuation correction factor (F) for given energy E , were estimated from the equation 2 (Bilgici Cengiz G., 2018).

$$F = \frac{1 - e^{-\mu_s d_s}}{\mu_s d_s} \times \frac{\mu_r d_r}{1 - e^{-\mu_r d_r}} \quad (2)$$

where μ_r and μ_s are attenuation coefficient of reference and sample respectively; and d_r and d_s are heights of reference and sample, respectively.

The attenuation coefficient values of reference and samples were determined with the help of XCOM software package which uses chemical parameters of a mixture.

In black obsidian, the activity concentrations of ^{238}U (^{236}Ra), ^{232}Th and ^{40}K were found to be 0.0812 ± 0.015 , 0.0802 ± 0.022 , and 1.528 ± 0.076 Bqg⁻¹, respectively. The activity concentrations of ^{238}U , ^{232}Th and ^{40}K were found to be 0.0735 ± 0.016 , 0.0755 ± 0.023 and 1.767 ± 0.080 Bqg⁻¹ in brown obsidian, respectively. It was observed that the activity concentrations of ^{40}K are quite higher than both ^{226}Ra and ^{232}Th in two samples.

The results showed that the activity values of ^{238}U (^{226}Ra) and ^{232}Th radionuclides are approximately same in two samples, while the activity value of ^{40}K in brown obsidian is about %15 higher than that of black obsidian. This difference may be related to the chemical composition of obsidian samples. Because Brown obsidian is more reach in terms of K_2O content than black obsidian (Çolak and Aygün., 2011).

Table 1 shows the comparison of the radioactivity concentrations of above-mentioned radionuclides in obsidian samples with the values reported by Chiozzi et al., 2000.

Table 1. The comparison of the activity concentrations of ^{238}U (^{226}Ra), ^{232}Th , and ^{40}K in the obsidian samples with the values reported in the literature

| References | Location of sample | Type of sample | Activity concentrations (Bqg ⁻¹) | | |
|----------------------|--------------------|----------------|--|-------------------|-----------------|
| | | | ^{238}U | ^{232}Th | ^{40}K |
| Present Study | Sarıkamış, Turkey | Black Obsidian | 0.0812±0.015 | 0,0802±0.022 | 1.528±0.076 |
| | | Brown Obsidian | 0,0735±0,016 | 0,0755±0,016 | 1,767±0.080 |
| Chiozzi et al., 2000 | Italy | Obsidian | 0.183±0.002 | 0.219± 0.004 | 1.379±0.017 |
| | | Obsidian | 0.167±0.002 | 0.193± 0.003 | 1.368±0.015 |
| | | Obsidian | 0.175±0.002 | 0.197±0.004 | 1.314±0.016 |

As shown in Table 1, the activity concentration values of ^{238}U (^{226}Ra) and ^{232}Th measured in this study for obsidian samples are quite lower than those of the reported in Italian obsidian. However, the obtained activity concentrations for ^{40}K are slightly higher than the values reported by (Chiozzi et al., 2000).

Conclusion

The optical absorption properties and the natural radioactivity levels of the black and the brown obsidians collected from the north east part of Anatolia/Turkey has been studied. It is found that the natural radioactivity level of the of ^{40}K radionuclide in brown obsidian is about %15 higher than that of black obsidian, while the activity values of ^{238}U (^{226}Ra) and ^{232}Th radionuclides are quite same in two samples. Additionally, those values were also compared with the literature and was found to be almost same for the ^{238}U (^{226}Ra) and ^{232}Th radionuclides and slightly higher for ^{40}K than the values given in the literature.

References

- Bilgici Cengiz G. (20189). Transfer factors of ^{226}Ra , ^{232}Th and ^{40}K from soil to pasture-grass in the northeastern of Turkey. *Journal of Radioanalytical and Nuclear Chemistry* 329(1); 83-89
- Chataigner, C.; Işıklı, M.; Gratuze, B.; Çil, V. (2014). Obsidian Sources in the Regions of Erzurum and Kars (North-East Turkey): New Data. *Archaeometry* 56(3), 351-374.
- Chiozzi P., De Felice P., Fazio A., Pasquale V., Verdoya M., (2000). Laboratory application of NaI(Tl) γ -ray spectrometry to studies of natural radioactivity in geophysics. *Applied Radiation and Isotopes* 53; 127-132.
- Çolak, A., Aygün H., (2011) Sarıkamış (Kars) civarı obsidiyenleri bilgi notu. MTA. Maden Etüt ve Arama Dairesi Başkanlığı SERKA Raporu. Kars.
- El-Farrash A.H., Yousef H.A., Hafez A.F., (2012). Activity concentrations of ^{238}U and ^{232}Th in some soil and fertilizer samples using passive and active techniques. *Radiation Measurements* 47; 644-648
- Tzortzis, M., Tsertos, H., Christofides, S., George Christodoulides, G., (2003). Gamma-ray measurements of naturally occurring radioactive samples from Cyprus characteristic geological rocks. *Radiation Measurements* 37; 221-229.
- United Nations Scientific Committee on the Effect of Atomic Radiation (2000) Report to the general assembly, Effects and risks of ionizing radiations. United Nations, New York.

Author Information

Gulcin Bilgici Cengiz

Kafkas University
Department of Physics
36100 Kars / TURKEY
Contact E-mail: gulcincengiz@kafkas.edu.tr

Ilyas Caglar

Kafkas University
Kazım Karabekir Vocational School of Technical Sciences
36100 Kars / TURKEY

Gokhan Bilir

Kafkas University
Department of Physics
36100 Kars / TURKEY

Quantum Chemical Calculations for Corrosion Inhibition of Pyrimidine Derivatives

Esvet AKBAS

YuzuncuYil University

Erdem ERGAN

Van Vocational School of Security, Department of Property Protection and Security

Hakan DONMEZ

YuzuncuYil University

Abstract: The inhibition properties of compounds have been correlated with frontier orbital energy of highest occupied molecular orbital energy (E_{HOMO}), lowest unoccupied molecular orbital energy (E_{LUMO}), and energy gap ($\Delta E_{\text{LUMO-HOMO}}$). There is a good correlation between the speed of corrosion and E_{HOMO} that is often associated with the electron donating ability of the molecule. The literature shows that the adsorption of the molecule on the metal surface can occur on the basis of donor–acceptor interactions between the lone pairs on hetero atoms or π electrons of the molecule and the empty d orbital of the metal atom. In the present work, pyrimidine derivatives have been investigated as corrosion inhibitors for iron using density functional theory.

Keywords: Pyrimidine, Corrosion, Quantum chemical calculation

Introduction

The deterioration of materials due to corrosion causes economic loss. A wide variety of research is conducted to prevent this harmful process. One of the excellent methods to protect materials against corrosion is use of heterocyclic compounds containing π -electrons (Elmors, at al., 1999). The physicochemical parameters of the molecules are important because they determine adsorption on the metal surface. Most effective inhibitor molecules behave as both electron donor and electron acceptor (Ikpi, at al., 2017). When using heterocyclic compounds for corrosion inhibition are sharing the lone pairs on hetero atoms or π electrons to over metal surface and the molecule is adsorb on the metal surface (Lagrenée, at al., 2002).

The quantum chemical calculations have been widely used to the reactivity of organic compounds for corrosion inhibition (Khalil, 2003). The inhibitor activities are involved molecular geometry and orbitals of the organic compounds and correlated with frontier orbital energy. The highest occupied molecular orbital energy (E_{HOMO}) is associated with the electron donating ability of the molecule. There is a good correlation between the speed of corrosion and E_{HOMO} . The adsorption of the molecule on the metal surface can occur on the basis of donor–acceptor interactions between the lone pairs on hetero atoms or π electrons (Caliskan, at al., 2012). The high E_{HOMO} value has a molecule tendency to give electrons, while a low E_{LUMO} value indicates the ability of the molecule to accept electrons. The difference between E_{LUMO} and E_{HOMO} energies is called energy gap. Larger values of the energy gap will provide low reactivity to a chemical interaction and inhibition efficiency. But the lower values of the ΔE will render good reactivity to a chemical interaction and inhibition efficiency (Karzazi, at al., 2014).

The ionization potential (I) and electron affinity (A) of the inhibitor molecule and E_{HOMO} and E_{LUMO} are related to each other. The absolute electronegativity (χ) and the global hardness (η) depending on the ionization potential and electron affinity of the inhibitor molecules, the following can be given (1) (Karzazi, at al., 2014).

- This is an Open Access article distributed under the terms of the Creative Commons Attribution-Noncommercial 4.0 Unported License, permitting all non-commercial use, distribution, and reproduction in any medium, provided the original work is properly cited.

- Selection and peer-review under responsibility of the Organizing Committee of the Conference

$$\chi = -\mu = -\left(\frac{\partial E}{\partial N}\right)_{v(\bar{r})} \quad \eta = \left(\frac{\partial^2 E}{\partial N^2}\right)_{v(\bar{r})} = \left(\frac{\partial \mu}{\partial N}\right)_{v(\bar{r})} \quad (1)$$

The chemical softness (S) is a chemical descriptor measuring the molecular stability and reactivity. The relation between chemical softness (S) and chemical hardness can be given as follows (2) (Karzazi, at al., 2014).

$$S = \frac{1}{\eta} \quad (2)$$

The global electrophilicity index (ω) is a measure of energy lowering due to maximal electron flow between donor and acceptor. It can be given as a function of the dipole moment and the chemical hardness as follows (3) (Karzazi, at al., 2014).

$$\omega = \frac{\mu^2}{2\eta} \quad (3)$$

The global electrophilicity index measures the tendency of molecules to accept electrons. A molecule with a high ω value has an electrophile and with a low ω value has a nucleophilic character.

The transferred electrons fraction index (ΔN) measures the stabilization in energy when the system acquires an additional electronic charge from the environment. Thus the fraction of electrons transferred from the inhibitor to metallic surface (4) (Chattaraj, at al., 2006).

$$\Delta N = \frac{\chi_{F_e} - \chi_{inh}}{2(\eta_{F_e} + \eta_{inh})} \quad (4)$$

According to the simple charge-transfer model there are occurring governing the interaction between the inhibitor molecule and the metal surface (5) (Ramírez-Ramírez, at al., 2010).

$$\Delta E_{back\ donation} = -\frac{\eta}{4} \quad (5)$$

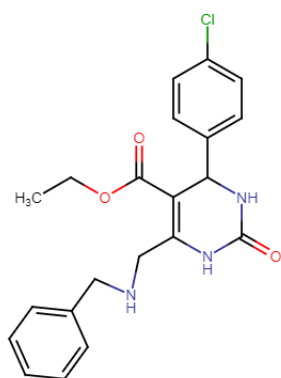
The $\Delta E_{back\ donation}$ implies that when $\eta > 0$ and $\Delta E_{back\ donation} < 0$ the charge-transfer to a molecule, followed by a back donation from the molecule, is energetically favored.

Method of Calculation

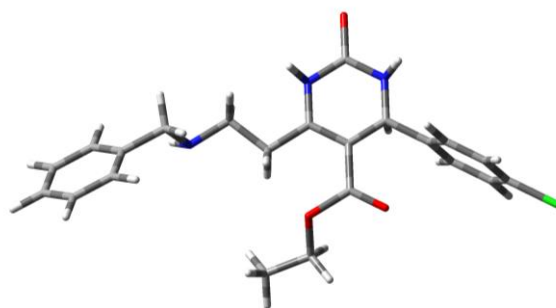
The quantum chemical parameters of the earlier pyrimidine derivatives (Fatima, at al., 2018) were calculated using DFT based on Beck's three parameter exchange functional and Lee–Yang–Parr nonlocal correlation functional (B3LYP) and the 6-31G (d, p) orbital basis sets in Gaussian09 program (Becke,1993; Lee, at al., 1988; Frisch, at al., 2009).

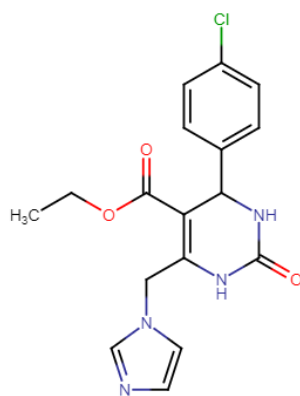
Results and Discussion

The quantum chemical calculations of the all molecules have been performed using DFT based on Beck's three parameter exchange functional and Lee–Yang–Parr nonlocal correlation functional (B3LYP) and the 6-31G (d, p) orbital basis sets in Gaussian09 program (Fig.1). This method has been widely implemented to study the relationship between corrosion inhibition efficiency of the molecules and their electronic properties (Young, 2001).

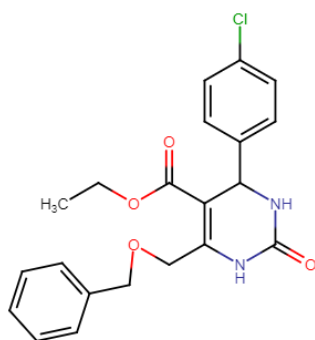
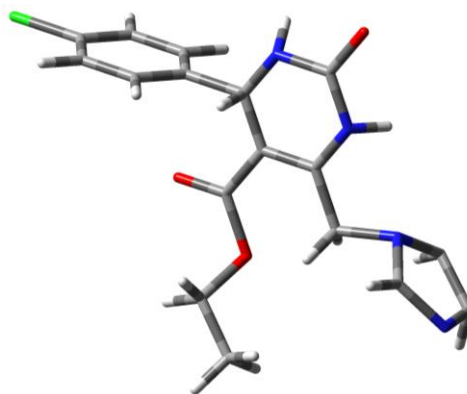


Compound. 1_(Fatima, at al., 2018)





Compound. 2_(Fatima, at al., 2018)



Compound. 3_(Fatima, at al., 2018)

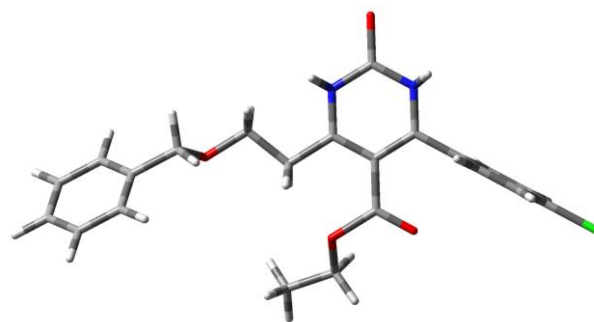


Figure 1. Names, molecular and optimized structures of the compounds

The quantum chemical parameters of all compounds such as the energies of highest occupied molecular orbital (E_{HOMO}) and the lowest unoccupied molecular orbital (E_{LUMO}), the energy gap (ΔE), dipole moment (μ), ionization potential (I), electron affinity (A), absolute electronegativity (χ), chemical hardness (η), global electrophilicity index (ω), chemical softness (S), fraction of electrons transferred (ΔN) and back donation energy ($\Delta E_{\text{back donation}}$) were calculated (Table 1).

Table 1. Calculated quantum chemical parameters of the studied molecules

| Compounds | 1 | 2 | 3 |
|---|---------|---------|---------|
| E_{HOMO} (eV) | -5.9053 | -6.2560 | -6.0301 |
| E_{LUMO} (eV) | -1.9619 | -2.4420 | -2.0686 |
| Ionization potential: I (eV) | 5.9053 | 6.2560 | 6.0301 |
| Electron affinity: A (eV) | 1.9619 | 2.4420 | 2.0686 |
| Electronegativity: χ (eV) | 3.9336 | 4.3490 | 4.0894 |
| Chemical hardness: η (eV) | 3.9434 | 3.8140 | 3.9615 |
| Chemical softness: S | 0.2536 | 0.2622 | 0.2524 |
| Dipole moment: μ (debye) | 4.3615 | 4.6606 | 3.7917 |
| Electrophilicity index: (ω) | 2.4119 | 2.8476 | 1.8148 |
| Transferred electrons fraction: (ΔN) | 0.3888 | 0.3475 | 0.3674 |
| Energy gap: $\Delta E = E_{\text{LUMO}} - E_{\text{HOMO}}$ (eV) | 3.9434 | 3.8140 | 3.9615 |
| $\Delta E_{\text{back donation}}$ | -0.9858 | -0.9535 | -0.9904 |

According to the frontier molecular orbital theory of the chemical reactivity is depends interaction between highest occupied molecular orbital (HOMO) and lowest unoccupied molecular orbital (LUMO). The energy of the highest occupied molecular orbital (E_{HOMO}) measures the tendency towards the donation of electron by a molecule. Therefore, higher values of E_{HOMO} indicate better tendency towards the donation of electron, enhancing the adsorption of the inhibitor on metal and therefore better inhibition efficiency. E_{LUMO} indicates the ability of the molecule to accept electrons. The binding ability of the inhibitor to the metal surface increases with increasing of the HOMO and decreasing of the LUMO energy values. Frontier molecular orbital diagrams of 1, 2 and 3 are represented in fig. 2.

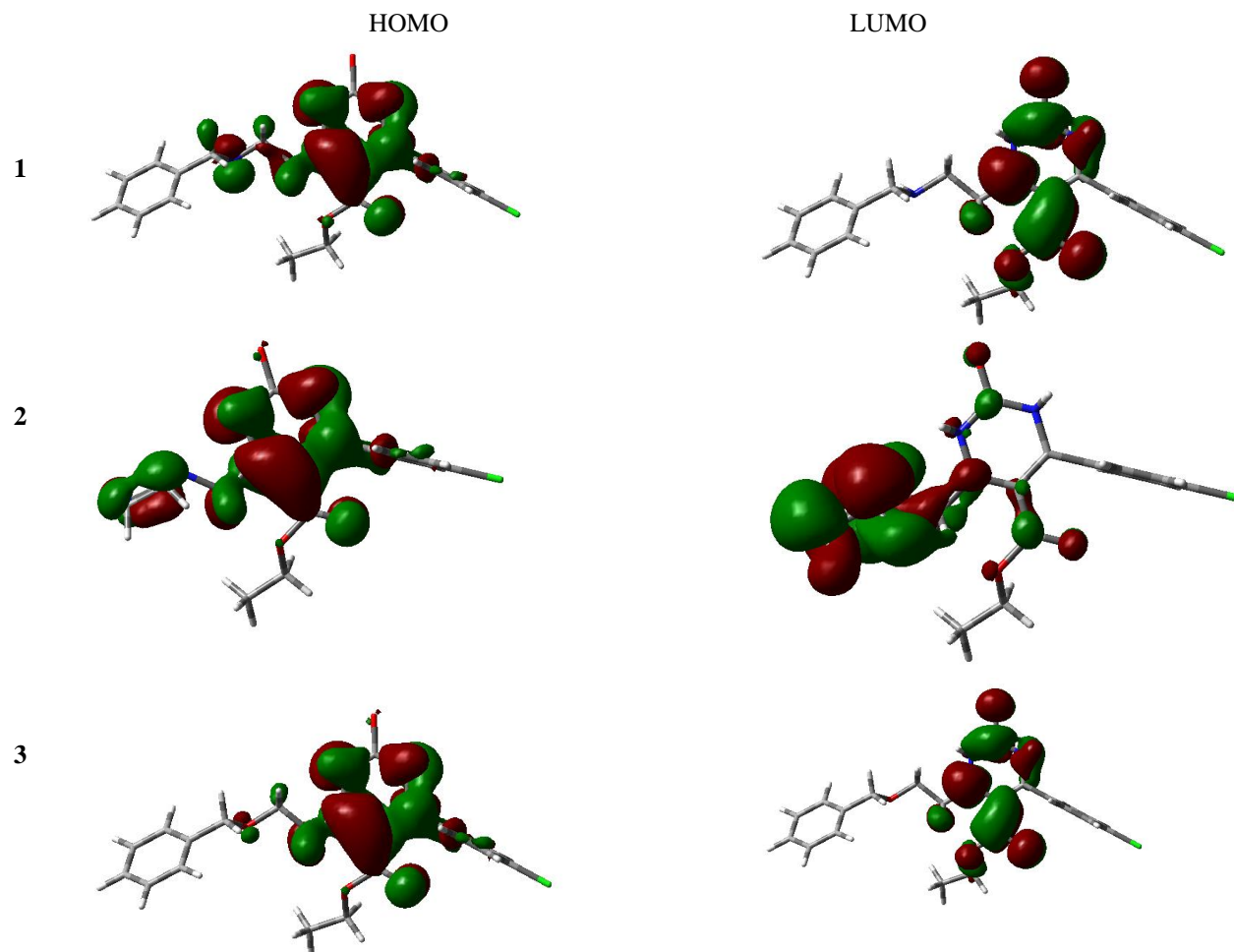


Figure 2. Frontier molecular orbital diagrams of 1, 2 and 3

E_{HOMO} for the three compounds follows the order; $1 > 3 > 2$ which implies that 1 has the highest tendency to donate electrons (Table 1). High value of E_{HOMO} is likely to a tendency of the molecule to donate electrons to appropriate acceptor molecule of low empty molecular orbital energy.

The ionization energy is one of a fundamental descriptor the chemical reactivity of molecules. High ionization energy indicates high stability and chemical inertness and small ionization energy indicates high reactivity of the molecules (Karzazi, at al., 2014). The compound 1 has the lowest ionization energy when compared with other compounds. This indicates that 1 has a high inhibitory effect.

The electron transferred (ΔN) and back-donation ($\Delta E_{\text{back-donation}}$) were also calculated (table 1). If $\Delta N < 3.6$, the inhibition efficiency increases by increasing electron-donating ability of these inhibitors to donate electrons to the metal surface (Karzazi, at al., 2014). The highest fraction of electrons transferred is associated with the best inhibitor.

The calculated $\Delta E_{\text{back donation}}$ values for the inhibitors reveal that back donation is favored for the molecule 1 which is the best inhibitor (table 1).

The molecular electrostatic potential (MEP) provides information about reactive sites for electrophilic and nucleophilic attack. In order to predict reactive sites for electrophilic and nucleophilic attack in all molecules, the MEP maps were also fixed in figure 3. The electrostatic potential on the surfaces have been represented by colors. The blue regions of MEP maps shows electrophilic, while the red areas shows nucleophilic reactivity.

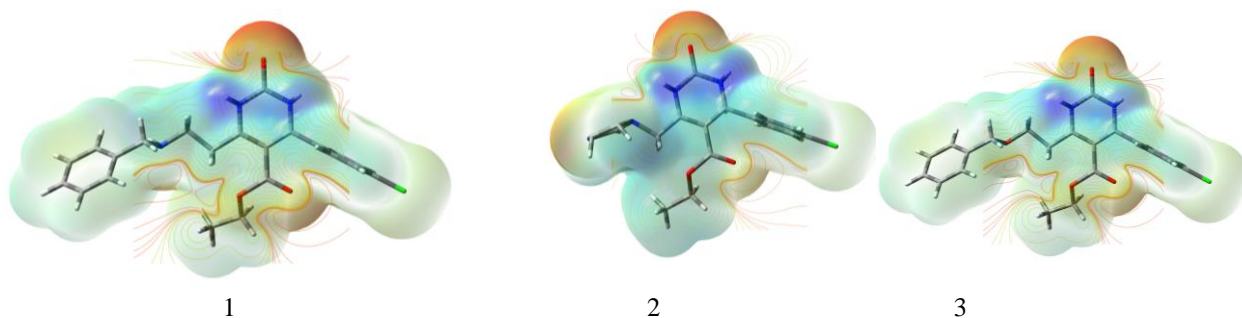


Figure 3. The molecular electrostatic potentials (MEPs)

Conclusion

The pyrimidine derivatives were investigated as corrosion inhibitors using density functional theory (DFT) at B3LYP/6-31G(d,p) level. From the results, it can be concluded that the compound 1 is good inhibitors for the corrosion.

Acknowledgements

This work was supported by the VYYU of Turkey FYL-2016-5291.

References

- Elmors, M.A., Hassanein, A.M. (1999) Corrosion inhibition of copper by heterocyclic compounds. *Corrosion Science* 41(12), 2337.
- Ikpi, M. E., Okonkwo, B. O. (2017) Electrochemical investigation on the corrosion of API 5L X52 carbon steel in simulated soil solutions. *Journal of Materials and Environmental Sciences*, 8(11), 3809.
- Lagrenée, M., Mernari, B., Bouanis, M., Traisnel, M., Bentiss, F. (2002) Study of the mechanism and inhibiting efficiency of 3,5-bis(4-methylthiophenyl)-4H-1,2,4-triazole on mild steel corrosion in acidic media. *Corrosion Science*, 44(3), 573.
- Khalil, N., (2003) Quantum chemical approach of corrosion inhibition. *Electrochimica Acta*, 48(18), 2635.
- Caliskan, N., Akbas, E., (2012) Corrosion inhibition of austenitic stainless steel by some pyrimidine compounds in hydrochloric acid. *Materials and Corrosion*, 63(3), 231.
- Karzazi, Y., Belghiti, M. E. A., Dafali, A., Hammouti, B. (2014) A theoretical investigation on the corrosion inhibition of mild steel by piperidine derivatives in hydrochloric acid solution. *Journal of Chemical and Pharmaceutical Research*, 6(4), 689.
- Ramírez-Ramírez, J.Z., Rubicelia Vargas, R., Garza, J., Gázquez, J.L. (2010) Simple Charge-Transfer Model for Metallic Complexes. *The Journal of Physical Chemistry A*, 114(30), 7945.
- Fatima, I., Farhana, Y., Nida, T., Muhammad Saeed, J., Abdul, S., Saba, T., Tahira, B., Basit, N., Farzana Latif, A., Muhammad Iqbal, C., Umer, R., (2018) Design, synthesis, in-vitro thymidine phosphorylase inhibition, in-vivo antiangiogenic and in-silico studies of C-6 substituted dihydropyrimidines, *Bioorganic Chemistry* 80, 99-111.
- Becke, A.D. (1993) A new mixing of Hartree-Fock and local density-functional theories. *The Journal of Chemical Physics*, 98, 1372.
- Lee, C., Yang, W., Parr, R.G. (1988) Development of the Colle-Salvetti correlation-energy formula into a functional of the electron density. *Physical Review B*, 37(2), 785.
- Frisch, M.J., Trucks, G.W., Schlegel, H.B., Scuseria, G.E., Robb, M.A., Cheeseman, J.R., Scalmani, G., Barone, V., Mennucci, B., Petersson, G.A., Nakatsuji, H., Caricato, M., Li, X., Hratchian, H.P., Izmaylov, A.F., Bloino, J., Zheng, G., Sonnenberg, J.L., Hada, M., Ehara, M., Toyota, K., Fukuda, R., Hasegawa, J., Ishida, M., Nakajima, T., Honda, Y., Kitao, O., Nakai, H., Vreven, T., Montgomery, J.A., Jr., Peralta,

J.E., Ogliaro, F., Bearpark, M., Heyd, J.J., Brothers, E., Kudin, K.N., Staroverov, V.N., Kobayashi, R., Normand, J., Raghavachari, K., Rendell, A., Burant, J.C., Iyengar, S.S., Tomasi, J., Cossi, M., Rega, N., Millam, N.J., Klene, M., Knox, J.E., Cross, J.B., Bakken, V., Adamo, C., Jaramillo, J., Gomperts, R., Stratmann, R.E., Yazyev, O., Austin, A. J., Cammi, R., Pomelli, C., Ochterski, J. W., Martin, R.L., Morokuma, K., Zakrzewski, V.G., Voth, G.A., Salvador, P., Dannenberg, J.J., Dapprich, S., Daniels, A.D., Farkas, Ö., Foresman, J.B., Ortiz, J.V., Cioslowski, J., Fox, D.J. Gaussian, Inc., Wallingford CT, 2009.

Young, D.C. (2001) A practical guide for applying techniques to realworld problems in Computational Chemistry (New York: JohnWiley & Sons Inc.) p. 630.

Author Information

Esvet Akbas

Van YuzuncuYil University,
Faculty of Science,
Department of Chemistry, Van, Turkey
Contact E-mail: esvakbas@hotmail.com

Erdem Ergan

Van Vocational School of Security,
Department of Property Protection and Security,
Van, Turkey

Hakan Donmez

Van YuzuncuYil University,
Faculty of Science,
Department of Chemistry, Van, Turkey

A Perturbative Approach in the Minimal Length of Quantum Mechanics

Bekir Can LUTFUOGLU
Akdeniz University

Abstract: There are many pieces of evidence for a minimal length of the order of Planck length in the problems in quantum gravity, string theory, and black-hole physics etc. Existing of such a minimal length description modifies the traditional Heisenberg uncertainty principle. The novel form is called "the generalized uncertainty principle" in the jargon. Such a deformation in the uncertainty relation changes the corresponding wave equation. The latter Schrodinger equation is now no more a second-order differential equation. Consequently, this causes a great difficulty to obtain the analytic solutions. In this study, we propose a perturbative approach to the bound state solutions of the Woods-Saxon potential in the Schrodinger equation by adopting the minimal length. Here, we take the extra term as a perturbative term to the Hamiltonian. Then, we calculate the first order corrections of the energy spectrum for a confined particle in a well by a Woods-Saxon potential energy.

Keywords: Schrödinger equation, Generalized uncertainty principle, Perturbation theory

Introduction

Since the foundation of quantum mechanics, there has been a growing interest in investigating exact solutions in the relativistic and non-relativistic regime. Especially, in the ordinary non-relativistic quantum mechanics examination of the analytical solutions of the Schrödinger equation with various potential energies is an ongoing research area in molecular physics [Eshghi et al 2019].

Recently, a new concept, namely the Generalized Uncertainty Principle (GUP), is being a subject to the studies on quantum mechanics [Chung et al 2019], quantum gravity [Villalpando et al 2019], quantum cosmology [Bosso et al 2019] and black-hole physics [Xiang et al 2018]. The novelty in the GUP is the modification of the commutation relation among the position and the momentum operator.

$$[\hat{x}, \hat{p}] = i\hbar\delta_{ij}(1 + \beta p^2).$$

Here, β is the deformation parameter and usually known as the minimal length (ML) parameter. Since p represents the momentum, the unit of the ML parameter is the inverse momentum square. Consequently, the Heisenberg Uncertainty Principle is modified with

$$\Delta x \Delta p \geq i\hbar(1 + \beta (\Delta p)^2).$$

In 2012, Hassanbadi et al. examined the Woods-Saxon potential energy in the existence of the ML [Hassanbadi et al 2012]. In that paper, the authors made an approach to obtain the solutions. In this text, we emphasize the author's misleading approach and give the true treatment of the problem in the contents of the perturbative quantum mechanics.

Method

In one dimension the Schrödinger equation

- This is an Open Access article distributed under the terms of the Creative Commons Attribution-Noncommercial 4.0 Unported License, permitting all non-commercial use, distribution, and reproduction in any medium, provided the original work is properly cited.

- Selection and peer-review under responsibility of the Organizing Committee of the Conference

$$\hat{H} \Psi(x, t) = \hat{E} \Psi(x, t).$$

is given with Hamilton and Energy operators. It is a very well-known result that when the potential energy does not depend on time, Schrödinger equation turns to a time-independent eigenfunction problem of the form of

$$\left[\frac{\hat{p}\hat{p}}{2m} + V(x) \right] \psi(x) = E\psi(x).$$

In presence of the GUP, one dimensional time-independent Schrödinger equation becomes

$$\left[\frac{(\hat{p} + \beta\hat{p}^3)^2}{2m} + V(x) \right] \psi(x) = E\psi(x).$$

Then,

$$\left[\frac{\hat{p}^2 + 2\beta\hat{p}^2\hat{p}^2 + \beta^2\hat{p}^2\hat{p}^2\hat{p}^2}{2m} + V(x) \right] \psi(x) = E\psi(x).$$

Since the ML parameter is a very small parameter, we ignore the second-order ML parameter terms. After simple algebra we get

$$\hat{p}^2\psi(x) = 2m[E - V(x)]\psi(x) - 2\beta\hat{p}^2\hat{p}^2\psi(x).$$

At this point, Hassanabadi et al. made an approximation

$$\hat{p}^2(\hat{p}^2\psi(x)) = \hat{p}^2(2m[E - V(x)]\psi(x) - 2\beta\hat{p}^2\hat{p}^2\psi(x)),$$

$$\hat{p}^2(2m[E - V(x)]\psi(x) - 2\beta\hat{p}^2\hat{p}^2\psi(x)) = 2m[E - V(x)](\hat{p}^2\psi(x)) - 2\beta\hat{p}^2\hat{p}^2\hat{p}^2\psi(x).$$

This approximation is not valid since

$$\hat{p}^2(V(x)\psi(x)) \neq V(x)(\hat{p}^2\psi(x)).$$

Instead, the correct form should be

$$\hat{p}^2(\hat{p}^2\psi(x)) = 2m[E - V(x)](\hat{p}^2\psi(x)) - 2m[(\hat{p}^2V(x))\psi(x) + 2(\hat{p}V(x))(\hat{p}\psi(x))] - 2\beta\hat{p}^2\hat{p}^2\psi(x).$$

Therefore, the final expression becomes

$$\left[\frac{\hbar^2}{2m} \frac{d^2}{dx^2} + \left(E - 4m\beta(E - V(x))^2 - V(x) - 2\beta \left(\frac{d^2V(x)}{dx^2} + 2 \frac{dV(x)}{dx} \frac{d}{dx} \right) \right) \right] \psi(x) = 0.$$

This result differs from the one that is given in the article of Hassanabadi et al. For the solution of this differential equation, we suggest the non-degenerate perturbation theory can be employed. We briefly discuss the non-degenerate perturbation theory in the next section.

Results and Discussion

In a standard text book of quantum mechanics, for example [Flügge 1974], the non-degenerate perturbation theory is given with the serial expansion of the Hamilton operator, energy eigenvalue of the n^{th} state, and the n^{th} stationary state function $|n\rangle$ via a small perturbation constant as follows

$$\begin{aligned} \hat{H} &= \hat{H}_0 + \beta\hat{H}_1, \\ E_n &= E_n^0 + \beta E_n^1 + \dots, \\ |n\rangle &= |n^0\rangle + \beta|n^1\rangle + \dots, \end{aligned}$$

When these expansion are inserted in the time-independent Schrödinger equation, we get

$$\begin{aligned} E_n^0 &= \langle n^0 | \hat{H}_0 | n^0 \rangle, \\ E_n^1 &= \langle n^0 | \hat{H}_1 | n^0 \rangle, \\ |n^0 \rangle &= \frac{|m^0 \rangle \langle m^0 | \hat{H}_1 | n^1 \rangle}{E_n^0 - E_m^0}. \end{aligned}$$

Since, the exact solution of the Woods-Saxon potential is given in the textbook of Flügge [Flügge 1974], we conclude that the formalism can be applied.

Conclusion

In this work, we discuss a perturbative approach to a non-relativistic problem in the presence of a minimal length formalism. Initially, we first showed the improper approach which exists in the literature. Then, we derived the correct approach to the problem, and then, point out the formalism where it can be solved perturbatively.

Acknowledgements

The author thanks to the organization committee for being very kind and helpful not only during the meeting ICRES 2019 but after too. This work was supported by The Scientific Research Projects Coordination Unit of Akdeniz University. Project Number is FBA-2018-3471.

References

- Eshghi, M., Sever, R. & Ukhdair, S.M.. (2019). Thermal and optical properties of two molecular potentials. *Eur.Phys. J. Plus*, 134, 155.
- Chung, W.S. & Hassanabadi, H.. (2019). A new higher order GUP: one dimensional quantum system. *Eur. Phys. J. C*, 79, 213.
- Villalpando, C. & Modak, S.K.. (2019). Minimal length effect on the broadening of free wave packets and its physical implications. *Phys. Rev. D*, 100, 052101.
- Bosso, P. & Obregon, O.. (2019). Quantum cosmology and the Generalized Uncertainty Principle. <http://arxiv.org/pdf/1904.06343>.
- Xiang, L., Ling, Y., Shen, Y.-G., Liu, C.-Z., He, H.-S. & Xu, L.-F.. (2018). Generalized uncertainty principles, effective Newton constant and the regular black hole. *Ann. Phys.*, 396, 334.
- Hassanabadi, H., Zarrinkamar, S. & Maghsoodi, E.. (2012). Scattering states of Woods-Saxon interaction in minimal length quantum mechanics. *Phys. Lett. B*, 718, 678.
- Flügge, S.. (1974). *Practical Quantum Mechanics*. Berlin: Spinger.

Author Information

Bekir Can Lutfuoglu

Akdeniz University
Faculty of Science, Department of Physics, 07058 Campus,
Antalya, Turkey.
+90 242 310 23 13
+90 242 227 89 11 (Fax)
Contact E-mail: bclutfuoglu@akdeniz.edu.tr

Synthesis, Investigation and X-Ray Powder Diffraction (XRD) of Some Oxadiazole Complexes

Amerah Jihad AHMED SHAHEEN
University of Mosul

Abstract: New ligand; 2-(1,1-dimethoxymethane) thio-5- (phenyl)-1,3,4-oxadiazole (L)(3) and its complexes with Mn(II), Fe(III), Co(II), Ni(II), Cd(II) and Zr(IV), have been synthesized and characterized on the basis of physicochemical investigations including infrared and electronic spectroscopy, magnetic moment measurements, molar conductance and elemental analysis. The structures of the compounds and some complexes have been investigated by X-ray powder diffraction and ¹H NMR spectra. was recorded on broker shield 300 MHz using deuterated DMSO-d₆ as a solvent. for ligand. They have been found to have the formula; [M L (H₂O)₃Cl]Cl_n; M= Mn(II) n = 1, (4) and M= Fe(III), n = 2 (5), [ML (H₂O) Cl] Cl, M= Co(II) (7), Cd(II) (8) and [NiLCl₂](6), [ZrOL(H₂O) Cl₂]Cl₂ (9), in molar ratio 1:1. Infrared spectral data suggest that the ligand L: behaves as a, bidentate ligand with N,S, donor sequence towards the metal ions. According to the above physicochemical data, octahedral and tetrahedral geometries were assigned for the complexes.

Keywords: Complexes, Oxadiazole, X-ray studies

Introduction

Oxadiazole ring is an electron deficient, resulting in poor hole transport but good transport properties. Although some types of metal complexes have found to be good emitters and/or excellent electron transport with excellent thermal properties (1). 1, 3,4- oxadiazoles and their derivatives are known to exhibit diverse pharmacological activities such as antimicrobial, antihistaminic, anticancerous, anti- inflammatory, antihypertensive and anticonvulsant activities (2 ,3). 1,3,4 -Oxadiazole derivatives are also among the most widely employed electron conducting and hole blocking (ECHB) materials in organic light- emitting diodes (LEDs).(4).The. application of 1,3,4 -Oxadiazole derivatives lie in the field of liquid crystals.(5) .The heterocyclic thiones represent an important type of compound in the field of coordination chemistry because of their potential multifunctional donor sites, viz either exocyclic sulfur or endocyclic nitrogen (6). For this reason our aim was synthesize various 1,3,4 -oxadiazole derivatives to make notable contributions to this class of heterocyclic compounds. There are a few reports on the metal complexes of -5-phenyl-1,3,4-oxadiazole. 2-substituted thione.

Experimental

Chemicals

All chemicals and metal salts were commercially available pure samples and used throughout this investigation available from Merck, B.D.H Aldrich or Fluka.

Analytical and Physical Measurements

Melting point and decomposition temperature were determined using SMP30 melting point apparatus. IR spectra measurements were recorded using FTIR-Tensor 27-Burker Co. Germany 2003 as KBr pellets in the range (400-4000 cm⁻¹) . UV- visible spectral measurements were done on Shimaduz UV-Visible

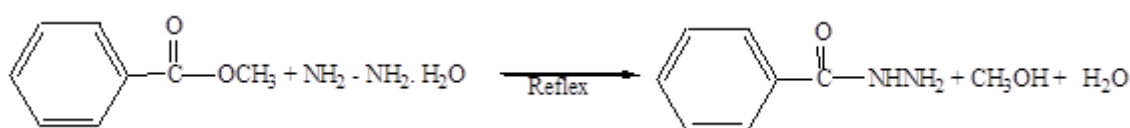
- This is an Open Access article distributed under the terms of the Creative Commons Attribution-NonCommercial 4.0 Unported License, permitting all non-commercial use, distribution, and reproduction in any medium, provided the original work is properly cited.

- Selection and peer-review under responsibility of the Organizing Committee of the Conference

1800 Spectrophotometer for 10⁻³ M complexes in DMF solvent at room temp. using 1cm quartz cell in range (200-1100) nm. The ¹H NMR analysis was recorded on Bruker Ultra Shield 300 MHz using deuterated DMSO-d₆ as solvent and Me₄ Si as internal reference .Elemental analysis were carried out on a CHN analyzer type 4010 model 2011 Costech Elemental Combustion. Metal contents were estimated spectrophotometrically using atomic absorption Spectrophotometer Scientific Equipment. X-ray powder diffraction data were measured for the ligand (3) and complexes (5 & 7) at General Company for Geological Survey and Mining-Bagdad by using Shimadzu X-ray Diffraction 7000 model 2009 and the crystal data for complexes were analyzed by using Match Program Version 1.6 c. Molar conductance of complexes were measured at room temp. for 10⁻³ M in DMF using (BC 3020 professional Bench top conductivity) . Magnetic susceptibility of the complexes was measured by Bruker -BM6 using Faraday method.

Preparation of benzoylhydrazine (1)⁽⁷⁾

On the first step hydrazine hydrate (5g, 0.1mole) was added drop-wise to methylbenzoate (18.1g, 0.1 mole) in absolute ethanol, after adding, the mixture was refluxed for 2 hours and then cooled and the creamy solid product formed was collected by filtration, washed with cold ethanol and purified by crystallization from ethanol and dried at 50 °c as in the following equation , yield (96%), m.p 112-113 °c empirical formula. C₇H₈N₂O

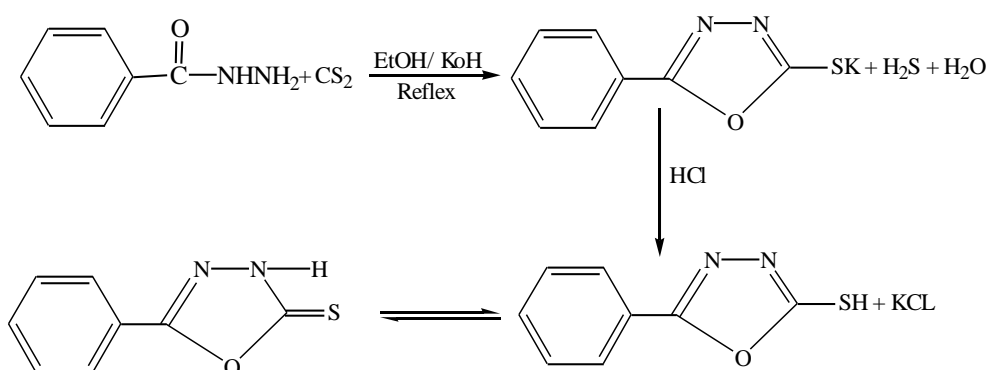


| | %C | %H | %N |
|-------|-------|------|-------|
| Calc. | 61.69 | 5.87 | 20.58 |
| Found | 61.63 | 5.84 | 20.52 |

Preparation of 2-thio-5-phenyl -1,3,4-Oxadiazole (2)⁽⁸⁾

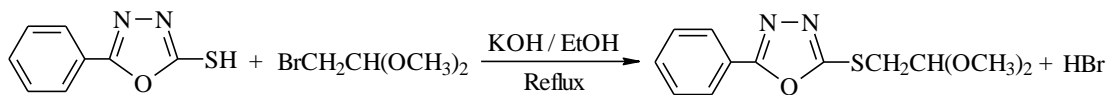
In the second step, this ligand was prepared according to the modified procedure (young wood. The hydrazide of the step 1(benzoyl hydrazine) (13.6 g, 0.1M). was allowed to react with carbon disulphide (120 ml, 0.2 M of CS₂) in the presence of ethanolic potassium hydroxide (5.6 g ,0.1M of KOH in 70 ml absolute ethanol) under reflux conditions until the liberation of H₂S gas has been stopped and is detected with lead(II) acetate paper it turns grey in the presence of H₂S gas followed by acidification with dilute HCl to give yellowish precipitate, which was filtered ,wash with cold water , and dried under vacuum as in the following equation. The yield (85%) , mp 219-220 °c , empirical formula C₈H₆N₂OS.The yield product was characterized by CHN analysis, IR and ¹H NMR.

| | %C | %H | %N |
|-------|-------|------|-------|
| Calc. | 53.93 | 3.37 | 15.73 |
| Found | 53.71 | 3.28 | 15.81 |



Preparation of 2- thio (1,1-dimethoxyethane) -5- phenyl-1,3,4-Oxadiazole (3) ⁽⁹⁾

A 2-thio-5-phenyl -1,3,4-Oxadiazole (A1) (17.8. g , 0.1 M) was dissolved in ethanolic potassium hydroxide (5.6g ,0.1M of KOH in 100 ml absolute ethanol) followed by slow addition of drop wise of 2-bromodimethoxyethan (16.9, 0.1M) .The mixture has been refluxed for 3 hours with stirring, followed by cooling, then evaporated to half its volume, cooled, filtered, the yellowish precipitate recrystallized from ethanol and dried under vacuum as in the following equation. . The yield (62%), mp 195--196 °c , empirical formula C₁₂H₁₄N₂O₃S. The yield product was characterized by IR and H¹NMR.



| | %C | %H | %N |
|-------|-------|------|-------|
| Calc. | 51.96 | 5.51 | 11.02 |
| Found | 52.03 | 5.80 | 10.89 |

Preparation of the Complexes^{(4,5,6,7,8&9)(10)}

A general procedure has been adopted for the preparation of all complexes in Molar Ratio (1:1) Ligand: Metal. An ethanolic solution of the ligand (compound(3)) (2.66 g, 0.01 M in 25 ml ethanol) has been added to a solution of 0.01mol of each of metal salts 0.01M in 20 ml of distilled water or ethanol solution. The mixture has been refluxed for 1/2 - 2 hours with stirring ,followed by cooling and .The product has been filtered off, recrystallized from ethanol then evaporated to half its volume, cooled, filtered, washed and dried examination of elemental analyses data, as given in Table (1&2).

Results and Discussion

The prepared ligand (3) and its complexes are solid and coloured ,insoluble in water, but soluble in DMF. Table 1 revealed conductivity data obtained in DMF at 10⁻³ M .The molar conductance values of the complexes (4,7 and 8) are in the range (50-70) $ohm^{-1} cm^2 mol^{-1}$ indicating a (1: 1) electrolytic nature of these complexes ⁽¹¹⁾ .While the molar conductance values of the complexes (5and 9) are in the range (130-140) $ohm^{-1} cm^2 mol^{-1}$ indicating (1:2) electrolytic nature of these complexes . On other hand, the complex (6) is non- electrolytic indicating neutral complex ⁽¹²⁾ in nature. The molar conductance values are in a good agreement with given formulations .(Tables 1&2).

Table 1.Analytical data and some physical properties of the complexes

| Comp. No. | Metal Salt | Wt(g) Metal Salt | Wt(g) L | Ω $ohm^{-1} .cm^2$ mol^{-1} | Complexes | m.p or d ^o C | Color |
|-----------|---------------------------------------|------------------|---------|--|---|----------------------------|------------|
| 4 | MnCl ₂ .6H ₂ O | 1.9 7 | 2.66 | 70 | [MnL (H ₂ O) ₃ Cl]Cl | 214 | pale brown |
| 5 | FeCl ₃ | 1.6 2 | 2.66 | 130 | [FeL (H ₂ O) ₃ Cl]Cl ₂ | 140 | deep brown |
| 6 | NiCl ₂ .6H ₂ O | 2.3 4 | 2.66 | 10 | [NiLCl ₂] | 152 | olive |
| 7 | CoCl ₂ .6H ₂ O | 1.8 | 2.66 | 50 | [CoL (H ₂ O) Cl]Cl | 193 | blue |
| 8 | CdCl ₂ | 1.8 3 | 2.66 | 70 | [CdL (H ₂ O)Cl]Cl | 218 | pale brown |
| 9 | ZrOCl ₂ .8H ₂ O | 3.2 2 | 2.66 | 170 | [ZrOL (H ₂ O) Cl ₂]Cl ₂ | 130 | pale brown |

d = decomposition temp.

Table 2. Elemental analysis of the complexes

| Comp.No. | Complexes | % Found (Calc.) CHN, M | | | |
|----------|---|------------------------|--------|--------|---------|
| | | C | H | N | M |
| 4 | [MnL (H ₂ O) ₃ Cl]Cl | (30.41) | (4.60) | (6.45) | (12.67) |
| | | 30.50 | 4.91 | 6.71 | 12.40 |
| 5 | [FeL (H ₂ O) ₃ Cl]Cl ₂ | (28.05) | (4.25) | (5.95) | (11.90) |
| | | 28.22 | 4.35 | 6.00 | 12.02 |
| 6 | [NiLCl ₂] | (34.46) | (5.22) | (7.31) | (15.32) |
| | | 34.77 | 5.45 | 7.61 | 15.53 |
| 7 | [CoL (H ₂ O) Cl]Cl | (32.83) | (5.47) | (3.81) | (14.67) |
| | | 33.00 | 5.77 | 4.00 | 14.87 |
| 8 | [CdL (H ₂ O)Cl]Cl | (29.01) | (4.83) | (6.15) | (24.61) |
| | | 28.89 | 5.11 | 6.45 | 24.88 |
| 9 | [ZrOL (H ₂ O) Cl ₂]Cl ₂ | (26.13) | (2.57) | (5.54) | (18.01) |
| | | 26.00 | 2.84 | (5.83) | 17.87 |

Infrared Spectra

The ligand (3) is basically composed of different groups of potent ability to coordinate with the metal ions. The coordination sites of the ligand involved in the bonding with metal ions had been determined by careful comparison of the infrared spectra of those compounds with that of the parent ligand. The IR spectra of the compound (2) shows two bands a weak band at 2350cm^{-1} which is characteristic of stretching vibration of the SH group and sharp band at 3434cm^{-1} due to NH stretching vibration⁽¹³⁾. These bands which subsequently disappeared in the ligand L(compound 3, Fig.1), indicating a vibration substitution occurred on position 2, and a new absorption bands appeared at 1397cm^{-1} , which has been attributed to bending frequency of -SCH₂ group. This is further supported by the appearance of the band at 652cm^{-1} due to stretching vibration of C-S bond and, these bands shifted to a higher value in complexes as shown in Fig. 2 for (complex 4), ν - C-S (672)& ν - S-CH₂ (1415) cm^{-1} (14). In the spectra of the ligand (3) showed, a weak band at 2925cm^{-1} due to sym.& asym. C-H aliphatic of CH₂ group, and his band remains unaltered on complexation(15). The IR spectra of the ligand (3) show a strong band in the region 1608cm^{-1} , which is characteristic of the azomethane(16) indicating coordination of the L through azomethine nitrogen atoms to the metal center (through the nitrogen atom, of the oxadiazole ring) and, this band shifts to a higher value on coordination as shown in (complex 4) ν -C=N at (1618) cm^{-1} . This view is further supported by the appearance of a band corresponding to the metal-nitrogen(17) stretching vibration at $460-501\text{cm}^{-1}$ in the complexes and for complex 4 has been appeared at 501cm^{-1} . The spectra also shows a broad band at 946cm^{-1} due to N-N group shifts towards higher frequency ($1000-1020$) cm^{-1} on complexation (18), while in complex(4) this band appears at 1014cm^{-1} . In the ligand 3 spectra shows a characteristic band at 1077cm^{-1} which was assigned to the stretching was assigned to C-O-C group of the oxadiazole ring and this band remains unaltered on complexation indicating the absence of coordination through oxygen of this group (19). The aqua complexes contain weak to medium a broad band at ($3099-3477$) cm^{-1} due to stretching vibration OH of water (20) and a sharp shoulder at (1117) cm^{-1} may be assigned to bending vibration of water molecules are coordinated, confirmed by occurrence of additional strong and sharp band at $672-720\text{cm}^{-1}$ due to OH rocking vibrations. Also is further supported by the appearance of a band corresponding to the metal-oxygen stretching vibration at $546-571\text{cm}^{-1}$ and for complex 4 3477 , ν -OH₂ 2766 , ν -OH₂ 571 , ν -M-OH₂. (21). In addition the coordination of chloride could not be inferred from infrared spectra of the complexes because the band occurred beyond the range of our infrared spectrophotometer, whereas for Cl⁻ ionic has been checked by AgNO₃. All chloride complexes show a band at $584-618\text{cm}^{-1}$ and for complex (4) 584 , cm^{-1} has been attributed to ionic chloride (15) as shown in (Table 3).

Table 3. Selected I.R. bands of the ligand and its complexes (cm⁻¹)

| Comp. No. | ν -C=N | ν - N-N | ν - C-S | ν -M-N | ν - M-S | Others |
|-----------|------------|-------------|-------------|------------|-------------|---|
| 3 | 1608 | 946 | 652 | - | - | 1397, ν - S-CH ₂ 1024, ν - C-O-C 2925, ν - C-H |
| 4 | 1618 | 1014 | 672 | 501 | 410 | 584, ν - IonicCl- 3477, ν - OH ₂ 766, ν - OH ₂ 571, ν - M-OH ₂ |
| 5 | 1600 | 1018 | 676 | 460 | 423 | 600, ν - ionic C ⁺ 3420, ν - OH ₂ 752, ν - OH ₂ 546 ν - M-OH ₂ |
| 6 | 1580 | 1019 | 665 | 462 | 415 | - |
| 7 | 1585 | 1020 | 666 | 476 | 410 | 618 ν - Ionic Cl ⁻ 3300 ν - OH ₂ 680 ν - OH ₂ 558 ν - M-OH ₂ |
| 8 | 1592 | 1000 | 675 | 470 | 416 | 612 ν - Ionic Cl ⁻ 3475 ν - OH ₂ 690 ν - OH ₂ 556 ν - M-OH ₂ |
| 9 | 1575 | 1007 | 675 | 480 | 420 | 600 ν - Ionic Cl ⁻ 3472 ν - OH ₂ 741 ν - OH ₂ 552 ν - M-OH ₂ |

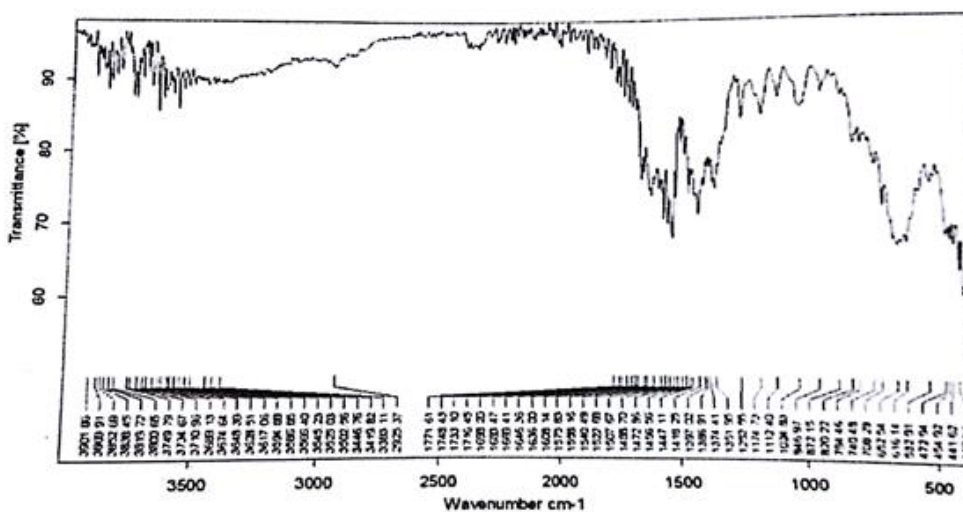


Figure 1. Ft-IR spectrum of the ligand (3)

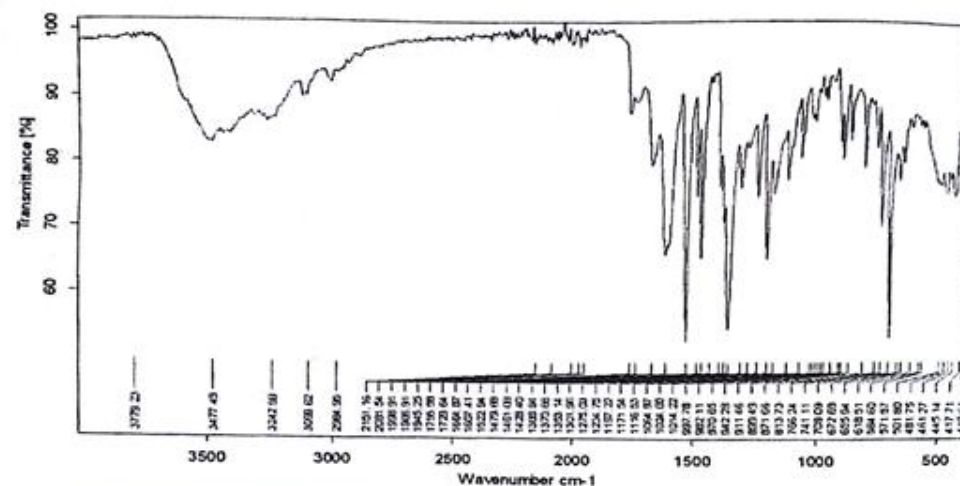


Figure 2. Ft-IR spectrum of the complex 4

Electronic Spectra and Magnetic Moment

The electronic spectra of the ligand (3) and its complexes) in DMF solution have been recorded giving ultraviolet spectra, d-d spectra and charge transfer spectra (Table 4). The ultraviolet spectra for ligand exhibited two bands in the UV intervals at 31847 cm^{-1} and 377351 cm^{-1} , assigned to $n \rightarrow \pi^*$ (C=S), and $\pi \rightarrow \pi^*$ (C=N) transitions, respectively. All these transitions were also found in the spectra of the complexes but they were shifted to lower frequencies confirming the coordination of the ligand to the metal ions⁽²³⁾. The electronic spectrum of Fe(III) complex (5) exhibited, only sextet term ${}^6A_{1g}$ of the d^5 configuration octahedral geometry and does not split by the ligand field. Consequently, all the excited states have different spin multiplicity from the ground term and transition to them is forbidden, and many weak bands were observed at $9794, 10928, 13333\text{ cm}^{-1}$ and assigned as due to transition from ${}^6A_{1g}$ to ${}^4T_{2g}(G)$ and ${}^4T_{2g}(G)$, and are characteristic of an octahedral geometry as shown in (Fig. 4). In addition, high intensity band was observed in the ultraviolet region of the spectra at 27472 cm^{-1} and assigned to C-T transition. Complex 5 shows magnetic moments at room temperature calculated from the corrected magnetic susceptibilities is 5.38 B.M. revealing the presence of five unpaired electrons are present in the complex molecule and indicating high spin octahedral complex⁽²⁴⁾. The experimental electronic spectrum of Co(II) complex (7) showed less intense band in the region 14833 cm^{-1} which correspond to the ${}^4A_2(F) \rightarrow {}^4T_1(P)$ v_3 transition. This band is specific to the Co(II) ion in tetrahedral stereochemistry, a geometry also confirmed by the magnetic moment of the complex which is 4.61 B.M. and the blue colour. The other two bands due to ${}^4A_2(F) \rightarrow {}^4T_2(F)$ v_1 and ${}^4A_2(F) \rightarrow {}^4T_1(F)$ v_2 transitions⁽²⁴⁾ were absent because they fall below the limits of our instrument. While in the spectrum of the Ni(II) complex (6) exhibits electronic spectrum. One strong band at $13881, 14566$ and 37593 cm^{-1} , respectively and assigned to transitions ${}^3A_{1g}(F) \rightarrow {}^3T_{2g}(F)$ v_1 , ${}^3A_{1g}(F) \rightarrow {}^3T_{1g}(F)$ v_2 and $A_{1g}(F) \rightarrow {}^3T_{1g}(p)$ v_3 and this tetrahedral geometry is also supported by the value of the magnetic moment of 3.85 B.M.⁽²⁵⁾. The electronic spectrum of manganese (II) complex 4 exhibited bands at 14880 cm^{-1} and 32362 cm^{-1} since the d-d transitions as shown in Fig.3, doubly forbidden from the term ${}^6A_{1g}$ towards, the quartet terms ${}^4T_{1g}(G)$, ${}^4T_{2g}(G)$, ${}^4A_{1g}$, 4E_g , exhibit a very small intensity and are concealed by the intraligand transitions. The absorption band at 32362 cm^{-1} can be attributed to the charge transfer of ligand to metal. The complex 4 shows magnetic moment 5.09 B.M. basing on this discussion a high spin octahedral arrangement may be proposed around Mn(II) ion in complex(4)⁽²⁶⁾. The two transitions of the ligand are found also in the spectra of the Cd(II) and Zr(IV) complexes but they shifted towards a lower frequencies, confirming the coordination of the ligand to these ions. They were found to be diamagnetic as expected for d^{10} system,⁽²⁴⁾ Table 4.

Table 4. Electronic spectra data of the complexes

| Comp.No. | Electronic transitions of d-d cm^{-1} | | | |
|----------|--|---------|---------|-------------------|
| | ν_1 | ν_2 | ν_3 | CT |
| 4 | 14880 | - | - | 32362 |
| 5 | 9794 | 10928 | 13333 | 27472 |
| 6 | 13881 | 14566 | 37593 | 37812 |
| 7 | - | - | 14833 | 35668 |
| 8 | - | - | - | 31446,37250,41615 |
| 9 | - | - | - | 31440,37133,41611 |

CT = charge transfer band

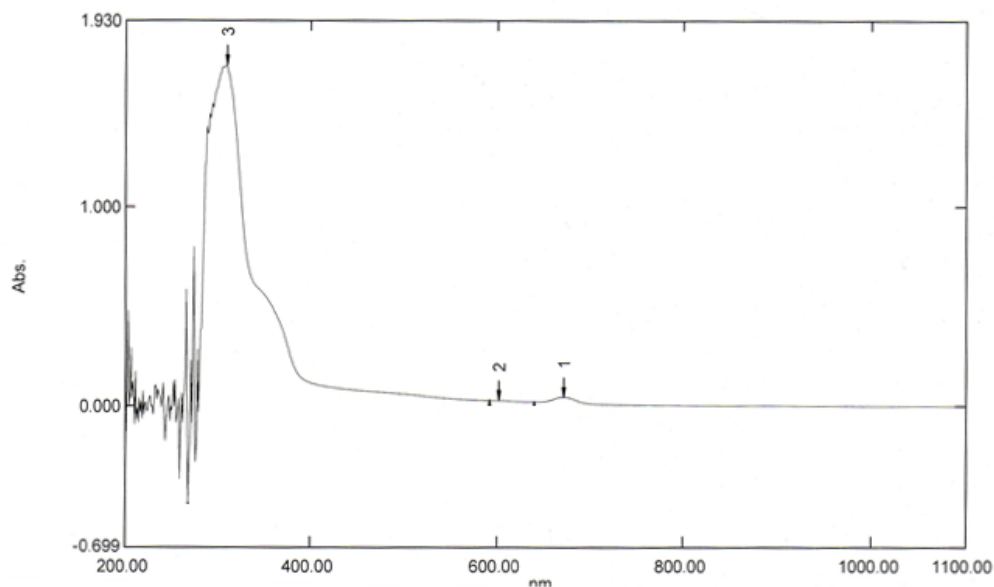


Figure 3. UV-Visible spectrum of the complex 4

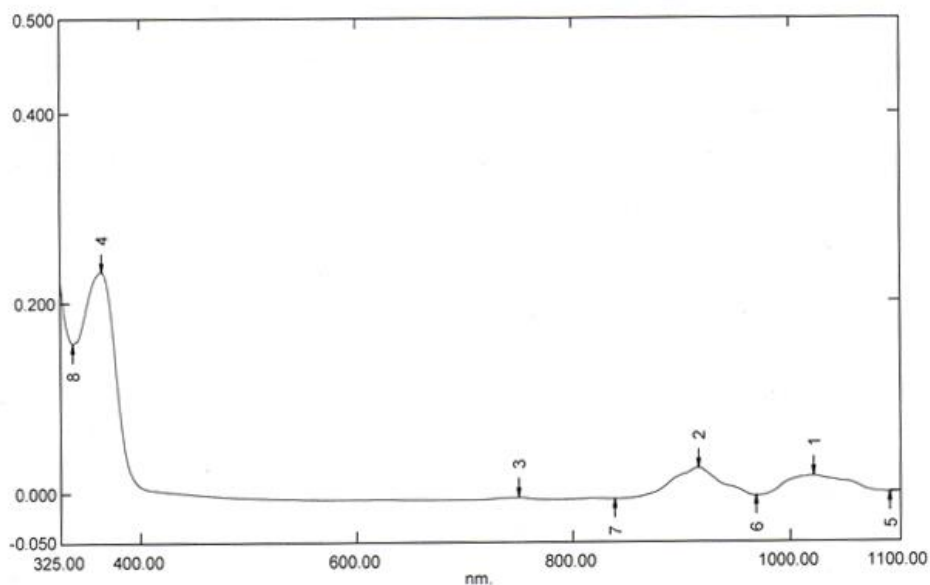


Figure 4. UV-Visible spectrum of the complex 5

^1H NMR Spectra

Compound 2 exhibits a sharp singlet at 10.7 ppm due to SH group and this peak is expected for thiol- 1,3,4-oxadiazole signal, While compound 3 exhibits a singlet signal at $\delta = 4.52$ ppm due to $\text{CH}_2\text{-S}$ group

protons attached to S atom and oxadiazole ring, and this is an electron withdrawing group. On the other hand, aromatic protons were observed in region 7.15–7.46 ppm, the signal at ($\delta = 3.24$ ppm) is assigned to O-CH₃ group and absorption signal at ($\delta=4.47$ ppm) due to CH group⁽²²⁾.

X-ray Powder Diffraction Analysis

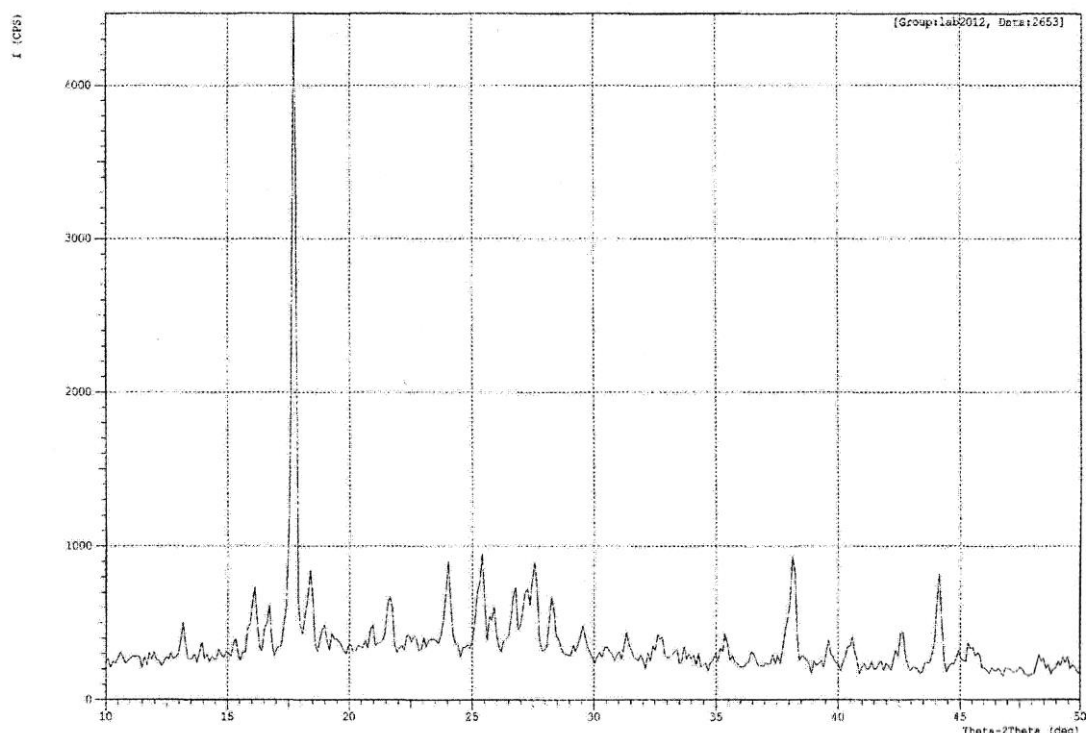
X-ray powder diffraction analysis of the parent metal salts from which they were prepared metal complexes was carried out to determine the type of crystal system, lattice parameters, and the cell volume. The XRD patterns of complex 4 indicate a crystalline nature for metal complexes. Indexing of the diffraction patterns was performed using high Score Plus Software (Match program)⁽²⁷⁾. For Fe(III) and Co(II) complexes, for example, their Miller indices (hkl) along with observed and calculated 2θ angle, d values, and relative intensities, from the indexed data the unit cell parameters were also calculated and the powder XRD patterns of the compounds are completely different from those of the starting materials⁽²⁸⁾, demonstrating the formation of coordination compounds. It is found that Fe(III) and Co(II) complexes have orthorhombic and tetragonal structure. Moreover, using diffraction data, the mean crystallite sizes of the complexes, D , were determined according Scherrer equation ($D = 0.9 \lambda / (\beta \cos \theta)$), where λ X-ray wavelength (1.5406 \AA), θ is Bragg diffraction angle, and β is the full width at half maximum of the diffraction peak^(29,30) as shown in Table 5.

Table 5 .Crystal data and structure refinement for complexes

| No | Complex | 5 |
|----|-------------------------------|--|
| 1 | Molecular Formula | FeC ₁₂ H ₂₀ N ₂ O ₆ SCl ₃ |
| 2 | Molecular weight | 482 |
| 3 | Crystal system | Orthorhombic |
| 4 | Space group | Pca (61) |
| 5 | Unit cell parameters (A°) | a= 11.101 , b= 12.229 , c= 9.079 |
| 6 | Cell Volume (A ³) | 1271.93 |
| 7 | Z | 8 |
| 8 | θ range , deg | 2.08 – 30.52 |
| 9 | Index ranges | $0 \leq h \leq 2, 0 \leq k \leq 3, 0 \leq L \leq 4$ |

| No | Complex | 7 |
|----|-------------------------------|--|
| 1 | Molecular Formula | CoC ₁₂ H ₁₆ N ₂ O ₄ SCl ₂ |
| 2 | Molecular weight | 414 |
| 3 | Crystal system | Tetragonal |
| 4 | Space group | P-4(81) |
| 5 | Unit cell parameters (A°) | a= 7.22 A° , c= 14.33 A° |
| 6 | Cell Volume (A ³) | 1253.37 A° |
| 7 | Z | 4 |
| 8 | θ range , deg | 10.55 – 50.06 |
| | | $0 \leq h \leq 6$ |
| 9 | Index ranges | $0 \leq k \leq 4$ |
| | | $0 \leq L \leq 2$ |

| No. | Metal Salt | Cobalt chloride hexa hydrate |
|-----|--------------------------------|---------------------------------------|
| 1 | Molecular Formula | CoCl ₂ .6H ₂ O |
| 2 | Molecular weight | 237.93 |
| 3 | Crystal system | monoclinic |
| 4 | Space group | P21/c(14) |
| 5 | Unit cell parameters (Ao) | a=8.86,b=7.07, c=13.12, $\beta=97.28$ |
| 6 | Cell Volume (Ao ³) | 815.21 |
| 7 | Z | 4 |
| 8 | θ range , deg | 14.26-69.36 |
| 9 | Index ranges | $-5 \leq h \leq 6$ |



Scheme 1. Powder x-ray diffraction (PXRD) of complex 4

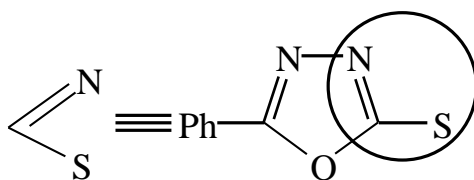
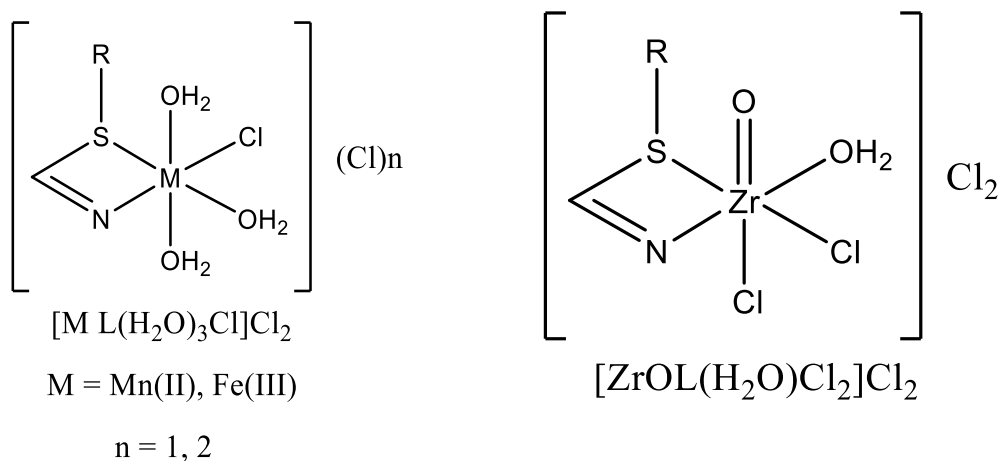


Figure 5. Proposed Structure of some complexes

Conclusion

Simple efficient methods have been followed to synthesize new ligand of oxadiazole derivative and its complexes and they were characterized by physicochemical measurements and spectral studies. Moreover, the newly synthesized ligand(3)and complexes (5&7) were evaluated for XRD analysis to estimate the crystal geometries and we concluded that an octahedral structure has been suggested for manganese, iron and zirconium complexes as shown in (Fig. 5).Whereas cadmium, nickel and cobalt complexes have tetracoordinate

geometries. The IR spectroscopic and analytical data showed that ligand (L) (3) acts as bidentate coordinated to the metal ions through sulfur thioether and azomethine nitrogen atoms.

Acknowledgement

The author would like to thank Head of Chemistry Department in Education college for Pure Science of Mosul University for providing laboratory facilities, the author also is thankful to Central Geological Survey and Mining-Baghdad for the use of Shimadzu X-ray Diffraction 7000 model 2009.

References

- Kalagudasi G, Manjula P, Ramesh, V., Rashmisheoy and Sidappa P. "(2007), Transition metal complexes with a new tridentate ligand, 5-(5-mercapto-1,3,4-oxadiazol-2-yl)pyridin-2-yl-1,3,4-oxadiazole-2-thiol", *J. Serb. Chem. Soc.* 72, (4) 357–366.
- Almasirad, A; Tabatabai, S.A and Faizi, M; (2004) "Synthesis and biological activity of 1,3,4-oxadiazole derivatives"; *Biorg. Med. Chem. Lett*; 14, pp. 6057,.
- Abdel Hamid, M; (2008) "Synthesis and cyclization reactions with oxadiazole derivatives and their enzymic activity"; *Acta. Chim. Slov*; 55, 492-501
- Bhat, M. A; Siddiqui, N and Khan, S.A; (2008). "Synthesis of novel 3-(4-Acetyl-5H-methyl-5-substituted phenyl-4,5-dihydro-1,3,4-oxadiazol-2-yl)-2H-chromen-2-ones as potential anticonvulsant agent, *Polish. Pharm. Soc*; 65, pp.235-239.
- Shabbir Akazi (2011), "Synthesis and characterization of a new bidentate ligand 5-substituted-(2-methyl-5-nitro-1-imidazomethyl)-1,3,4-oxadiazole-2-thione and its metal complexes of Ag(I), Cu(II) and Zn(II)", *E-J. of Chemistry* 8(S1), S127-S136.
- Najat A. obaidy, K.K. Abid, Yusra, (2006). "Transition metal complexes of 1,3,4-oxadiazole ligands", *National J. of Chem.*, 24, 629-641
- H.L. Yale, K. Losee, J. Martins, M. Holsing, F.M. Pery and J. Bernstein, (1953), "Chemotherapy of experimental tuberculosis. VIII. The synthesis of acid hydrazides, Their derivatives and related compounds", *J. Am. Chem. Soc.*, 75, 1933
- Yong Wood (1955), "The cyclization of 3-acyl dithiocarbazates ester", *J. Am. Chem. Soc.*, 77.
- Amira Jihad Al-Shaheen, Tamem A. Al-Muhger, (2016) "Synthesis, Spectroscopic and X-ray Powder Diffraction (XRD) of Some Oxadiazole Complexes." *International Journal of Enhanced Research in Science, Technology & Engineering*, ISSN :2319-7463, Vol.5 issue 6, June-, p.1339.
- Amira Jihad Al-Shaheen, Mustafa R.A. Al-Bayati and Amal M.A. Abid Allah, (2018) "Synthesis and Characterization of some Metals(II) complexes with 2-(6-methoxy naphthalene-2-yl)Propionic acid(2-hydroxyl benzylidene) hydrazine ligand". *International Journal of Enhanced Research in Science, Technology & Engineering*, ISSN :2319-7463, ISSN: 2319-7463, Vol 7 Issue 4 april-, Impact Factor: 4.059.
- Geary W.J (1971). "The use of conductivity measurement in organic solvent for Characterization of coordination compounds", *Coord. Chem. Rev.*, 7, 8
- Al-Sabaawi S.A. A. J. Al-Shaheen, (2019). "Preparation and Physicochemical Investigation of Manganese (II) complexes with Hydrazone Ligands.", *Raf. J. Sc.*, Vol.28, No.2, Special Issue for third Scientific Conference of Chemistry pp.204-210.
- Mamata Singh R. J. Butcher, N.K. Singh., (2008). "Syntheses and X-Structural Studies of the novel complexes", [Ni(en)2(3-pyt)2] and [Cu(en)2](3-pyt)2 based on 5-(3-pyridyl)-1,3,4-oxadiazole-2-thione, *Polyhedron* 27, 3151–3159.
- Hoggarth, (1949), "Compounds Related to Thiosemicarbazide-3-Phenyl-1,2,4-triazole derivatives", *J. Chem. Soc* 2, 113
- Cotton F.A. and G. Wilkinson, (1980), "Advance Inorganic Chemistry", 4th Ed., John Wiley and Sons, Interscience, New York, P.783
- Bellamy L.J. (1966). "The infrared Spectra of complex molecules 3rd ed. Methuen, London.
- Dogan, Alev Sakyan Iffet KA+A+C, Esma., (2014) "Synthesis and characterization of amino acid Schiff base complexes", *J Solution Chemistry*, 33, 1539-1547,
- Satapathy S. and Sahoo B, (1970). "Salicyl-alazine metal chelates and their IR spectra", *J. Inorg. Nucl. Chem.*, 12, 2223-2227
- William K., (1991) "Organic spectroscopy, 3rd ed., Macmillan Education Ltd, London, 49 54, 60-75

- Gamo (1960)., "Infrared spectra of water of crystallization in some inorganic chlorides and Sulfate",*Bull .Chem.Soc.*, 34,760,1430
- Chira Bhattacharjee, Pankak Gosurimi, Sankar Neogi and Saptarshi Dhibar . (2010)., "Transition metal complexes of furfuraldehyde and hydrazine hydrate", *J.of Sci & Technol.*, 5(2), 81,87.
- Tok T. T., O. Ozasik, D. Sarlgol, and A. U. Baran (2015). , "Synthesis and Molecular Modeling Studies of Naproxen-Based Acyl Hydrazone Derivatives.", *Turk. J.Chem.* 39(1), 54-83
- D. Suttan(1998)., " Electronic Spectra of Transition Metal Complexes", Mc. Grow- Hill Publishing London, pp. 11-21.
- D. Nicholls(1975) , " The Chemistry of iron, cobalt and nickel", Pergamon Press Oxford, pp.1087.
- Spina C., M. Pleniceau and C. Tigae(2008) , "Biologically Active New Fe(II), Co(II), Ni(II)," *Chem. Soc.*,73 (4), 415-421.
- Lever ,A.B.P (1968), "Inorganic Electronic Spectroscopy," Amsterdam- London, New -Y ork Soc.
- Match!(2003-2007)"Crystal impact,phase Identification from Powder Diffraction",version1.6c Licensed to Ankara Uni.Dep.of Geological Engineering site license(c),([http://www. Crystal impact. com](http://www.Crystalimpact.com)).
- Stout, C. H L.H. Jensen (1968), "X-ray Structure Determination", Macmillan, New.York.
- Amira Jihad Al- Shaheen,(2017)., "Physicochemical Studies and X-ray Powder Diffraction of New Homodinuclear Schiff Base Ccomplexes", *International Journal of Enhanced Research in Science ,Technology & Engineering* , ISSN :2319-7463 , ISSN: 2319-7463, Vol. 6 Issue 10, October-2017, Impact Factor: 4.059.
- Aroyo, Mois I. Ulrich Müller and Hans Wondratschek (2007), "Historical Introduction:, *International Tables for Crystallography*", (Springer) A1 (1:1): 2-5. Doi: 1107/97809.

Author Information

Amerah Jihad Ahmed Shaheen

University of Mosul

Mosul/Iraq

Contact E-mail: a.inorganic@yahoo.com

Spectroscopic, Electronic and Non-Linear Properties of 2-[3-Phenyl-4,5-dihydro-1*H*-1,2,4-triazol-5-one-4-yl]-phenoxyacetic Acide

Murat BEYTUR
Kafkas University

Haydar YUKSEK
Kafkas University

Abstract: In this study, 2-[3-phenyl-4,5-dihydro-1*H*-1,2,4-triazol-5-one-4-yl]-phenoxyacetic acide was optimized by using B3LYP/6-311G+(d,p) and HF/6-311G+(d,p) basis sets. Firstly, calculated IR data of compound were calculated in gas phase by using of 6-311G+(d,p) basis sets of B3LYP and HF methods and are multiplied with appropriate adjustment factors. Theoretical infrared spectrums are formed from the data obtained according to B3LYP and HF methods. Experimental IR values and theoretical values were compared. In the identification of calculated IR data was used the veda4f program. Also, ¹H-NMR and ¹³C-NMR spectral data values were calculated according to the method of GIAO using the program package Gaussian G09W Software. Experimental and theoretical values were inserted into the graphic according to equation of $\delta_{exp} = a + b \cdot \delta_{calc}$. The standard error values were found via SigmaPlot program with regression coefficient of a and b constants. Furthermore, molecular structure, HOMO and LUMO energy analysis, total static dipol moment (μ), the mean polarizability ($\langle\alpha\rangle$), the anisotropy of the polarizability ($\Delta\alpha$), the mean first-order hyperpolarizability ($\langle\beta\rangle$), electronegativity (χ), hardness (η), molecular electrostatic potential maps (MEP) and Mulliken charges of 2-[3-phenyl-4,5-dihydro-1*H*-1,2,4-triazol-5-one-4-yl]-phenoxyacetic acide molecule have been investigated by using B3LYP and HF levels with the 6-311G+(d,p) basis set.

Keywords: 1,2,4-Triazol-5-one, GIAO, Non-Linear Properties, Electronegativity HOMO and LUMO

Introduction

Triazole is an unsymmetrical heterocyclic organic compound having three nitrogen atoms in the five-membered ring. 1,2,4-Triazole and 4,5-dihydro-1*H*-1,2,4-triazol-5-one derivatives are reported to possess a broad spectrum of biological activities such as antimicrobial, antifungal, antitumor, anti-HIV, antiviral, anticancer, anti-inflammatory, analgesic and antioxidant properties (Alkan et al., 2007; Hashem et al., 2007; Aytac et al., 2009; Bayrak et al., 2010; Gürsoy Kol and Yüksek, 2010; Güzeldemirci and Kucukbasmaci, 2010; Sancak et al., 2010; Beytur et al., 2019; Turhan Irak and Beytur, 2019). Also, several articles reporting the synthesis of some *N*-arylidenamino-4,5-dihydro-1*H*-1,2,4-triazol-5-one compounds and derivatives have been published (İkizler and Yüksek, 1994; Bahçeci et al., 2002; Yüksek et al., 2004; Yüksek et al., 2005; Yüksek et al., 2006; Turhan Irak and Gümüş, 2017).

In this paper, the optimized molecular structure, vibrational frequencies, spectroscopic parameters, atomic charges and frontier molecule orbitals (HOMO and LUMO) of the 2-[3-phenyl-4,5-dihydro-1*H*-1,2,4-triazol-5-one-4-yl]-phenoxyacetic acide have been calculated by using DFT/B3LYP and HF method with 6-311G+(d,p) basis set. All quantum chemical calculations were carried out by using Gaussian 09W (Frisch et al., 2009; Wolinski, Hilton & Pulay, 1990) program package and the GaussView molecular visualization program (Frisch, Nielson & Holder, 2003). The molecular structure and vibrational calculations of the molecule were computed by using Becke-3-Lee Yang Parr (B3LYP) (Becke, 1993; Lee et al., 1998) density functional method and Hatree-Fock with 6-311G+(d,p) basis set in ground state. IR absorption frequencies of analyzed molecule were calculated by two methods. Then, they were compared with experimental data (Çiftçi et al., 2018), which are shown to be accurate. The assignments of fundamental vibrational modes of the title molecule were performed

- This is an Open Access article distributed under the terms of the Creative Commons Attribution-NonCommercial 4.0 Unported License, permitting all non-commercial use, distribution, and reproduction in any medium, provided the original work is properly cited.

- Selection and peer-review under responsibility of the Organizing Committee of the Conference

on the basis of total energy distribution (TED) analysis by using VEDA 4f program (Jamroz, 2004). Furthermore, molecular structure, HOMO and LUMO energy analysis, total static dipole moment (μ), the mean polarizability ($\langle\alpha\rangle$), the anisotropy of the polarizability ($\Delta\alpha$), the mean first-order hyperpolarizability ($\langle\beta\rangle$), electronegativity (χ), hardness (η), molecular electrostatic potential maps (MEP) and Mulliken charges of titled compound have been investigated by using B3LYP and HF levels with the 6-311G+(d,p) basis set.

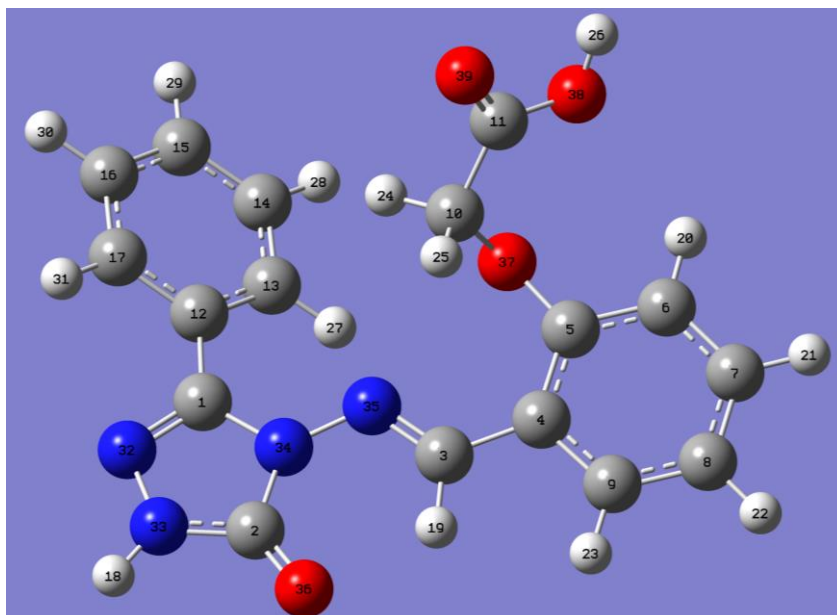


Figure 1. The optimized molecular structure (Gaussview Appearance) of 2-[3-phenyl-4,5-dihydro-1H-1,2,4-triazol-5-one-4-yl]-phenoxyacetic acid with DFT/B3LYP 6-311G+(d,p) level.

Method

The molecular structure of the title compound in the ground state is computed by performing both the density functional theory (DFT) and Hartree-Fock (HF) (Becke, 1993; Lee, 1998) at 6-311G+(d,p) level. Density functionals for all studies reported in this paper have been in the following form

$$E_{XC} = (1 - a_0)E_X^{LSDA} + a_0E_X^{HF} + a_X\Delta E_X^{B88} + a_C E_C^{LYP} + (1 - a_C)E_C^{VWN}$$

where the energy terms are the Slater exchange, the Hartree-Fock exchange, Becke's exchange functional correction, the gradient corrected correlation functional of Lee, Yang and Parr, and the local correlation functional of Vosko, Wilk and Nusair (Vosko et al., 1980). The theoretical geometric structure of the title compound is given in Figure 1. Molecular geometry is restricted and the optimized geometrical parameters of the title compound in this study are carried out by using Gaussian 09W program package (Frisch et al., 2009) and the visualization parts were done with GaussView program (Dennington et al., 2009) on personal computer employing 6-311G+(d,p) basis set. Additionally, harmonic vibrational frequencies for the title compound are calculated with these selected methods and then scaled by 0.9516 and 0.9905, respectively (Avcı and Atalay, 2008) and these results were compared with the experimental data (Çiftçi et al., 2018).

Results and Discussion

Analysis of vibrational modes

In spectroscopic field, the vibrational spectra of substituted benzene derivatives have been greatly investigated by various spectroscopic, since the single substitution can have a tendency to put greater changes in vibrational wavenumbers of benzene (Tereci et al., 2012; Pir et al., 2013). In other words, molecular system of benzene is greatly affected by the nature of substituents. The number of potentially active fundamentals of non-linear molecule which have N atoms is equal to (3N-6) apart from three translational and three rotational degrees of freedom. The title molecule contains 39 atoms and 111 normal vibration modes have C1 symmetry (Table 1).

Experimentally (Çiftçi et al., 2018), the investigated titled compound, as expected the IR spectra data, the N-H stretching vibration at 3179 cm^{-1} and two C=O peak at 1708 cm^{-1} range was observed. In addition, C=N stretching vibration at 1597 cm^{-1} and COO stretching vibrations at 1229 cm^{-1} are occurred. Theoretically and experimentally (Çiftçi et al., 2018), the calculated vibrational frequencies for the 2-[3-phenyl-4,5-dihydro-1H-1,2,4-triazol-5-one-4-yl]-phenoxyacetic acid are summarized in Table 1. Furthermore the experimental IR (Çiftçi et al., 2018) and simulated spectra by using B3LYP/6-311G+(d,p) and HF/6-311G+(d,p) levels of the titled compound under investigation are given in Figure 2.

Table 1. The calculated frequencies values of the titled compound

| Selected Vibrational Types | Experim. | Scaled DFT | Scaled HF |
|---|----------|------------|-----------|
| δ O ₃₇ C ₅ C ₆ (23) | 423 | 439 | 447 |
| τ C ₁ C ₁₃ C ₁₇ C ₁₂ (21) | 484 | 502 | 507 |
| δ C ₁₂ O ₃₇ C ₅ (12), τ C ₅ C ₆ C ₇ C ₈ (32), τ O ₃₇ C ₄ C ₆ C ₅ (10), τ H ₂₀ C ₆ C ₇ C ₈ (12) | 544 | 572 | 582 |
| δ O ₃₉ C ₁₁ O ₃₈ (34), δ O ₃₇ C ₅ C ₆ (10), δ C ₁₁ C ₁₀ O ₃₇ (20) | 576 | 587 | 602 |
| δ C ₁₅ C ₁₄ C ₁₃ (30), δ O ₃₆ C ₂ N ₃₃ (18) | 596 | 614 | 623 |
| τ O ₃₆ N ₃₃ N ₃₄ C ₂ (73) | 678 | 714 | 734 |
| τ H ₂₇ C ₁₃ C ₁₄ C ₁₅ (39), τ N ₃₂ N ₃₄ C ₁₂ C ₁ (10), τ C ₁ C ₁₃ C ₁₇ C ₁₂ (19) | 758 | 760 | 787 |
| τ H ₂₀ C ₆ C ₇ C ₈ (36) | 802 | 831 | 859 |
| δ C ₅ C ₆ C ₇ (38), δ C ₄ C ₃ N ₃₅ (11) | 839 | 877 | 899 |
| δ H ₂₇ C ₁₃ C ₁₄ (23), τ H ₂₇ C ₁₃ C ₁₄ C ₁₅ (35), τ H ₃₁ C ₁₇ C ₁₆ C ₁₅ (28) | 880 | 913 | 948 |
| τ H ₁₉ C ₃ N ₃₅ N ₃₄ (79) | 943 | 980 | 1013 |
| ν O ₃₇ C ₁₀ (40) | 1028 | 1039 | 1061 |
| ν C ₁₄ C ₁₃ (24), δ H ₂₄ C ₁₃ C ₁₄ (22), ν N ₃₃ N ₃₂ (14) | 1066 | 1079 | 1082 |
| O ₃₇ C ₅ (25), C ₁₀ C ₁₁ (10), δ H ₂₆ O ₃₈ C ₁₁ (41) | 1111 | 1141 | 1106 |
| δ H ₂₄ C ₁₀ O ₃₇ (12), ν O ₃₇ C ₅ (19) | 1168 | 1199 | 1201 |
| δ H ₂₄ C ₁₀ O ₃₇ (51) | 1229 | 1267 | 1265 |
| δ H ₁₉ C ₃ N ₃₅ (18), δ H ₁₈ N ₃₃ N ₃₂ (40) | 1354 | 1367 | 1405 |
| δ H ₂₀ C ₆ C ₇ (11), δ H ₂₇ C ₁₃ C ₁₄ (11) | 1423 | 1434 | 1457 |
| ν N ₃₂ C ₁ (29), ν C ₁₄ C ₁₃ (12) | 1488 | 1542 | 1588 |
| ν N ₃₂ C ₁ (40), ν C ₅ C ₆ (12) | 1597 | 1602 | 1704 |
| ν O ₃₉ C ₁₁ (86), ν O ₃₆ C ₂ (74), ν N ₃₃ C ₂ (11) | 1708 | 1753 | 1805 |
| ν C ₁₀ H ₂₄ (99) | 2791 | 2973 | 2935 |
| ν C ₁₀ H ₂₄ (99) | 2916 | 3016 | 2982 |
| ν C ₃ H ₂₇ (77) | 2936 | 3068 | 3013 |
| ν C ₁₃ H ₂₇ (53) | 3011 | 3089 | 3036 |
| ν C ₁₇ H ₃₁ (83) | 3076 | 3102 | 3048 |
| ν N ₃₃ H ₁₈ (100) | 3179 | 3558 | 3556 |
| ν O ₃₈ H ₂₆ (100) | 3208 | 3632 | 3722 |

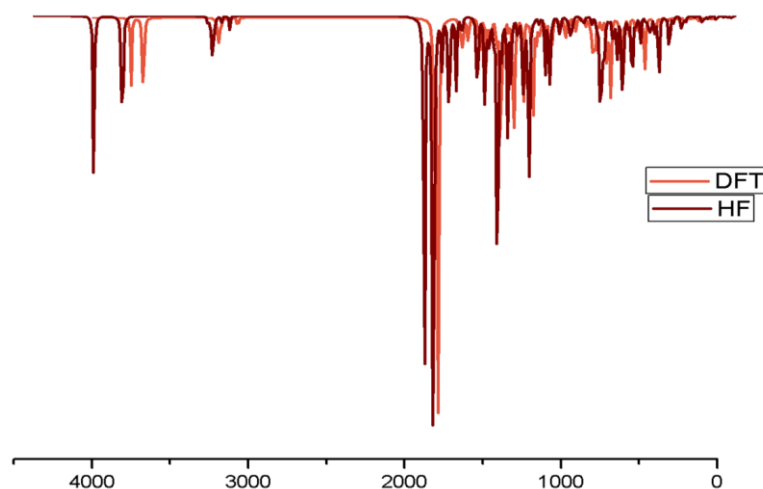


Figure 2. IR spectra simulated with DFT/B3LYP/6-311G+(d,p) and HF/6-311G+(d,p) levels of the titled compound

NMR spectral analysis

the isotropic chemical shift analysis allows us to identify relative ionic species and to calculate reliable magnetic properties in nuclear magnetic resonance (NMR) spectroscopy which provide the accurate predictions of molecular geometries, (Wade, 2006; Rani, et al., 2010; Subramanian et al., 2010). For this purpose, the optimized molecular geometry of the 2-[3-phenyl-4,5-dihydro-1*H*-1,2,4-triazol-5-one-4-yl]-phenoxyacetic acid was obtained by using B3LYP and HF methods with 6-311G+(d,p) basis level in DMSO solvent. By considering the optimized molecular geometry of the titled compound. The ^1H and ^{13}C NMR chemical shift values were calculated at the same level by using Gauge-Independent Atomic Orbital method (Table 2). Theoretically and experimentally values (Çiftçi et al., 2018) were plotted according to $\delta_{\text{exp}} = a \cdot \delta_{\text{calc}} + b$, Eq. a and b constants regression coefficients with a standard error values were found using the SigmaPlot program. The correlation graphics are given Figure 3 and the linear correlation data of the titled compound by considering the results are given in Table 2. Therefore the (R^2) values (DFT/HF) for ^1H NMR (DMSO) and ^{13}C NMR (DMSO) chemical shifts in different solvents has been found as 0.2228 and 0.98849 for the 2-[3-phenyl-4,5-dihydro-1*H*-1,2,4-triazol-5-one-4-yl]-phenoxyacetic acid (Figure 3). In our study, the ^1H -NMR spectrum of the titled compound was observed belong to H181 proton peak at 12.38 ppm because acidic show feature (Yüksek, 1992; Yüksek et al., 2005; Yüksek et al., 2006, Çiftçi et al., 2018). H19 protons were observed at 10.01 ppm. Therotically, DMSO solvent these values for the mentioned proton atoms were found as 8.05/7.15 and 10.54/9.53 ppm, respectively. In Table 2, the biggest ^{13}C chemical shift value of the molecule are observed at 170.38 ppm for the C11 carbon atom double bounded to the oxygen in carbonyl group (Anderson et al., 2004). DMSO solvent the calculated ppm values (DFT/HF) for C11 carbon atom were theoretically found as 179.70/163.08 ppm. Additionaly, due to the electronegative property of nitrogen atoms in molecule, the experimental NMR chemical shift values for C1 and C2 carbon atom the bounded to nitrogen atoms in 1,2,4-triazol ring and C3 carbon atom with sp^2 hybride are observed at 145.16, 151.83 and 152.17 ppm, respectively.

Table 2. The calculated and experimental ^1H and ^{13}C NMR isotropic chemical shifts of the titled compound

| | Experiment. | DFT/631d/DMSO | Diff./DMSO | HF/631d/DMSO | Diff./DMSO |
|-----|-------------|---------------|------------|--------------|------------|
| C1 | 145,16 | 153,48 | -8,32 | 143,66 | 1,50 |
| C2 | 151,83 | 155,64 | -3,81 | 144,63 | 7,20 |
| C3 | 152,17 | 158,19 | -6,02 | 149,49 | 2,68 |
| C4 | 122,19 | 132,27 | -10,08 | 116,63 | 5,56 |
| C5 | 157,78 | 165,80 | -8,02 | 150,23 | 7,55 |
| C6 | 121,89 | 130,72 | -8,83 | 116,79 | 5,10 |
| C7 | 130,53 | 137,77 | -7,24 | 128,76 | 1,77 |
| C8 | 113,43 | 130,09 | -16,66 | 116,97 | -3,54 |
| C9 | 133,55 | 141,78 | -8,23 | 131,50 | 2,05 |
| C10 | 65,36 | 73,69 | -8,33 | 52,62 | 12,74 |
| C11 | 170,38 | 179,70 | -9,32 | 163,08 | 7,30 |
| C12 | 126,30 | 132,98 | -6,68 | 119,42 | 6,88 |
| C13 | 127,19 | 133,01 | -5,82 | 123,99 | 3,20 |
| C14 | 128,48 | 133,44 | -4,96 | 121,29 | 7,19 |
| C15 | 128,97 | 135,74 | -6,77 | 126,46 | 2,51 |
| C16 | 126,30 | 132,83 | -6,53 | 120,21 | 6,09 |
| C17 | 128,48 | 134,80 | -6,32 | 126,34 | 2,14 |
| H18 | 12,38 | 8,05 | 4,33 | 7,15 | 5,23 |
| H19 | 10,01 | 10,54 | -0,53 | 9,53 | 0,48 |
| H20 | 7,56 | 7,88 | -0,32 | 7,45 | 0,11 |
| H21 | 7,49 | 7,68 | -0,19 | 7,48 | 0,01 |
| H22 | 7,53 | 7,57 | -0,04 | 7,18 | 0,35 |
| H23 | 7,06 | 7,85 | -0,79 | 7,61 | -0,55 |
| H24 | 4,88 | 3,95 | 0,93 | 2,92 | 1,96 |
| H25 | 4,88 | 4,19 | 0,69 | 3,01 | 1,87 |
| H26 | 13,15 | 6,60 | 6,55 | 5,68 | 7,47 |
| H27 | 7,85 | 8,26 | -0,41 | 7,91 | -0,06 |
| H28 | 7,55 | 7,85 | -0,30 | 7,45 | 0,10 |
| H29 | 7,54 | 7,72 | -0,18 | 7,61 | -0,07 |
| H30 | 7,07 | 7,68 | -0,61 | 7,48 | -0,41 |
| H31 | 7,91 | 8,56 | -0,65 | 8,00 | -0,09 |

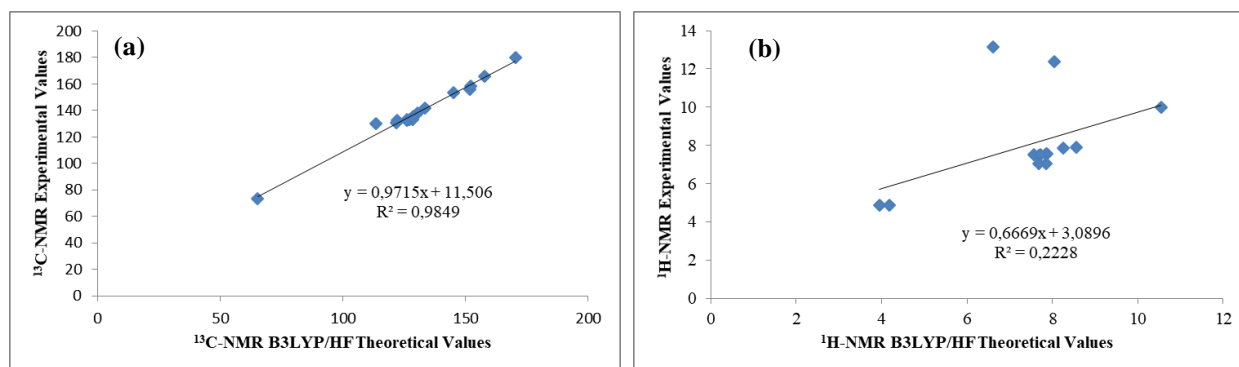


Figure 3. The correlation graphics for ^{13}C -NMR (a), ^1H -NMR (b), ^{13}C -NMR (DMSO) (c) and ^1H -NMR (DMSO) (d), chemical shifts of the titled compound

Frontier molecular orbital analysis

The energies of two important molecular orbitals of the title molecule; the second highest and highest occupied MO's (HOMO), the lowest and the second lowest unoccupied MO's (LUMO) were calculated by using DFT/B3LYP and HF methods with 6-311G+(d,p) level and are presented in Table 3. The energy gap of the title molecule was calculated at DFT/B3LYP and HF level, which reveals the chemical reactivity and proves the occurrence of eventual charge transfer. The HOMO is located almost over the carbon atoms, oxygen atoms and also slightly delocalized in hydrogen atom and the LUMO is mainly delocalized in carbon atoms of benzene ring. The energy gap (energy difference between HOMO and LUMO orbital) is a critical parameter in determining molecular electrical transport properties (Fukui, 1982). The HOMO-LUMO energy gap of the title molecule is found to 4.272/2.752 eV. obtained at DFT/HF method with 6-311G+(d,p) basis set.

Table 3. The calculated HOMO-LUMO energies of the titled compound (3) according to DFT/B3LYP/6-31G(d) and HF/B3LYP/6-31G(d) levels

| Electronic properties | B3LYP | HF |
|---------------------------------|-------|-------|
| I; Ionization Potential (eV) | 6.145 | 8.430 |
| A; Electron Affinity (eV) | 1.873 | 5.679 |
| η ; Chemical Hardness (eV) | 2.136 | 1.376 |
| S; Molecular Softness (eV) | 1.068 | 0.689 |
| χ ; Electronegativity (eV) | 4.009 | 7.05 |
| Total Energy (a.u.) | -1497 | -1492 |
| ΔE ; Energy Gap (eV) | 4.272 | 2.752 |

Mulliken's atomic charges

The Mulliken atomic charges at the HF/6-311G+(d,p) and B3LYP/6-311G+(d,p) level of 2-[3-phenyl-4,5-dihydro-1H-1,2,4-triazol-5-one-4-yl]-phenoxyacetic acid in gas phase are given in Table 4 (Mulliken, 1955). The electronegative N32, N33, N34, N35, O36, O37, O38 and O39 atoms of the titled compound have negative atomic charge values. The Mulliken atomic charges (B3LYP/HF) of the mentioned atoms were calculated as -0,18358/-0,06376, -0,18470/-0,38072, -0,18497/-0,19111, 0,04705/-0,03712, -0,36908/-0,49686, 0,07053/0,05755, -0,18642/-0,30668 and -0,26420/-0,36914a.u., respectively. The C2, C3, C4, C6, C13 and C16 carbon atoms bounded to the mentioned electronegative atoms in the molecule under study have positive atomic charge values. The values of the positive charges of the mentioned carbon atoms were found as 0,54508/0,77855, 0,13796/0,47904, 0,88901/1,20224, 0,03142/0,20002, 0,58601/0,74340 and 0,02243/0,47360 a.u., respectively. Therefore the C1 atom surrounded with two electronegative N32 and N34 atoms. In the titled compound the atomic charges of all hydrogen atoms have positive values.

Table 4. Mulliken atomic charges of the titled compound

| | B3LYP | HF | | B3LYP | HF | | B3LYP | HF |
|------------|--------------|-----------|------------|--------------|-----------|------------|--------------|-----------|
| 1C | -0,08604 | -0,04616 | 14C | -0,02262 | - | 27H | 0,31520 | 0,17005 |
| 2C | 0,54508 | 0,77855 | 15C | -0,21346 | - | 28H | 0,13673 | 0,14209 |
| 3C | 0,13796 | 0,47904 | 16C | -0,52235 | - | 29H | 0,12864 | 0,14123 |
| 4C | 0,88901 | 1,20224 | 17C | -0,45032 | - | 30H | 0,13096 | 0,14147 |
| 5C | -0,47927 | -1,03838 | 18H | 0,33533 | 0,37704 | 31H | 0,14235 | 0,15549 |
| 6C | -0,20818 | -0,30140 | 19H | 0,17444 | 0,20726 | 32N | - | - |
| 7C | -0,23333 | -0,32372 | 20H | 0,14732 | 0,16557 | 33N | 0,18358 | 0,06376 |
| 8C | -0,20602 | -0,38056 | 21H | 0,13554 | 0,14630 | 34N | - | - |
| 9C | -0,60935 | -0,47661 | 22H | 0,13182 | 0,14150 | 35N | 0,18470 | 0,38072 |
| 10C | -0,54042 | -0,41960 | 23H | 0,13945 | 0,14896 | 36O | - | - |
| 11C | 0,03142 | 0,20002 | 24H | 0,22609 | 0,24619 | 37O | 0,36908 | 0,49686 |
| 12C | 0,58601 | 0,74340 | 25H | 0,19323 | 0,19155 | 38O | 0,07053 | 0,05755 |
| 13C | 0,02243 | -0,47360 | 26H | 0,27772 | 0,30292 | 39O | - | - |
| | | | | | | | 0,18642 | 0,30668 |
| | | | | | | | - | - |
| | | | | | | | 0,26420 | 0,36914 |

Nonlinear Optic Properties

The materials having nonlinear activity possess a nonlinear response to the electric fields associated with the light of a laser beam. It is well known that the higher values of dipole moment, polarizability, and hyperpolarizability are important for more active NLO properties. In this study dipole moment, polarizability and first hyperpolarizability of the titled molecule were investigated by using B3LYP method at 6-311G+(d,p) basis set. The following formulas are used for calculating the magnitude of total static dipole moment (μ), polarizability (α) and first hyperpolarizability (β):

$$\mu = \left(\mu_x^2 + \mu_y^2 + \mu_z^2 \right)^{\frac{1}{2}}$$

$$\alpha = \frac{1}{3} (\alpha_{xx} + \alpha_{yy} + \alpha_{zz})$$

$$\beta = \sqrt{(\beta_{xxx} + \beta_{yyy} + \beta_{zzz})^2 + (\beta_{yyy} + \beta_{xxy} + \beta_{yyz})^2 + (\beta_{zzz} + \beta_{xxz} + \beta_{yyz})^2}$$

Where, the total static dipole moment (μ), linear polarizability (α) and the first hyperpolarizability (β) using the x , y , z components are defined as (Abraham et al., 2008; Karamanis et al., 2008). The energy gap ΔE_g , dipole moment (μ), linear polarizability (α) and the first hyperpolarizability (β) values of conformer ct of the titled molecule are investigated as a function of the two torsional angle using B3LYP/6-311G+(d,p) level of theory (Govindarajan et al., 2012) (Table 5).

Table 5. Calculated polarization and hyperpolarizability values of the molecule (B3LYP/6-311G+(d,p) and HF/6-311G+(d,p))

| | B3LYP | HF | | B3LYP | HF |
|-----------------------|------------------------------|------------------------------|---------------|--------------------------|-----------------------------|
| μ_x | -2.2250 debye | -3.8219 debye | β_{xxx} | 7774.61 a.u. | 3821.35 a.u. |
| μ_y | 6.7852 debye | -0.8012 debye | β_{xyy} | 1053.82 a.u. | 538.44 a.u. |
| μ_z | 2.3422 debye | 2.0819 debye | β_{yyy} | 823.08 a.u. | 495.47 a.u. |
| μ_{Toplam} | 7.2818 debye | 4.4253 debye | β_{yyy} | -340.62 a.u. | 161.42 a.u. |
| α_{xx} | 74.364 a.u. | 60.185 a.u. | β_{xxz} | -1001.26 a.u. | -903.63 a.u. |
| α_{yy} | 41.696 a.u. | 37.522 a.u. | B_{xyz} | -154.56 a.u. | -181.90 a.u. |
| α_{zz} | 33.325 a.u. | 30.965 a.u. | B_{yyz} | -309.57 a.u. | -202.32 a.u. |
| α | 49.795x10 ⁻²⁴ esu | 42.891x10 ⁻²⁴ esu | β_{zzz} | -295.06 a.u. | 87.33 a.u. |
| $\Delta\alpha$ | 37.560x10 ⁻²⁴ esu | 26.556x10 ⁻²⁴ esu | β_{yzz} | 669.31 a.u. | 523.13 a.u. |
| β_x | -9651.51 a.u. | 4855.26 a.u. | B_{zzz} | 1193.83 a.u. | 866.30 a.u. |
| β_y | -1496.43 a.u. | -944.53 a.u. | B | 8.567 ⁻³⁰ esu | 5.006x10 ⁻³⁰ esu |
| β_z | 1568.10 a.u. | 1476.75 a.u. | | | |

Conclusion

In this paper, the structure of the titled compound is characterized by using ¹H, ¹³C NMR and FT-IR spectroscopic methods. The molecular structures, vibrational frequencies, ¹H and ¹³C NMR chemicals shifts, UV-vis spectroscopies, HOMO and LUMO analyses and atomic charges of 2-[3-phenyl-4,5-dihydro-1H-1,2,4-triazol-5-one-4-yl]-phenoxyacetic acid obtained have been calculated by using DFT/B3LYP and HF methods. By considering the results of experimental works it can be easily stated that the ¹H and ¹³C NMR chemical shifts, and vibrational frequencies spectroscopic parameters obtained theoretically are in a very good agreement with the experimental data. Also, the electronic structure of titled compound are determined electronic structure identifiers such as the Energy of the Highest Occupied Molecular Orbital, Energy of the Lowest Unoccupied Molecular Orbital, molecular hardness, chemical softness, electronegativity, chemical potential, electrophilicity index, nucleophilicity index and dipole moment. Finally, in this study, The nonlinear optical properties of the compound were calculated theoretically. It was found that the molecule concerned had a higher hyperpolarizability value than urine (0.77x10⁻³⁰esu).

References

- Abraham, J. P., Sajan, D., Hubert, Joe I. H., & Jayakumar, V. S. (2008). Molecular structure, spectroscopic studies and first-order molecular hyperpolarizabilities of p-amino acetanilide, *Spectrochimica Acta Part A: Molecular and Biomolecular Spectroscopy*, 71 (2), 355-367.
- Alkan, M., Yuksek, H., Islamoglu, F., Bahceci, S., Calapoglu, M., Elmastas, M., Aksit, H., & Ozdemir, M. (2007). A study on 4-acylamino-4,5-dihydro-1H-1,2,4-triazol-5-ones, *Molecules*, 12 (8), 1805-1816.
- Anderson, R. J., Bendell, D. J., & Groundwater, P. W. (2004). Organic Spectroscopic Analysis, *The Royal Society of Chemistry: Sanderland, UK*.
- Aytac, S. P., Tozkoparan, B., Kaynak, F. B., Aktay, G., Goktas, O., & Unuvar, S. (2009). Synthesis of 3,6-disubstituted 7H-1,2,4-triazolo[3,4-b]-1,3,4-thiadiazines as novel analgesic/anti-inflammatory compounds, *European Journal of Medicinal Chemistry*, 44 (11), 4528-4538.
- Avci, D., & Atalay, Y. (2008). Theoretical analysis of vibrational spectra and scaling-factor of 2-aryl-1,3,4-oxadiazole derivatives, *International Journal of Quantum Chemistry*, 109, 328-341.
- Bahçeci, Ş., Yüksek, H., Ocak, Z., Köksal, C., & Ozdemir, M. (2002). Synthesis and non-aqueous medium titrations of some new 4,5-dihydro-1H-1,2,4-triazol-5-one derivatives. *Acta Chimica Slovenica*, 49, 783-794.
- Bayrak, H., Demirbas, A., Demirbas, N., & Karaoglu, S. A. (2010). Cyclization of some carbothioamide derivatives containing antipyrine and triazole moieties and investigation of their antimicrobial activities, *European Journal of Medicinal Chemistry*, 45 (11), 4726-4732.
- Becke A. D. (1993). Density functional thermochemistry. III. The role of exact Exchange, *The Journal of Chemical Physics*, 98, 5648-5652.

- Beytur, M., Turhan Irak, Z., Manap, S., and Yüksek, H. (2019). Synthesis, Characterization and Theoretical Determination of Corrosion Inhibitor Activities of Some New 4,5-Dihydro-1H-1,2,4-Triazol-5-one Derivatives, *Heliyon*, 5 (6), e01809, 1-8.
- Çiftçi, E., Beytur, M., Calapoğlu, M., Gürsoy Kol, Ö., Alkan, M., Toğay, V. A., Manap, S., & Yüksek, H. (2018). Synthesis, Characterization, Antioxidant and Antimicrobial Activities and DNA Damage of Some Novel 2-[3-alkyl (aryl)-4,5-dihydro-1H-1,2,4-triazol-5-one-4-yl]-phenoxyacetic acids in Human Lymphocytes, *Research Journal of Pharmaceutical, Biological and Chemical Sciences*, 9 (5), 1760-1771.
- Dennington, R., Keith, T., & Millam, J. (2009). GaussView, Version 5, SemicheM Inc., Shawnee Mission KS.
- Frisch, A., Nielson, A.B., & Holder, A.J. (2003). Gaussview User Manual, Gaussian, Inc., Wallingford, CT.
- Frisch, M. J., Trucks, G., Schlegel, H. B., Scuseria, G. E., Robb, M. A., Cheeseman, J. R., Scalmani, G., Barone, V., Mennucci, B., Petersson, G. A., Nakatsuji, H., Caricato, M., Li, X., Hratchian, H. P., Izmaylov, A. F., Bloino, J., Zheng, G., Sonnenberg, J. L., Hada, M., Ehara, M., Toyota, K., Fukuda, R., Hasegawa, J., Ishida, M., Nakajima, T., Honda, Y., Kitao, O., Nakai, H., Vreven, T., Montgomery, J. A., Jr. Vreven, T., Peralta, J. E., Ogliaro, F., Bearpark, M., Heyd, J. J., Brothers, E., Kudin, N., Staroverov, V. N., Kobayashi, R., Normand, J., Raghavachari, K., Rendell, A., Burant, J. C., Iyengar, S. S., Tomasi, J., Cossi, M., Rega, N., Millam, J. M., Klene, M., Knox, J. E., Cross, J. B., Bakken, V., Adamo, C., Jaramillo, J., Gomperts, R., Stratmann, R. E., Yazyev, O., Austin, A. J., Cammi, R., Pomelli, C., Ochterski, J. W., Martin, L. R., Morokuma, K., Zakrzewski, V. G., Voth, G. A., Salvador, P., Dannenberg, J. J., Dapprich, S., Daniels, A. D., Farkas, O., Foresman, J. B., Ortiz, J. V., Cioslowski, J. & Fox, D. J. (2009). Gaussian Inc., Wallingford, CT.
- Govindarajan, M., Periandy, S., & Carthigayen, K. (2012). FT-IR and FT-Raman spectra, thermo dynamical behavior, HOMO and LUMO, UV, NLO properties, computed frequency estimation analysis and electronic structure calculations on α -bromotoluene. *Spectrochimica Acta Part A: Molecular and Biomolecular Spectroscopy*, 97, 411-422.
- Gürsoy Kol, Ö., and Yüksek, H. (2010). Synthesis and invitro antioxidant evaluation of some novel 4,5-dihydro-1H-1,2,4-triazol-5-one derivatives, *E-Journal of Chemistry*, 7 (1), 123-136.
- Guzeldemirci, N. U., & Kucukbasmaci, O. (2010). Synthesis and antimicrobial activity evaluation of new 1,2,4-triazoles and 1,3,4-thiadiazoles bearing imidazo[2,1-b]thiazole moiety, *European Journal of Medicinal Chemistry*, 45 (1), 63-68.
- İkizler, A. A., & Yüksek, H. (1994). Reaction of 4-amino-4,5-dihydro-1H-1,2,4-triazol-5-ones with 2,5-dimetoxytetrahydrofuran, *Collection of Czechoslovak Chemical Communications*, 59 (3), 731-735.
- Jamróz, M. H. (2004). Vibrational Energy Distribution Analysis: VEDA 4 program, Warsaw.
- Karamanis, P, Pouchan, C., & Maroulis, G., (2008). Structure, stability, dipole polarizability and differential polarizability in small gallium arsenide clusters from all-electron ab initio and density-functional-theory calculations, *Physical Review A*, 77, 013201-013208.
- Lee, S. Y. (1998). Molecular Structure and Vibrational Spectra of Biphenyl in the Ground and the lowest Triplet States. Density Functional Theory Study, *Bulletin of the Korean Chemical Society*, 19 (1), 93-98.
- Mulliken, R. S., (1955). Electronic population analysis on LCAO-MO molecular wave functions. *Journal of Chemical Physics*, 23, 1833-1840.
- Pir, H., Günay, N., Tamer, Ö., Avcı, D., & Atalay, Y. (2013). Theoretical investigation of 5-(2-Acetoxyethyl)-6-methylpyrimidin-2, 4-dione: Conformational study, NBO and NLO analysis, molecular structure and NMR spectra, *Spectrochimica Acta Part A: Molecular and Biomolecular Spectroscopy*, 112, 331-342.
- Rani, A. U., Sundaraganesan, N., Kurt, M., Çınar, M., & Karabacak, M. (2010). FT-IR, FT-Raman, NMR spectra and DFT calculations on 4-chloro-N-methylaniline, *Spectrochimica Acta Part A: Molecular and Biomolecular Spectroscopy*, 75, 1523-1529.
- Sancak, K., Unver, Y., Kazak, C., Dugdu, E., and Arslan, B. (2010). Synthesis and characterizations of some new 2,4-dihydro-[1,2,4]-triazol-3-one derivatives and X-ray crystal structures of 4-(3-phenylallylideneamino)-5-thiophen-2-yl-methyl-2,4-dihydro-[1,2,4]triazol-3-one, *Turkish Journal of Chemistry*, 34 (5), 771-780.
- Subramanian, N., Sundaraganesan, N., & Jayabharathi, J. (2010). Molecular structure, spectroscopic (FT-IR, FT-Raman, NMR, UV) studies and first-order molecular hyperpolarizabilities of 1,2-bis(3-methoxy-4-hydroxybenzylidene)hydrazine by density functional method, *Spectrochimica Acta Part A: Molecular and Biomolecular Spectroscopy*, 76, 259-269.
- Turhan Irak, Z., & Beytur, M. (2019). 4-Benzilidenamino-4,5-dihidro-1H-1,2,4-triazol-5-on Türevlerinin Antioksidan Aktivitelerinin Teorik Olarak İncelenmesi, *Iğdır University Journal of the Institute of Science and Technology*, 9 (1), 512-521.
- Yüksek, H. (1992). 3-Alkil(aril)-4-amino-4,5-dihidro-1,2,4-triazol-5-on'ların bazı reaksiyonlarının incelenmesi. Doktora Tezi, KTÜ Fen Bilimleri Enstitüsü, Trabzon.

- Yüksek, H., Bahçeci, S., Ocak, Z., Alkan, M., Ermis, B., Mutlu, T., Ocak, M., & Ozdemir, M. (2004). Synthesis of some 4,5-dihydro-1H-1,2,4-triazol-5-ones, *Indian journal of heterocyclic chemistry*, 13 (4), 369-372.
- Yüksek, H., Üçüncü, O., Alkan, M., Ocak, Z., Bahçeci, Ş., & Özdemir, M. (2005). Synthesis and Determination of pKa Values of Some New 3,4-Disubstituted-4,5-Dihydro-1H-1,2,4-triazol-5-one Derivatives in Non-aqueous Solvents, *Molecules* 10, 961-970.
- Yüksek, H., Küçük, M., Alkan, M., Bahçeci, S., Kolaylı, S., Ocak, Z., Ocak, U., Şahinbas, E., & Ocak, M. (2006). Synthesis and antioxidant activities of some new 4-(4-hydroxybenzylidenamino)-4,5-dihydro-1H-1,2,4-triazol-5-one derivatives with their acidic properties, *Asian Journal of Chemistry*, 18 (1), 539-550.
- Tereci, H., Askeroğlu, İ., Akdemir, N., Uçar, İ., & Büyükgüngör, O. (2012). Combined experimental and theoretical approaches to the molecular structure of 4-(1-formylnaphthalen-2-yloxy)phthalonitrile, *Spectrochimica Acta Part A: Molecular and Biomolecular Spectroscopy*, 96, 569-577.
- Turhan Irak, Z., & Gümüş, S. (2017). Heterotricyclic compounds via click reaction: A computational study. *Noble International Journal of Scientific Research*, 1(7), 80-89.
- Vosko, S. H., Wilk, L. :& Nusair, M. (1980). Accurate spin-dependent electron liquid correlation energies for local spin density calculations: a critical analysis, *Canadian Journal of Physics*. 58, 1200.
- Wade, Jr. L.G. (2006). *Organic Chemistry*, 6nd ed.; Pearson Prentice Hall: New Jersey.
- Wolinski, K., Hinton, J. F. & Pulay, P. (1990). Efficient implementation of the gauge-independent atomic orbital method for NMR chemical shift calculations. *Journal of the American Chemical Society*, 112, 8251-8260.

Author Information

Murat Beytur

Kafkas University
Faculty of Science and Letters, Department of Chemistry,
Kars, Turkey
Contact E-mail: muratbeytur83@gmail.com

Haydar Yuksek

Kafkas University
Faculty of Science and Letters, Department of Chemistry,
Kars, Turkey

Comparison of Bridge Piers Shapes According to Local Scour Countermeasures

Abdulnaser KASHMOOLA
Northern Technical University

Adnan ISMAEL
Northern Technical University

Saleh SULEIMAN
Northern Technical University

Abstract: Comparison of experimental study was carried out between bridge piers to find out the efficient bridge pier to countermeasures the local scour. In addition the present study is to provide a new method to reduce scour depth in front of bridge pier. The idea of this method is dependent on change the position of two piers (normal pier (10-4) cm and straight aero foil shaped pier) with respect to flow direction (named after here as opposite bridge pier and opposite aero foil pier). The down flow deflected away from the front the opposite piers and the horseshoe vortex becomes small and does not affect the piers. In the present study five piers (normal pier (10-4), opposite pier (4-10), straight aero foil, opposite aero foil and circular) were tested under live-bed condition with flow intensity 58 l/sec. for duration 3 hrs. The velocity field measurements were obtained using an Acoustic Doppler Velocimeter. The results showed that the opposite piers reduce the local scour around the piers. For opposite pier the reduction of scour depth was about 40% compared with normal pier and 54% compared with circular pier. The reduction of the scour hole volume was about 83% compared with circular pier and 23.6% when normal pier compared with circular. For opposite aero foil the maximum depth of scour reduced 58% compared with straight aero foil and 69% compared with circular pier. The reduction of the scour hole volume was about 89% compared with circular pier and straight aero foil reduced scour hole volume about 27% when compared with circular pier. It is clearly from the comparison that the opposite piers are effective countermeasures for reducing local scour depth and scour hole volume, especially opposite aero foil pier. We hope that the results of the present study will be benefitted by the designers and engineers.

Keywords: Bridge pier position, Scour reduction, Local scour, Aero foil pier

Introduction

A common reason of bridge failures is local scour around bridge foundations such as piers and abutments. Local scour erodes the soil around the piers and reduces the lateral capacity of the foundations (Rambabu et al 2003). Local scour is the engineering term for erosion of the soil surrounding an obstruction caused by flowing water. The key element in the scour process is the formation of vortices due to pressure differences that occur when the water velocity profile meets the obstruction.

According to our knowledge, the present study is the first experimental work to place bridge pier in opposite direction according to flow direction. The idea behind the change the position of pier (opposite bridge pier) is that a significant amount of the flow will be deflect away from the pier, which will sufficiently prevent the mechanisms of local scour, particular the down flow and horseshoe vortex.

Scour countermeasures can be basically divided into two groups: armoring countermeasures and flow altering countermeasures. The main idea behind flow altering countermeasures is to minimize the strength of the down

- This is an Open Access article distributed under the terms of the Creative Commons Attribution-Noncommercial 4.0 Unported License, permitting all non-commercial use, distribution, and reproduction in any medium, provided the original work is properly cited.

- Selection and peer-review under responsibility of the Organizing Committee of the Conference

flow and subsequently horseshoe vortices, which are the main causes of pier scour. In contrast the principle of armor countermeasures is to provide a protection layer acts as a resistant layer to hydraulic shear stress and therefore provides protection to the more erodible materials underneath. It has been long established that the basic mechanism causing local scour at bridge piers is the down flow at the upstream face of the pier and subsequent formation of vortices at the base of pier. Muzzammil, Gangadharaiah and A.K. Gupta (2004).

Tafarajnoruz et al. 2012. Evaluated experimentally the performance of six different types of flow-altering countermeasures against pier scour. They found some countermeasures, which were recommended as highly efficient in the literature; do not perform well under test conditions Chen et al. (2012) examined the use of a hooked collar for reducing local scour around a bridge pier. The efficiency of collars was studied through experiments and compared with an unprotected pier. The velocity field measurements were obtained using an Acoustic Doppler Velocimeter. Results showed that a hooked-collar diameter of 1.25b has effectiveness similar to a collar diameter of 4.0b used by Zarrati et al. (1999) where b is the pier width. With hooked collar installed at the bed level, there was no sign of scouring and horseshoe vortex at the upstream face of the pier. In contrast, with unprotected pier, the down flow and turbulent kinetic energy were reduced under the effects of the hooked collar.

Application of aerofoil and opposite pier as a countermeasure for local scour at bridge piers

Drysdale (2008) applied dimensional analysis to examine the effectiveness of an aerofoil shaped bridge pier by comparing a scaled circular pier with a scaled aero foil shaped pier of the same diameter. Drysdale found that for the same flow condition, the vortex shedding from the aero foil shaped pier was significantly less than the circular pier.

Christensen (2009) examined the effectiveness of a slotted aero foil shaped bridge pier in reducing local scour, as compared to an aero foil and circular pier. Christensen concluded that, the aero foil shaped pier reduces local scour by a volume of 27% when compared to the circular shaped pier. The slotted aero foil shaped pier had a reduction in the scour hole volume of 85% when compared to the circular shaped pier.

Gibson (2010) examined the effectiveness of skirted, straight aerofoil shaped bridge pier in reducing local scour. Results demonstrate that symmetrical aero foil shaped piers are an effective countermeasure in the reduction of local scour hole volume.

The present study the same aerofoil shaped pier was investigated experimentally and compared with circular pier, the result showed the aero foil pier reduces local scour. In spite of aero foil reduces the local scour the opposite aero foil more effective in reducing local scour. Beside a comparison between opposite pier and opposite aerofoil was conducted. It is clearly from the comparison that the opposite piers are effective countermeasures for reducing local scour depth and scour hole volume, especially opposite aerofoil pier.

Dimensional Analysis

Dimensional analysis was used to define the dimensionless parameters based on the selection of all variables governing the maximum scour depth at upstream of the bridge pier.

$$ds = f_1(v, \rho, h, g, d_{50}, ks) \quad (1)$$

In which, v is the flow velocity, ρ is the density of fluid, h is the flow depth, g is the gravitational acceleration, d_{50} is the mean size of sand particles, ks and is the pier shape factor.

The maximum relative depth of scour was assumed to be correlated to the other independent parameters as given by Eq. (2).

$$ds/h = f_2(Fr, \frac{d_{50}}{h}, ks) \quad (2).$$

ds = maximum depth of scour and Fr =Froude number.

Experimental Work

The experiments were carried out in the Hydraulic laboratory of Civil Engineering Department of Gaziantep University. The flume is 12 m long, 0.8m width and 0.9 m depth as shown in Figure 3 with glass sides and steel bottom.

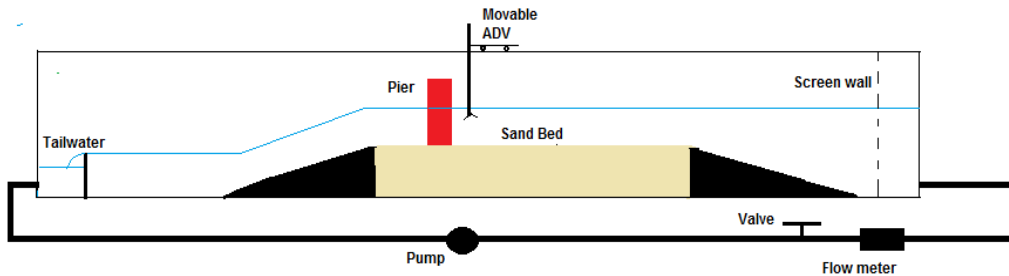


Figure 3. Schematic layout of the flume

The test section was made with a ramp which is located at the beginning and the end of the section. The test section is 3 m long and 0.2 m depth as shown in Figure 3.

The test section was filled with sediment of median particle size $d_{50} = 1.45$ mm and standard deviation, $\sigma_g = 3.16$ with the specific gravity of 2.65, the sieve analysis of the sand is given in Figure 4.

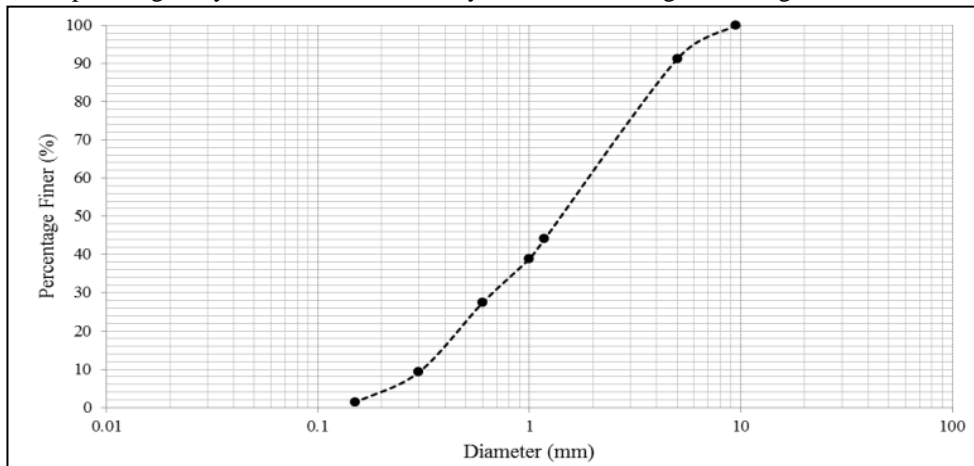
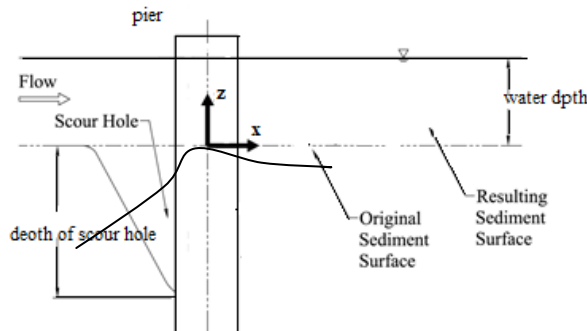


Figure 4. Grain size distributions

Flume discharge was measured by a Magnetic flow meter installed in the pipe system before the inlet of channel. The scour hole and the elevation of the bed was measured by laser meter, the instrument mounted on a manually moving carriage sliding on rails on the top of the flume wall. Depth of scour hole at the center line, extension of scour hole and a cross-section of the resulting scour were measured Figure 5.



Plan view

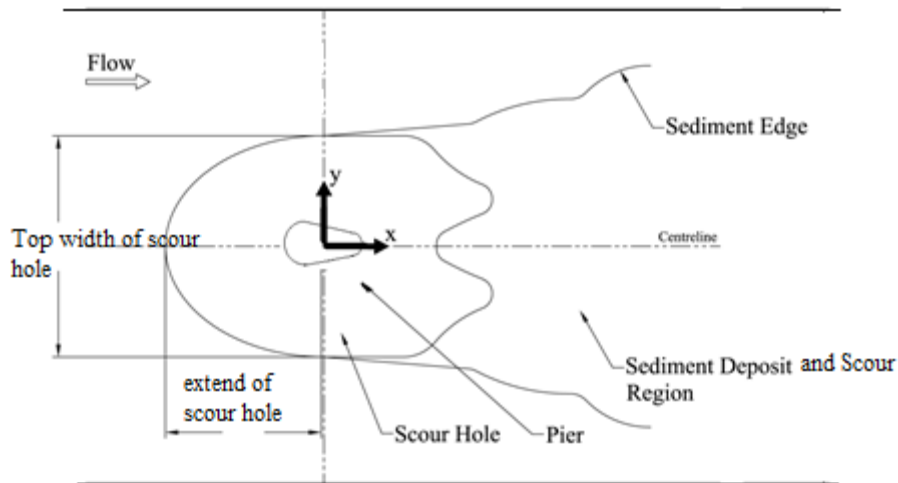


Figure 5. Centerline profile and plan view of a typical scour hole and deposit region

Five piers circular, opposite, normal piers, straight aero foil and opposite aerofoil as shown in Figure 6 were tested.

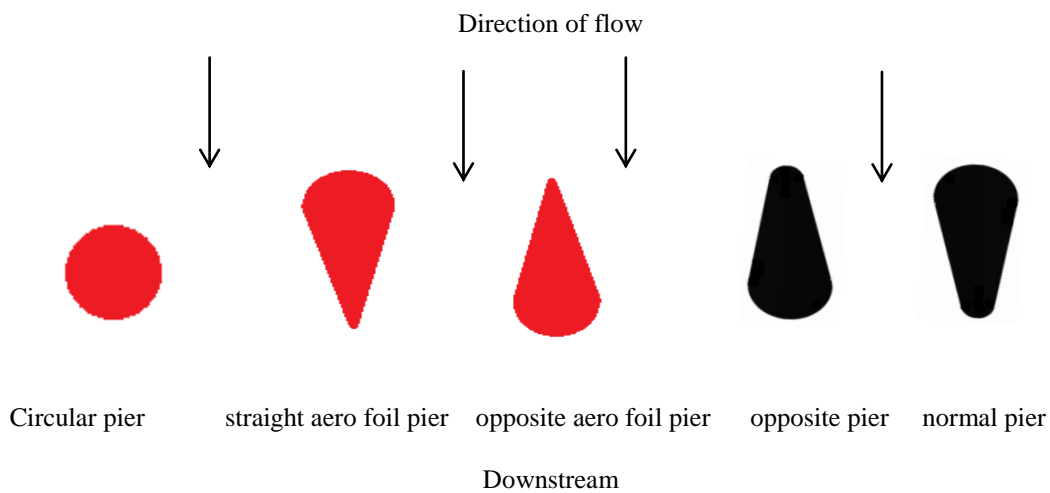


Figure 6. Views of tested piers

Experiments were performed under a live-bed water scour regime. The discharge was measured as 58 l/s with 12.5 cm flow depth. Initial bed elevations were taken randomly to check the leveling of the test section by using laser meter. The flume was first filled with water until desirable flow depth to avoid undesirable scour. Inlet flow to the flume was then gradually increased until the desired discharge, and the temporal variation of scour was monitored. The scour depth was measured under an intense light. The progress of scour depth was observed 3 hrs. At the end of each test, the pump was shut down and the water was slowly drained without disturbing the scour topography. The test section was then allowed to dry and frozen by pouring glue material (varnish).

Acoustic Doppler Velocimeter Measurements

During each experiment, the velocity is periodically monitored using an Acoustic Doppler Velocimeter (ADV). Stream velocity is measured upstream of the pier using the ADV in the center of the flume. The typical ADV setup is shown in Figure 8.

The ADV probe was then positioned above the scour hole and velocities were recorded for a period of 180 seconds. The sample period of 180 seconds was chosen to ensure that sufficient flow variations were captured.

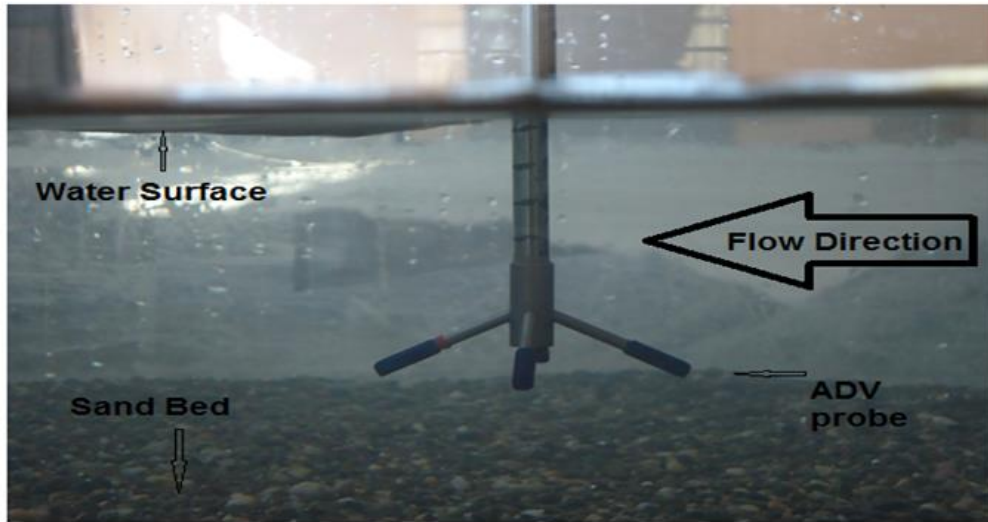


Figure 8. Typical ADV setup

Prediction of Scour Depth

Using step-wise regression (squared + Interaction Method), Eq. (3) was developed to correlate the relative maximum scour depth to the Froude number, Fr, and the pier shape factor, Ks

$$\frac{ds}{h} = 0.567 + 28.3 * d_{50} * Fr * \ln K_s - 5.02 * K_s * \frac{d_{50}}{h} * \ln K_s \quad (3)$$

The correlation coefficient (R^2) and the standard error of estimate for Eq. (3) are 84% and 0.032 respectively. Figure 7 presents the predicted values of ds/h using Eq. (3) versus the measured ones. Figure 7 indicate that Eq. (3) represented the measured data very well and hence could be used safely to predict the relative maximum depth of scour for different shape of piers.

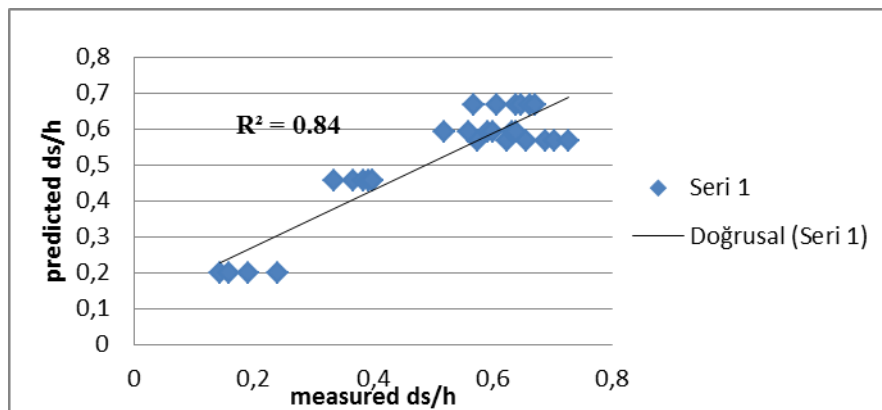


Figure 7. Measured ds/h versus predicted ds/h

Results and Discussion

Dimensions of the scour holes for each run of experiments were measured. The top width of scour in the transverse direction, distance from upstream face to front outer edge of hole, and depth at upstream face were compared for each of the five bridge piers as shown Table 1. The results of elapsed time taken from the start of each experiment for the scour hole to develop for five piers is given in Table 2.

Table 1. Scour hole dimensions from physical modeling

| Scour Hole Dimensions | Opposite bridge pier Diameter = 4-10 cm. | Normal bridge pier Diameter = 10-4 cm. | Straight Aerofoil Diameter = 10 cm | opposite aero foil Diameter = 10 cm | Circular bridge pier Diameter = 10 cm. |
|--|---|---|---------------------------------------|--|---|
| Top Scour Hole Width | = 30 c m | = 36 c m | = 34 cm | =24 cm | = 50 cm |
| Distance from Upstream face to front outer edge of hole | = 7.0 c m | = 16 cm | =12 cm | =4 cm | = 18 cm |
| Depth at Upstream face | = 5.0 cm | = 8.4 cm | = 8.0 cm | = 3.4 cm | = 10.9 cm |

Table 2. Time evolution of the maximum scours depth

| Time (min.) | Depth of scour for Straight aero foil 10 cm | Depth of scour for Opposite aero foil 10 cm | Depth of scour for circular pier 10 cm | Depth of scour for normal pier(10-4) cm | Depth of scour for opposite pier(4-10) cm |
|-------------|---|---|--|---|---|
| 5 | 6.5 | 1.8 | 8.6 | 7.1 | 4.2 |
| 15 | 7.0 | 2.0 | 9.2 | 7.5 | 4.6 |
| 30 | 7.4 | 2.4 | 9.8 | 8.0 | 4.8 |
| 60 | 7.5 | 3.0 | 10.2 | 8.1 | 4.9 |
| 120 | 7.9 | 3.2 | 10.4 | 8.3 | 5.0 |
| 180 | 8.0 | 3.4 | 10.9 | 8.4 | 5.0 |

Experimental results of the model piers within cohesion less bedding material will be compared and discussed in this section. The results are a comparison of scour and sediment scour hole depths for the circular, straight aero foil and normal piers were quite similar as expected, due to the identical shape on the upstream side of the pier as illustrated in Figure 9. A 54 % reduction in scour hole depth of the opposite pier was observed as compared to the circular pier and 40 % reduction as compared to the normal pier. For opposite aero foil 69% reduction in scour hole depth as compared to circular and 58% reduction as compared straight aero foil.

In addition to a reduction of the scour depth, the rate of scouring is also reduced considerably for both opposite aero foil and opposite pier as in Figure 9. Reduction in the rate of scouring can reduce the risk of pier failure when the duration of floods is short (Melville and Chiew, 1999).

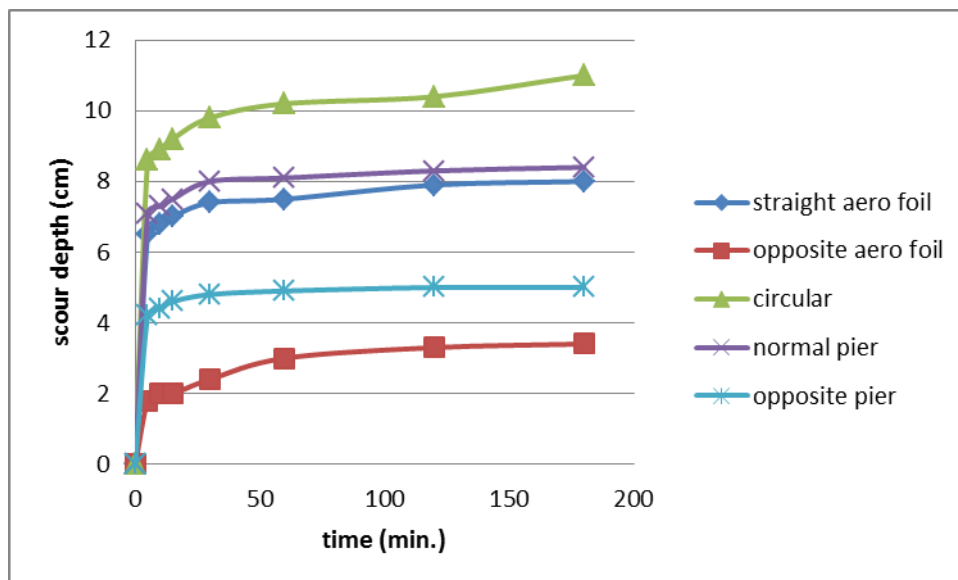


Figure 9. Scour hole development measured at the upstream face of each tested pier

Figure 10 demonstrate the top scour holes of five bridge piers .The top scour hole width of opposite pier was 20 cm or 40% less than the circular pier and 6.0 cm or 17 % less than the normal pier. For opposite aero foil top scour hole width was 52% less than the circular pier and 29% less than straight aero foil because the effect of the horseshoe vortex was reduced due to the down flow being deflected away from the base of opposite pier.

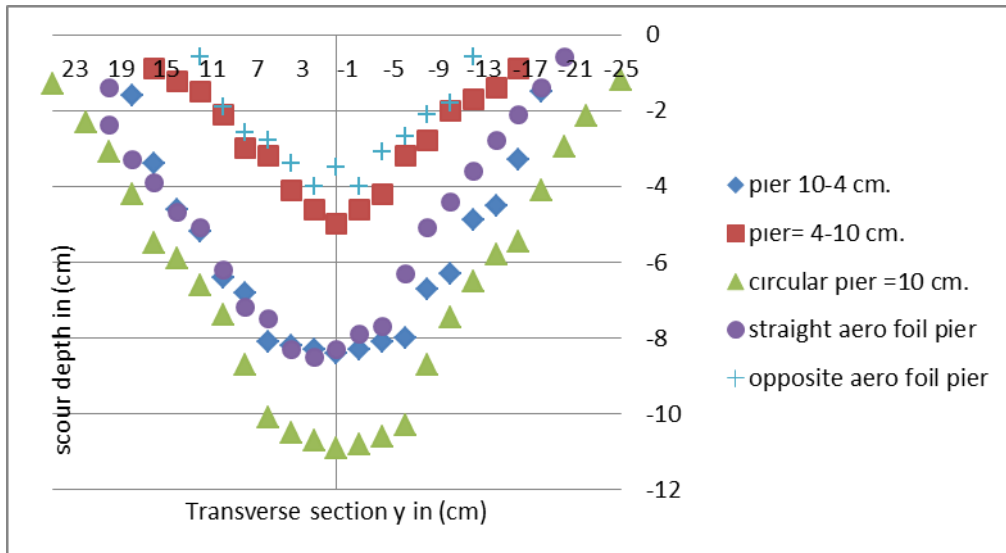


Figure 10. Transverse scour holes of three bridge piers

The effect of sediment gradation on local scour was investigated by many researchers, such as Ettema (1980), Chiew (1984), Dey (1995), and Molinas (2003). The general conclusion was that both the scour rate and the scour depth decrease as the geometric standard deviation (σ_g) increases. At a higher value of ($\sigma_g > 1.3$) (Melville and Raudkivi, 1997) (for non-uniform sediment), armoring occurs on the upstream bed and at the bottom of the scour hole, resulting in a considerable reduction of the scour depth as illustrated in Figure 11.

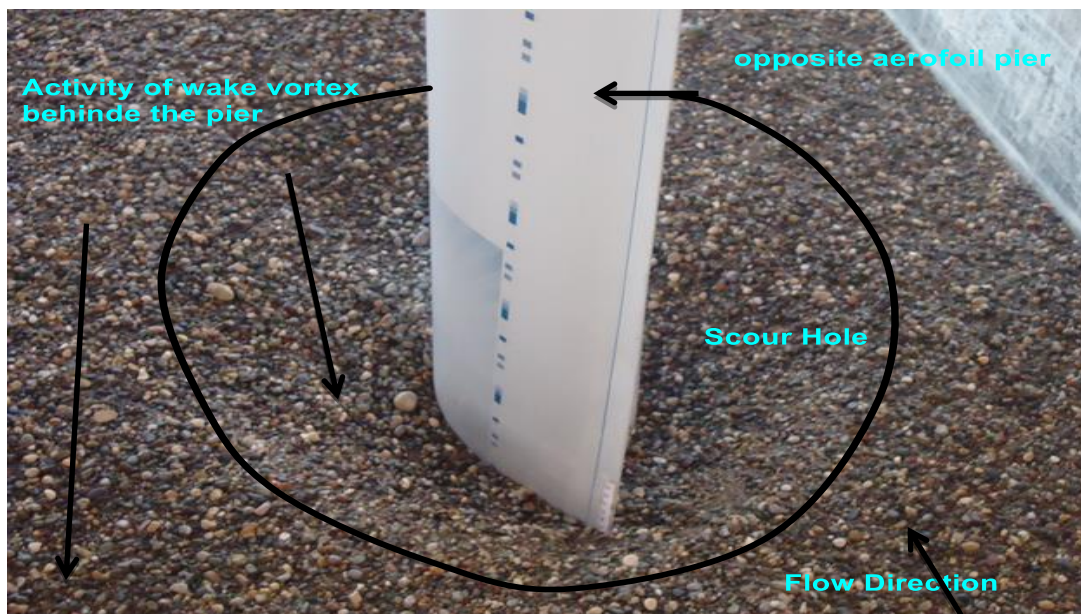


Figure 11. Armoring the channel bed and the scour hole

From Figure 12 it was observed that the activity of vortices (horse shoe vortex and wake vortex.) At the upstream face of normal, straight aero foil and circular piers a strong horseshoe vortex was detected, positioned at the base of piers. In contrast for opposite pier and opposite aerofoil the effect of horseshoe vortex reduced (not so visible) due to the down flow being deflected away from the base of opposite piers. It was seen from Figure 12 that, a strong wake vortex was visible and leading into scour hole in the downstream reach of circular, opposite aero foil and opposite piers.

Figure 13 shows the scour pattern around the normal, straight aerofoil, opposite aerofoil, opposite pier and circular piers. The opposite pier and opposite aerofoil minimize the scour depth, producing a little scour in the front and on the sides of the pier, but the scour in the pier's rear was more than that of straight aerofoil and normal pier due to the separation of flow occurred with a small amount at the beginning (upstream face) and then increased gradually according to the shape of opposite pier. In contrast for straight aerofoil and normal pier the separation increased and then decreased, producing a little scour at the wake region.

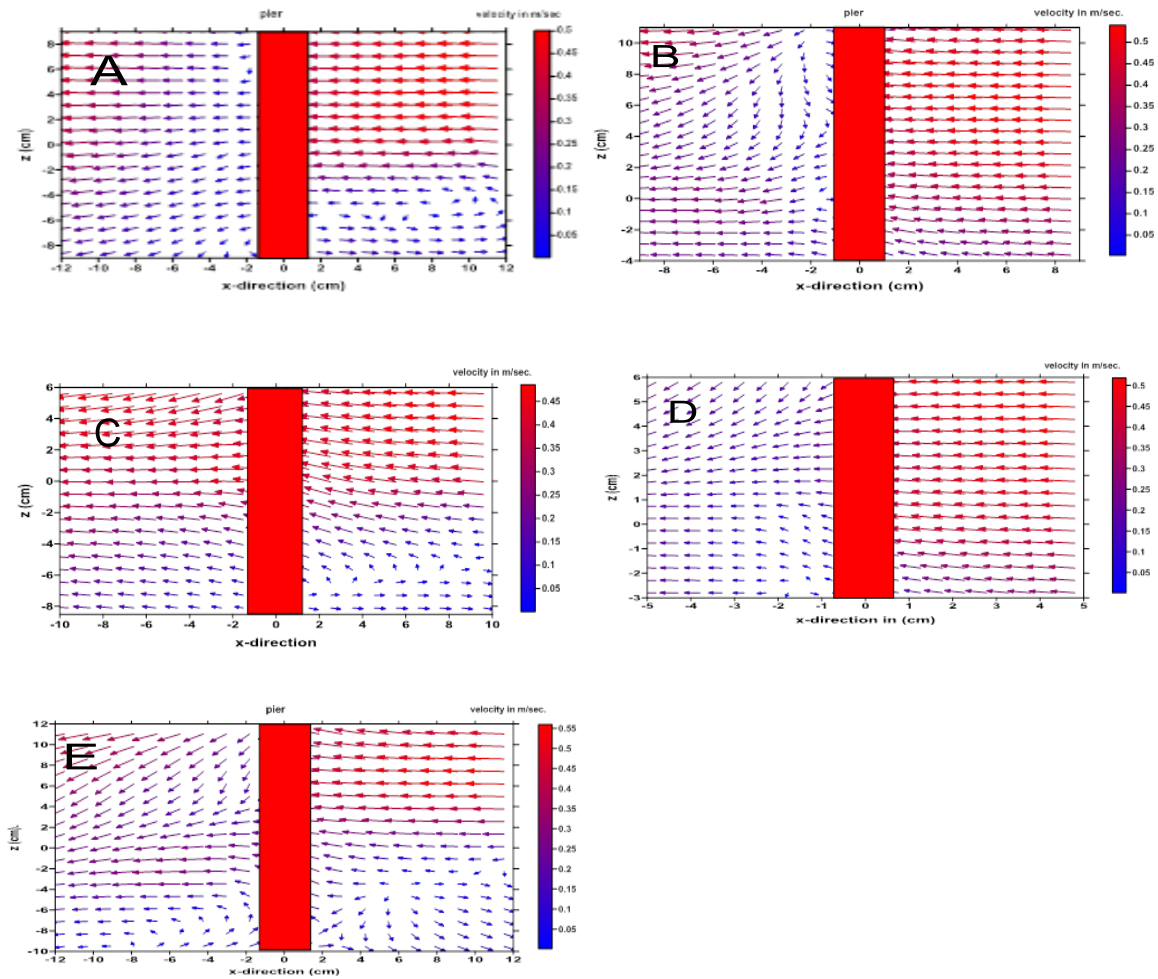


Figure 12 Velocity vectors at vertical plane for three tested piers

. (A) normal pier. (B) opposite pier,(C) straight aerofoil,(D) opposite aerofoil (E) circular pier.

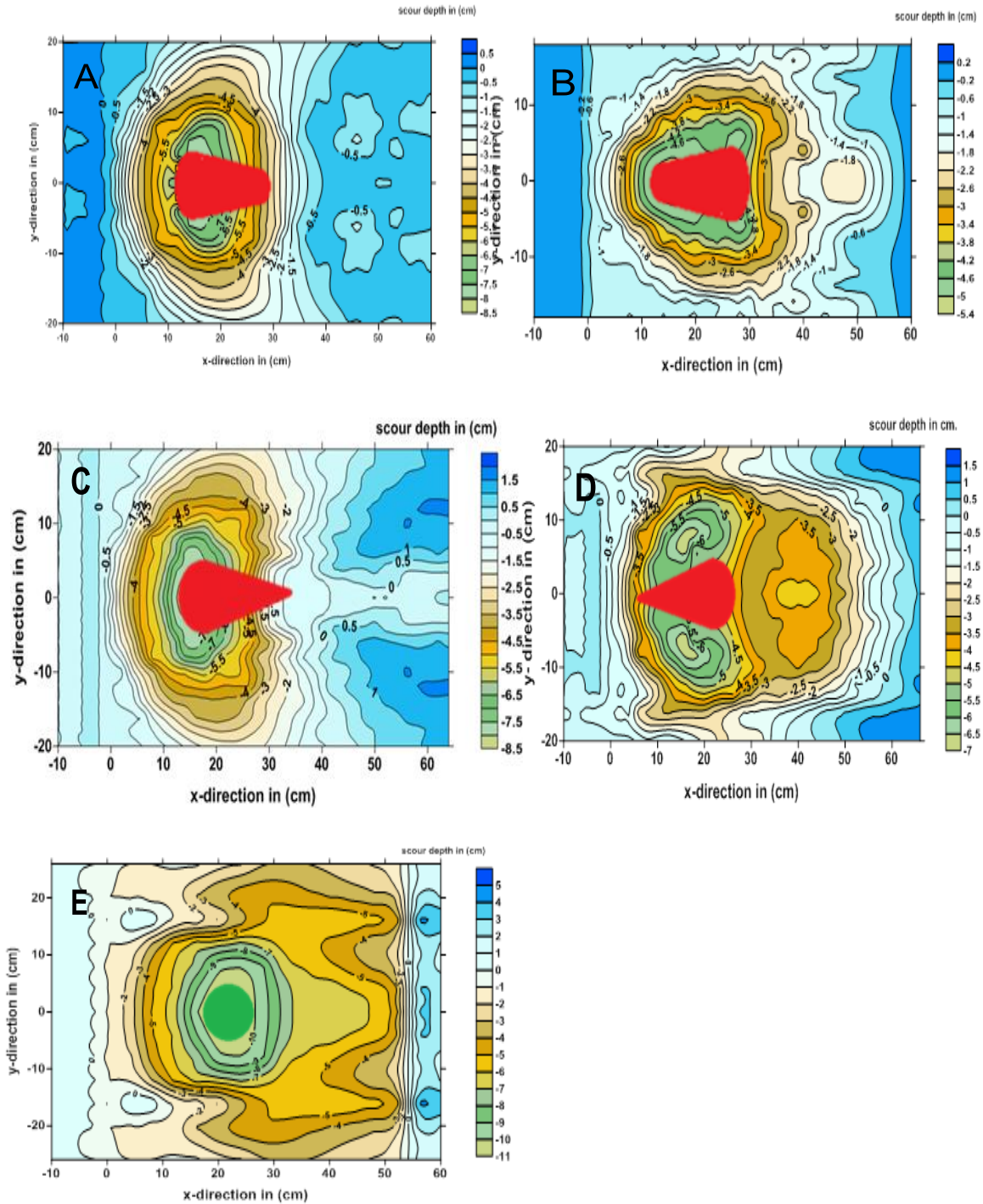


Figure 13 The scour pattern around (A) normal, (B) opposite (C) straight aerofoil, (D) opposite aerofoil, (E) circular piers.

Conclusion

Comparison between five bridge piers was carried out to find out the efficient bridge pier to countermeasures the local scour and the paper experimentally examined the application of a new method of placing the pier in the opposite direction of flow to reduce local scour on bridge pier. Changing the position of pier is not only

effective for reducing scour but it is also much more economic when it is compared to countermeasure techniques like riprap and slot.

Opposite pier and opposite aerofoil have effectiveness as a countermeasure to decrease local scour. Compared to straight aerofoil and normal pier, the down flow was reduced under the effect of changing the position of pier, with the new method there was a very little sign of down flow and horseshoe vortex at the upstream side of pier. For opposite pier the maximum depth of scour reduced 40 % and 54 % as compared with normal pier and circular pier respectively. The reduction in the scour hole volume for the opposite pier was 83% as compared with the circular pier. Opposite aerofoil reduces depth of scour 58% and 69% as compared with straight aerofoil and circular pier, and the scour hole volume reduced 89% as compared with circular pier.

The top scour hole width of opposite bridge pier was 40% less than the circular pier, and 17% for normal pier. For opposite aerofoil the top scour hole width was 52% less than the circular pier and 29% less than straight aero foil It is clearly from the results that opposite aerofoil and opposite pier are effective countermeasure the scour depth, particularly opposite aerofoil because a big amount of downflow deflected away the pier, resulting the strength of horseshoe decreased and the scour depth reduced. The present experimental study does not need to countermeasure the scour depth by armoring or flow altering devices, the new idea only to change the position of pier according to flow direction.

References

- T. M. Muzzammil, Gangadharaiyah and A.K. Gupta. (2004)"An experimental investigation of a horseshoe vortex induced by a bridge pier." *Water Manage.* 157: 109-119.
- Tafarojnoruz et al. (2012). "Evaluation of Flow-Altering Countermeasures against Bridge Pier Scour" *Journal of Hydraulic Eng.*138:297-305.
- Chen et al. (2012). Experimental investigation of the Flow Field around a Bridge Pier with Hooked collar" *ICSE6 Paris - August 27-31A.*
- Drysdale, DM (2008). 'The effectiveness of an aerofoil shaped pier in reducing down stream vortices and turbulence', University of Southern Queensland.
- ZM. Christensen. (2009). Reduction of Local Scour around Bridge Piers: Combined System of Aerofoil and Slot", University of Southern Queenlan, Toowoomba.
- D. Gibson. (2010). Evaluating Comparative Performance of Various Shaped Bridge Pers: Experimental Investigation of Sediment Transport and Scouring" , University of Southern Queenlan.
- Melville, B.W. and Chiew, Y.M. (1999). Time scale for local scour at bridge piers. *Journal of Hydraulic Engineering, ASCE*, 125(1): 59-65.
- Ettema, R. (1980). Scour at bridge piers. PhD Thesis. University of Auckland, Auckland, New Zealand.
- Chiew, Y.M.(1984). Local scour at bridge piers. PhD Thesis. University of Auckland, Auckland, New Zealand.
- Dey, S. (1995). Three-dimensional vortex flow field around a circular cylinder in a quasiequilibrium scour hole. *Sadhana, Proc. Indian Acad. Sci.*, 20 : 771-785.
- Molinas, A. 2003. Bridge Scour in Non-uniform Sediment Mixtures and in Cohesive Materials: Synthesis Report. Report Nr. FHWA-RD-03-083.
- B. W.Melville and A.J. Raudkivi .(1997) "Flow Characteristics in Local scour at Bridge Piers", *J. Hydr. Res. IAHR*, 15, 373–380.

Author Information

Abdulnaser Kashmoola

Northern Technical University,
Mosul/Iraq
Contact E-mail: *naser102525@yahoo.com*

Adnan Ismael

Northern Technical University,
Mosul/Iraq

Saleh Suleiman

Northern Technical University,
Mosul/Iraq

Comparison of Conventional and Encapsulated Urea on Growth and Yield of Wheat (*triticum aestivum L.*)

Saima Kalsoom BABAR

Sindh Agriculture University Tandojam

Nazeer Ahmed HASSANI

Sindh Agriculture University Tandojam

Inayatullah RAJPAR

Sindh Agriculture University Tandojam

Shakeel Ahmed BABAR

Naushahro Feroze Agricultural Research Institute

Zia-ul-Hassan SHAH

Sindh Agriculture University Tandojam

Imran KHAN

Sindh Agriculture University Tandojam

Abstract: Nitrogen (N) is necessary sustenance for healthy plant growth and its yield. Urea is a primary source of N in solid fertilizers. The hydrolysis rate of urea accelerates as it stays in surface application. However, Controlled-Release Fertilizers (CRF) has proven to reduce N losses, thereby increasing fertilizer efficiency. Wheat is the leading food grain of Pakistan occupying the largest area under single crop. It accounts for 9.6 percent of the value added in agriculture and 1.9 percent GDP. However, the production is recorded less as compared to previous years due to imbalance fertilizer application practices. The recommended doses of fertilizers may vary time to time for wheat. This study is therefore, planned to evaluate the method and appropriate rate of N for wheat, based on these specific objectives: 1) to evaluate an appropriate method and dose of N application for wheat and 2) to find out the effect of different N applications on growth and yield of wheat. In this regard, a field experiment was conducted at Wheat Section, Agriculture Research Institute Tandojam. There were 5 treatments examined on one variety (TD1) of wheat with three replications. The encapsulated urea was prepared manually in the laboratory of Department of Soil Science, Sindh Agriculture University Tandojam. Results revealed that wheat yield was markedly influenced by encapsulated urea as compared to surface applied urea. Maximum yield (40.5 % increment over control) was observed from encapsulated urea (N 140 kg ha⁻¹). However, the difference between the rates of N was non-significant ($p > 0.05$).

Keywords: Wheat, Encapsulated urea, Nitrogen, Yield

Introduction

Nitrogen (N) is one of the most important nutrients for plant growth and yield. Consistently it is required in larger amount than any other nutrients (Babar et al., 2016). It is commonly assumed that increasing application of N fertilizer is an effective way to improve crop yields. Though, N fertilizer application is an important practice for increasing crop efficiency in agricultural production (Wang et al., 2015; Behera et al., 2013), but its loss concern is a different scenario. The drawbacks of N fertilization for agricultural lands in excess of crop requirements may negatively affect groundwater, surface water, and the atmosphere through leaching, runoff,

- This is an Open Access article distributed under the terms of the Creative Commons Attribution-Noncommercial 4.0 Unported License, permitting all non-commercial use, distribution, and reproduction in any medium, provided the original work is properly cited.

- Selection and peer-review under responsibility of the Organizing Committee of the Conference

and volatilization of N (Drecht et al., 2003; Galloway et al., 2008). Moreover, low Nitrogen Use Efficiencies (NUEs) is an indication to lower economic returns for farmer's fertilizer investments. Pakistani soils are deficient in N therefore; urea turns into the most widely used nitrogenous fertilizer, due to its easily available approach and high N percentage (46%). Nitrogen losses upon surface application of urea have been reported worldwide. As urea applied in the form direct application, the amount of applied N is expected to loss more than 50% in the form of volatilization as NH_3 (Sommer et al., 2004). It is very important to overcome on N-losses. So that alleviates environmental pollution and increase N-efficiency (Chien et al., 2009). In this regard, controlled release urea is one of the appropriate solutions, as it expected to improve crop yield by reducing the hazardous emission of ammonia and nitrous oxide gases (NH_3 , N_2O) from urea (Shaviv, 2005).

Thus the substitute for the conventional urea is to coat it, which harmonizes time, the release of nutrients and the sequential plant requirements. An effective method of justifying the problem is to develop slow-release urea. Much research has reported on the improved performance of the coated urea where a central part is encapsulated within an inert carrier (Han et al., 2009; Liu et al., 2008). The release and dissolution rates of water soluble fertilizers depend on the coating materials (Wu et al., 2008). The N losses to the environment may be reduced with the use of coated fertilizers (Sato and Morgan, 2008). The coated fertilizers offer low N volatilization (10 to 30%) when compared to the conventional fertilizers (Medina et al., 2008). Controlled release urea (CRU) was designed to release nutrients into the soil solution at rates which closely match the N demands of crops, which maximizes NUEs and reduces N losses (Shaviv, 2005). Therefore, its designed to release N in close association with the crop N requirement and it can reduce residual nitrates in soil solutions. CRU also requires only a single basal fertilization, thereby reducing labor and energy cost compared to split applications of urea (Ribeiro et al., 2016). The application of CRFs can potentially decrease fertilizer use by 20 to 30 percent of the recommended rate of a conventional fertilizer while obtaining the same yield (Trenkel et al., 2010).

Therefore, using controlled-release N fertilizer for wheat may be a cost-effective management practice that improves crop performance and possibly allows custom applicators to apply fertilizer once in the fall (Nelson et al., 2014). Wheat (*Triticum aestivum* L.) is the leading food grain of Pakistan occupying the largest area under a single crop. It accounts for 9.6 percent of the value added in agriculture and 1.9 percent GDP; In Pakistan wheat was cultivated on an area of 9052 thousand hectares with the total production of 25,750 million tons during 2016-17 (Pakistan Economic Survey 2016-17), this figure is actually less than the previous year. It is due to imbalance fertilizer practices. The recommended doses of fertilizers may vary time to time. The reasons are the lack of awareness and resources. Wheat is the most important cereal crop of Rabi season and self-sufficiency is a prerequisite for the sustainable food security. The food availability can be secured through increasing productivity, especially of small farmers who are majority in Pakistan and putting emphasis on major wheat growing districts (Mazhar et al., 2007).

Consequently, this study is proposed to evaluate the effect of surface applied and encapsulated urea on growth and yield of wheat under filed conditions of alkaline soils and to identify an appropriate recommendation of urea rate.

Method

Experimental Field and its preparation

Research trial was conducted at Wheat Section, Agriculture Research Institute (ARI), Tandojam, Sindh, Pakistan. Experimental plot was located on the latitude of 25° - $24'54''\text{N}$ and longitude of 68° - $32'11''\text{E}$ (Figure 1). A piece of 252 m^2 ($18 \text{ m} \times 14 \text{ m}$) land was selected for this experiment. The area was equally being divided in 15 experimental units of 9 m^2 ($3 \text{ m} \times 3 \text{ m}$). Experiment was laid out in Randomized Complete Block design with five treatments and three replications. Variety TD1 was used under test trial to observe its behavior towards capsulated urea along with different N-rates. Five Treatments combination was based on T_1 as control (No N-application), T_2 (surface application of N at the rate of 140 kg ha^{-1}), T_3 (surface application of N at the rate of 160 kg ha^{-1}), T_4 (encapsulated application of N at the rate of 140 kg ha^{-1}), T_5 (encapsulated application of N at the rate of 160 kg ha^{-1}). Each treatment also received recommended doses of P_2O_5 at the rate of 90 kg ha^{-1} and K_2O at the rate of 50 kg ha^{-1} . The urea in the form of capsulated coating was applied once at the time of sowing. Whereas, surface application of urea (one-third) applied at the time of seedbed preparation and remaining N was applied with subsequent irrigations. Phosphorus and potassium were applied as a full dose. The capsulated urea was prepared manually in the laboratory, Department of Soil Science, Sindh Agriculture University Tandojam. In this regard, the normal empty capsules were bought (to serve as coating material) from the chemical store to refill with urea fertilizer.

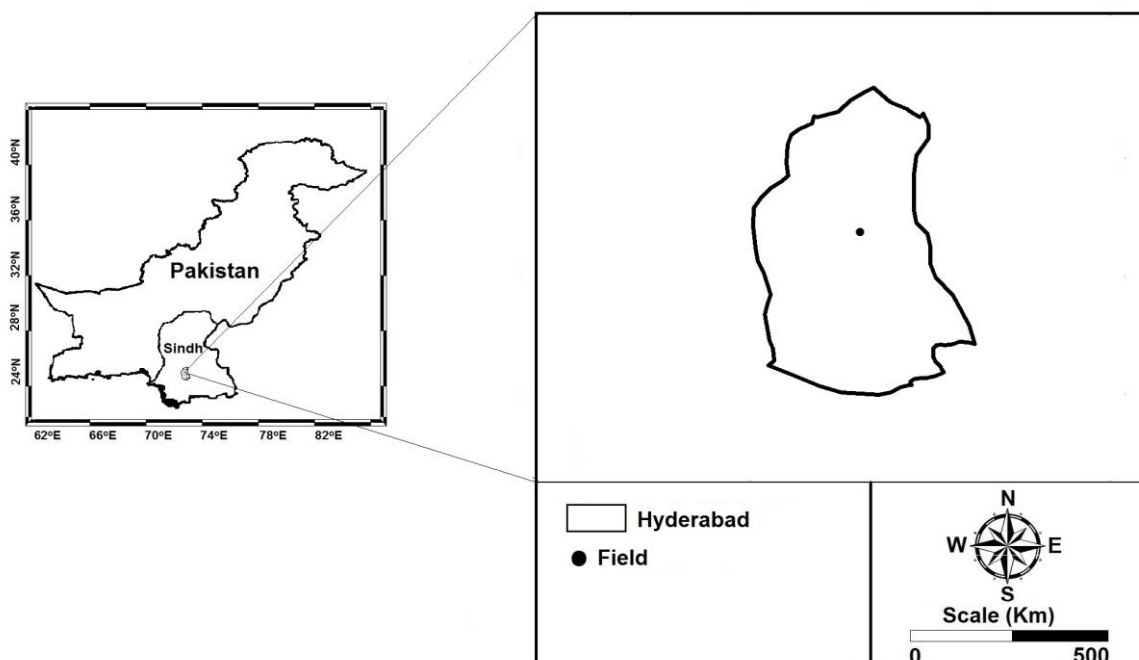


Figure 1. Experimental unit at Agriculture Research Institute Tandojam

The soil was well prepared by plowing and leveling the land to make a fine seedbed. Seed was sown with single coulter hand drill at the depth of 3 cm. The 360 counted numbers of wheat seeds were sown in each plot (This calculation was based on the recommended seed rate of particular variety; 50 kg acre⁻¹). The first irrigation was applied at the crown root initiation stage i.e., after three weeks of sowing. The subsequent irrigation was applied according to the need of crop.

Soil sampling and analysis

Soil samples were collected from sixteen different soil cores at the depth of 0-15 cm and 15-30 cm to make a representative soil sample. Samples were then brought to the laboratory for air-drying and grinding then passed through a 2mm sieve. Soil samples were placed in polyethylene bags for the further analysis. Soil texture done by using standard hydrometer method (Bouyoucos, 1962), soil pH and EC were measured in soil-water extract (1:5) by using digital pH and EC meters. Lime contents were determined by employing acid neutralization method discussed in practical agriculture chemistry (Kanwar and Chopra, 1959). Organic carbon was obtained by following Walkley black method (Jackson, 1959; Jackson and Barak, 2005) and N was analyzed by Kjeldhal method.

Observations to be recorded

Plant height (cm) was recorded at the time of maturity, Number of tillers plant⁻¹, 1000 grain weight (g), biomass (g m⁻²) and Grain yield (kg ha⁻¹), were recorded accordingly. The data recorded, transmitted through the statistical analysis by using Statistix 8.1 software to find out the treatment effect. The means were compared with Tukey's range test (HSD)/ honest significant difference.

Results and Discussion

The effect of different rates and methods of application of urea on the growth and yield of wheat revealed the significant effects of encapsulated urea on the tiller production, plant height, seed index, wheat biomass and grain yield of wheat crop.

The soil characteristics before planting wheat crop are given in Table 1. According to the results, soil was slightly alkaline in nature (pH 7.8), low in OM (0.67 %) and found deficient in N contents (0.04 %). The soil was silty clay loam in textural class and found non-saline in nature.

Table 1. Soil physical and chemical properties before planting wheat crop

| Physical properties | |
|-----------------------------|-----------------|
| Textural class | Silty Clay loam |
| Sand% | 0.48 |
| Silt% | 41.27 |
| Clay% | 50.32 |
| Chemical properties of soil | |
| Soil pH | 7.8 |
| OM% | 0.67 |
| CaCO ₃ % | 7.4 |
| EC dS/m | 0.13 |
| Total N% | 0.04 |

Effect of Encapsulated urea on the growth and yield of wheat

The effect of method of urea application (direct and encapsulated urea) was analyzed on the growth and yield of TD1 (wheat variety). According to the observations made, it was noted that the various growth and yield parameters of wheat were highly affected by the method of urea application. Encapsulated urea (at the rate of 140 kg ha⁻¹ (T₄)) gave the positive significant effect ($p < 0.05$) as compared to rest of the other treatments (Table 2). It was perceived that the difference between the rates of urea was non-significant ($p > 0.05$). The range values showed the difference of treatments in the various growth parameters of wheat as: number of tillers plant⁻¹ 5.68 to 11.69, plant height 65.56 to 90.01 cm, seed index 34.02 to 45.87 g, biomass 653.0 to 1107.43 g plot⁻¹, grain yield 3240.11 to 5478.23 kg ha⁻¹. The results revealed are supported by Laghari et al, 2010, who have observed the significant effect of fertilizer use and management on three cultivars of wheat. Fertilizer rates and combinations affected on the growth and yield of different wheat varieties. They have reported that the N at the rate of 120 kg ha⁻¹ enhanced the yield of TD1, However the higher rates of N were found non-significant on wheat variety TD1. Whereas, rest of the other two wheat varieties (Mehran-89 and TJ-83) showed the positive response in all aspects of growth and yield upon the higher fertilizer rates (180 N kg ha⁻¹). Tall plants, maximum nodes stem⁻¹, internode length, grain weight spike⁻¹, seed index, prolonged maturity days and higher lodging tendency in Mehran-89 and TJ-83 were recorded under the highest rate of urea. The similar results were also obtained by Oad et al, 2007, who analyzed that the proper cultural practices can have positive results in terms of higher yield due to nutrients management.

Table 2. Effect of encapsulated urea on the growth and yield of wheat

| Treatments | Tillers plant ⁻¹ | Plant height (cm) | 1000 grain wt (g) | Wheat biomass (g m ⁻²) | Grain yield (kg ha ⁻¹) |
|-------------------------------|-----------------------------|-------------------|-------------------|------------------------------------|------------------------------------|
| T1 Control | 5.68 d | 65.56 c | 34.02 c | 653.00 d | 3240.11 d |
| T2 SN 140 kg ha ⁻¹ | 7.28 bc | 71.57 bc | 38.89 b | 790.89 bc | 4000.14 c |
| T3 SN 160 kg ha ⁻¹ | 7.79 cd | 75.13 b | 39.52 b | 824.13 b | 4413.21 b |
| T4 CN 140 kg ha ⁻¹ | 11.54 a | 89.97 a | 45.42 a | 1110.76 a | 5410.23 a |
| T5 CN 160 kg ha ⁻¹ | 11.69 a | 90.01 a | 45.87 a | 1107.43 a | 5478.23 a |
| HSD (5%) | 1.568 | 3.92 | 2.56 | 25.61 | 4.56 |

Means with the different letters in each of the column are significantly different at Tukey's (HSD) $p < 0.05$

*SN= Surface Nitrogen

*CN= Capsulated Nitrogen

The rate of N remains fluctuating as the self-sufficiency in nitrogen use efficiency (NUE) is still beyond the range. Overall in Pakistan, a number of research trials have been conducted to evaluate the appropriate rate of N, but no makeable results have been achieved. In 2016, at the Northern areas of Pakistan a research experiment was conducted to evaluate proper rate of N along with the seed rate and number of irrigations. It was manifested from the results that as the N rate decreased the yield of wheat crop was also declined. However, the rate of 120 kg N ha⁻¹ showed the positive effect on the increasing seed rate (60 kg ha⁻¹). Soils at northern areas of Pakistan are fertile but still the yield is not desirable (Shah et al, 2016). Therefore, it is required to analyze the actual myths behind the NUE. The conventional urea resulted in 1 - 60% of N losses in the form of ammonia

volatilization and nitrous oxide emission, hence the solution is to eliminate this risk with the application of slow released urea (coated urea), that can capable to provide the nutrients at precise and tardy manner (Babar et al., 2016, Chien et al., 2009; Jiang et al., 2012; Shaviv, 2005). Coating of urea has proven the efficiency regarding N-uptake and minimizing NH₃ volatilization loss as reported in the laboratory studies (Babar et al., 2016). The growth parameters increment might be attributed with the adequate supply of N, that contributes in accelerated enzymatic activities (Khan et al., 2012). Since decades, it is realized that the hydrolysis rate of urea is faster if it would be applied in conventional form. Reports have mentioned that about 70% of the applied urea losses in different forms, the common one is ammonia volatilization loss (Fenn and Miyamoto, 1981). Current studies also observed that NUE was markedly affected when the urea was applied as surface application. Therefore, the highest yield value was observed under encapsulated urea. CRF (controlled release fertilizer) is a solution, as it assumes to improve crop yield by minimizing the hazardous emission of NH₃ and N₂O gases from the fertilizers (Shaviv, 2005).

Conclusion

Wheat yield of TD1 variety was expressively subjective towards encapsulated urea. The 40.5% yield increment was recorded under T4 (CN 140 kg ha⁻¹) and T5 (CN 160 kg ha⁻¹) respectively as compared to control (no nitrogen application). However, the difference between T4 and T5 was found non-significant (p >0.05) therefore; the rate of urea can be adjusted at 140 kg ha⁻¹ (encapsulated) to skip the price increment of fertilizer application.

Recommendations

It is recommended that urea can be applied in coating form as compared to surface application. In this regard, the coating materials can be changed accordingly. Natural products should be selected to see their effects on the hydrolysis rate of urea. To minimize the N-losses such coated urea fertilizers are suggested to apply. This study was concern only with one wheat variety which may be suggested to test on the other varieties as well as on the other crops too.

Acknowledgements

Authors are highly grateful towards the Department of Soil Science, Sindh Agriculture University Tandojam, and Wheat Section, Agriculture Research Institute Tandojam for providing the laboratory and field facilities. Authors would like to express their special thanks of gratitude to Higher Education Commission of Pakistan for the financial assistance to present this paper.

References

- Babar, S. K., Yusop, M. K., Babar, S. A., & Khooharo, A. A. (2016). Consequences OF Cu and Zn Coated Urea to minimize ammonia volatilization. *JURNAL TEKNOLOGI*, 78(6-12), 1-6.
- Babar, S. K. (2016). *Effects of Cu and Zn coated urea on rice production in acidic and alkaline soils*. (Doctoral dissertation). <http://ezproxy.upm.edu.my>.
- Behera, S. N., Sharma, M., Aneja, V. P., & Balasubramanian, R. (2013). Ammonia in the atmosphere: a review on emission sources, atmospheric chemistry and deposition on terrestrial bodies. *Environmental Science and Pollution Research*, 20(11), 8092-8131.
- Bouyoucos, G. J. (1962). Hydrometer method improved for making particle size analyses of soils. *Agronomy Journal* 54(5): 464-465.
- Chien, S., Prochnow, L. & Cantarella, H. (2009). Recent developments of fertilizer production and use to improve nutrient efficiency and minimize environmental impacts. *Advances in Agronomy* 102, 267-322.
- Fenn, L. and Miyamoto, S. (1981). Ammonia loss and associated reactions of urea in calcareous soils. *Soil Science Society of America Journal* 45: 537-540.
- Galloway, D. K., Özel, F., & Psaltis, D. (2008). Biases for neutron star mass, radius and distance measurements from Eddington-limited X-ray bursts. *Monthly Notices of the Royal Astronomical Society*, 387(1), 268-272.

- Han, X., Chen, S., & Hu, X. (2009). Controlled-release fertilizer encapsulated by starch/polyvinyl alcohol coating. *Desalination*, 240(1-3), 21-26.
- Jackson, N. L. (1958). Soil chemical Analysis constable. *Ltd. Co., London*, 498.
- Jackson, M. L. (2005). *Soil chemical analysis: advanced course*. UW-Madison Libraries, Parallel Press.
- Kanwar, J. S. and Chopra, S. L. (1959). Practical agricultural chemistry.
- Khan, P., Memon, M., Imtiaz, M., Depar, N., Aslam, M., Memon, M. and Shah, J. (2012). Determining the zinc requirements of rice genotype Sarshar evolved at NIA, Tandojam. *Sarhad Journal of Agriculture* 28: 1-7.
- Laghari, G. M., Oad, F. C., Tunio, S., Gandahi, A. W., Siddiqui, M. H., Jagirani, A. W., & Oad, S. M. (2010). Growth, yield and nutrient uptake of various wheat cultivars under different fertilizer regimes. *Sarhad Journal of Agriculture*, 26(4), 489-497.
- Liu, X., Hua, X., Guo, J., Qi, D., Wang, L., Liu, Z., ... & Liu, G. (2008). Enhanced tolerance to drought stress in transgenic tobacco plants overexpressing VTE1 for increased tocopherol production from Arabidopsis thaliana. *Biotechnology Letters*, 30(7), 1275-1280.
- Mazhar, F., Buckles, D., & Satheesh, P. V. (2007). *Food sovereignty and uncultivated biodiversity in South Asia: Essays on the poverty of food policy and the wealth of the social landscape*. Academic Foundation.
- Medina, L. C., Obreza, T. A., Sartain, J. B., & Rouse, R. E. (2008). Nitrogen release patterns of a mixed controlled-release fertilizer and its components. *HortTechnology*, 18(3), 475-480.
- Nelson, K. A., Motavalli, P. P., & Nathan, M. (2014). Nitrogen fertilizer sources and application timing affects wheat and inter-seeded red clover yields on claypan soils. *Agronomy*, 4(4), 497-513.
- Oad, F. C., Siddiqui, M. H., & Buriro, U. A. (2007). Growth and yield losses in wheat due to different weed densities. *Asian Journal of Plant Sciences*, 6, 173-176.
- Pakistan Economic Survey. 2016-17. *Economic adviser's wing, finance division*, Government of Pakistan, Islamabad. <http://www.finance.gov.pk>
- Ribeiro, V. J., Andrade, F. V., de Souza, C. H. E., & Sa Mendonca, E. (2016). Volatilization of ammonia in stabilized slow-release nitrogen fertilizer under controlled conditions. *Australian Journal of Crop Science*, 10(6), 793.
- Sato, S., & Morgan, K. T. (2008). Nitrogen recovery and transformation from a surface or sub-surface application of controlled-release fertilizer on a sandy soil. *Journal of plant nutrition*, 31(12), 2214-2231.
- Shah, W. A., Khan, H. U., Anwar, S., & Nawab, K. (2016). Yield and yield components of wheat as affected by different seed rates and nitrogen levels. *Sarhad Journal of Agriculture*, 27(1), 17-25.
- Shaviv, A. (2005). Controlled release fertilizers. In *IFA International Workshop on Enhanced-Efficiency Fertilizers*, pp. 28-30. Frankfurt. International Fertilizer Industry Association Paris, France.
- Sommer, S. G., Petersen, S. O., Sørensen, P., Poulsen, H. D., & Møller, H. B. (2007). Methane and carbon dioxide emissions and nitrogen turnover during liquid manure storage. *Nutrient Cycling in Agroecosystems*, 78(1), 27-36.
- Trenkel, M. E. (2010). *Slow-and controlled-release and stabilized fertilizers: an option for enhancing nutrient use efficiency in agriculture*. IFA, International fertilizer industry association.
- Van Drecht, G., Bouwman, A. F., Knoop, J. M., Beusen, A. H. W., & Meinardi, C. R. (2003). Global modeling of the fate of nitrogen from point and nonpoint sources in soils, groundwater, and surface water. *Global Biogeochemical Cycles*, 17(4).
- Wang, S., Zhao, X., Xing, G., Yang, Y., Zhang, M., & Chen, H. (2015). Improving grain yield and reducing N loss using polymer-coated urea in southeast China. *Agronomy for sustainable development*, 35(3), 1103-1115.
- Wu, L., & Liu, M. (2008). Preparation and properties of chitosan-coated NPK compound fertilizer with controlled-release and water-retention. *Carbohydrate Polymers*, 72(2), 240-247.

Author Information

Saima Kalsoom Babar

Department of Soil Science,
Sindh Agriculture University, Tandojam, 70060, Pakistan
Contact E-mail: skbabar@sau.edu.pk

Nazeer Ahmed Hassani

Department of Soil Science,
Sindh Agriculture University, Tandojam, 70060, Pakistan

Inayatulah Rajpar

Department of Soil Science,
Sindh Agriculture University, Tandojam, 70060, Pakistan

Shakeel Ahmed Babar

District Soil & Water Testing Laboratory, Naushehro
Feroze, Agriculture Research Institute, Sindh, Pakistan.

Zia-ul-Hassan Shah

Department of Soil Science,
Sindh Agriculture University, Tandojam, 70060, Pakistan

Imran Khan

Department of Soil Science,
Sindh Agriculture University, Tandojam, 70060, Pakistan

Enhancement Conventional Concrete using locally available Waste Material

Ali Hussein ALI

Northern Technical University

Saleh Jaafer SULEIMAN

Northern Technical University

Mahmoud Majid HAMEED

Engineering Technical College

Abstract: Concrete is a nifty construction material. Concrete has some attractive properties when it is newly mixed, it is plastic and malleable, but when it is hardened it becomes very strong and durable. These qualities make concrete unique from other materials. For the reason that concrete is the main construction material across the world and widely used in all kinds of civil engineering works, such as for building skyscrapers, dams, bridges, barrage, highways, and houses. As we know that aggregate represents about 70-80% of concrete elements, so it will be useful to recycle the aggregate for construction works and also to solve the environmental problems. Iraq is suffering a lot of the problem of rubble(debris) as a result of the wars that occurred during the past years, on the other hand in some places have been converted buildings from residential buildings to commercial buildings, so these destroyed buildings constitute the problem of environmental pollutants. To minimize the trouble of excess of waste material it is suitable steps to utilize the recycled aggregates provide that the desired final product will meet the standards. In the present investigation adjustments to traditional mix designs of concrete using locally available waste material was studied experimentally. The experimental program consisted of nine mixes with mix proportions [1:2:4] and constant slump equal to (13) cm were constructed and tested. These nine mixes classified into three groups based on the types of sand and gravel used in all mixes. The experimental results showed that, the optimum mix was Mix₂ in Group (B) with (cement : 50% naturally sand and 50% crushed recycled concrete as sand : crushed boulder as gravel), which enhance the properties of the existing concrete, such that, increasing compressive strength by (18.6%), flexural strength by (8.3%) and splitting strength by (28.9%), as comparing with Mix₁ (Reference mix).

Keywords: Conventional concrete, Concrete locally waste material, Compressive strength, Flexural strength, Splitting strength

Introduction and Literature Review

The environmental effect of the production of the raw components of concrete (such as cement, coarse and fine aggregate) is large (Buck 1977 & Hansen 1984). Generally concrete is the main construction material in the world and the widely used in all kinds of civil engineering works. Amount of aggregate in concrete is about 70-80% of concrete components so it will be useful to recycle the aggregate for construction works as well as for the purpose of solving the environmental problems. The scale of the problem makes it prudent to investigate other origins of raw materials in order to reduce the consumption of energy and available natural origins, and to obtain a more "green" concrete. Crushing concrete to produce aggregate for the production of new concrete is one common mean for obtaining a more environment-friendly concrete. This reduces the consumption of the natural resources as well as the consumption of the landfills required for waste concrete (Rahal 2007).

Concrete destruction waste has been proved to be an excellent origin of aggregate for new concrete production. There are abundant studies proved that concrete made with this kind of aggregate can have mechanical

- This is an Open Access article distributed under the terms of the Creative Commons Attribution-NonCommercial 4.0 Unported License, permitting all non-commercial use, distribution, and reproduction in any medium, provided the original work is properly cited.

- Selection and peer-review under responsibility of the Organizing Committee of the Conference

properties similar to those of conventional concrete is nowadays a possible goal for this environmentally sound practice (Buck 1977 & Hansen 1984).

Iraq is suffering a lot of the problem of rubble (debris) as a result of the wars that occurred during the past years, on the other hand in some places have been converted buildings from residential buildings to commercial buildings, so these destroyed buildings constitute the problem of environmental pollutants. To reduce the surplus of waste material it is a suitable step to use the recycled aggregate provided that can meet the standards to provide the desired final product.

Experimental Work

In the present investigation adjustments to traditional mix designs of concrete using locally available waste material was studied experimentally as shown in plate (1). The experimental program consisted of nine mixes with mix proportions [1:2:4] and constant slump equal to (13) cm were constructed and tested. These nine mixes classified into three groups based on the types of sand and gravel used in all mixes, as follows:

Group (A) was divided into three mixes depending on the types of gravel [Mix₁ "Reference mix", included (cement : sand : gravel), Mix₂, included (cement : sand : crushed boulder as gravel) and Mix₃, included (cement : sand : crushed recycled concrete as gravel)].

Group (B) was the same as in Group (A) divided into three mixes except types and percentage of sand [Mix₁, Mix₂ and Mix₃ are included 50% naturally sand and 50% crushed recycled concrete as sand].

Group (C) was the same as in Group (A) except type of sand [Mix₁, Mix₂ and Mix₃ are included 100% crushed recycled concrete as sand].



Plate 1. Locally Concrete available waste material

Materials

Cement

Ordinary Portland cement (OPC) produced by Badoosh cement factory. Tables (1 and 2) showed the physical properties and chemical compositions of cement. Both physical and chemical properties are with compliance to Iraqi standard specification "IQS: 5/1984".

Table (1) physical and mechanical properties of ordinary portland cement

| Physical properties | Test results | Limits of Iraqi specification No.5/1984 |
|---|--------------|---|
| Specific surface area, Blain's method, m ² /kg | 290 | ≥ 230 |
| Soundness, Autoclave's Method, % | 0.03 | < 0.8 |
| Setting time, Vicat's method | | |
| Initial setting hr:min | 1:49 | ≥ 45 min |
| Final setting hr:min | 3:25 | ≤ 10 hours |
| Compressive strength | | |
| 3 days N/mm ² | 22 | ≥ 15 |
| 7 days N/mm ² | 30 | ≥ 23 |

Table (2) Chemical Composition of Ordinary Portland Cement

| Main oxide | CaO | SiO ₂ | Fe ₂ O ₃ | Al ₂ O ₃ | So ₃ | Mgo |
|-----------------|------|------------------|--------------------------------|--------------------------------|-----------------|--------|
| % | 62.2 | 21.31 | 2.67 | 5.89 | 2.6 | 3.62 |
| (IIS No.5/1984) | — | — | — | — | Max 2.8% | Max 5% |

Fine aggregate

Natural fine aggregate: it obtained from Kanhash region (Mosul). This type of sand is identical with british standard (B.S.)882:1992. Its sieve analysis is shown in table (3) .The grading limits with compliance to ASTM C 33-02.

Recycled fine aggregate: it obtained from the destroyed building in the engineering technical college in (Mosul/Iraq). This type of sand is passing from sieve no.4(4.75mm).

Table 3. Sieve analysis of the natural sand

| Sieve size (mm) | Total limit | Percentage passing of the sand used | Percentage passing | | |
|-----------------|-------------|-------------------------------------|--------------------|--------|--------|
| | | | Coarse | Medium | Fine |
| 4.75 | 89-100 | 100 | - | - | - |
| 2.36 | 60-100 | 87 | 60-100 | 65-100 | 80-100 |
| 1.18 | 30-100 | 70.4 | 30-90 | 45-100 | 70-100 |
| 0.6 | 15-100 | 56.8 | 15-54 | 25-80 | 55-100 |
| 0.3 | 5-70 | 13.2 | 5-40 | 5-48 | 5-70 |
| 0.15 | 0-15 | 3 | - | - | - |

Coarse aggregate

Crushed boulder Coarse aggregate: it obtained from Zako city in Iraq with M.A.S (19) mm. This gravel is in compatible with ASTM C33-03. The sieve analysis was performed, Table (4) show the results of the sieve analysis.

Table 4. Sieve analysis of the crushed boulder aggregate

| Sieve size (mm) | Weight passing (%) | Total limits (ASTM C33-3) |
|-----------------|--------------------|---------------------------|
| 37.5 | 100 | 100 |
| 25 | 100 | 100 |
| 19 | 100 | 90-100 |
| 12.5 | 60.8 | 35-80 |
| 9.5 | 29.3 | 20-55 |
| 4.75 | 6.6 | 0-10 |
| 2.36 | 2.9 | 0-5 |

Natural coarse aggregate: it obtained from the Tigris river (Mosul/Iraq) with M.A.S(19)mm. Table (5) shows the sieve analysis of the gravel according to ASTM C33-03

Table 5. Sieve analysis of the natural coarse aggregate

| Sieve size (mm) | Weight passing (%) | Total limits (ASTM C33-3) |
|-----------------|--------------------|---------------------------|
| 37.5 | 100 | 100 |
| 25 | 100 | 100 |
| 19 | 100 | 90-100 |
| 12.5 | 58.4 | 35-80 |
| 9.5 | 28.8 | 20-55 |
| 4.75 | 7.2 | 0-10 |
| 2.36 | 2.6 | 0-5 |

Recycled Coarse Aggregate: obtained from the destroyed building in the engineering technical college in (Mosul/Iraq) with M.A.S(19)mm. Table (6) shows the sieve analysis of the gravel according to ASTM C33-03.

Table 6. Sieve analysis of the recycled coarse aggregate

| Sieve size (mm) | Weight passing (%) | Total limits (ASTM C33-3) |
|-----------------|--------------------|---------------------------|
| 37.5 | 100 | 100 |
| 25 | 100 | 100 |
| 19 | 100 | 90-100 |
| 12.5 | 63.3 | 35-80 |
| 9.5 | 32.1 | 20-55 |
| 4.75 | 5.2 | 0-10 |
| 2.36 | 3.3 | 0-5 |

Water

Tap water was used in this research for both mixing and curing the concrete specimens in accordance with ASTM C1602.

Results and Discussion

Compressive strength

Compressive strength of the concrete mixtures obtained in this paper are shown in table(7) and Figure (1). The optimum mix was Mix₂ in Group (B) with (cement : 50% naturally sand and 50% crushed

recycled concrete as sand : crushed boulder as gravel), which enhance and increase the compressive strength by (19%), as comparing with Mix₁ (Reference mix).

Table 7. Compressive strength of the concrete mixtures

| Mix no. | Compressive strength (Mpa) | |
|---------|----------------------------|---------|
| | 7 days | 28 days |
| Mix 1 | 23.8 | 40.37 |
| Mix 2 | 25 | 41.42 |
| Mix 3 | 21.192 | 34.27 |
| Mix 4 | 23.195 | 36.695 |
| Mix 5 | 29.241 | 42.11 |
| Mix 6 | 20.22 | 31.328 |
| Mix 7 | 22.124 | 35.165 |
| Mix 8 | 23.575 | 32.82 |
| Mix 9 | 13.789 | 22.91 |

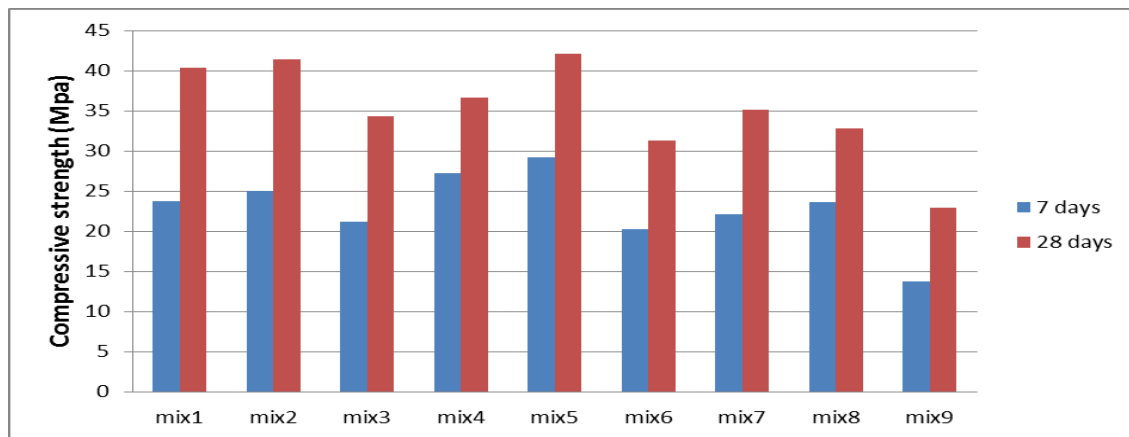


Figure 1. Compressive strengths of the concrete mixtures.

Flexural strength

Flexural strength of the concrete mixtures obtained in this paper are shown in table(8) and Figure (2). The optimum mix was Mix₂ in Group (B) with (cement : 50% naturally sand and 50% crushed recycled concrete as sand : crushed boulder as gravel), which enhance and increase the flexural strength by (8%), as comparing with Mix₁ (Reference mix).

Table(8) Flexural strength of the concrete mixtures

| Mix no. | Flexural strength (Mpa) | |
|---------|-------------------------|---------|
| | 7 days | 28 days |
| Mix 1 | 4.11 | 4.65 |
| Mix 2 | 4.136 | 4.72 |
| Mix 3 | 4 | 4.22 |
| Mix 4 | 4.377 | 4.57 |
| Mix 5 | 4.481 | 4.81 |
| Mix 6 | 3 | 3.44 |
| Mix 7 | 3.32 | 3.63 |
| Mix 8 | 3.56 | 3.74 |
| Mix 9 | 2.9 | 3.284 |

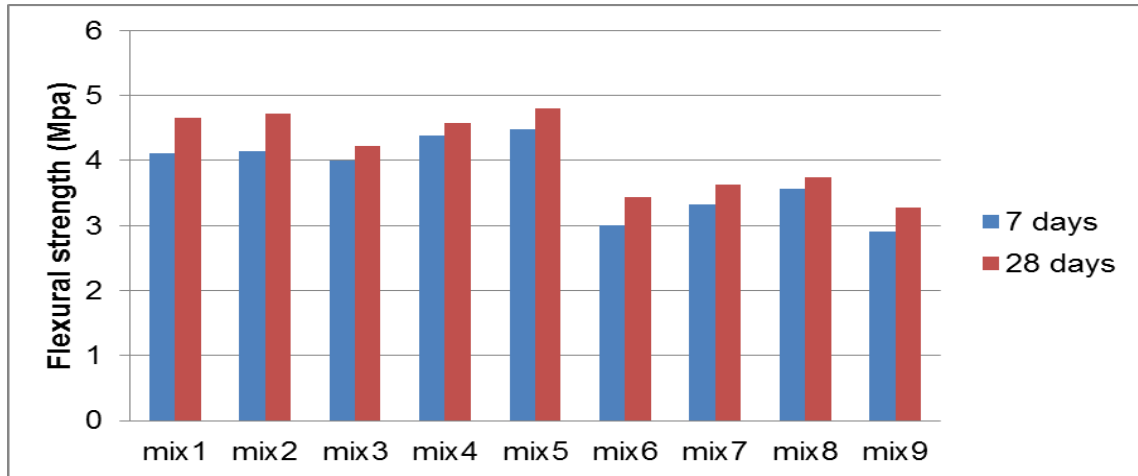


Figure 2. Flexural strengths of the concrete mixtures

Splitting tensile strength

Splitting tensile strength of the concrete mixtures obtained in this paper are shown in table(9) and figure (3). The optimum mix was Mix₂ in Group (B) with (cement : 50% naturally sand and 50% crushed recycled concrete as sand : crushed boulder as gravel), which enhance and increase the splitting tensile strength by (29%), as comparing with Mix₁ (Reference mix).

Table(9) splitting tensile strength of the concrete mixtures

| Mix no. | Splitting tensile strength (Mpa) | |
|---------|----------------------------------|---------|
| | 7 days | 28 days |
| Mix 1 | 2.051 | 3.68 |
| Mix 2 | 2.368 | 3.82 |
| Mix 3 | 2.757 | 3.46 |
| Mix 4 | 2.741 | 3.39 |
| Mix 5 | 2.884 | 3.96 |
| Mix 6 | 2.1 | 2.38 |
| Mix 7 | 1.9 | 2.68 |
| Mix 8 | 2.275 | 2.91 |
| Mix 9 | 1.44 | 1.83 |

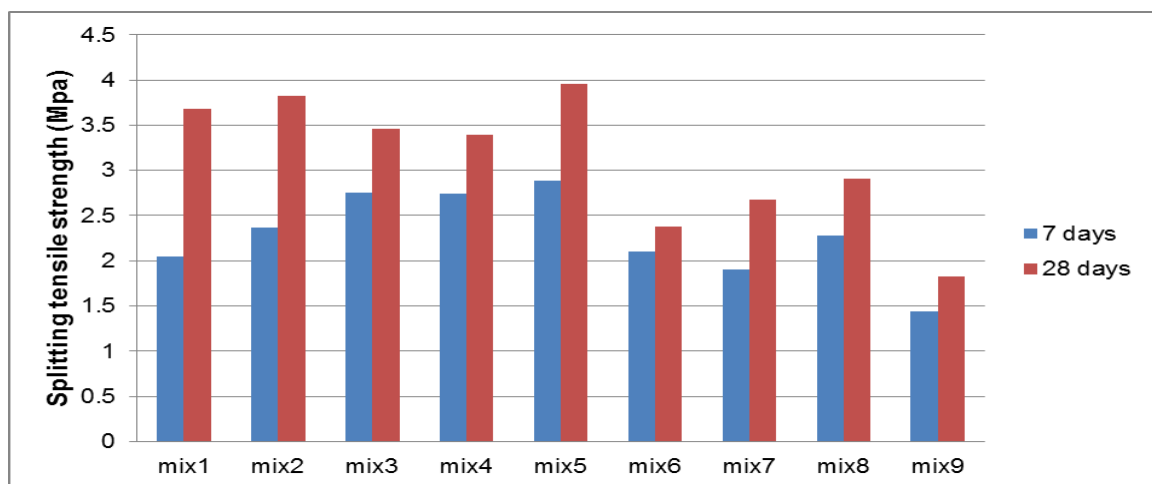


Figure 3. Splitting tensile strengths of the concrete mixtures

Conclusion

The experimental results showed that the optimum mix was Mix₂ in Group (B) with (Cement : 50% naturally sand and 50% crushed recycled concrete as sand : crushed boulder as gravel), which enhance the mechanical properties of the existing concrete , such that, increasing compressive strength by (19%), Flexural strength by (8%) and Splitting strength by (29%), as comparing with Mix₁ (Reference mix), The use of recycled concrete aggregate reduced the density of the new concrete, Recycling waste concrete aggregate in concrete production may help to solve the problem of the environment.

Recommendations

It is not recommended to use fine or coarse recycled aggregate as a ratio of 100% because they are reduced the strength of concrete.

References

- Buck, A., D., (1977). "Recycled concrete as a source of aggregate". *ACI Journal*,74, 212–219.
- Hansen, T., C., & Hedegkd, S. E. (1984, January). "Properties of recycled aggregate concretes as affected by admixtures in original concretes". In *Journal Proceedings* (Vol. 81, No. 1, pp. 21-26).
- Rahal, K., (2007). "Mechanical properties of concrete with recycled coarse aggregate". *Building and environment*, 42(1), 407-415.
- Specification, I., S., No. 5 1984 Portland cement. Ministry of Planning, Central Organization for Standardization and Quality Control.
- ASTM., (2012). ASTM C1602/C1602M-12: Standard specification for mixing water used in the production of hydraulic cement concrete.

Author Information

Ali Hussein Ali

Assistant professor
Northern Technical University/
Engineering Technical College
Mosul / Iraq
Contact E-mail: alihussainali@ntu.edu.iq

Saleh Jaafer Suleiman

Northern Technical University
Engineering Technical College
Mosul / Iraq

Mahmoud Majid Hameed

Northern Technical University
Engineering Technical College
Mosul / Iraq
